Leveraging Electron Microscopy and Electrical Diagnostics to Address Challenges in Plasma Catalysis

Robin De Meyer

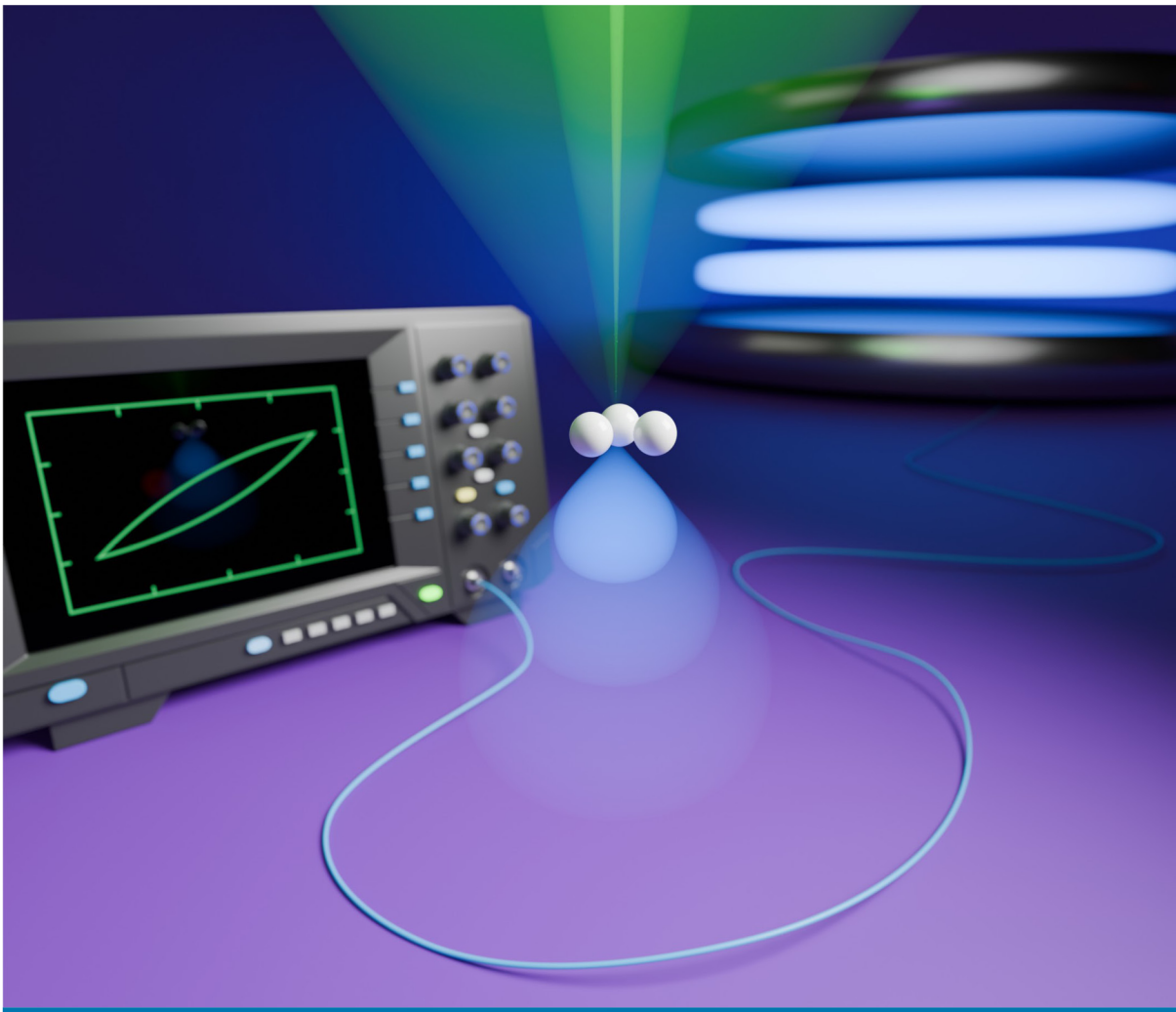

Supervisor **Prof. Dr. Sara Bals, Prof. Dr. Annemie Bogaerts, Prof. Dr. Jo Verbeeck**

Thesis submitted for the degree of Doctor of Science: Physics
Faculty of Science | Antwerp, 2025

University of Antwerp

Faculty of Science
Department of Physics

Leveraging Electron Microscopy and Electrical Diagnostics to Address Challenges in Plasma Catalysis

Thesis submitted for the degree of

Doctor of Science: Physics

At the University of Antwerp

To be defended by

Robin DE MEYER

Promotors:
Prof. dr. Sara Bals
Prof. dr. Annemie Bogaerts
Prof. dr. Jo Verbeeck

Antwerp, 2025

The PhD researcher and supervisors declare that the PhD research was conducted according to the principles of scientific integrity, as mentioned in the general PhD regulations and charter for PhD researchers of UAntwerp and the integrity charter for PhD researchers and supervisors affiliated with the University of Antwerp.

A part of this research was funded by the FWO (V447124N)

Dutch Title: “Elektronenmicroscopie en elektrische diagnostiek om uitdagingen in plasmakatalyse aan te pakken”

Dutch Qualification of the Degree: “Doctor in de wetenschappen: fysica”

University of Antwerp
Faculty of Science
Groenenborgerlaan 171, 2610, Antwerp, Belgium

Research group EMAT
Electron Microscopy for Materials Science
Department of Physics

Research group PLASMANT
Plasma Lab for Applications in Sustainability and Medicine – ANTwerp
Department of Chemistry

Members of the Jury

Chair

Prof. dr. Nick Van Remortel, University of Antwerp, Belgium

Promotors

Prof. dr. Sara Bals, University of Antwerp, Belgium
Prof. dr. Annemie Bogaerts, University of Antwerp, Belgium
Prof. dr. Jo Verbeeck, University of Antwerp, Belgium

Members

Prof. dr. Pegie Cool, University of Antwerp, Belgium
Prof. dr. Maria Seo, KU Leuven, Belgium
Prof. dr. Jan Benedikt, Kiel University, Germany

Summary

Gas conversion by plasma (ionized gas) is gaining interest as a potential candidate to contribute to the electrification of the chemical industry. Several approaches are considered, and this work mainly focuses on plasma catalysis. In plasma catalysis, a catalytic material is combined with a plasma with the aim of improving the performance of the process. However, several aspects of plasma catalysis are poorly understood, with many complex underlying mechanisms hindering a straightforward understanding, optimization, and implementation of this technology.

This work takes a multidisciplinary approach to address current challenges in plasma catalysis. On the one hand, the electrical diagnostics of dielectric barrier discharges are employed to understand the discharge properties and correlate them to other observations. On the other hand, electron microscopy is leveraged to gain insights into the microscopic structure of the relevant materials in this research.

The first chapter provides a general introduction to plasma, plasma catalysis, and current challenges in the field, after which an outline of this work is presented. In the second chapter, relevant concepts of electron microscopy and electrical diagnostics of dielectric barrier discharges are discussed.

Then, the effect of the catalytic material on the plasma discharge is illustrated. The microscopic properties of the catalytic material, elucidated by electron microscopy, clearly influence the plasma discharge characteristics. Moreover, these discharge characteristics can dominate the overall performance of the plasma-catalytic process. These results highlight the need for detailed electrical diagnostics in plasma catalysis, as purely catalytic effects can only be proven when understanding the contribution of the plasma chemistry.

Further, erosion of the exposed electrode in the dielectric barrier discharge is found to contaminate the material inside the plasma reactor, such as a catalyst. This behavior is found to be persistent across several gases and plasma reactors. However, electrical characterization of the discharge combined with several electron microscopy techniques reveal that the discharge characteristics influence the formation and microscopic properties of these erosion products.

Next, a simplified system is employed to investigate the effect of a material on the dielectric barrier discharge. This material-plasma interaction is found to be crucial in

many applications, such as plasma catalysis, but it is often challenging to study. A diffuse discharge is generated in a double-dielectric barrier discharge, where both electrodes are covered by a dielectric. One of these dielectrics is coated with a thin layer of Fe nanoparticles by pulsed laser ablation, yielding a conductive layer when sufficient material is deposited. This conductive layer is found to significantly influence the electrical properties of the system, thus affecting the discharge characteristics. Further, the results indicate that the material can additionally affect the plasma through other processes, such as enhanced electron emission, enabling a discharge at lower voltages.

Furthermore, a plasma setup is presented that enables the investigation of a material with a scanning electron microscope while it is exposed to a plasma. A stable glow discharge can be generated inside the microscope chamber while operating the microscope. This system is characterized and the effect of the plasma on materials is investigated. As the plasma operates with a constant electric field, the sample is continuously bombarded with ions and sputtering can be observed. This process is further illustrated by the formation of microscopic conical structures by plasma exposure. In addition, oxidation of the sample is observed when exposed to an oxygen-containing plasma, highlighting the potential of this system in the field of plasma catalysis and beyond.

Finally, the general conclusions of this work are summarized and put into a broader context. Further, a general outlook on the field based on these results is provided.

Samenvatting

Gasconversie met behulp van plasma (geïoniseerd gas) wint aan interesse als een potentiële kandidaat om bij te dragen aan de elektrificatie van de chemische industrie. Verschillende pistes worden hierbij overwogen, en dit werk focust voornamelijk op plasmakatalyse. In plasmakatalyse wordt een katalytisch materiaal gecombineerd met plasma, met als doel de prestatie van het proces te verbeteren. Verschillende aspecten van plasmakatalyse zijn echter onvoldoende begrepen, met vele complexe onderliggende mechanismen die eenvoudig begrip, optimalisatie en implementatie van deze technologie verhinderen.

Dit werk gebruikt een multidisciplinaire benadering om huidige uitdagingen in plasmakatalyse aan te pakken. Enerzijds wordt elektrische karakterisatie van de diëlektrische barrière ontlading toegepast om de eigenschappen van de ontlading te begrijpen en te correleren met andere observaties. Anderzijds wordt elektronenmicroscopie gebruikt om inzichten te bekomen in de microscopische eigenschappen van relevante materialen binnen dit onderzoek.

Het eerste hoofdstuk biedt een inleiding tot plasma, plasmakatalyse, en huidige uitdagingen binnen het veld, waarna een overzicht van dit werk wordt voorgesteld. In het tweede hoofdstuk worden relevante concepten rond elektronenmicroscopie en elektrische diagnostiek van diëlektrische barrière ontladingen toegelicht.

Vervolgens wordt het effect van het katalytisch materiaal op de plasma-ontlading geïllustreerd. De microscopische eigenschappen van het katalytisch materiaal, bestudeerd met elektronenmicroscopie, hebben duidelijk een invloed op de kenmerken van de plasma ontlading. Bovendien kunnen deze kenmerken van de ontlading een dominante invloed hebben op de algemene prestatie van het plasma-katalytisch proces. Deze resultaten benadrukken de nood aan gedetailleerde elektrische karakterisatie van de ontlading in plasmakatalyse, aangezien een zuiver katalytisch effect enkel aangetoond kan worden wanneer de bijdrage van de plasmachemie duidelijk is.

Dan wordt aangetoond dat de blootgestelde elektrode van de diëlektrische barrière ontlading erodeert en zo het materiaal in de plasmareactor, zoals een katalysator, contamineert. Dit effect blijkt hardnekkig te zijn en wordt beschreven voor meerdere plasma-experimenten in verschillende gassen en reactoren. De elektrische karakterisatie van de ontlading, gecombineerd met verschillende elektronenmicroscopie technieken,

tonen echter wel aan dat de kenmerken van de ontlading de vorming en microscopische eigenschappen van de erosieproducten beïnvloeden.

Daarna wordt een vereenvoudigd systeem gebruikt om het effect van een materiaal op de diëlektrische barrière ontlading te onderzoeken. Deze interactie tussen materialen en plasma is cruciaal in vele toepassingen, zoals ook in plasmakatalyse, maar is vaak erg moeilijk om te bestuderen. Een diffuse ontlading wordt gegenereerd in een dubbele-diëlektrische barrière ontlading, waarbij beide elektroden bedekt zijn met een diëlektricum. Een van deze diëlektrica wordt door gepulste laser ablatie bedekt met een dunne laag Fe nanodeeltjes, wat een geleidende laag oplevert wanneer voldoende materiaal wordt gedeponeerd. Deze geleidende laag blijkt de capaciteiten van het systeem gevoelig te beïnvloeden, wat op zijn beurt een effect heeft op de kenmerken van de ontlading. Verder geven de resultaten ook aan dat het materiaal nog een bijkomend effect kan hebben op het plasma via andere mechanismen, zoals versterkte elektronenemissie, waardoor de ontlading kan plaatsvinden bij lagere spanningen.

Vervolgens wordt een plasma-opstelling ontwikkeld die het mogelijk maakt om een materiaal te bestuderen met een rasterelektronenmicroscoop terwijl het wordt blootgesteld aan een plasma. Een stabiele gloei-ontlading kan gegenereerd worden in de kamer van de microscoop terwijl de microscoop operationeel is. Dit systeem wordt gekarakteriseerd en de invloed van het plasma op materialen wordt onderzocht. Aangezien het plasma wordt onderhouden door een constant elektrisch veld, worden ionen continu naar het materiaal versneld waardoor sputteren kan worden vastgesteld. Dit proces wordt verder geïllustreerd door de vorming van kegelvormige structuren door blootstelling aan het plasma. Daarnaast wordt ook oxidatie van het materiaal geobserveerd wanneer het wordt blootgesteld aan een zuurstofhoudend plasma, wat het potentieel van dit systeem voor plasmakatalyse en andere toepassingen verder benadrukt.

Tot slot worden de algemene conclusies van dit werk samengevat en in een bredere context geplaatst. Daarnaast wordt ook een vooruitzicht op het veld gepresenteerd op basis van deze resultaten.

Acknowledgements

My PhD has been an incredible journey in which I learned a lot about science, research, and myself. I have been immensely fortunate and privileged to have been able to do this PhD in two (large) research groups, surrounded by many fantastic people, while being supervised by three promotors. Where I am today and what I have achieved was only possible thanks to the many opportunities I was given and the tremendous support of many people throughout these years.

First of all, I want to thank my promotors. Thank you for giving me the opportunity to do this research and for your faith in me, allowing me to explore my own scientific interests. Thank you for your continued support throughout the years, for letting me work in the incredible environment of your labs, and for giving me the opportunity to do a research stay, travel, and build my own network, allowing me to grow as a scientist.

Sara, to me, the journey of this PhD started all the way back in my first bachelor year, when you presented your research to our class, immediately sparking my fascination for the world of electron microscopy. I still remember sitting in that lecture room, seeing the video where the camera moved through the atoms of a nanoparticle in 3D, being blown away and thinking: “I want to do that too”. Thank you for letting an inexperienced teenager (me) work with state-of-the-art equipment during my bachelor thesis, truly opening my eyes to scientific research. When during my master I mentioned I wanted to do a PhD, not only were you immediately enthusiastic, you even asked me what topic I wanted to work on. That faith you had in me and the freedom and opportunities that came with is something I remain very grateful for. I also want to thank you for your support throughout the PhD, continuously motivating me and allowing me to learn and grow.

Annemie, curiously, our first interactions also go back to my very early days at the university, years before my PhD would start. In my second bachelor year, you gave a lecture about plasmas to the small group of honors students of our year. I was immediately fascinated by plasma and decided to spend some time in your group as a part of that honors program, which further grew my interest in the research topic. In the final report I had to write, I casually noted that there were quite some physicists in the group, being part of the chemistry department, after which you swiftly responded that I would be welcome to do a PhD as well… How forward-looking. When I suggested to Sara I could do a joint PhD with your group, you were both very enthusiastic from the start.

Thank you, for that incredible opportunity, and the faith you had in me. I'm also very grateful for the freedom I had doing my research, allowing me to explore and find my own interests. Thank you for your empathy and enthusiasm, and for always finding time for your students.

Jo, you got involved a little later in my PhD, but nevertheless it was a pleasure to be able to work with you. Your creativity and (sometimes moderately crazy) ideas were inspiring and helped me learn a lot. After every discussions with you, I would have learned something, gotten new ideas, and was motivated to try new things. Thank you for your enthusiasm and inspiring me to think outside the box.

Next, I would like to thank Sylvain, who I consider my promotor *ad interim*. Thank you for giving me the incredible opportunity of spending 3 months in your lab, doing the research I wanted to do. This experience, both doing the research and living abroad, was incredibly enriching, and will have a profound and lasting impact on me. Thank you for your enthusiasm and mentorship, and for your faith in me.

Thank you, to my many(!) colleagues, at PLASMANT, EMAT, and CPPE, for your help and advice, creating a nice working environment, making delicious treats, and so much more.

Starting at PLASMANT: Pepijn, you are an exceptional scientist, and spending these years in the same office as you was a privilege. Our countless discussions, your critical and analytical mind and your honest feedback have been incredibly valuable and inspiring. Callie, thank you for your continuous support and for the positive energy your bring to every occasion, and for the roller coaster that were our (sometimes late-night) lab endeavors. Joran, thank you for your critical mindset and the many thought provoking (and fun) discussions, and for teaching me all about catalysis – quite the blind-spot when starting this PhD… Elli, thank you for the enjoyable collaborations, teaching me about microwave plasmas and for being such a warm and welcoming person. Rani, thank you for your support and advice, and our wonderful conversations. Bart, thank you for the many(!) hours at the GC and teaching me so much about it. Ivan, thank you for the insightful discussions and your critical input. Stein, thank you for the interesting conversations, ranging from deeply technical and scientific to downright absurd – much appreciated. Helder, thank you for bringing a fun and positive energy wherever you go – your time in our office was far too short. Talking about our office, thank you Sara C. and Sarah for regularly checking in, making sure everyone was doing well, for bringing a friendly atmosphere to the office, and most of all, for your amazing baking skills and the many treats you brought. Omar, thank your kindness and wisdom. Thank you to Yury

and Radu (not technically Plasmant, but the same building so close enough) for teaching me how to work in a chemical lab and for the productive collaboration. Thank you to Karen, Karel, Thomas K., Herman, Luc and Priyanka for your technical and administrative support. Thank you to all the other Plasmant colleagues for making it such a warm and fun environment to work in.

Further, I would like to thank my (current and former) EMAT colleagues, who taught me many things and created a nice environment. Nathalie, thank you for being such a calm and kind person. Over the years, already from my master thesis, I learned countless things from you and you were always there to listen and support me. Robin G., thank you for the nice conversations, good advice and valuable feedback. Nick S., from making me excited about experimental physics in the first bachelor year, to encouraging my curiosity in the honors program and being a mentor and a colleague as we were teaching together, your warm and enthusiastic approach to science and education have had a profound impact on me, thank you. Lukas, thank you for all those days at the microscope, filled with excitement, disappointment, and lots of trial and error, and for teaching me so much about SEMs. Dmitry, thank you for your invaluable contribution to the development of the plasma setup inside the SEM. Rajesh, thank you for your positivity, the nice collaboration and many wonderful conversations. Tom, thank you for the many lunches and conversations and for your help with my statistics questions. Safiyye, thank you for your help and your kindness. Evgenii, thank you for your valuable advice and support. Deema, thank you for bringing such a warm and kind atmosphere to our office, for taking care of the tropical forest that became our office flora, and of course for the wonderful treats you brought us. Luca, it was a pleasure having you in the office, you kindness and creativity are inspiring. Arno, it was always enjoyable conversing with you, and I greatly appreciate your honesty and critical mind, I learned a lot from you, thank you. Fran, thank you for your advice and fun spirit, ensuring things never got too serious in the office. Tama and Thomas, thank you for the wonderful treats you brought to the office, always a feast. Sven, thank you for the conversations and support. I also want to thank Lars, Stijn, Saeid, Alex, and Armand for their help with all my technical issues, and thank you Lydia, Miek, Catherine, and Gert for their invaluable administrative and practical support.

I also want to thank my colleagues at CPPE. Although my stay was relatively brief, I am grateful for the warm welcome and support I received. Dante, thank you for your incredible engineering and problem-solving skills, and for all the support in getting the setup operational. Phil, thank you for your help with the sample preparation and

characterization. Lynn, thank you for the warm and welcoming atmosphere you created. Though not directly involved in the research stay, I would also like to thank Ronny B. for his support and advice in the interpretation of the data from this research stay.

Finally, I want to thank my family and friends for supporting me throughout the PhD. Isaac, thank you for your kindness, understanding, and unwavering support. Further, I want to thank my parents and my sister for supporting me in so many ways. Thank you for taking care of various practical things, ensuring I could dedicate my time and energy to my PhD, while also providing me with all the support I could imagine and for encouraging me to pursue my passion.

List of Abbreviations

AC	Alternating Current
APTD	Atmospheric Pressure Townsend Discharge
BET	Brunauer-Emmett-Teller
BF	Bright Field
BSE	Backscattered Electrons
CTEM	Conventional Transmission Electron Microscopy
DBD	Dielectric Barrier Discharge
DC	Direct Current
DRM	Dry Reforming of Methane
EC	Energy Cost
EDX	Energy-Dispersive X-ray Spectroscopy
ESEM	Environmental SEM
ETD	Everhart-Thornley Detector
FFT	Fast Fourier Transform
FOV	Field Of View
GC	Gas Chromatograph
HAADF	High-Angle Annular Dark Field
IF	Influx Fraction
IGP	Ion Getter Pump
IR	Infrared
LFD	Large-Field Detector
MFC	Mass Flow Controller
MFR	Mass Flow Rate
mln	Normal ml
mls	Standard ml

MW	Microwave
NDIR	Non-Dispersive Infrared (Sensor)
NRP	Nanosecond Repetitive Pulsed (Plasma)
PLA (Chapter 5)	Pulsed Laser Ablation
PLA (Chapters 2, 6)	Pressure-Limiting Aperture
PSU	Power Supply Unit
RF	Radio Frequency
SC	Spray-Coating
sccm	Standard Cubic Centimeter per Minute
SE	Secondary Electrons
SEI	Specific Energy Input
SEM	Scanning Electron Microscope
STEM	Scanning Transmission Electron Microscope
STP	Standard Temperature and Pressure
TEM	Transmission Electron Microscope
WDX	Wavelength-Dispersive X-ray Spectroscopy
WI	Wet Impregnation
XRD	X-ray Powder Diffraction

Table of Contents

Chapter 1

General Introduction

1. Context

Rapid change in the earth's climate due to anthropogenic greenhouse gas emissions is a well-known phenomenon, which poses significant challenges to our current societies [1,2]. These changes in our climate are already noticeable today, and are predicted to only get worse in the coming decades. In order to limit these changes in the long term and eventually stabilize the climate, the solution is clear. Greenhouse gas emissions, the most common being CO_2, should be drastically reduced. On the one hand, this can be achieved by replacing CO_2-generating processes by alternatives that do not produce this greenhouse gas. On the other hand, CO_2 could be captured to be permanently stored, or even converted into useful chemicals, closing the carbon loop [3].

One of the largest CO_2 emitters is the industry, being responsible for approximately 38% of global greenhouse gas emissions due to fuel combustion in 2022 [4]. Currently, many of the processes we need for the fabrication of essential products require high temperatures and pressures, and are generally highly energy-intensive. Often, the main energy source used in these processes is based on fossil fuels. In order to eliminate the corresponding greenhouse gas emissions, a fundamentally different energy source is required. A natural choice for many of these processes, would be to use electrical energy. An advantage of using electricity is that it can be generated in multiple sustainable ways, and it is relatively easy to transport (over short and medium distances). In addition, the electrical processes would be inherently suitable for an emission-free industry [3].

Several technologies can potentially contribute to an electrified chemical industry to produce the chemicals we need while eliminating the greenhouse gas emissions. One of the options that is being considered is plasma technology. Plasma-based processes have several key advantages. For example, they are inherently electricity-based, can often operate at atmospheric pressure (making the overall installation generally less expensive), and usually allow for fast on/off switching, making them potentially interesting to work in unison with intermittent energy sources such as solar or wind energy [5,6]. In addition, plasmas can be highly reactive, potentially enabling the conversion of the stable CO_2 molecule.

2. Plasma

Plasmas can be described as (partially) ionized gases, consisting of free electrons, ions, radicals and excited species, in addition to the neutral gas molecules or atoms [7,8]. Often, plasmas are generated by an electrical discharge, where a sufficiently strong electric field causes a breakdown in a gas, causing charged species to collide with gas molecules, forming additional charged species, which are accelerated in the electric field to sustain the discharge. A huge variety of plasmas exist, many of which occur naturally. A typical example of a natural plasma is lightning, where a discharge takes place inside clouds, or between clouds and the earth. Other examples of naturally occurring plasmas are the northern lights and the sun, though these are generated in a very different way. Such large scales, however, are not necessary to generate a plasma. For example, when you get a static discharge when touching something conductive, a microscopic plasma discharge is generated between your skin and the conductive object.

In addition to naturally occurring plasmas, a wide variety of plasmas can be generated and are already exploited in technological applications. For example, high current arcs can easily reach very high temperatures, and are therefore used for welding or for melting materials with high melting points [9]. Due to the presence of many highly reactive species in a plasma, it can also be used for chemical conversion. For example, dielectric barrier discharges have been widely used for ozone generation [10]. Furthermore, these chemically reactive plasmas can also be used for materials applications. One of the major industrial applications of plasmas is in the semiconductor industry, where it is used for etching and cleaning in the fabrication process of computer chips [11].

Figure 1-1 illustrates the wide variety of plasmas that exist (though it is not exhaustive). Several types of plasma are placed on the graph based on their gas temperature and their electron temperature. The gas temperature is a common concept, and represents the temperature of the bulk of the gas. The electron temperature is a metric that describes the kinetic energy of the free electrons in the plasma. In the electric field of a discharge, all charged species are accelerated. However, since electrons are several orders of magnitude lighter than the heavy particles (i.e., ions), they will gain velocity much faster. Therefore, under certain discharge conditions, the temperature of the electrons can be orders of magnitude higher than the temperature of the gas. The plasmas that exhibit such a notable discrepancy between the gas and electron temperature are called non-equilibrium or non-thermal plasmas. Indeed, for some

plasmas the gas temperature can be near room temperature, whereas the electron temperature reaches several thousand Kelvin [12,13].

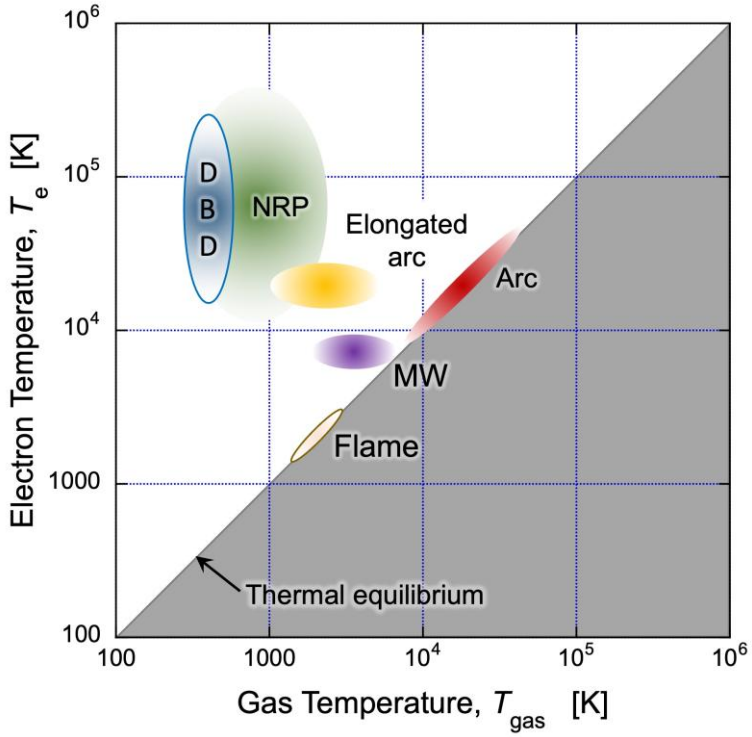

Figure 1-1: Various types of plasma represented based on their typical gas- and electron temperatures. DBD stands for dielectric barrier discharge, NRP for nanosecond repetitive pulsed (plasma), and MW for microwave (plasma). Thermal equilibrium indicates that the gas- and electron temperature are equal. DBDs typically exhibit low gas temperatures and high electron temperatures. Reproduced from [14], CC BY 4.0 [15].

These high electron temperatures make plasma a highly reactive environment, even when the gas temperature may be limited. Therefore, plasmas could be of interest for inducing chemical reactions that may not be typically favorable at lower temperatures. This work focuses mainly on plasmas for gas conversion. Plasmas may be used for producing chemicals that currently rely on fossil fuels, or even for directly converting CO_2. Specifically, this work explores the field of plasma catalysis, where a catalyst is combined with the plasma to enhance the overall process [16]. In catalysis, a catalyst is used to reduce the activation barrier of a chemical reaction [17]. Hereby, the desired reaction can take place notably quicker, and depending on the specific catalyst, the reaction may be steered toward the desired products. Thermal catalysis forms the

backbone of the modern chemical industry, and can therefore be considered as highly effective. However, given the described issues with regard to greenhouse gas emissions, an electrified alternative is needed. Given the great successes of thermal catalysis, and the promise (and in part proven effectiveness) of plasma-based gas conversion, combining plasma with catalysis is considered as a potential candidate to contribute to a sustainable future.

3. Plasma Catalysis

As mentioned in the previous section, and illustrated in Figure 1-1, a great variety of plasmas exist. However, when aiming to combine plasma with catalysts, not all plasmas are suitable. For gas conversion, heterogeneous catalysis is typically used. Here, a solid material acts as the catalyst, offering so-called active sites. On these active sites, species can adsorb from the gas phase, chemical reactions can take place, after which the desired products can desorb and leave the system in the gas phase. In order to create such a catalytic system in combination with plasma, the catalytic materials should be compatible with the plasma discharge. A major limiting factor here is the temperature. Certain plasmas, such as arcs, can reach very high temperatures (above 10 000 K), making them generally incompatible with catalytic materials.

Considering the properties of the various discharges presented in Figure 1-1 with the aim of combining plasma with a catalytic material, a clear distinction can be made. In this graph, the dielectric barrier discharge (DBD) stands out for having a low gas temperature and a high electron temperature. In addition to the DBD, nanosecond repetitively pulsed (NRP) plasmas can have similar temperatures. However, in order to maintain such low gas temperatures, the power deposition into the NRP plasma should be strongly restricted, which limits its potential for large-scale gas conversion applications. Therefore, the DBD holds more promise for the direct combination of a plasma with a catalytic material [18].

4. Dielectric Barrier Discharge

Dielectric barrier discharges are a fascinating and complex type of plasma. A DBD is generated by creating a sufficiently strong electric field between two electrodes, where at least one of the electrodes is covered by a dielectric. This dielectric will charge as the discharge takes place, which locally reduces the electric field and usually quickly stops

the discharge. Therefore, sustained high current arcs cannot be formed, and the gas temperature remains low. In addition, this behavior requires the DBD to be driven by an alternating current (AC) or pulsed voltage [8,19].

Although the DBD is currently of great interest for plasma catalysis, it is hardly a new technology. The DBD was first described in the 1850s [20] and has been developed and studied ever since. One of the greatest successes of the DBDs is the synthesis of ozone, for which they are still being used today [10]. In addition, DBDs have been used in CO_2 lasers and plasma displays, where the light-emitting properties of plasma are exploited. Furthermore, DBDs are applied in the treatment and modification of surfaces, such as polymer films [10,21].

Thanks to the decades of research and development on DBDs, many aspects of the physical processes governing these discharges are well understood [12,22]. Generally, the DBD operates in a so-called filamentary mode. Herein, the gap between the two electrodes is bridged by individual filaments of plasma, rather than filling the entire volume homogeneously. In these filaments, many microdischarges take place, which are short-lived, but very intense bursts of current. These intense currents are due to the streamer discharge taking place in the DBD [19]. As illustrated in Figure 1-2 A, a streamer discharge starts by electrons being accelerated in the electric field. These initial charges can be formed by, e.g., cosmic rays or radioactive decay, but could also originate from a previous discharge (so-called memory effect). The electrons gain energy in the electric field and collide with gas molecules. When the electrons are sufficiently energetic, these collisions cause ionization of the gas molecules, and charge multiplication takes place. As more charges are created in the volume, the electric field can be locally enhanced. Consider a cloud of positive and negative charges in an electric field. Due to the electrostatic forces caused by the external electric field, the electrons and positive ions will drift in opposite directions (in practice the electrons move much faster than the heavy species, so the ions can often be considered almost stationary compared to the mobile electrons). This separation of the positive and negative charges generates an additional electric field outside the separated charges, locally enhancing the original electric field near the ionized volume, accelerating electrons close to the streamer even more. In addition to the electrons being accelerated, these processes also generate photons which in turn can photoionize molecules “ahead” of this ionization front, accelerating the process even more. This type of discharge is called a streamer breakdown and causes the formation of filaments in the gap of the DBD [19,23]. Once the streamer connects both electrodes, effectively a conductive channel (of ionized gas)

is formed in the presence of a strong electric field. Therefore, a high current will suddenly flow through the system. However, as the charges move across the gap, the surface of the dielectric will locally charge rapidly. When the dielectric charges, an opposing electric field is generated, which quickly extinguishes the discharge. This is why these microdischarges are intense, but very short-lived [12].

Under certain conditions, a different breakdown mechanism can take place, schematically presented in Figure 1-2 B. The so-called Townsend discharge is a diffuse discharge, in contrast to the discrete filaments for a streamer discharge, and is generally less common in DBDs [24–27]. In order to generate a Townsend discharge, a relatively high level of pre-ionization is required. This pre-ionization offers many free electrons in the volume, which collectively accelerate as an electric field is present. Again, the collisions of the electrons with neutral gas species will cause ionization and an avalanche of charge multiplication. However, in order to sustain this Townsend discharge, the ionization rate in the gas phase should be sufficiently low, to prevent the self-reinforcing electric field that eventually generates a streamer discharge. The pre-ionization required for the Townsend discharge is typically provided by memory effects in the DBD. The precise mechanisms of these memory effects can be very complex and are not always fully understood. One of the Townsend discharges that is reasonably well described is a discharge in pure N_2 [22]. Herein, metastable excited N_2 species can exist for a relatively long time (compared to the period of the discharge). These excited species generate secondary electrons as they collide with the electrode, providing the system with the needed charges in order to ignite and sustain the Townsend discharge. As a Townsend discharge requires pre-ionization, provided by previous discharges, the initial ignition of such a plasma tends to be filamentary, after which it quickly becomes a Townsend discharge [26].

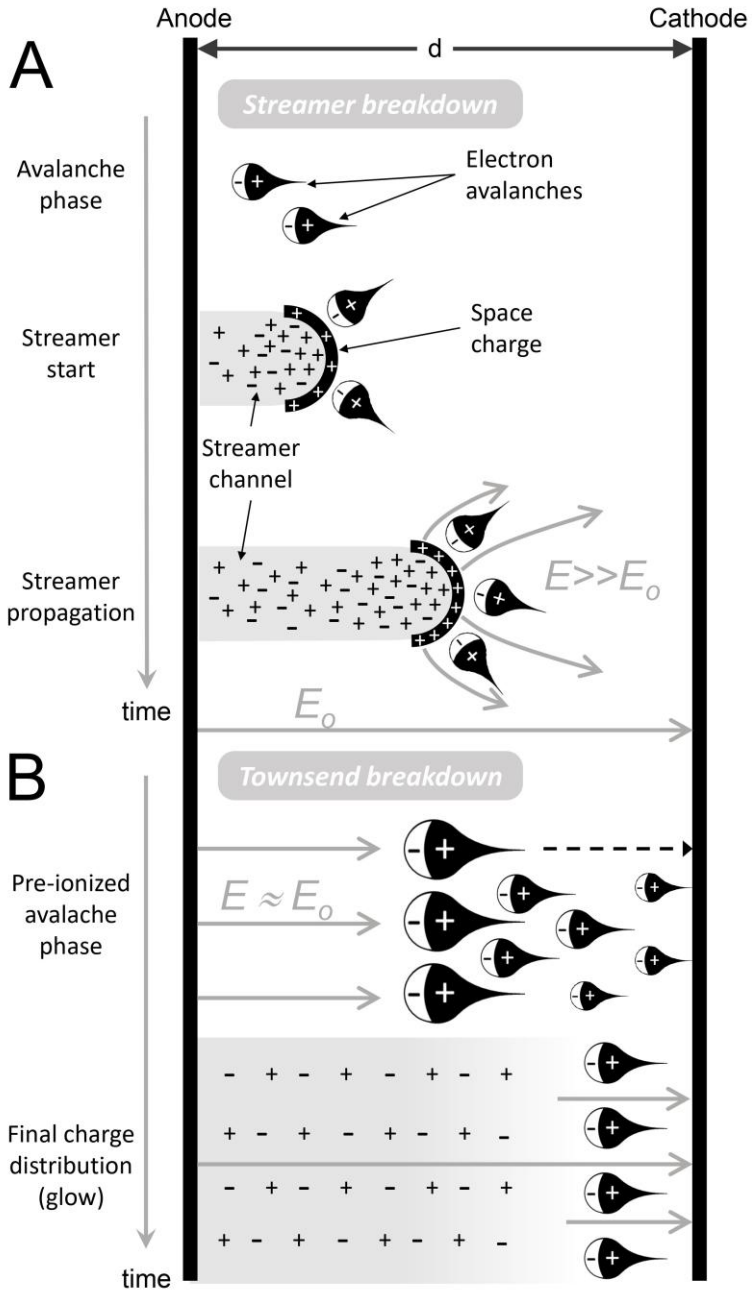

Figure 1-2: Illustration of the phases of a streamer breakdown (A) and a Townsend breakdown (B). (A): In a streamer breakdown, the head of the streamer can locally enhance the electric field, causing a self-reinforced discharge that leads to the formation of a streamer that crosses the gap between the electrodes. (B): In a Townsend discharge, sufficient pre-ionization is required which enables a diffuse discharge across the entire electrode area. Reproduced with permission from [12].

5. Challenges in Plasma Catalysis

There are several major challenges preventing the industrial implementation of plasma catalysis for gas conversion at this time. From an economic point of view, the performance of most plasma-catalytic processes is simply insufficient, with high energy costs for often poor yields [28]. From a more fundamental point of view, however, this is largely due to a lack of understanding of the relevant underlying mechanisms [16,29,30].

Although improvements in overall performance upon introduction of a catalyst are observed in many experiments, these results are not always consistent and reproducible. For example, Gorbanev et al. investigated plasma-catalytic NH_3 synthesis, using several metals supported on Al_2O_3 spheres [31]. The authors report a notable increase in NH_3 production when introducing the metals compared to using the blank support material. However, the difference in performance between the different investigated metals (i.e., Fe, Ru, Co, and Cu) is small. Barboun et al. performed similar experiments, investigating Ru, Co, and Ni supported on Al_2O_3 in plasma-catalytic NH_3 synthesis [32]. Interestingly, these authors report very different results. They again observe a notable increase in performance when introducing Ni or Co, compared to the blank support material. However, for Ru they only saw a very minor increase in performance, and it was notably worse compared to the Co catalyst, resulting in an opposite conclusion from Gorbanev et al. [31].

A similar discrepancy can also be found for other reactions. For example, in plasma-catalytic dry reforming of methane (DRM), some works report only minor or even negative effects of a Ni/Al_2O_3 catalyst [33,34]. On the other hand, certain studies find significant increases in conversion when introducing Ni catalysts [35,36]. Some authors attribute the observed performance to catalytic effects, whereas others stipulate it could be due to changes in the plasma discharge.

There can be several reasons for the inconsistencies in reported results for plasma-catalytic experiments. A likely cause, for at least some of the observed discrepancies, is changes in the plasma discharge characteristics. It is important to note that plasma catalysis is fundamentally different from thermal catalysis in the sense that gas-phase chemistry cannot be neglected. In many thermal catalysis systems, the temperatures are too low for any reactions to take place in the gas phase. Therefore, one can fairly assume that changes in observed performance are directly linked to the catalytic activity of the

investigated material. In plasma catalysis, this is no longer valid. Indeed, plasma on its own is highly reactive, and many reactions can take place in the gas phase. Therefore, changes observed in overall performance when introducing a catalyst are not necessarily due to the catalytic activity of the material. There have been several studies highlighting the changes in plasma discharge characteristics when a packing material (i.e., catalyst) is introduced in the discharge gap [33,37–39]. Although the underlying effects causing these changes are not fully understood, it does highlight the complexity of these systems, since introducing a catalyst could also affect the plasma behavior.

An additional challenge, especially considering the complexity of these systems, is a lack of uniformity and standardization [40]. Indeed, when different reactors and operating conditions are used, the plasma properties are likely to be different, thus making a direct comparison of the catalytic performance difficult. However, even if an effort is made toward more standardized plasma systems, reaching truly identical circumstances is extremely difficult. This is due to the inherent complexity of dielectric barrier discharges, where memory effects play a crucial role in determining the discharge characteristics [8,41]. At the same time, these memory effects can be greatly influenced by the (surface) properties of the used materials. An example illustrating how sensitive discharge mechanisms can be to material/surface properties is provided by Belinger et al., who investigated the frequency range in which a diffuse discharge can be sustained in air [42]. They report significant differences in discharge properties when using the same dielectric materials obtained from different manufacturers. Even though, in theory, the material properties of the used dielectrics (e.g., composition and dielectric constant) are the same, the frequency range in which a diffuse discharge can be sustained varies from 1.1 kHz to 4 kHz.

Because of this high sensitivity to the precise material and operating conditions, standardizing the plasma reactor across many research labs might not be feasible. However, these challenges posed by the high sensitivity of the discharge do highlight the need to characterize and report the plasma discharge. Indeed, a main reason for the lack of understanding of the plasma-catalytic performance is the difficulty distinguishing between the contributions of the gas-phase and the catalytic surface to the overall performance.

Further, the characterization of the employed materials is critical when investigating plasma-catalytic systems. Previous work found indications that the precise microscopic structure of the catalyst can influence the discharge properties [37]. Moreover, many of

the plasma-catalyst interactions take place on a microscopic scale, and thus characterization of these materials down to the (sub-)µm-scale is crucial.

In addition to the influence of the catalyst on the plasma, another challenge is understanding how the plasma affects the catalyst [43,44]. On the one hand, thermal effects which also play a role in thermal catalysis should be considered. Examples hereof are sintering, restructuring, or potentially even strong metal-support interactions. Chemical interactions between the reactive plasma and the catalyst, such as oxidation or reduction, may also occur. On the other hand, there are several additional complexities when exposing a material/catalyst to the plasma. For example, the material will charge, which can affect its electronic properties. In addition, there are often strong electric fields present in the plasma, which can further influence some of the material properties. Furthermore, charged or excited species can interact with the surfaces, causing additional energy transfer and potentially even structural changes [44].

6. Outline of this Thesis

It is clear that plasma-catalytic systems are highly complex, and that many challenges and open questions remain. These challenges can be summarized as a lack of fundamental understanding of the relevant underlying processes. The processes of interest span a wide variety of disciplines, going from purely gas-phase plasma chemistry, to the influence of the catalyst on the plasma discharge, but also regarding the effect of the plasma on the catalytic material, and finally the role of the catalyst in enabling enhanced plasma-driven chemistry.

The **main objective** of this work is to address key challenges that limit the understanding and implementation of plasma catalysis. Specifically, a thorough fundamental understanding of the many intricate processes that govern overall plasma-catalytic performance is required. In order to gain these fundamental insights, this work takes a unique multidisciplinary approach. On the one hand, advanced and innovative plasma discharge characterization is employed to obtain a detailed understanding of the discharge properties. On the other hand, this work exploits electron microscopy as a powerful technique to investigate nanoscale properties of relevant materials, which isn't commonly utilized for plasma catalysis investigations. By combining the results revealed through these techniques, novel insights can be obtained, as outlined in the following chapters.

In **Chapter 2**, an introduction to the characterization techniques used throughout this work is provided. Relevant general concepts of electron microscopy are briefly introduced, after which the techniques employed in this work are presented. The valuable capabilities of several techniques are discussed, and some limitations are described as well. Furthermore, the foundations of electrical diagnostics of dielectric barrier discharges are presented.

In **Chapter 3**, several plasma catalysis experiments are presented and a detailed characterization of the discharge is performed. In addition, the catalytic packing material is investigated by electron microscopy, revealing key properties of the various catalysts. By combining these results, it becomes clear that the packing material drastically affects the plasma discharge. Moreover, the discharge characteristics appear to dominantly determine the overall performance of the experiment, whereas the true catalytic effects seem negligible.

In **Chapter 4**, similar plasma experiments to those from Chapter 3 are performed, but this time without focusing on gas conversion. Instead, using several electron microscopy techniques, it is shown that the exposed electrode of the plasma reactor erodes. Furthermore, the erosion products are deposited on the packing material, potentially affecting plasma-catalytic performance. Moreover, a clear dominating effect of the plasma discharge characteristics on the erosion processes is found.

In **Chapter 5**, the plasma discharge is studied using a more fundamental approach. It is clear that the discharge characteristics play a crucial role in plasma catalysis, and that the catalysts critically affect the discharge. However, these interactions are poorly understood, and investigating them in packed-bed plasma reactors is hindered significantly by the complex geometry. Therefore, a Townsend discharge is employed, since it is very stable and reproducible, contrary to the stochastic filamentary discharge. In addition, a simplified parallel-plate geometry is used without a packing material to investigate how the discharge is affected by a (conductive) layer of nanoparticles on one of the dielectric barriers.

In **Chapter 6**, a plasma setup was built to operate inside a scanning electron microscope. This setup allows for true *in situ* characterization of a sample as it is exposed to a plasma discharge. Both in plasma catalysis and in other plasma-based processes, microscopic effects are often of great importance, highlighting the need for an advanced *in situ* characterization method with high spatial and temporal resolution. Characterization of the plasma-in-SEM system illustrated sputtering and nano-scale restructuring of

materials exposed to the plasma. Furthermore, oxidation of the sample could be observed after exposure to an oxygen-containing plasma.

In **Chapter 7**, general conclusions based on this work are discussed. In addition, an outlook on the field as a whole is presented.

Chapter 2

Introduction to Electron Microscopy and Electrical Diagnostics

1. Electron Microscopy

In a conventional visible-light microscope, light interacts with a sample to form an image that is magnified using lenses. In an electron microscope, a beam of accelerated electrons is used, rather than visible light. Using electrons has some distinct advantages compared to using visible light, but also comes with its challenges.

One of the major advantages of electron microscopes is their resolution (i.e., the smallest features that can be resolved), which is proportional to the wavelength of the used radiation. Thus, when employing visible light, the resolution of the microscope is limited to hundreds of nm, even when there are no lens aberrations [45]. Electrons, on the other hand, can be accelerated to achieve wavelengths several orders of magnitude below the wavelength of visible light [46]. Therefore, the limitation on the resolution of an electron microscope is much smaller than for a light microscope, enabling the investigation of nano-systems, even down to the atomic scale in advanced modern microscopes.

The advantages of electron microscopy go beyond an enhanced resolution. The interaction of energetic electrons with matter (i.e., the sample) is complex, based on many underlying mechanisms, generating a variety of signals. Depending on the operating conditions and the signals acquired, information can be obtained on various properties of the sample. For example, in certain imaging modes, as discussed in the following sections, the contrast scales with the mass density of the sample, enabling a more direct physical interpretation of an image. Furthermore, these high energy electrons cause the excitation of core-electrons in the sample, which in turn can generate characteristic X-rays as an electron fills that vacancy. This enables the investigation of the elemental composition of the sample, as discussed in more detail in this chapter.

In addition to the many advantages of electron microscopy, it also comes with challenges. For example, analyses are typically performed under high-vacuum conditions to prevent the interaction of the energetic electrons with gas molecules inside the microscope. Even when materials are stable under vacuum conditions, this does not necessarily represent a realistic environment of the material being investigated. Another challenge with this technique is potential damage to the sample caused by the energetic electrons, thus caution is required when designing an experiment and interpreting the data. Furthermore, the sample under investigation should be compatible with the

desired analyses, which might require complex sample preparation techniques. Typical examples of the requirements for electron microscopy characterization are sufficiently low thickness and electrical conductivity.

An inherent, but not always immediately obvious, limitation of electron microscopy is potential bias. Electron microscopes can have an outstanding spatial resolution, enabling the detailed investigation of individual nanoparticles, but that also makes this technique inherently local and small-scale. Even when investigating mm or even cm-scale samples, it is possible to resolve nm-scale features. However, it is practically not feasible to investigate the entire mm/cm-sized sample down to the nm-scale. Several approaches can be employed to determine regions of interest, but they often rely on the microscope operator to identify features worth characterizing. Therefore, there is an inherent risk to introduce bias in the dataset. This potential bias does not prevent the quantitative analysis and interpretation of electron microscopy data, though it is important to be aware of the related challenges.

The work outlined in this thesis employs several electron microscopy and nano-scale investigation techniques for precise characterization of materials to gain insights in plasma processes. The concepts and microscopy modes that are used in the next chapters are introduced in the following sections.

1.1 Transmission Electron Microscopy

In transmission electron microscopy (TEM), electrons are accelerated to high energies (typically between 60 and 300 keV) and interact with the sample under investigation. Due to the high energy of the electrons and the low thickness of the investigated material, the majority of the electrons are transmitted and an image can be formed based on these transmitted electrons. Several imaging and characterization modes can be employed in the TEM, and the most common ones, which are also used throughout this thesis, are introduced in the following sections. This section is largely based on [47].

1.1.1 Bright Field Transmission Electron Microscopy

In bright field transmission electron microscopy (BF-TEM; sometimes also called conventional TEM, CTEM), the sample is illuminated by a parallel beam of electrons which can be further manipulated by electromagnetic lenses to form and magnify an image. This optical system is very similar to a conventional visible-light microscope. A schematic representation of the optical system for BF-TEM is provided in Figure 2-1.

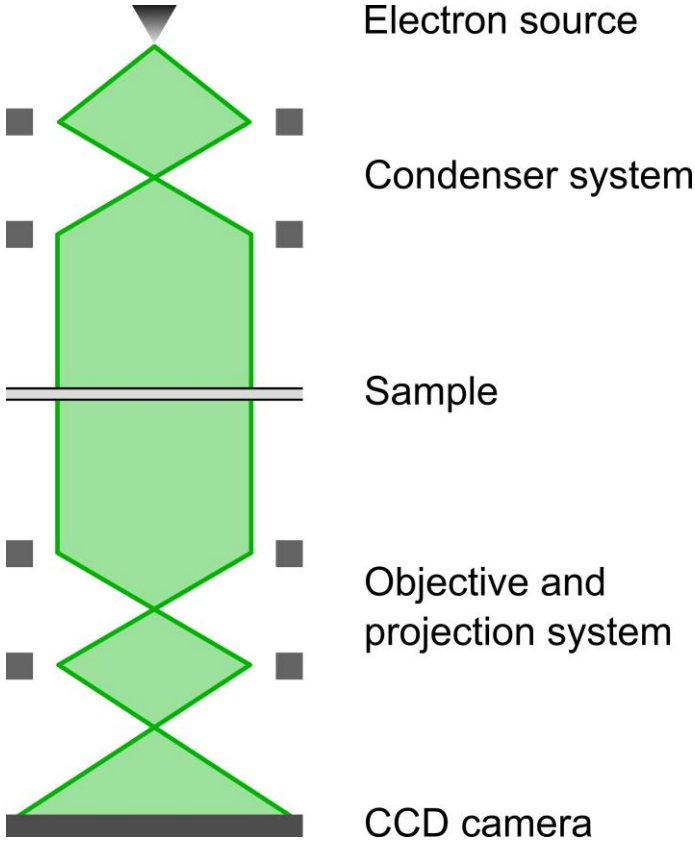

Figure 2-1: Schematic of the optical system of a BF-TEM. The condenser system manipulates the electrons to form a parallel beam that illuminates the sample. The image formed due to the interaction of the electrons with the sample is magnified, after which the image is captured by the 2D detector (here CCD camera).

The electrons are ejected from an electron gun and accelerated to the required energy. The electron beam then passes through the condenser system where the lenses manipulate the electrons to illuminate the sample as a parallel beam. After interacting with the sample, the transmitted electrons are manipulated by the objective and projection lenses to form a magnified 2D image on the detector.

Although the optical system in BF-TEM is similar to a conventional visible-light microscope, the image formation in BF-TEM can be complicated. Many different interactions can (and generally will) take place between the electrons and the sample, each resulting in different contributions to the final image. The contrast in the BF-TEM image generated by these interactions can generally be divided in two categories: amplitude contrast and phase contrast.

Amplitude contrast arises when electrons are scattered away from the optical axis, no longer contributing to the final image and thus reducing the number of electrons (i.e., amplitude of the electron wavefront) in the final image. This amplitude contrast is often related to the mass-thickness of the sample. The scattering probability of an electron increases monotonically with the atomic mass of the sample, so when the sample consists of heavier atoms and/or when there are more atoms (i.e., the sample is thicker), the mass-thickness increases, more electrons scatter, leading to a stronger mass-thickness contrast. These higher mass-thickness areas appear dark in the image, due to the lack of electrons.

Phase contrast formation is more complex and is caused by the wave-character of electrons. As the electron wavefront interacts with the sample, diffraction and phase shifts can occur, leading to a convoluted image contrast. Further, phase contrast is often highly dependent on the precise imaging conditions, such as the focus. Therefore, BF-TEM images can be challenging to interpret quantitatively, especially at higher magnifications, since all these effects can contribute to the overall image and elucidating the individual contributions in not always straightforward. However, due to the high sensitivity of phase contrast, it can enable the visualization of small-scale features, even in very light and weakly scattering samples.

An example of a BF-TEM image is presented in Figure 2-2, exhibiting both amplitude and phase contrast. In this image, a steel particle with graphitized carbon on its surface is shown. The steel particle appears dark because it is much heavier than the material surrounding it, scattering more electrons and thus leaving fewer electrons at that location in the image due to the mass-thickness amplitude contrast. At the surface of the particle, alternating dark and bright lines are visible. These are fringes caused by the phase contrast, as the electron wavefront interacts with the regular atomic planes of the graphitized carbon at the surface of the particle.

Due to the complicated image formation, BF-TEM images are not always straightforward to quantitatively interpret. However, they do offer valuable (qualitative) microscopic information on the structure of a material, making it a powerful characterization technique when studying the nano-scale properties of a material.

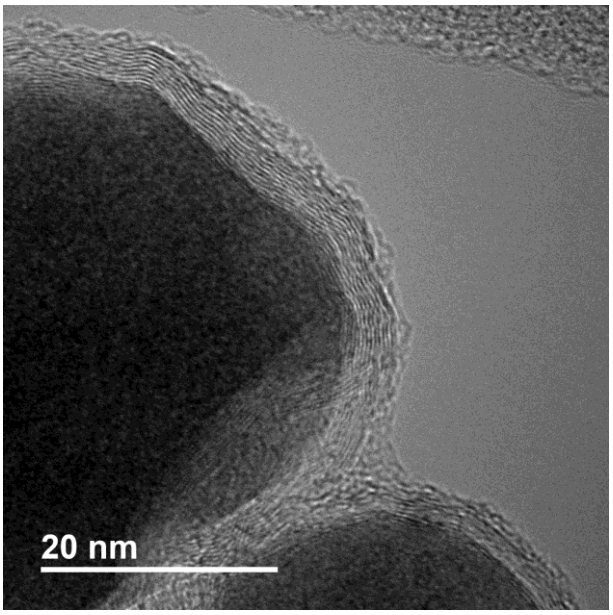

Figure 2-2: BF-TEM image of a steel particle covered in graphitized carbon. The dark area represents a heavy steel particle and illustrates mass-thickness contrast, whereas the bright and dark lines at the surface of the particle are formed by phase contrast.

1.1.2 Scanning Transmission Electron Microscopy

Another common imaging technique is scanning transmission electron microscopy (STEM), which is based on a fundamentally different image formation principle compared to BF-TEM. In STEM, the electrons are focused onto a very small area of the sample and form a converging beam (also called the probe) as they arrive at the sample. The electrons then pass through the sample and many interactions between the electrons and the sample can take place, generating various signals that can be acquired. The probe is then scanned across the sample, typically in a 2D raster, and the signals can be acquired at every probe position. The image is generated by representing the signal strength at a certain probe position as an intensity in the corresponding pixel in the image.

A common signal to acquire is the electrons scattered at high angles, typically using an annular detector below the sample. This technique is called high-angle annular dark field STEM (HAADF-STEM). The term dark field indicates that, contrary to bright-field imaging, the primary electrons that did not interact with the sample do not contribute to the final image, and thus a lack of sample (i.e., no scattering) is illustrated by a low/dark signal. A particular advantage of HAADF-STEM is that the signal scales with the mass thickness of

the sample. The heavier an atom, the higher the probability that an electron will be scattered at a high angle. In addition, the probability that an electron will scatter under these high angles increases monotonically with the amount of matter (up to a certain point; when the sample is too thick, cupping artefacts may arise [48]). This makes HAADF-STEM images typically much more straightforward to interpret quantitatively, as a higher signal in the image will correspond to a higher mass thickness in the sample. A schematic of the optical system of a STEM with the HAADF detector is presented in Figure 2-3.

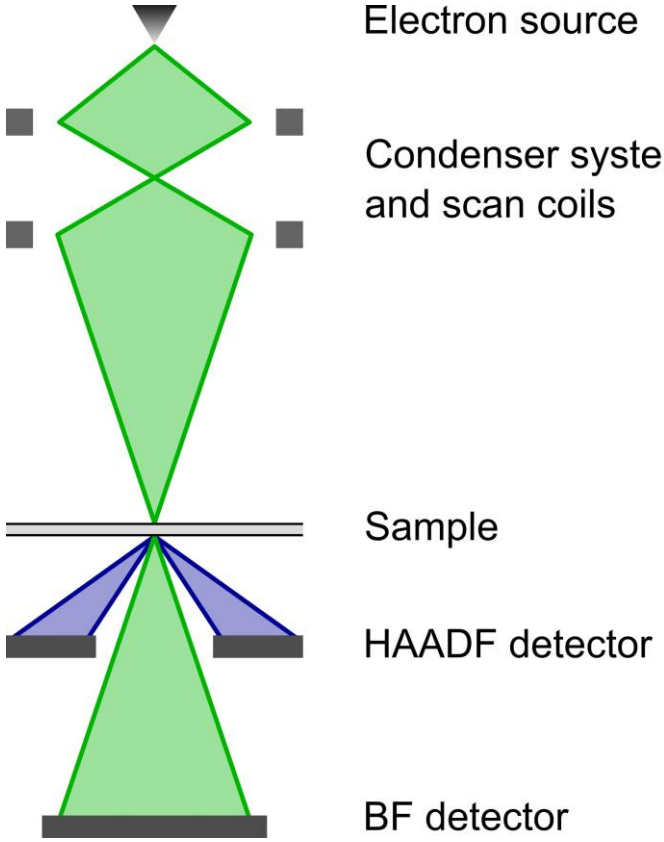

Figure 2-3: Schematic of the optical system of a HAADF-STEM. The condenser system focuses the electron beam in a small point on the sample. This focused electron beam is then scanned across the sample by the scan coils. At every probe position, the electrons scattered at high angles are collected by the HAADF detector.

An example of an HAADF-STEM image is provided in Figure 2-4 A, illustrating the mass-thickness contrast. This image shows a steel particle with an oxide shell on a light support material. The particle itself is the brightest in the image, indicating its higher mass-

thickness. Given the sharp transition from the brighter to the less bright area at the surface of the particle, it can be understood that the shell consists of a material with a lower mass density compared to the particle itself (indicated by dashed lines in the image). The lighter support material contributes very little to the background signal in the image, indicated by the dark area around the particle.

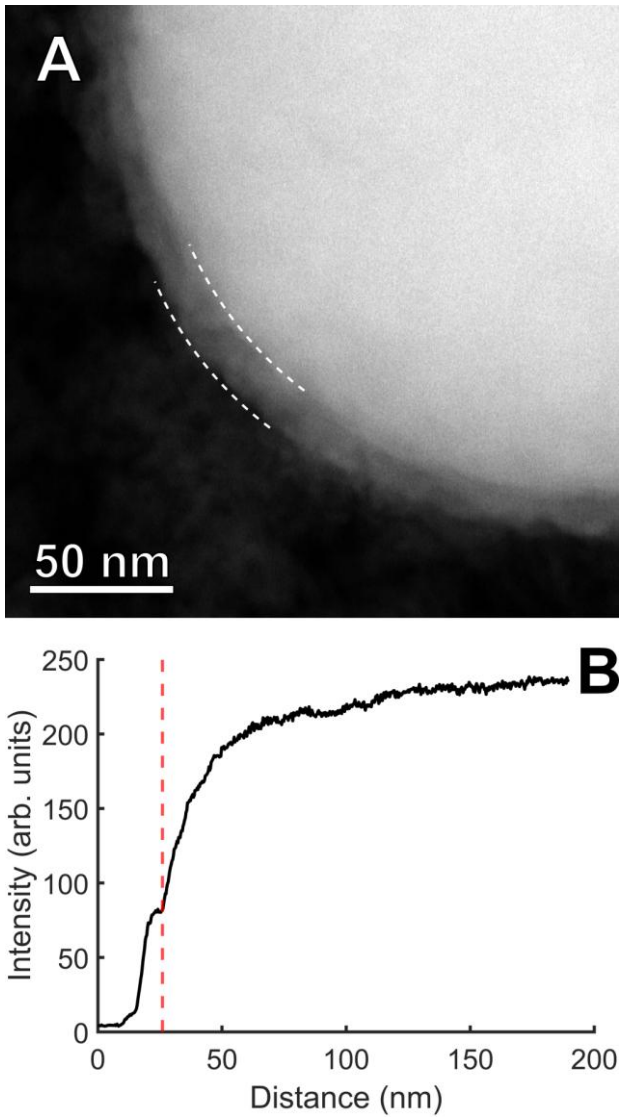

Figure 2-4: (A): HAADF-STEM image of a steel particle with an oxide shell (indicated by the dashed lines). The particle is brighter than the shell, indicating a higher mass density. This is further quantified by the line profile (B), determined on a line diagonal in (A), from outside the particle to its center. The transition from the shell to the particle is clearly visible in the line profile and is indicated by the dashed red line.

This image is further quantified by analyzing a line profile from this image. On a diagonal line in the HAADF-STEM image starting outside of the particle to the center of the particle, the intensity is extracted and averaged over a width of 7.5 nm along the line and plotted in Figure 2-4 B. It is clear that the shell is indeed less intense than the particle, indicating its lower mass-thickness. Further, there is a sharp transition from the shell to the core of the particle, indicating a transition to a different material. Moreover, the intensity keeps increasing monotonically from the edge of the particle to the center, indicating a continuously increasing thickness. This is consistent with the assumption that the particle is spherical. However, in order to accurately determine the full 3D morphology of a nanoparticle, electron tomography would be required [49].

1.2 Scanning Electron Microscopy

The main difference between a scanning electron microscope (SEM) and a TEM, is that in a SEM the electrons do not transmit through the sample. Instead, signals are acquired from above the sample, which can have distinct advantages. For example, the sample no longer needs to be extremely thin, avoiding complicated sample preparation steps and allowing for the characterization of larger systems. In addition, since the relevant signals are generated near the surface of the sample, the acceleration voltage of the electron beam can be much lower (typically 1 – 30 kV), making the microscope generally smaller and cheaper.

Although the signals may be acquired at different locations relative to the sample, the image formation principle of SEM is similar to that of STEM. The electron beam is focused in a small point on the surface of the sample, where various signals are generated. The probe is then scanned across the sample, acquiring one or more signals at every probe position. The intensities of a signal are again represented as corresponding pixel values, thus forming an image. A schematic of a SEM is presented in Figure 2-5.

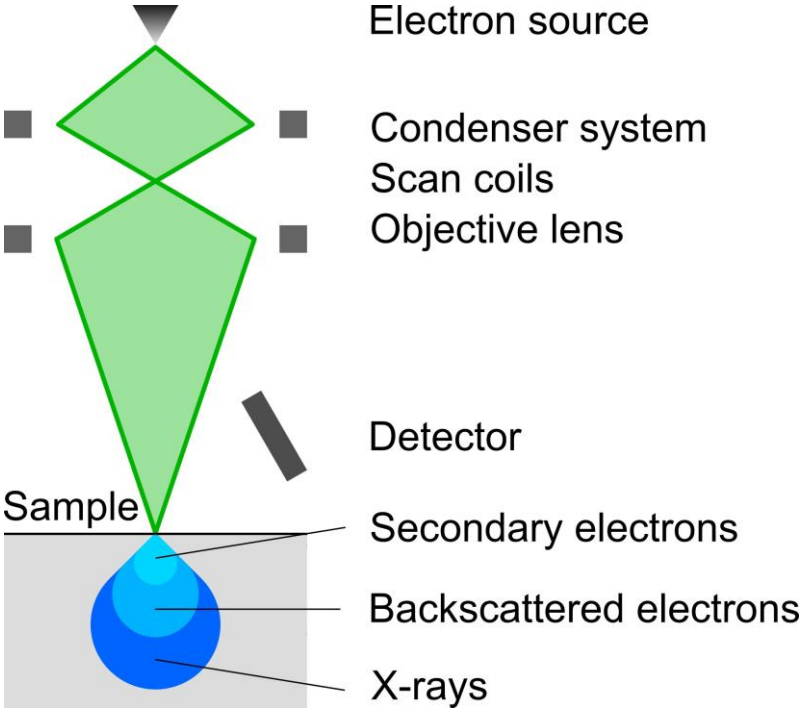

Figure 2-5: Schematic of a scanning electron microscope. The electrons are focused onto a small area of the sample. This electron beam is then scanned across the sample, collecting signals at every probe position. Depending on the signal, different detectors can be employed.

Just like in TEM, the interaction between the energetic electrons and the sample is complex. Several mechanisms can generate measurable signals, each revealing some information about the sample. Two common signals and corresponding imaging principles are discussed here. This section is largely based on the book by Goldstein et al. [50].

1.2.1 Secondary Electron Imaging

As the highly energetic electrons interact with the sample, secondary electrons (SE) are generated. These SE originate from inelastic scattering of energetic primary electrons with the sample, where electrons from the valence or conduction band can be ejected. These secondary electrons have very low energies, typically just a few eV. In order to detect these low-energy SE, an Everhart-Thornley detector (ETD) is used. When using an ETD, the low-energy electrons are attracted by a low positive voltage (few hundred V) on a Faraday cage. Once inside the Faraday cage, the electrons are accelerated by a high

voltage (e.g., 10 kV) after which they interact with a scintillator. The light generated in the scintillator is then guided to a photomultiplier where an electrical signal is generated. The combination of these components make the ETD highly efficient in detecting low-energy electrons. Note that by applying a slightly negative bias on the Faraday cage, the low-energy electrons are repelled and only higher-energy electrons are detected, making the detector selectively sensitive to backscattered electrons (see next section).

In order to be detected, the secondary electrons must escape the sample, but given their low energy, they can only escape the sample when the SE are generated near the surface. Therefore, the detection of SE, and thus SE-SEM, is highly sensitive to the surface of the sample. Furthermore, the SE signal will also increase with increasing inclination angle of the sample. This can be geometrically understood, since at higher inclination angles, the primary beam will remain closer to the surface of the material, thus allowing more of the generated SE to escape. This property makes SE-SEM highly suitable for the visualization of microscopic surface features of a material. An example of an SE-SEM image is shown in Figure 2-6, where the facets of some nanocrystals are clearly visualized. The inclined facets of the crystals yield a higher signal in the image compared to the flat top facets which are oriented (more) parallel to the sample plane.

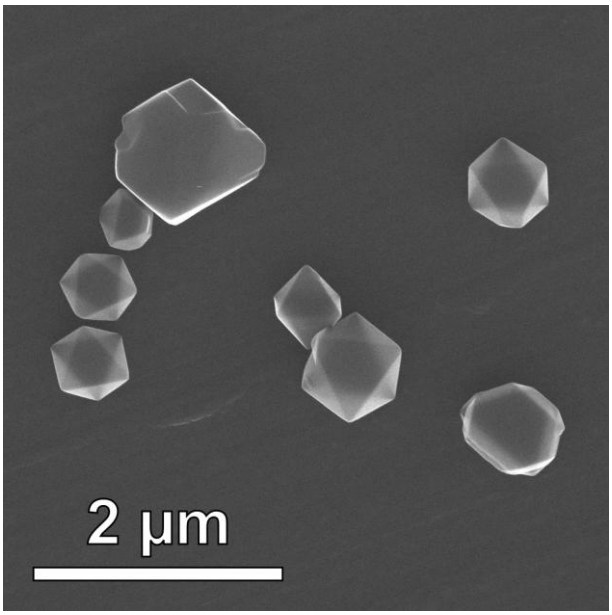

Figure 2-6: SE-SEM image of faceted nanoparticles. The flat top surfaces of the particles are relatively dark, whereas the inclined or vertical facets of the crystals yield a higher signal.

1.2.2 Backscattered Electron Imaging

When the primary electrons interact with the sample, a fraction of the primary electrons can eventually escape the sample due to one or several scattering events. These electrons are called backscattered electrons (BSE) and typically have much higher energies than the SE. By employing a detector that selectively detects these BSE, additional information can be extracted based on these BSE-SEM images. Typically, the default lens mounted solid state BSE detector is employed throughout this thesis. Only under certain circumstances in Chapter 6, where more details are provided, is the ETD used with a negative voltage on the Faraday cage, so it repels the low-energy SE.

The number of BSE generated per incident electron dose increases monotonically with the atomic number of the sample. In addition, BSE generation is much less sensitive to the surface topography compared to SE, because the primary electrons can travel hundreds of nm before escaping the sample. Therefore, BSE-SEM is often a valuable complementary technique to SE-SEM, as it can give additional insights into the elemental composition of the sample. This sensitivity of BSE-SEM to the mass density of the sample is illustrated in Figure 2-7. Here, a steel particle is shown on an aluminum oxide support (background). The signal is notably more intense at the position of the heavier steel particle compared to the lighter aluminum oxide background.

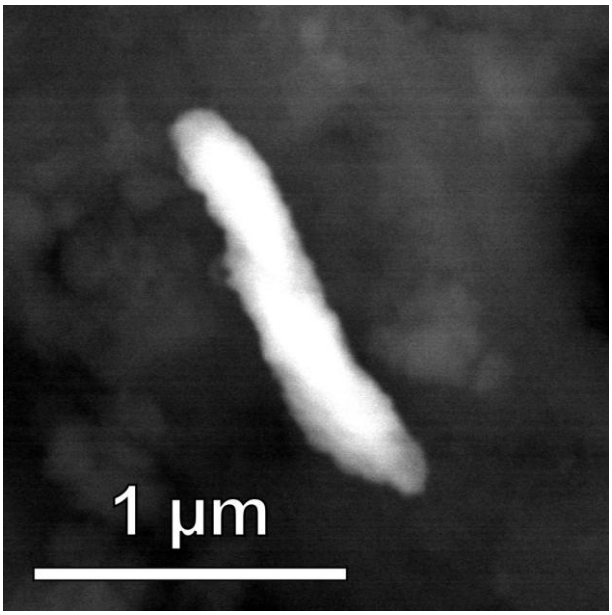

Figure 2-7: BSE-SEM image of a steel particle on a aluminum oxide support. The heavier steel particle yields a much higher signal in the image compared to the lighter aluminum oxide background.

1.2.3 Environmental SEM

Although SEM analyses are usually performed under high-vacuum conditions (in the order of 10^{-2} Pa or lower), some microscopes are able to operate at higher pressures. In such a so-called environmental SEM (ESEM), the chamber can be flooded with a gas or even water vapor, and pressures up to hundreds or even a few thousand Pa can be reached. When combined with a cooling stage, it is possible to characterize a sample in liquid water. Using an ESEM can be advantageous in so-called *in situ* experiments. In such experiments, the sample is investigated under relevant conditions. By introducing certain gases or water vapor in the chamber, their effect on the sample can be investigated in real-time. Furthermore, *in situ* investigations reduce the time between the sample treatment and SEM investigation, and also eliminate possible oxidation or contamination due to exposure to ambient conditions.

An additional advantage of operating at higher pressures is the reduction of surface charging. As the primary electron beam interacts with the sample, charges can accumulate locally which can drastically deteriorate the image. Normally, samples (or at least their surface) are required to be conductive to prevent this charge accumulation. However, when operating at higher pressures, the primary electrons will ionize some of the gas molecules. The generated charged species can then locally compensate the accumulated charge, eliminating the requirement of a conductive sample. This can be especially advantageous when characterizing materials with complicated surface structures (the conductive coating typically cannot be applied on a vertical edge), or when employing spectroscopic techniques to determine the elemental composition of the sample (to avoid an undesired signal from the conductive coating).

Despite the advantages, operating the SEM at elevated pressures also has certain disadvantages. For example, as discussed before, the electrons will interact with the gas atoms and scatter. These scattered electrons will then no longer reach the sample at the location of the probe, but rather hit the sample (or another surface inside the microscope chamber) at a different location. Therefore, contributions from more areas of the sample than just the probe position will contribute to the measured signal, thus deteriorating the image quality. Furthermore, the ETD, which is the most common SE detector, cannot operate at elevated pressures, since a gas discharge can take place between the Faraday cage and the high potential of the scintillator. Therefore, other detectors should be used, which limits the imaging capabilities. Finally, to protect the sensitive electron gun, a pressure-limiting aperture (PLA) should be installed at the point where the column enters the chamber. This PLA limits the amount of gas that can diffuse

up the column. However, it can also drastically limit the field of view (FOV), which can hinder certain experiments.

1.3 X-ray Spectroscopy

Whenever highly energetic electrons interact with atoms (which occurs in TEM and SEM), they can undergo several inelastic scattering events. In such interactions, it is possible for an energetic primary electron to ionize an atom by transferring sufficient energy for a core-electron to be ejected from the atom. Next, an electron in that atom with a lower ionization energy can transition to the electron vacancy, as it is energetically more favorable. In this process, the residual energy can be transferred to a photon. Since the energy levels in atoms are discrete, and they are unique for every atom, the energy of this ejected photon is characteristic for the atom in which it was generated. Therefore, by analyzing the spectrum of the measured photons, typically in the hundreds to thousands of eV range (i.e., X-rays), the elemental composition of the sample can be investigated. When operating the electron microscope in a scanning mode (whether it's SEM or STEM), a 2D map can be generated, determining the spatial distribution of certain elements in the sample. Typically, these X-rays are analyzed using energy dispersive X-ray spectroscopy (EDX), though wavelength dispersive X-ray spectroscopy (WDX) also exists [51].

An example of such an EDX analysis is presented in Figure 2-8. Specifically, a particle on top of an Al_2O_3 bead is investigated by SEM and EDX. The SE- and BSE-SEM images are shown in Figure 2-8 A and B, respectively. The strong signal of the particle in the BSE image indicates that the particle is notably denser than the material in the background. The SEM-EDX analysis reveals the composition of the sample based on the characteristic X-ray energies observed in the spectrum. By visualizing the intensity of a certain element per pixel in the image, a map of the elemental composition of the sample can be obtained (Figure 2-8 C and D). This analysis reveals that the particle contains iron, whereas the background consists of Al and O. Further analysis of the EDX spectrum (Figure 2-8 E) reveals that the particle also contains Cr and Ni, indicating that the particle consists of stainless steel.

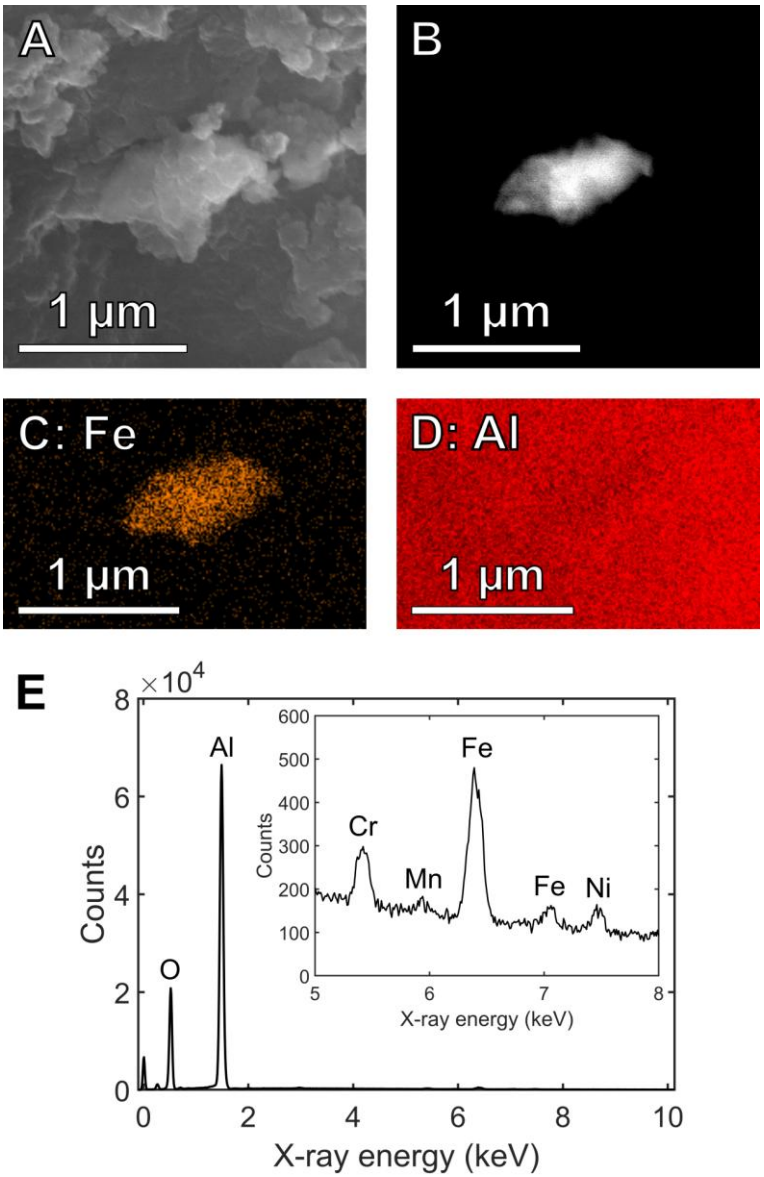

Figure 2-8: Example of the use of SEM-EDX. SE- (A) and BSE- (B) image of a particle on an Al_2O_3 support. Based on the BSE signal, it is clear that the particle is notably heavier than the material in the background. Using EDX, the elements in the sample can be identified and their distribution can be visualized. (C) and (D) illustrate the elemental distribution of Fe and Al, respectively. (E) shows the corresponding summed EDX spectrum. The strong Al and O signals are caused by the support material, which is confirmed by the homogeneous distribution of Al in (D). Clear Fe and Cr signals are also present, attributed to the particle, as confirmed in (C).

1.4 Electron Microscopy for Plasma Catalysis

As will be illustrated throughout this work, electron microscopy is a powerful characterization technique which is invaluable when studying plasma catalysis. Although packed-bed plasma reactors are relatively large, many relevant processes take place at a microscopic scale or are affected by (microscopic) material features. It is therefore essential to understand the nano-scale properties of the materials under investigation. On the one hand, the physical properties of the materials in contact with plasma are crucial, such as the particle size and morphology, and the distribution of the material of interest throughout a support. On the other hand, the chemical properties of the materials inside the plasma system, in particular oxidation of metals, can have significant effects. Indeed, as will become apparent throughout this work, the properties of the material in contact with the plasma can have a drastic impact on the plasma characteristics, and it is therefore important to investigate these materials.

In this work, SEM will be employed to determine the distribution of a catalyst metal on and throughout a support bead. Further, SEM and TEM will be employed to characterize particles that are generated inside the plasma reactor by erosion of the exposed electrode. Finally, a setup is presented that enables the generation of plasma inside a SEM. This system allows the investigation of the physical and chemical properties of a material and how these properties are affected by a plasma.

In addition to detailed characterization of the materials in contact with plasma, the analysis of the plasma discharge characteristics is also essential. The foundations of the electrical diagnostics utilized for the discharge characterization are introduced in the following section.

2. Electrical Diagnostics

In addition to the understanding of the theory of breakdown mechanisms, as introduced in Chapter 1, great progress has been made regarding the experimental characterization of the discharge, revealing relevant properties such as the deposited power. These experimental diagnostics were pioneered by Manley in 1943 [52], and have been developed further ever since. The general idea behind this electrical characterization is that the DBD can be considered as a combination of various capacitors [53]. In order to probe these capacitances, Manley introduced a monitoring capacitor with a known capacitance in series with the DBD reactor, as illustrated in Figure 2-9. By registering the voltage across this monitoring capacitor, the charge transferred through the reactor can be measured in real time, in addition to the voltage applied to the DBD system (here represented as a black box).

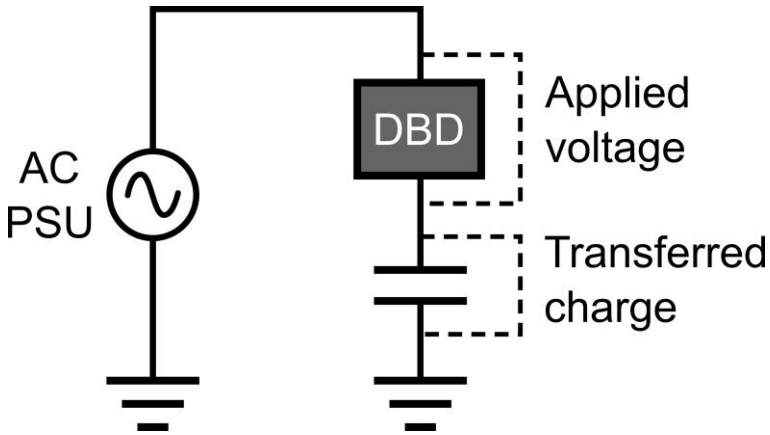

Figure 2-9: Simplified schematic of the electrical circuit employed to measure the transferred charge from the DBD reactor, here represented as a black box. By monitoring the voltage across a known capacitor in series with the DBD, the charge transferred through the DBD can be registered in real time. This value can then be correlated with the voltage applied to the actual DBD, as also discussed later.

By correlating this measured charge with the applied voltage, the effective capacitances of the system can be determined. In order to interpret the capacitances obtained from the electrical diagnostics, a theoretical model of the DBD is required, which is based on the so-called equivalent circuit where relevant parts of the DBD are represented by conventional electrical components. The simplest equivalent circuit of a DBD is presented in Figure 2-10. Note that the monitoring capacitor from the experimental setup in Figure 2-9 is no longer present in this diagram. The capacitances presented in Figure 2-10 are a virtual representation of the physical components of the DBD reactor

(i.e., the black box DBD system in Figure 2-9). Indeed, from an electrical point of view, the reactor can be separated in two capacitances: the dielectric capacitance and the gap capacitance. The dielectric capacitance represents the contribution of the dielectric barrier in the system, and the absolute value is determined by the geometry of the reactor and the material properties of the barrier. The gap capacitance represents the contribution of the gas gap (when there is no discharge), and is mostly dependent on the geometry of the system.

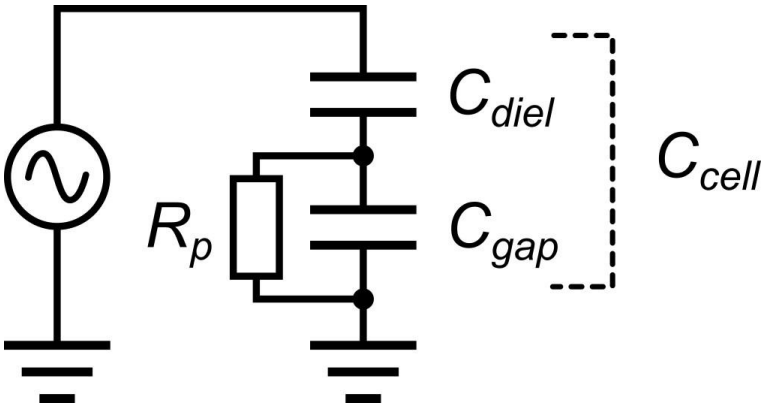

Figure 2-10: The simplest equivalent circuit of a DBD. When there is no plasma, the overall capacitance of the system (i.e., how much charge is stored as a function of the applied voltage) is C_{cell}, being the combination of the gap- and dielectric capacitances in series. When there is a discharge, the gap capacitance is eliminated as the charges can cross the gap in the plasma (here represented by the "plasma resistor" R_p), and the capacitance of the system is only determined by the dielectric capacitance.

When plotting the charge measured on the monitoring capacitor versus the applied voltage (these measurements are schematically presented in Figure 2-9), a voltage-charge diagram, also called a Lissajous figure, can be generated. A typical example of a voltage-charge diagram is presented in Figure 2-11. Based on the equivalent circuit of the DBD, presented in Figure 2-10, the different sections of the voltage-charge diagram can be interpreted physically, revealing relevant properties of the discharge, as will be discussed in detail throughout this work. When there is no discharge, the gap capacitance contributes to the overall capacitance of the system. So, as the applied voltage varies, the charge in the system varies proportionally with the overall (= cell) capacitance. This is visually represented in the voltage-charge diagram (Figure 2-11) as the blue ("plasma-off") sections. Conversely, when the plasma is on, charges can bridge the gas gap and the gap no longer contributes to the capacitance of the system, represented by the "plasma resistor" R_P in the equivalent circuit (Figure 2-10). Thus, when there is a discharge, the variation of the charge in the system as a function of the

applied voltage is only determined by the dielectric capacitance. The “plasma-on” phases are represented by the orange sections in the example voltage-charge diagram in Figure 2-11.

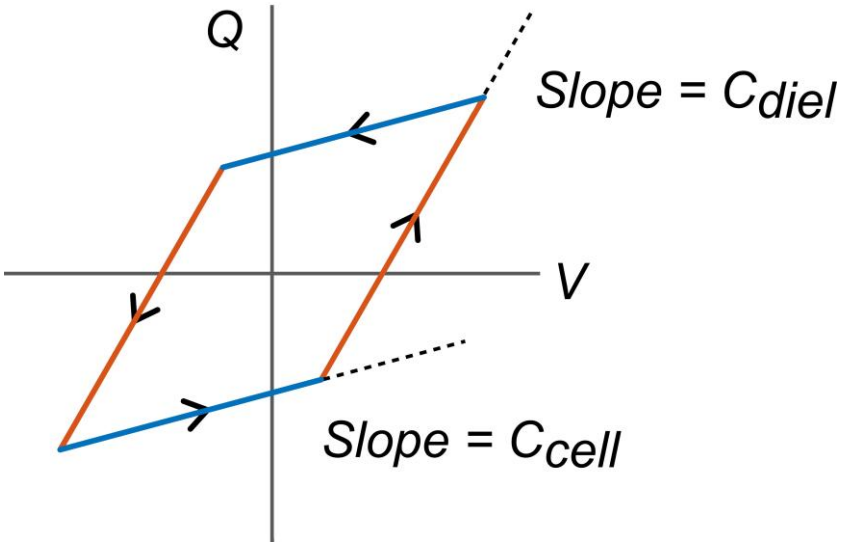

Figure 2-11: Ideal voltage-charge diagram with the interpretation of the sections based on the capacitances from the equivalent circuit indicated. When there is no plasma, the capacitance of the system (i.e., how the charge varies with the varying voltage = slope) equals the cell capacitance, indicated by the blue edges of the diagram. When there is a discharge, the capacitance of the system is only determined by the dielectric capacitance, indicated by the orange sections of the diagram.

This electrical model enables the characterization of several valuable discharge characteristics as discussed in detail throughout this work. Perhaps the simplest yet highly relevant parameter that can be directly extracted from this measurement is the energy dissipated in the system (thus revealing the plasma power) by calculating the area enclosed by the diagram. In addition, among other metrics, the electrical model allows the calculation of the gap voltage, i.e., the true voltage across the gap during the discharge, by determining the zero-charge crossings in the diagram.

Despite being introduced over 80 years ago, the general approach of this electrical diagnostic technique is still very relevant today. Over the last decades, several updates to this equivalent circuit model have been introduced, significantly improving the accuracy and applicability of this approach. These specific technical developments will be introduced throughout this work as they become relevant in the following chapters.

In addition to the measurement of the transferred charge using the monitoring capacitor, another common signal to acquire is the current in the circuit. The microdischarges discussed in the previous chapter will manifest as sharp peaks in the current signal, having a high intensity but short lifetime. In contrast, a Townsend discharge will exhibit a much smaller but broader peak in the current signal. In theory, measuring both the current and the transferred charge is redundant, since both can be calculated from the other signal (integrating the current yields the charge and the derivative of the charge results in the current). In practice, however, there can be challenges in doing this accurately, and thus it is recommended and common to acquire both signals simultaneously [53]. The current in the circuit is typically measured using a Rogowski coil or by measuring the voltage across a shunt resistor in series with the reactor. The current signal can reveal critical information on the characteristics of the DBD, and several processing and quantification steps can be applied to gain further insights. These techniques will be introduced and employed throughout this work as they become relevant in the coming chapters.

Chapter 3

Importance of Plasma Discharge Characteristics in Plasma Catalysis: Dry Reforming of Methane versus Ammonia Synthesis

In this chapter, several plasma catalysis experiments are performed. Specifically, various catalysts are synthesized and their performance for dry reforming of methane and NH_3 synthesis is evaluated employing a conventional packed bed dielectric barrier discharge reactor. These catalysts were designed to have different distributions of the metal particles throughout the oxide support beads. Electron microscopy reveals the distribution of the metal throughout the support, as well as the surface coverage of the packing materials. Further, detailed electrical characterization of the discharge shows that the catalysts notably affect the discharge characteristics. These altered discharge properties are found to be strongly correlated with the overall performance of the system, highlighting the importance of the employed electrical diagnostics.

The content of this chapter is based on:

Importance of plasma discharge characteristics in plasma catalysis: Dry reforming of methane vs. ammonia synthesis
Robin De Meyer, Yury Gorbanev, Radu-George Ciocarlan, Pegie Cool, Sara Bals, Annemie Bogaerts
Chemical Engineering Journal, 488, 150838, 2024

1. Introduction

As discussed in Chapter 1, there are two main approaches in which plasma-catalytic gas conversion can be employed to combat anthropogenic climate change. Firstly, greenhouse gases, with a main focus on CO_2, could be converted into environmentally harmless or even useful chemicals. Secondly, existing chemical processes that are responsible for significant greenhouse gas emissions could be electrified in order to produce the required chemicals with renewable energy sources. Examples of such approaches are dry reforming of methane (DRM), where CO_2 and CH_4 are converted into syngas, and NH_3 synthesis, potentially serving as a decentralized alternative to the energy-intensive Haber-Bosch process [28,54–57].

Packed-bed dielectric barrier discharge (DBD) plasma reactors are often employed in plasma catalysis, as they allow for a direct contact between the plasma and the catalytic material, since the packed catalyst can be placed inside the discharge volume [18]. The introduction of any packing material will unavoidably change the conditions of the plasma discharge. On the one hand, the packing will decrease the available gas volume, thus decreasing the residence time at a given mass flow rate of the gas, compared to an empty reactor. On the other hand, the packing material will alter the (di)electrical properties of the system, inevitably altering the discharge properties [58]. However, the effect of such packing material on the plasma discharge, and especially its subsequent effect on the plasma-catalytic performance, is not yet fully understood. Moreover, when comparing various catalytic materials in plasma catalysis, their effect on the plasma discharge is often overlooked. This makes it difficult to attribute certain changes in, e.g., conversion solely to a catalytic effect, when potential differences in the gas phase chemistry are neglected. In plasma catalysis, many physical and chemical processes contribute to the overall performance, which impedes straightforward interpretation and comparison of different studies [59]. Furthermore, optimal (plasma) conditions often differ vastly depending on the reaction of interest. Therefore, we decided to study both DRM and NH_3 synthesis, since they have very different reaction mechanisms and thermodynamic characteristics, the former being endothermic, and the latter being exothermic. Moreover, previous studies indicate that various plasma discharge characteristics could affect the overall performance of these reactions in a different way [60–62].

Often, adequate analysis of the plasma discharge is missing in existing literature reports [35,36,63–70], and while indeed sometimes the effect of the catalyst on the plasma

discharge was noted in DRM [33,34,71–73], NH_3 synthesis [37,74–81] or for other gas conversion applications [82–85], a systematic investigation of the discharge parameters is rare. Nevertheless, Peeters and van de Sanden proposed a detailed and profound electrical model of a DBD, enabling an extensive study of the discharge parameters based on conventional measurements (i.e., voltage-charge diagrams) and relatively straightforward calculations [86]. Moreover, modeling results indicate that certain aspects of the plasma discharge (e.g., filamentary versus diffuse discharge) could indeed affect the gas conversion, independently of any catalytic effect [60–62].

Recently, Brune et al. performed a detailed investigation of the effect of a catalytic packing on the plasma discharge for DRM, with a specific focus on the microdischarges [34]. It was shown that despite identical syntheses using incipient wetness impregnation, different metals had a different effect on the plasma discharge, notably the number of microdischarges. This aberrant behavior was in part attributed to differences in the chemical nature of the catalysts. Likewise, when using a higher metal loading in plasma-catalytic NH_3 synthesis, Ndayirinde et al. found that a similar synthesis technique yielded an increased metal concentration at the surface of the support (alumina) beads [37]. The exposed metal was expected to cause drastic alterations of the plasma discharge, which proved to be highly beneficial for NH_3 synthesis. Finally, Seynnaeve et al. studied the impregnation of such beads with Fe and Cu and found that small changes in the synthesis protocol could yield significantly different metal distributions [87].

Despite these recent developments, a clear understanding of what causes the changes in the plasma discharge and what precise properties of the plasma affect the overall performance is still lacking. Therefore, this chapter focuses on how the catalytic packing material affects the plasma discharge, and how that in turn influences the plasma-catalytic performance. Since metal-loaded (alumina) beads or pellets are often employed in plasma catalysis research, the distribution of the metal on and throughout the beads is emphasized. Two different types of catalysts are designed and synthesized to have drastically different distributions of metal throughout the support beads, deliberately aiming to influence the plasma discharge. These catalysts are synthesized with either Ni or Co as a catalytic metal, supported on porous γ-Al_2O_3 beads. Ni and Co are chosen because they are very often used in plasma-catalytic DRM [88,89] and NH_3 synthesis [31,37,90], respectively. By using metals that are studied frequently, we aim to enable a more straightforward comparison with previous and future work. At the same time, both metals will be used for both reactions in this work, in order to make a direct comparison between the reactions, attempting to understand how the reactions

perform under practically identical plasma-catalytic conditions, and to investigate how identical synthesis protocols for different metals can still yield different results. The first type of catalyst is synthesized using the common wet impregnation technique [31], resulting in metal nanoparticles scattered throughout the entire support bead. The second type of catalyst is synthesized by spray coating [91], a technique that concentrates all deposited metal at the surface of the alumina beads.

These sets of catalysts are used in plasma-catalytic DBD experiments for both DRM and NH_3 synthesis. The performance of the various catalysts is compared with an emphasis on the properties of each plasma discharge. The goal is to elucidate the influence of packed catalysts on the plasma discharge and its subsequent effect on the reaction performance. We explicitly note that the synthesized materials will be called catalysts throughout this work, even though their effect on the reaction may not always be entirely clear, being either physical, chemical, or a combination of both. However, as this is common practice in the plasma catalysis community, this phrasing seems most appropriate.

2. Methods

2.1 Catalyst Synthesis

All catalysts were synthesized starting with commercial γ-Al_2O_3 beads (Sasol, product number: 604130) with a diameter of 1.8 mm. Every type of catalyst was synthesized with approximately 30 g of dried beads so that the DRM and NH_3 synthesis experiments could be performed using pristine catalysts from the same batch. Filling the reactor entirely takes around 12.5 g of beads, leaving some margin for losses and characterization.

For the wet impregnation (WI), an aqueous solution of the respective precursor was prepared, $Ni(NO_3)_2.6H_2O$ (Sigma-Aldrich, 97.5 %) for the Ni catalyst and $Co(NO_3)_2.6H_2O$ (Sigma-Aldrich, >98 %) for the Co catalyst. The amount of precursor was chosen to yield a final metal loading of 10 wt% and the volume of the solution was chosen to correspond to 0.75 ml per g of Al_2O_3 beads, as that was empirically determined to be the volume of liquid the beads can absorb. After drying the beads, the precursor solution was added to the beads, followed by continuous stirring for a few minutes to ensure a homogeneous distribution of the precursor. Next, the beads were left to dry in ambient conditions overnight after which they were dried at 120 °C for 24 h. Further, the beads were calcined in air at 400 °C for 6 h and finally reduced in a tube furnace with 2% H_2 in Ar (Air

Liquide, >99.999 %) for 8 h at 550 °C. Note that this reduction step was only done overnight immediately prior to plasma-catalytic experiments, to limit the potential re-oxidation of the catalysts during prolonged storage.

The spray-coated (SC) catalysts were prepared according to a protocol adapted from Uytdenhouwen et al. [91]. In preliminary synthetic experiments, the 10 wt% catalysts proved to be too structurally unstable for further use in the plasma catalysis experiments, because the much thicker shell obtained with this high amount of metal partially detached from the beads, making the estimate of the loading highly inaccurate. Therefore, only 3.3 wt% and 1 wt% Ni and Co catalysts will be discussed from here onwards. An aqueous solution of the respective precursors was prepared ($Ni(NO_3)_2.6H_2O$ and $Co(NO_3)_2.6H_2O$) with a concentration of approximately 0.6 M in amounts to yield the correct metal loading of either 3.3 or 1 wt%. This solution was stirred and heated to 80 °C. Next, a 3 M NaOH (Acros Organics, 98.5%) solution of approximately the same volume as the Ni/Co solution was added to the precursor while stirring continuously. This volume ensured a very basic environment, promoting the precipitation of the Ni/Co species. When adding the NaOH solution, a Ni or Co hydroxide was formed and precipitated. After stirring for 2 h at 80 °C, the precipitate was left to settle under static conditions. Next, the clear supernatant was removed and 150 ml of water was added followed by stirring for a short time. The precipitate was again left to settle and this washing step was done three times in total. After the washing steps with water, the same washing steps were done three times using isopropanol (Merck, >99.8%). This procedure finally yielded a suspension of either Ni or Co hydroxides in isopropanol. For the actual spray-coating, the dried Al_2O_3 beads were placed in a rotating drum, after which the prepared suspension was slowly sprayed on the rotating beads. Warm air was sent into the drum to promote rapid evaporation of the solvent, while the spraying was done intermittently to prevent the suspension from entering the pores. Finally, after all the suspension was sprayed and most of the solvent evaporated, the beads were left to dry overnight in ambient conditions. Identical to the wet impregnated catalysts, these beads were then dried for 24 h at 120 °C, calcined in air at 400 °C for 6 h and reduced in 2% H_2 in Ar at 550 °C for 8 h prior to the plasma experiments.

2.2 Catalyst Characterization

Scanning Electron Microscopy: To investigate the metal distribution throughout the beads as well as the metal coverage at the surface of the beads, and the total metal loading of the WI catalysts, scanning electron microscopy (SEM) and energy dispersive X-ray spectroscopy (EDX) analyses were performed. For these analyses, a Thermo Fisher Scientific Quanta 250 ESEM equipped with an Oxford Instruments EDX detector was employed. Prior to SEM analysis, two beads of every batch were embedded in an epoxy resin (EPO-TEK 353ND-T4), ground and polished to expose a smoothened cross-section of each bead, as illustrated in Figure 3-1. These samples were then attached to a SEM stub and coated with a 10 nm layer of C to improve the conductivity during SEM analysis.

EDX maps were acquired from the cross section of the beads and quantified to yield a radial distribution of the catalyst metal throughout the bead, as illustrated in Figure 3-2 [37]. To quantify the radial distribution of the catalyst metal, the center and radius of the bead are determined in the image, after which the EDX-based elemental content can be quantified as a function of the distance from the center of the bead. To obtain a weight percentage of the catalyst metal (either Ni or Co), the original O signal was neglected and replaced by the stoichiometric amount based on the Al signal, since O is difficult to quantify accurately, and moreover, it was unclear which fraction of O would originate from Ni or Co oxides.

Furthermore, whole beads were glued to a SEM stub using silver paint and coated with a 10 nm layer of C to investigate their surface, as illustrated in Figure 3-3. Samples were analyzed using either secondary electron (SE) or backscattered electron (BSE) imaging [92]. SE-SEM imaging is very sensitive to surface topography, which was employed here to study the structure of the SC shell at the surface of the beads. BSE-SEM imaging is sensitive to the atomic mass of the sample and was therefore used to study the distribution and coverage of Ni or Co at the surface of the beads, yielding a stronger signal compared to the lighter Al_2O_3 background. More details on these imaging techniques are provided in Chapter 2.

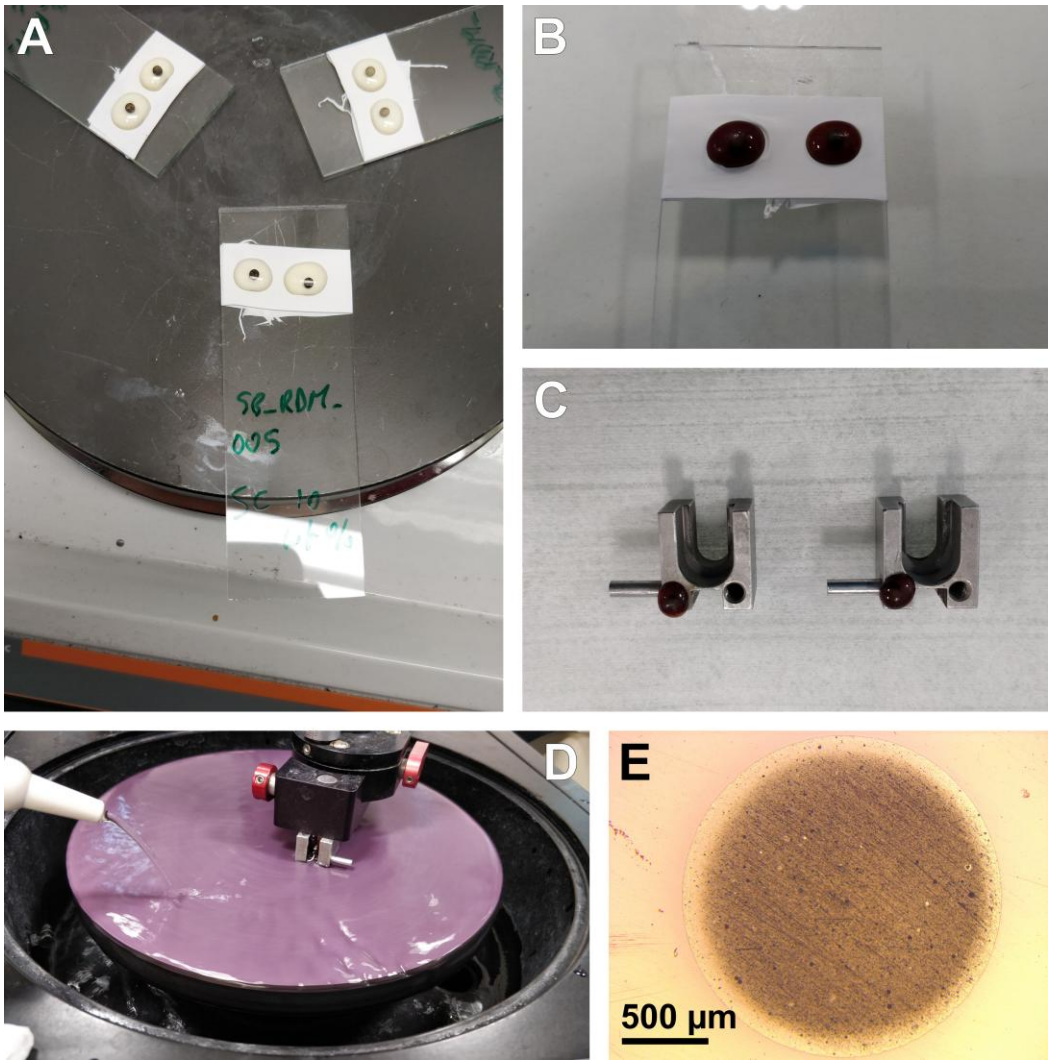

Figure 3-1: Overview of sample preparation for the SEM analysis of a cross-section of the catalyst. Individual spheres are immersed in a drop of epoxy resin, which is then heated on a hot plate (A). As the resin cures, it hardens and darkens (B), after which the hard resin with the catalyst bead inside can be attached to a polishing holder (C). The holder is then mounted on the polishing machine (D) and several sanding papers are used to first remove enough material to expose the cross-section of the catalyst sphere, and finally polish the sample to obtain a smooth surface. (E): An image from an optical microscope of the final cross-section.

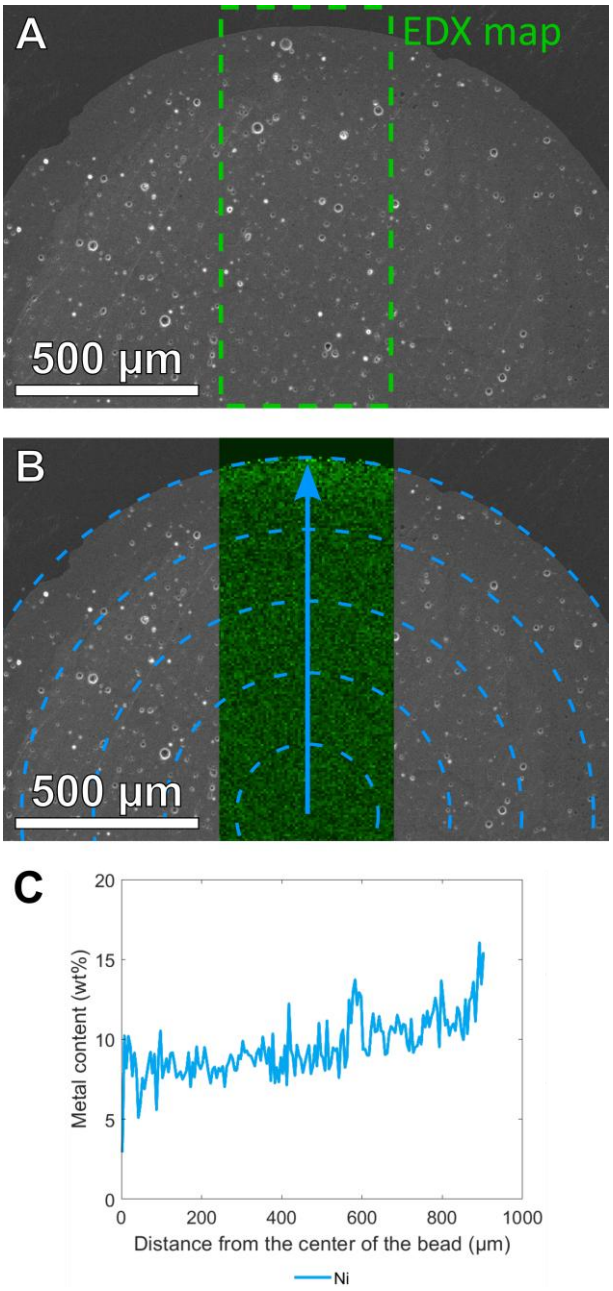

Figure 3-2: Illustration of the EDX-based quantification of the radial distribution of Ni or Co in a WI catalyst bead. (A): SEM image of a cross-section of a WI bead. An EDX map is acquired, indicated by the dashed rectangle in the image. (B): A circle is fitted to the edge of the bead, based on which the center of the circle (and thus the bead) is determined. Every pixel in the EDX map (green overlay on the SEM image) is then sorted in bins based on their distance from the center. By calculating the average elemental concentration within each bin, a radial distribution of the catalyst metal through the bead can be determined (C).

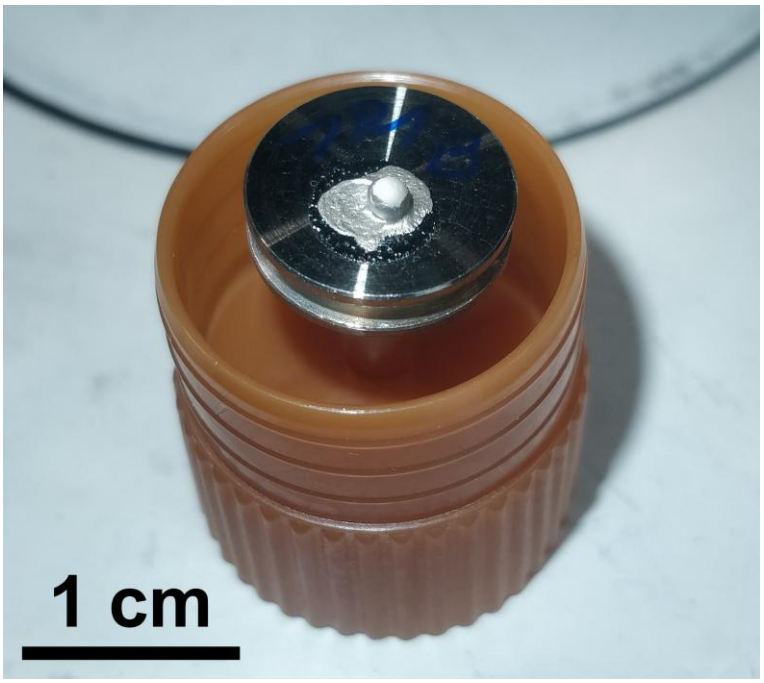

Figure 3-3: Example of an Al_2O_3 bead when mounted on a SEM stub. The edges of the bead are covered with silver paint to ensure an electrical contact with the stub to prevent charging. Once assembled, the bead on the stub is coated by 10 nm C to enhance the surface conductivity.

X-ray powder diffraction: To determine the oxidation state of the metal loaded on the catalyst, X-ray powder diffraction (XRD) was used to characterize the various samples. For these analyses, a Bruker D8 ADVANCE eco XRD machine was used, operating with a Cu K-α X-ray source. The beads were crushed in a mortar prior to XRD analysis.

N_2 sorption: In order to probe the specific surface area of the various catalysts, N_2 sorption at 77K and subsequent Brunauer-Emmett-Teller (BET) analysis was performed. The sorption measurements were performed using a Quantachrome Quadrasorb SI analyzer and the BET calculations were carried out using QuadraWin software.

2.3 Plasma Reactor Setup

A schematic representation of the setup is provided in Figure 3-4, whereas the exact dimensions of the reactor are presented in Figure 3-5 and a picture of the main components is presented in Figure 3-6. The reactor consists of a ceramic tube (alumina, Ceratec) wrapped with a 100 mm wide stainless steel mesh that acts as the powered electrode. A stainless steel rod placed through the ceramic tube acts as the grounded

electrode and creates a gap of 4.5 mm between the rod and the ceramic tube that is packed with the (catalyst) beads. The catalysts were held in place by glass wool at both ends and the gases were sent to the reactor through mass flow controllers (Bronkhorst). A 23.5 kHz sinusoidal voltage was applied by the G10 S-V (AFS GmbH) power supply unit (PSU) and sent to the outer electrode of the reactor through a transformer with a constant applied PSU power of 100 W. A high voltage probe (Tektronix P6015A) was used to measure the applied voltage via the digital oscilloscope (Pico Technology PicoScope 6402A). The central rod was connected to the ground through a capacitor (10 nF) over which the voltage was monitored by the oscilloscope through a voltage probe (Pico Technology TA150). The current through the grounded cable to the capacitor was measured using a current monitor (Rogowski coil; Pearson Electronics 4100), also connected to the oscilloscope.

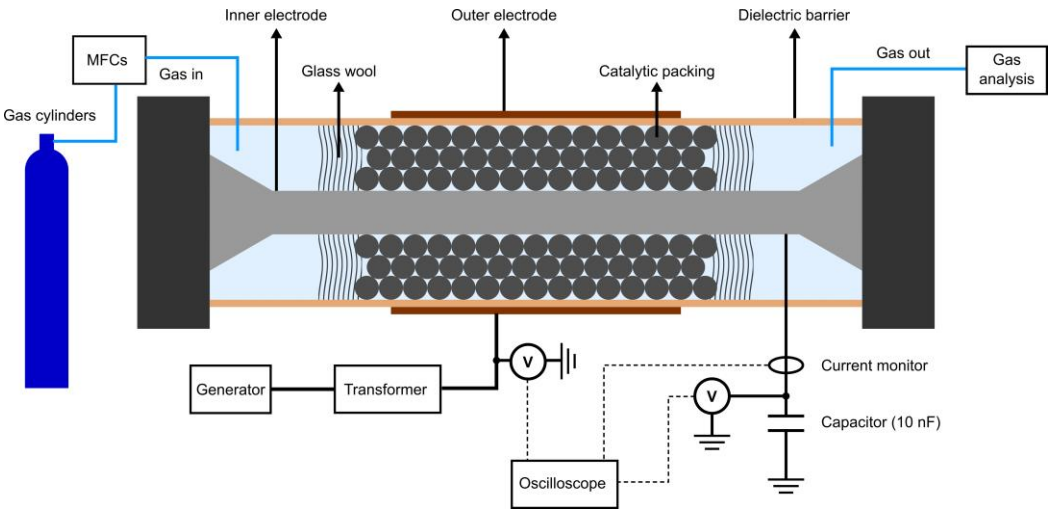

Figure 3-4: Schematic representation of the reactor setup. The gas analysis consists of an NDIR for NH_3 synthesis, or of a cold trap followed by a GC for the DRM experiments.

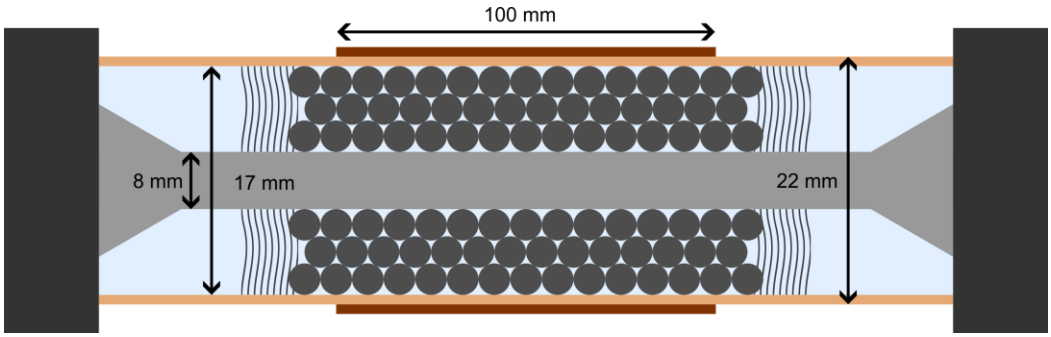

Figure 3-5: Graphical illustration of the dimensions of the reactor, the individual components are labeled in the previous figure.

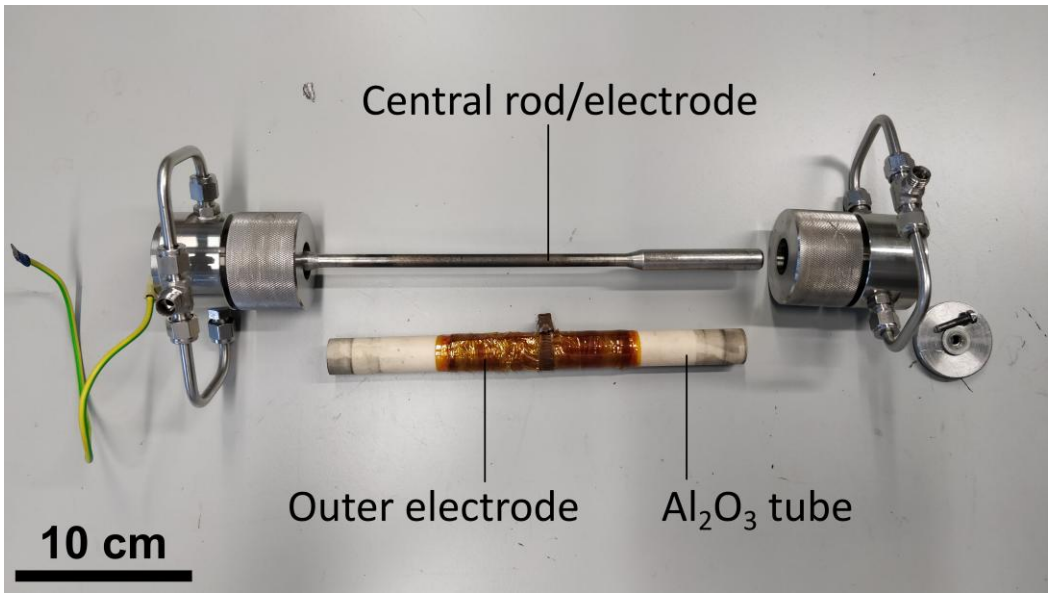

Figure 3-6: Picture of the main components of the packed-bed DBD reactor. The outer electrode is wrapper around the Al_2O_3 tube which acts as the dielectric barrier. This tube the slides over the central rod which acts as the grounded electrode in the reactor. The end pieces are mounted on either end of the tube to seal the system.

For the DRM experiments, a mixture of CO_2 and CH_4 (Air Liquide, >99.998 % and >99.995 %, respectively) was sent to the reactor at a total flow rate of 100 mln/min (normal ml per min) [93] in a CO_2/CH_4 ratio of 1:1 or 2:1. We emphasize that we controlled the mass flow rate (and not volumetric flow rate) in the experiments, which was measured in mln/min. The outflow of the reactor was sent through a cold trap to condense the liquid fraction, which was determined to be mostly water (>98 %) with small amounts of methanol and ethanol by a separate gas chromatography (GC) measurement. Further,

the total volume of the liquid fraction was very small (in the order of a few hundred µl), which prevented an accurate measurement. After the cold trap, the online GC (Agilent 990 Micro GC) sampled gas from the exhaust line to determine its composition. The GC was equipped and calibrated to measure CO_2, CH_4, CO, O_2, H_2, N_2, C_2H_2, C_2H_4, and C_2H_6. As gas expansion can influence the measurements [94,95], N_2 was used as a standard for the GC measurements, by adding a continuous flow of 20 mln/min N_2 to the outflow of the reactor before sampling by the GC. Before every experiment, the GC sampled at least three times to determine a baseline for the concentrations of the gases entering the reactor and used as a standard. The plasma was on for 1 h for each experiment with the GC sampling approximately every 5 min. This allowed the system to reach quasi-steady state after around 15 min, which then left enough samples to average the measurements. These peaks in the chromatograms were integrated, averaged over the samples during the quasi-steady state and converted to concentrations using our calibration. The standard deviation of the various peak areas and the error on the calibration were used to determine the error on the concentration of every component.

For the NH_3 synthesis experiments, a mixture of N_2 and H_2 (Air Liquide, >99.999 %) with a total flow rate of 100 mln/min was sent to the reactor. For these experiments, N_2/H_2 ratios of 3:1, 1:1 and 1:3 were used. The outflow of the reactor was then analyzed by a non-dispersive infrared sensor (NDIR, Rosemount X-stream Enhanced XEGP Continuous Gas Analyzer, Emerson). The plasma was on until the NH_3 concentration in the outflow remained stable for at least 10 minutes, which was then averaged over this stable area to determine an overall NH_3 concentration for that experiment. The standard deviation of the set of stabilized concentration measurements was used as the error on the measurements.

To mimic the residence time of a packed reactor, experiments for all gas mixtures were also performed with an empty reactor at 200 mln/min, as the packing is expected to occupy roughly half of the volume of the reactor, thus approximately reducing the apparent residence time by a factor of two [96].

2.4 Discharge Characterization

As introduced in Chapter 2, the discharge can be characterized by employing electrical diagnostics. These diagnostics are either based on the analysis of the voltage-charge diagram, or based on the current signal, which can be used to quantify the microdischarges. Both approaches are described in more detail in the following sections.

2.4.1 Analysis of the Voltage-Charge Diagram

During the plasma experiments, various snapshots were acquired by the oscilloscope, monitoring the applied voltage and the measured current. During operation, the voltage-charge (V-Q) diagram was also shown to monitor the discharge during the experiment. For the detailed analysis of the discharges, only the applied voltage and the measured current were used, and the current signal was integrated to yield the charge. This method was compared to the other common technique of using the voltage over the monitoring capacitor, which proved to be practically identical, as presented in Appendix A, Section 1. Many of the analyses characterizing the discharge are based on the work of Peeters et al. [53,86].

During each experiment, multiple (at least three) snapshots were acquired with the oscilloscope when a (quasi-)steady state was reached, saving the applied voltage and measured current. The electrical measurements coincided with the gas-phase analyses, thus not including the initial phase of the experiment. Each of these snapshots was analyzed to yield the various discharge characterizing metrics (i.e., plasma power, microdischarge quantity, effective dielectric and cell capacitances, burning voltage, conductively transferred charge, as discussed in detail in this section) and the variation between the snapshots was used to determine an error on the various characteristics.

The first important property of the DBD plasma is the power dissipated into the plasma, usually called the plasma power *P*. This is determined by multiplying the applied voltage *V* and the measured current *I* and taking the average of this product over a whole number of cycles (11 in one snapshot in our case). This is illustrated in Equation (1).

$$\bar{P} = \frac{1}{T}\int_0^T V(t) \cdot I(t)\, dt \tag{1}$$

Further analyses of the plasma discharge are based on the work of Peeters and van de Sanden [86], accounting for partial surface discharging. Note that the electrical model we employ here was developed for a system without explicitly including a packing material. Hence, caution is advised when applying these equations to our data. However, we believe this approach is justified because the packing can be seen as a part of the gap, indeed drastically changing its properties (as described later), but not necessarily breaking the proposed model.

In order to do these analyses, the geometric dielectric capacitance C_{diel} has to be determined. This capacitance is inherent to the reactor setup, but it is challenging to

accurately measure the contribution of just the dielectric in the system. Therefore, a theoretical calculation is used to approximate this capacitance, as shown in Equation (2)

$$C_{diel} = \frac{2\pi k \varepsilon_0 L}{\ln \frac{b}{a}} \quad (2)$$

with k the dielectric constant of the material used for the dielectric barrier (10, as provided by the manufacturer), ε_0 the permittivity of vacuum, L the length of the discharging part of the reactor (100 mm), b the outer diameter of the dielectric cylinder (22.0 mm) and a the inner diameter of the cylinder (17.0 mm). This yields a dielectric capacitance of 216 pF, which is needed for the further calculations. The dimensions of the reactor are known with a high precision, but since Equation (2) is based on an ideal system and the precision of the dielectric constant is not known, a relative error of 10 % on the dielectric capacitance will be used in further error propagation calculations.

Next, the relevant capacitances can be extracted directly from the voltage-charge diagrams by fitting a straight line to the beginning ("plasma-off" segment) and end ("plasma-on" segment) of the rising side of the curve to determine C_{cell} and ζ_{diel}, respectively (illustrated in Figure 3-7 and more generally introduced in Chapter 2). The dielectric capacitance as extracted from the voltage-charge diagram is the so-called effective dielectric capacitance ζ_{diel}, which can deviate from the true geometric dielectric capacitance C_{diel}, as will be discussed further. These calculations were performed for every full PSU cycle in the oscilloscope snapshots. The obtained values were found to be effectively identical to those extracted from averaged voltage-charge diagrams, as shown in Appendix A, Section 2.

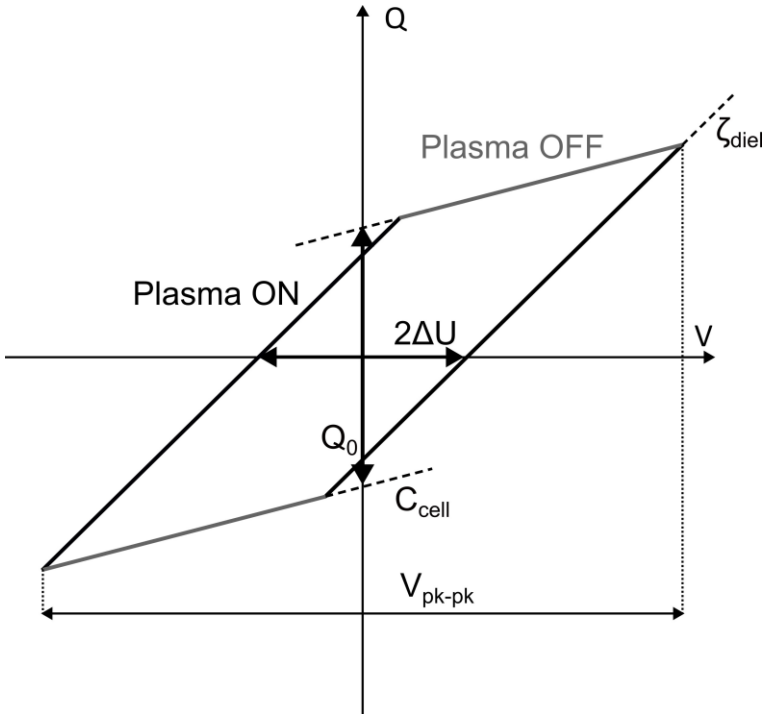

Figure 3-7: Illustration of parameters extracted from the voltage-charge diagram. The derivative of the "plasma off" section yields the cell capacitance C_{cell}, the derivative of the "plasma on" section yields the effective dielectric capacitance ζ_{diel}, the difference between the maximum and the minimum of the applied voltage yield the peak-to-peak voltage $V_{pk\text{-}pk}$, the difference between the voltages at which the charge crosses zero yields $2\Delta U$, which is used to calculate the burning voltage U_b, and the difference in charge between the (ideally parallel) "plasma off" sections yields Q_0, which is used to calculate the conductively transferred charge ΔQ_{dis}.

Further, the partial discharging can be quantified. Partial surface discharging is the effect where the plasma is only formed in a part of the reactor, thus neglecting certain areas of the dielectric barrier, the so-called non-discharging areal fraction α [86]. This is a defining characteristic of the DBD plasma discharge and, among other things, causes a discrepancy between the true and measured (or effective) dielectric capacitances (C_{diel} and ζ_{diel}, respectively). Equation (3) describes how α can be calculated based on the measured and estimated dielectric capacitances and cell capacitance, discussed earlier.

$$\alpha = \frac{C_{diel} - \zeta_{diel}}{C_{diel} - C_{cell}} \tag{3}$$

Analogously, the discharging areal fraction β can be defined as:

$$\beta = 1 - \alpha \tag{4}$$

In an ideal, fully discharging (i.e., $\alpha = 0$) DBD, the burning voltage is measured as half of the distance between the zeros ($Q = 0$) of the voltage-charge diagrams (see again Figure 3-7). When accounting for partial discharging, this measured burning voltage ΔU can be converted to a true burning voltage U_b:

$$U_b = \pm\left(1 + \frac{\alpha C_{cell}}{\beta C_{diel}}\right)\Delta U = \frac{1 - \frac{C_{cell}}{C_{diel}}}{1 - \frac{C_{cell}}{\zeta_{diel}}}\Delta U \tag{5}$$

Next, the conductively transferred charge ΔQ_{dis} can be calculated based on the measured charge difference between the two "plasma-off" phases Q_0. This Q_0 can be extracted from the measured voltage-charge diagrams by determining the difference between the intersects of the fitted "plasma-off" curves with the Q-axis (see again Figure 3-7). Then, ΔQ_{dis} can be calculated using the following equation:

$$\Delta Q_{dis} = \frac{Q_0}{1 - \frac{C_{cell}}{C_{diel}}} \tag{6}$$

Additional details and theoretical background regarding these equations can be found in the work of Peeters and van de Sanden [86].

2.4.2 Microdischarge Quantification

Another important, though hard to quantify, discharge characteristic in a DBD is the number and intensity of microdischarges. These short-lived, localized, and intense discharges are typical in many DBD experiments and they have a significant impact on the gas-phase chemistry [60–62], yet they are tricky to quantify [97]. Firstly, the hardware requirements to precisely measure the fast change in current are stringent. Further, the interpretation of the data is rarely straightforward. For example, it is challenging for an automated analysis to accurately count the number of microdischarges when multiple discharges are taking place at the same time in the reactor. Alternatively, manual counting is rarely desirable as it is labor-intensive and sensitive to human error and bias. As the current monitor used in this work (Rogowski coil, Pearson Electronics 4100, with a rise time of 10 ns [98]) struggles to capture the true structure of microdischarges, we did not attempt to count the number of microdischarges, let alone try to integrate them individually, as this would have introduced too many uncertainties. Rather, we took a more general and prudent approach by defining a "microdischarge quantity", based on the frequency spectrum of

the current signal. As our hardware is at its limit to measure the microdischarges, but not entirely incapable, we assume that microdischarges are still registered, albeit slightly deformed. First, we calculated the displacement current $I_{displacement}$ caused by the capacitive charging of the system as a function of the applied voltage, as illustrated in Equation (7). Next, the displacement current $I_{displacement}$ is subtracted from the measured current I to reveal the current signal from the actual discharge $I_{discharge}$. The displacement current $I_{displacement}$ is calculated using the following equation (see Appendix A, Section 3 for more details) [53,86]:

$$I_{displacement}(t) = C_{cell}\frac{dV(t)}{dt} \tag{7}$$

Next, we applied the fast Fourier transform (FFT) to the discharge current signal, and integrated the modulus over a wide frequency range from 10 to 100 MHz, corresponding to a time-scale range of 10 to 100 ns. This value does not have an immediate unambiguous physical interpretation, but it allows for an objective, relative comparison between experiments with various catalysts. For example, both a larger number of microdischarges, and a higher current spike during the microdischarges, will increase the microdischarge quantity, so it can be seen as a combination of the number and intensity of the microdischarges. Due to this ambiguity in its direct interpretation, the microdischarge quantity is presented unitless and rescaled between 0 and 1.

We compare a few oscillograms with their respective microdischarge quantity, to illustrate how these values can be interpreted. As a first example, we compare the empty reactor with the blank Al_2O_3 experiment for NH_3 synthesis (N_2/H_2 ratio of 1:1) in Figure 3-8. The microdischarge quantities are 0.737 ± 0.095 and 0.7100 ± 0.0081, respectively. Despite these very similar microdischarge quantities, the discharge current signals are notably different (note the different y-scales). As expected, two different properties of the microdischarges affect this global quantity, i.e., their intensity and their number (per cycle, or their frequency, though this terminology may be confusing in this context). In the empty reactor, just a few microdischarge occur every half cycle, but each one is very intense. Alternatively, when the reactor is packed with blank Al_2O_3, the number of discharges per half cycle is multiple times higher, but their intensity is much lower. In this case, these two effects compensate each other, leading to these very similar microdischarge quantities. This shows that the interpretation of this value is not straightforward and should always be complemented with additional (qualitative) analyses.

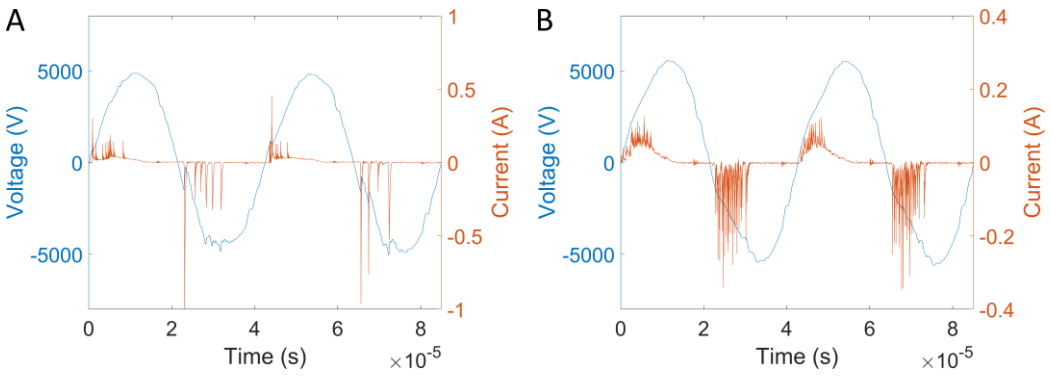

Figure 3-8: Voltage and discharge current oscillograms for NH_3 synthesis (1:1 ratio) with an empty reactor (A) and a reactor packed with blank Al_2O_3 (B). The corresponding microdischarge quantities are 0.737 ± 0.095 (empty, A) and 0.7100 ± 0.0081 (blank Al_2O_3, B). Despite the visibly different discharge characteristics, the microdischarge quantification yields similar values.

However, it is clear that major differences in microdischarge behavior, which may also be easily judged by visual comparisons, are unambiguously demonstrated by the microdischarge quantity as well. For example, when visually comparing the discharge current signals in Figure 3-9 (DRM, 1:1 ratio of CO_2/CH_4), it is obvious that the WI Ni catalyst exhibits a much higher amount and intensity of microdischarges compared to the SC Ni catalysts. This stark difference is also irrefutably clear in the microdischarge quantity: 0.782 ± 0.014 for WI Ni and 0.1022 ± 0.0035 for SC Ni 3.3 wt%.

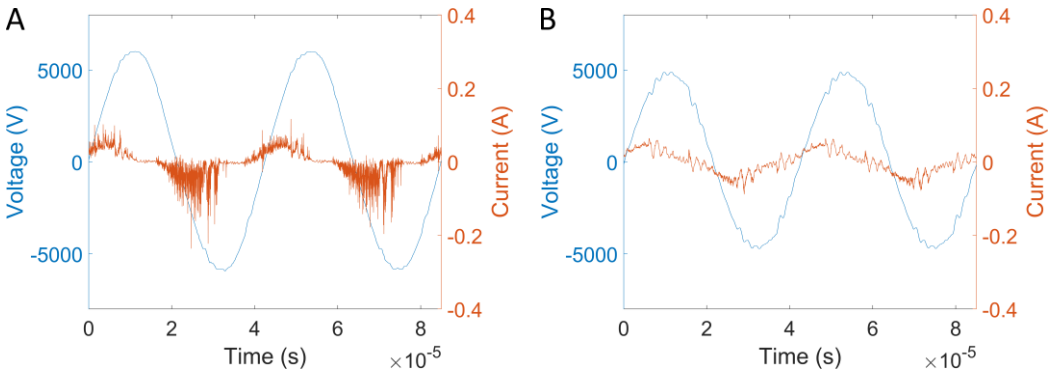

Figure 3-9: Voltage and discharge current oscillograms for DRM (1:1 ratio) for a reactor packed with WI Ni catalysts (A) and a reactor packed with SC Ni 3.3 wt% catalysts (B). The corresponding microdischarge quantities are 0.782 ± 0.014 (WI Ni, A) and 0.1022 ± 0.0035 (SC Ni 3.3 wt%, B). The microdischarge behavior between both oscillograms is clearly different, which is also reflected in the microdischarge quantities.

Furthermore, this technique is also capable of picking up smaller, more nuanced differences. For example, when we compare the discharge current signals for NH_3

synthesis (1:1 ratio) for the SC Ni 3.3 wt% catalysts, with the SC Co 3.3 wt% ones (Figure 3-10), the interpretation of the raw current signal may be less straightforward. The overall shape of the current traces is very similar, but the SC Co one shows some more high-frequency fluctuations, but with a small amplitude, making it tricky to directly interpret. The microdischarge quantity, however, shows a significant difference between these examples, i.e., 0.1479 ± 0.0062 for SC Ni 3.3 wt% and 0.2661 ± 0.0044 for SC Co 3.3 wt%. This indicates that despite the modest amplitude, these features do contribute to the frequencies corresponding to microdischarges, which allows for a more objective and justified interpretation of these results.

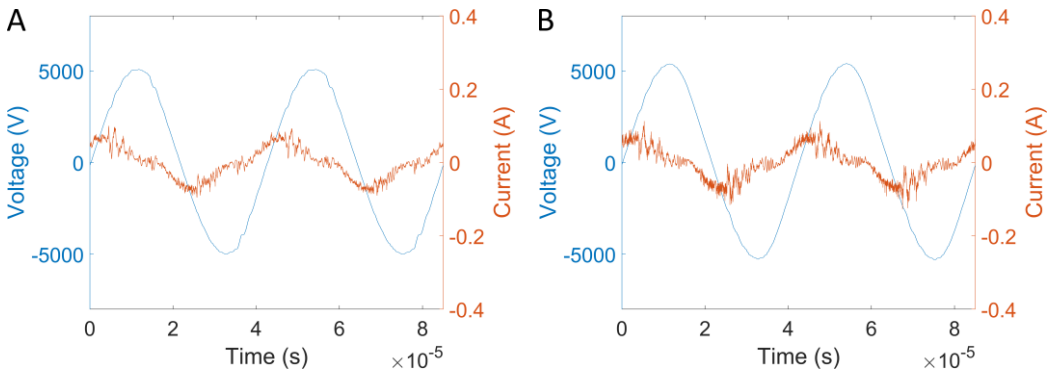

Figure 3-10: Voltage and discharge current oscillograms for NH_3 synthesis (1:1 ratio) with SC Ni 3.3 wt% (A) and SC Co 3.3 wt% (B). The corresponding microdischarge quantities are 0.1479 ± 0.0062 (SC Ni 3.3 wt%, A) and 0.2661 ± 0.0044 (SC Co 3.3 wt%, B). The more subtle differences in the microdischarge behavior are captured well by the microdischarge quantity.

We believe the strength of this approach is twofold. Firstly, by only looking at the frequencies that are relevant for microdischarges, this analysis immediately eliminates lower frequency current variations. Such lower frequency variations may still occur and can complicate a straightforward visual interpretation, but they are caused by different processes, and thus irrelevant when studying the microdischarge behavior. Secondly, this analysis can be automated easily and is objective, meaning it allows for a facile, straightforward, and direct comparison between experiments, e.g., when comparing different catalysts. As mentioned previously, these results should not be interpreted without any further analysis, but they can serve as a valuable part of the plasma discharge analysis.

2.5 Performance Metrics

The plasma-catalytic performance can be quantified based on the measured gas composition. Depending on the investigated reaction, different metrics are appropriate and various considerations should be taken into account, as discussed in the following.

2.5.1 Dry Reforming of Methane

The DRM reaction proceeds as follows:

$$CH_4 + CO_2 \rightarrow 2CO + 2H_2 \quad \text{(R1)}$$

Hence, the formation of additional gas molecules (see Reaction R1) causes an expansion of the gas. On the other hand, solid carbon deposition, formation of larger molecules, and condensation of liquid components could cause a contraction of the gas mixture. Therefore, the flux ratio α_{flux} was determined empirically with the standard method (i.e., by adding a fixed flow of the standard N_2 and monitoring its concentration), using the following equation [94,95]:

$$\alpha_{flux} = \frac{y_{in}^{IS}}{y_{out}^{IS}} \quad (8)$$

with y_{in}^{IS} the fraction of internal standard (N_2) without plasma and y_{out}^{IS} the fraction of N_2 with plasma, as measured with the GC.

Next, the absolute conversion X^{abs} of CO_2 and CH_4 can be calculated. The absolute conversion only considers the individual reactant and how much of the used reactant was actually converted:

$$X_i^{abs} = \frac{y_i^{in} - \alpha_{flux} y_i^{out}}{y_i^{in}} \quad (9)$$

with *i* the reactant of interest (either CO_2 or CH_4), y_i^{in} the fraction of reactant *i* as measured without plasma and y_i^{out} the fraction of reactant *i* as measured with plasma. The total conversion X^{tot} can then be determined by combining both absolute conversions, weighted by their respective fraction in the influx. The influx fractions *IF* are calculated based on the measured concentration of CO_2 and CH_4 without plasma:

$$IF_i = \frac{y_i^{in}}{y_{CO2}^{in} + y_{CH4}^{in}} \quad (10)$$

Combined with these influx fractions, the absolute conversions can be used to calculate the total conversion:

$$X_{tot} = X_{CO2}^{abs} * IF_{CO2} + X_{CH4}^{abs} * IF_{CH4} \quad (11)$$

Taking into account the measured plasma power *P*, the specific energy input (*SEI*) can be calculated:

$$SEI = \frac{P}{Q_{in}} \quad (12)$$

with Q_{in} the flow rate going into the reactor. Next, the energy cost (*EC*) can be determined by combining the *SEI* with the total conversion:

$$EC_{DRM} = \frac{SEI}{X_{tot}} \quad (13)$$

This EC_{DRM} has the same unit as the SEI, and they can be expressed in different units (e.g., kJ/l or kJ/mol), depending on conversion factors in the formulas [95]. It should be interpreted as the amount of energy used for the conversion of CO_2 and CH_4.

Further, the selectivity toward certain products *j* based on atoms *A* can be determined:

$$S_j^A = \frac{\mu_j^A \alpha_{flux} y_j^{out}}{\sum_i \mu_i^A (y_i^{in} - \alpha_{flux} y_i^{out})} \quad (14)$$

with μ_j^A the number of atoms *A* in product *j* and μ_i^A the number of atoms *A* in reactant *i*.

2.5.2 NH_3 Synthesis

During the NH_3 synthesis experiments, the outflow of the reactor was analyzed by an NDIR, measuring the NH_3 concentration in the gas mixture. As only one chemical reaction takes place, the stoichiometry of that reaction suffices to take the gas contraction into account (see Reaction R2).

$$N_2 + 3H_2 \rightarrow 2NH_3 \quad (R2)$$

Knowing this, the mass flow rate of NH_3 in the outflow of the reactor (MFR_{NH3}^{out}) can be calculated:

$$MFR_{NH3}^{out} = \frac{MFR_{tot}^{in} y_{NH3}^{out}}{1 + y_{NH3}^{out}} \quad (15)$$

where MFR_{tot}^{in} is the combined flow rate of N_2 and H_2 at the inlet and y_{NH3}^{out} is the measured fraction of NH_3 at the outlet. Similar to DRM, an energy cost (EC_{NH3}) can be defined for the NH_3 synthesis. However, this EC_{NH3} is defined slightly differently, namely as the amount of energy used for the production of the synthesized NH_3, rather than for the conversion of reactants, as in the case of DRM:

$$EC_{NH3} = \frac{P}{MFR_{NH3}^{out}} \tag{16}$$

3. Results and Discussion

Next, the characterization and various properties of the synthesized catalysts will be discussed. Then, the discharge is characterized for the various catalysts and the effects of the catalysts on the discharge properties are discussed. Furthermore, performance of the catalysts is investigated and correlated to the altered discharge characteristics.

3.1 Catalyst Synthesis and Characterization

For the WI catalysts, SEM-EDX maps were acquired from cross sections of the beads. These analyses yield a radial distribution of the catalyst metal throughout the alumina beads, as well as a total metal loading. The distributions, shown in Figure 3-11 A, illustrate that the catalyst metals are distributed homogeneously throughout the entire bead, penetrating to the center of the beads, with a slight increase in concentration toward the edge. The total metal loadings (11.1 wt% and 10.0 wt% for the Ni and Co beads presented in Figure 3-11 A, respectively) agree with the expected 10 wt%. Analyses of a second bead of each catalyst (not shown) yield total metal loadings of 11.1 wt% (Ni) and 9.3 wt% (Co), and are in good agreement with the first measurements.

Notably, the BSE-SEM images of the surfaces of the WI catalysts show a discrepancy in metal nanoparticle coverage between the Ni and Co catalyst, as illustrated in Figure 3-11 B-C. The BSE signal is higher at the position of heavier atoms, thus highlighting the Ni and Co nanoparticles against the Al_2O_3 background. It is clear that the WI Co catalyst have a substantially higher coverage of nanoparticles at the surface compared to the WI Ni catalyst. A similar accumulation of Co particles at the surface of the catalyst was observed by Ndayirinde et al. for their Co-based WI catalysts [37]. The accumulation they observed was even more pronounced, though they used an adapted synthesis method and used a much higher metal loading. More advanced synthesis protocols may be employed to obtain more control over the precise metal distribution [99,100].

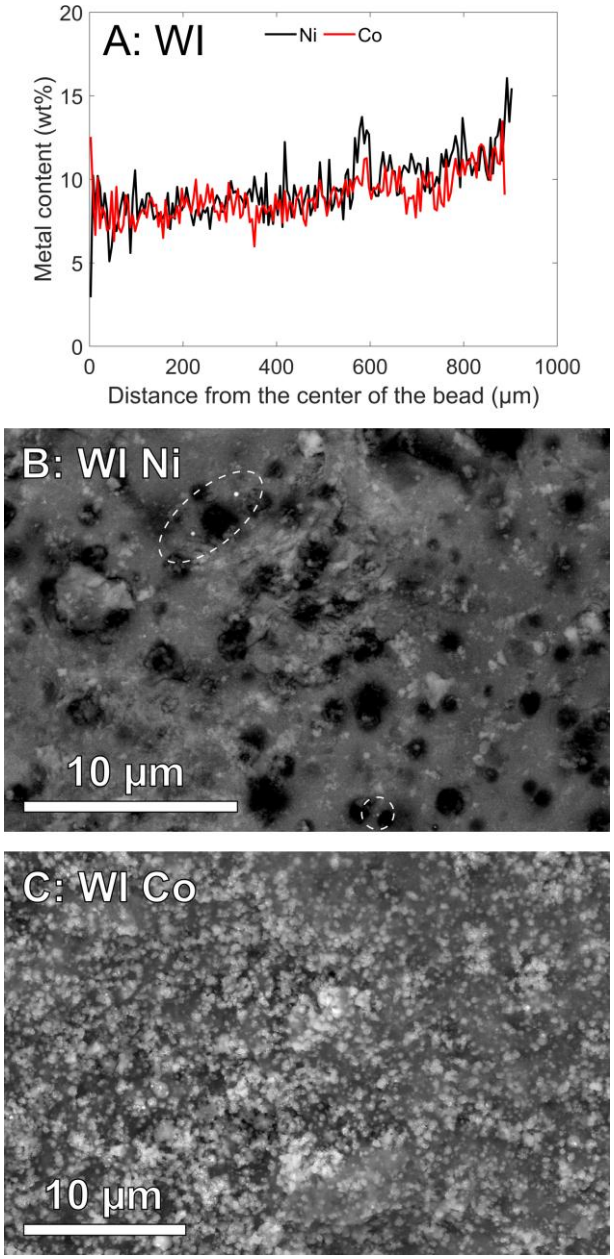

Figure 3-11: SEM analyses of the WI catalysts. (A): Radial distribution of Ni and Co throughout WI beads; total metal loadings for these catalysts are 11.1 wt% (Ni) and 10.0 wt% (Co). (B): BSE-SEM image of the surface of a WI Ni bead. A few heavy particles (Ni) are present at the surface of the bead (small bright spots in the image, indicated by the dashed ovals), but most of the exposed area is uncovered Al_2O_3. (C): BSE-SEM image of the surface of a WI Co bead. The surface contains many heavy (Co) particles (evidenced by the many bright particles), covering a significant fraction of the surface area.

The BSE-SEM images of the exterior surfaces of the SC beads, presented in Figure 3-12, reveal that the shell is relatively inhomogeneous for Ni, whereas for Co the layer at the surface is mostly intact, with some sections missing. This Ni or Co shell is further characterized by SE-SEM imaging of the cross-sections of the beads, presented in Figure 3-13. These analyses of the cross-sections reveal a clear (though often incomplete) shell at the surface of the beads, which consists of metal(oxide) nanoparticles. It is likely that by manipulating the beads, some parts of the shell detached, as a strong interaction between the particles in the shell is lacking. For the SC Ni catalysts, the thickness of the shell varies between hundreds of nm to a few µm, as observed in the cross-sectional images in Figure 3-13. For the SC Co beads, the shell thickness also varies, but it is much more consistent. In this case, it is also obvious that for the 3.3 wt% beads, the shell is clearly thicker (approximately 5 µm) than for the 1 wt% beads (0.5 - 2 µm).

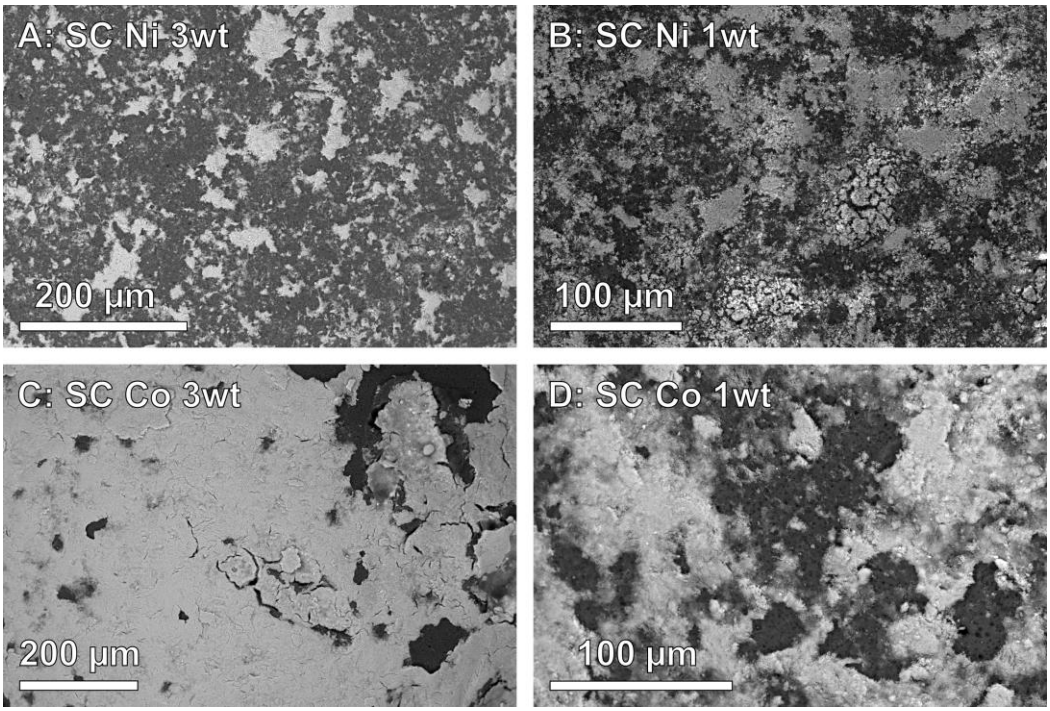

Figure 3-12: BSE-SEM images of the outer surface of a SC Ni 3 wt% (A), SC Ni 1 wt% (B), SC Co 3 wt% (C), and SC Co 1 wt% (D) bead. The bright areas indicate the heavy catalyst metal (Ni or Co) against the lighter Al_2O_3 background. For the SC Ni catalysts, the coating is patchy, with many areas of uncovered Al_2O_3 being present. The coating of the SC Co catalysts is more uniform and a much higher catalyst coverage can be observed compared to the SC Ni catalysts, especially for the 3 wt%.

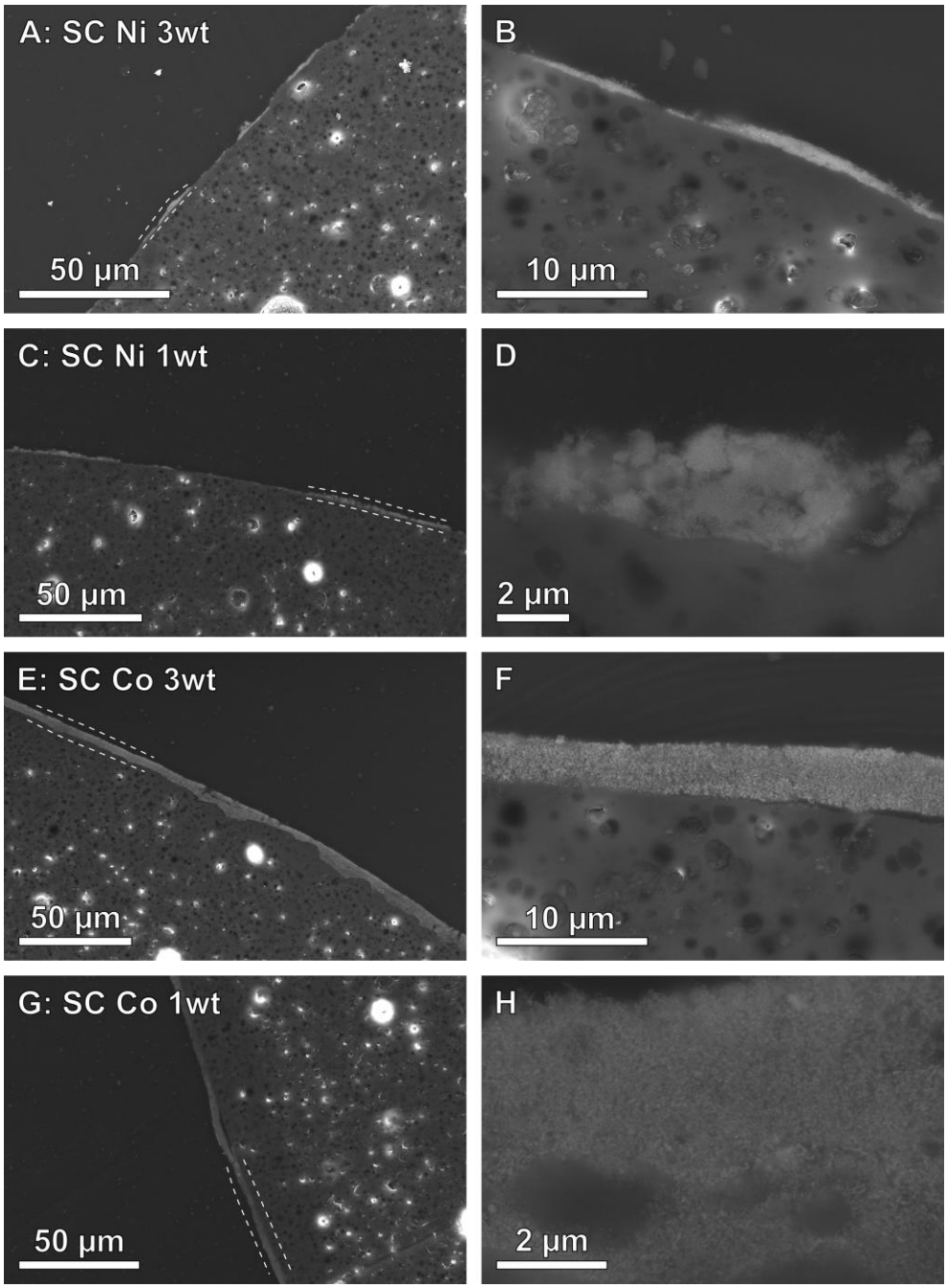

Figure 3-13: Cross-sectional SE-SEM images of the SC Ni 3.3 wt% (A, B), SC Ni 1 wt% (C, D), SC Co 3.3 wt% (E, F), and SC Co 1 wt% (G, H) catalysts. The metallic shell is indicated by the dashed lines in the lower magnification images (left), which indicate that the Ni shell is more patchy whereas the Co shell remains more intact. The higher magnification images (right) reveal that the shell consists of nanoparticles.

The XRD measurements presented in Figure 3-14 and Figure 3-15 show that the reduction of the SC catalysts was completed, as no reflections corresponding to either Ni- or Co-oxides remained (though amorphous oxides cannot be excluded). Note that although the 10 wt% SC catalysts were not stable enough for reliable plasma catalysis experiments, they are still included in the XRD results. Chemically, they should be identical to the catalysts with a lower Ni- or Co- loading, and given their higher loading, the Ni- and Co- based signals are more pronounced. For the WI catalysts, however, both Ni and Co metal and oxides phases are present. This is probably due to the inaccessibility of the innermost Ni- or Co-oxide particles during the reduction step, likely because H_2 cannot penetrate deep enough into the pores during the reduction. This hypothesis is further supported by the decrease in specific surface area of the WI catalysts, as presented in Table 3-1.

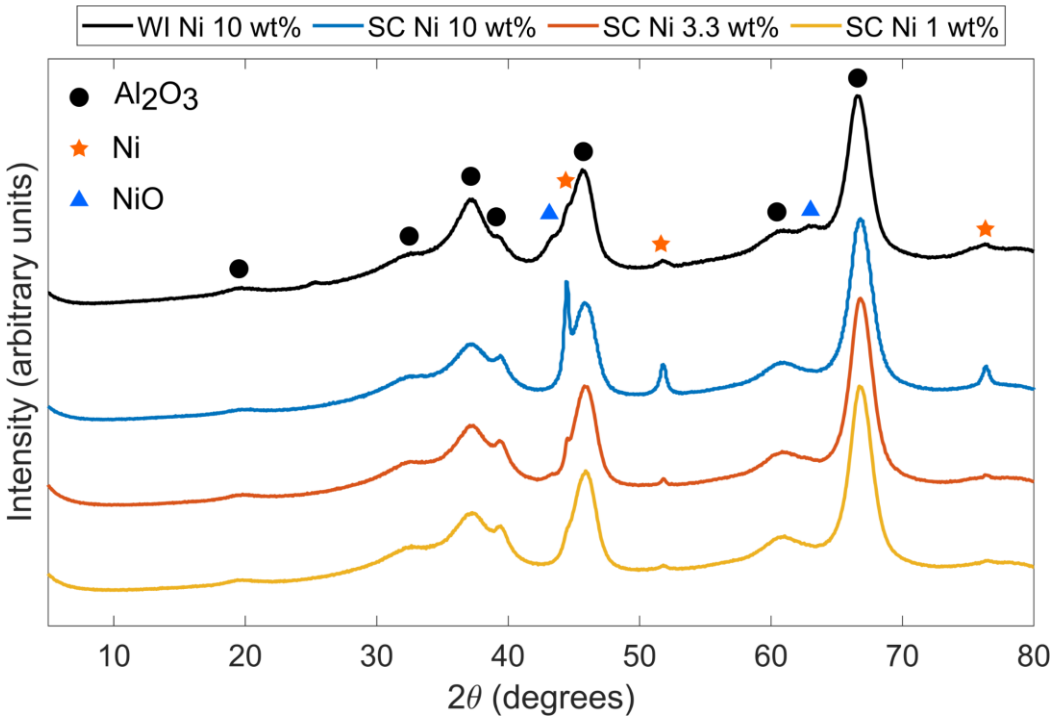

Figure 3-14: X-ray powder diffractograms of the reduced Ni-based catalysts. Naturally, all catalyst samples contain strong contributions from the Al_2O_3 support. All catalysts also contain metallic Ni, though the signal in the WI Ni catalyst is notable weaker than that in the SC Ni catalyst of the same metal loading. Moreover, the WI Ni catalyst contains NiO, which is not observed for the SC catalysts.

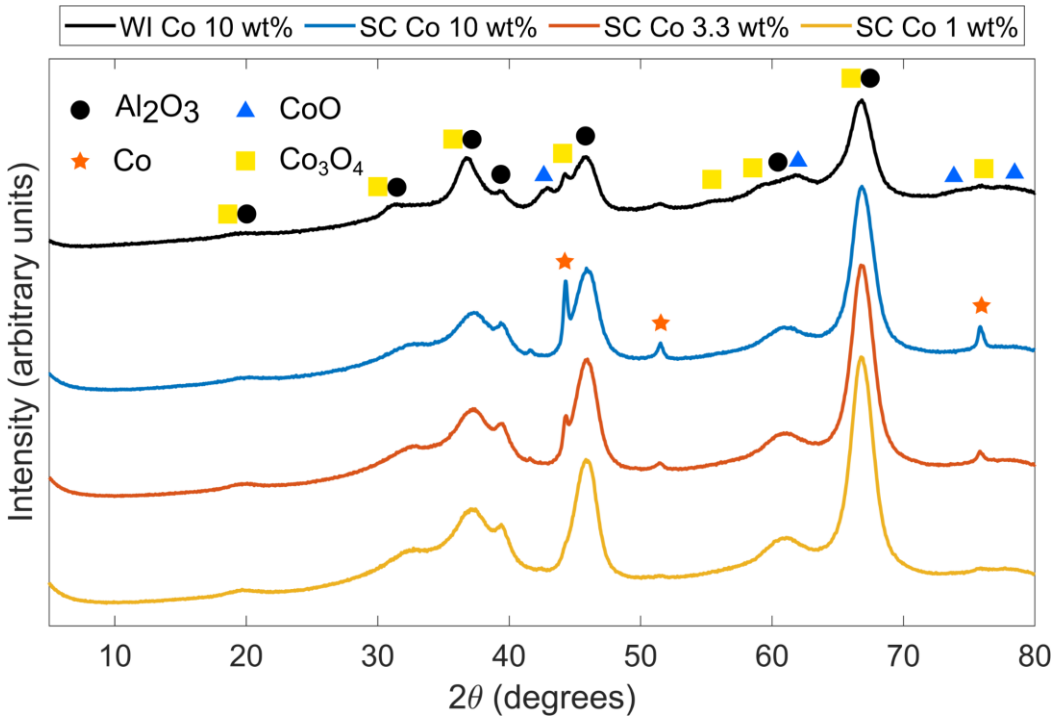

Figure 3-15: X-ray powder diffractograms of the reduced Co-based catalysts. As for the Ni catalysts, all samples contain contributions from Al_2O_3 and the reduced metal catalyst (Co in this case). In addition, the signal of metallic Co is weaker in the WI catalyst compared to the SC catalyst of the same loading, and the WI catalyst also contains Co oxides.

The N_2 sorption isotherms can all be categorized as IUPAC type IV(a) and their shape is illustrated by some examples presented in Figure 3-16. The quantification of these isotherms is presented in Table 3-1 and although no errors are available (triplicate measurements would have been needed), the typical relative error of these measurements is 5% or less [101]. This quantification indicates that the specific surface area decreases slightly after deposition of the catalysts compared to the blank alumina beads. The decrease of the specific surface area is the strongest for the WI catalysts (180 - 190 m^2/g) and is least pronounced for the 1 wt% SC catalysts (approximately 220 m^2/g), with a specific surface area of blank alumina of approximately 240 m^2/g. We attribute the observed effects for the WI catalysts to the penetration of the loaded metal/metal oxides deep inside the beads during WI, effectively blocking or filling the pores throughout the whole bead rather than just the surface, causing the more significant decrease in specific surface area. This further elucidates the partial oxidation of the WI catalysts, since the blocked pores are then inaccessible for the H_2 during the reduction

step. The SC particles, however, remain at the surface, preserving the porosity inside the beads. Further, the SC layer of Ni or Co is patchy and consists of particles (see Figure 3-13 and Figure 3-12), rather than a bulk layer, thus allowing most of the N_2 to penetrate inside the pores.

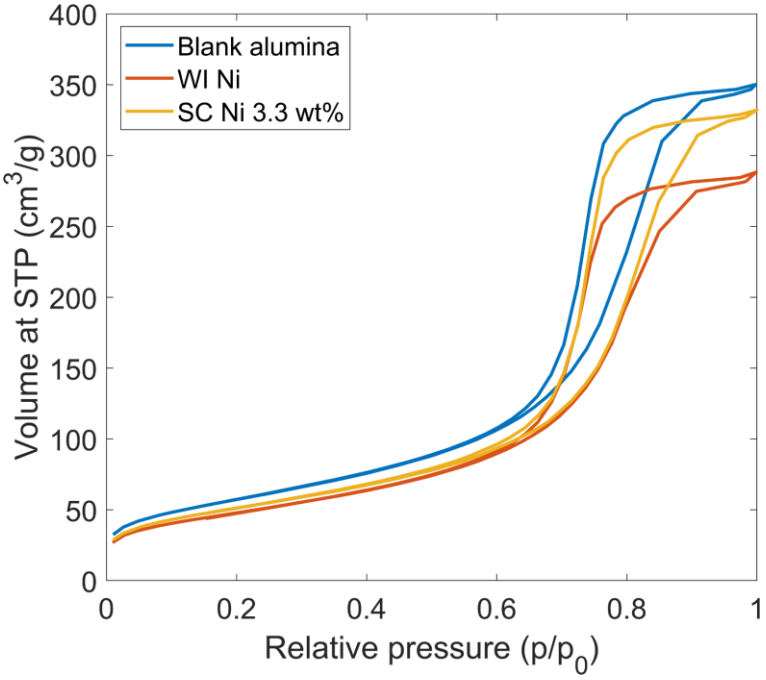

Figure 3-16: Illustrative N_2 sorption data of the blank Al_2O_3 catalyst, the WI Ni catalyst and the SC Ni 3.3 wt% catalyst. All isotherms have a similar shape, corresponding to the IUPAC type IV(a). STP = Standard Temperature and Pressure (= 1 atmosphere pressure, 0 °C). Alternatively, SI units would be 10^{-3} m^3/kg.

Table 3-1: Specific surface area of every catalyst, as determined by N_2 sorption.

	BET Specific surface area (m^2/g)
Blank Al_2O_3	244
WI Ni	193
SC Ni 3.3 wt%	202
SC Ni 1 wt%	220
WI Co	183
SC Co 3.3 wt%	211
SC Co 1 wt%	217

3.2 Effect of the Catalysts on the Plasma Discharge

The two main measurements of the plasma discharge and its properties are the current-voltage (I-V) characteristics and the voltage-charge diagrams. These measurements offer insights in the plasma discharge, enabling a direct comparison between the various experiments using different catalysts. Representative I-V characteristics displaying the calculated discharge current $I_{discharge}$ and voltage-charge diagrams of the DRM experiments and NH_3 synthesis experiments are provided in Figure 3-17 (I-V, DRM), Figure 3-18 (I-V, NH_3), Figure 3-19 (voltage-charge, DRM), and Figure 3-20 (voltage-charge, NH_3). The measured current and the capacitive displacement current are shown in Appendix A (Figure A-5 - Figure A-8). Although the overall shape of the current trace can be affected by the subtraction of the capacitive displacement current, the high-frequency characteristics of the various signals (i.e., the microdischarges) are preserved.

For the empty reactor, as well as when it is packed with blank Al_2O_3 beads or with the WI Ni catalysts, plenty of microdischarges are observed in the current signal, manifesting as short but intense bursts of current, illustrated in Figure 3-17 (A-D) for DRM and Figure 3-18 (A-D) for NH_3 synthesis. These microdischarges are strongly affected when introducing SC catalysts or the WI Co catalyst (see Figure 3-17 (E-I) for DRM and Figure 3-18 (E-I) for NH_3 synthesis). Note that the behavior of the SC Ni 1wt% is aberrant in the case of NH_3 synthesis (Figure 3-18 F), most likely due to the instability of the catalyst, where the shell detached significantly during the manipulation of the beads (also indicated by the SEM characterization in Figure 3-13 and Figure 3-12).

This drastic alteration of the discharge behavior is attributed to the presence of metallic nanoparticles at the surface of the beads (thus exposed to the plasma). The discrepancy in the behavior between WI Ni and WI Co further supports this hypothesis, as the WI Co had significantly more Co particles at the surface compared to Ni particles on the WI Ni beads (see the SEM analysis, Figure 3-11). We hypothesize that the exposed metal throughout the reactor volume seeds the plasma with electrons, so that the discharge can be initiated and sustained uniformly throughout the reactor volume. Alternatively, the discharge may consist of many, very weak microdischarges, yielding this seemingly more uniform discharge, rather than the more common highly filamentary discharge mode [102]. The underlying mechanism that provides these electrons is not fully understood and may be a combination of various effects, such as secondary electron emission [103] (potentially due to enhanced surface roughness [104]), surface Penning ionization (also known as Auger de-excitation) [22,105], field emission [106], or others.

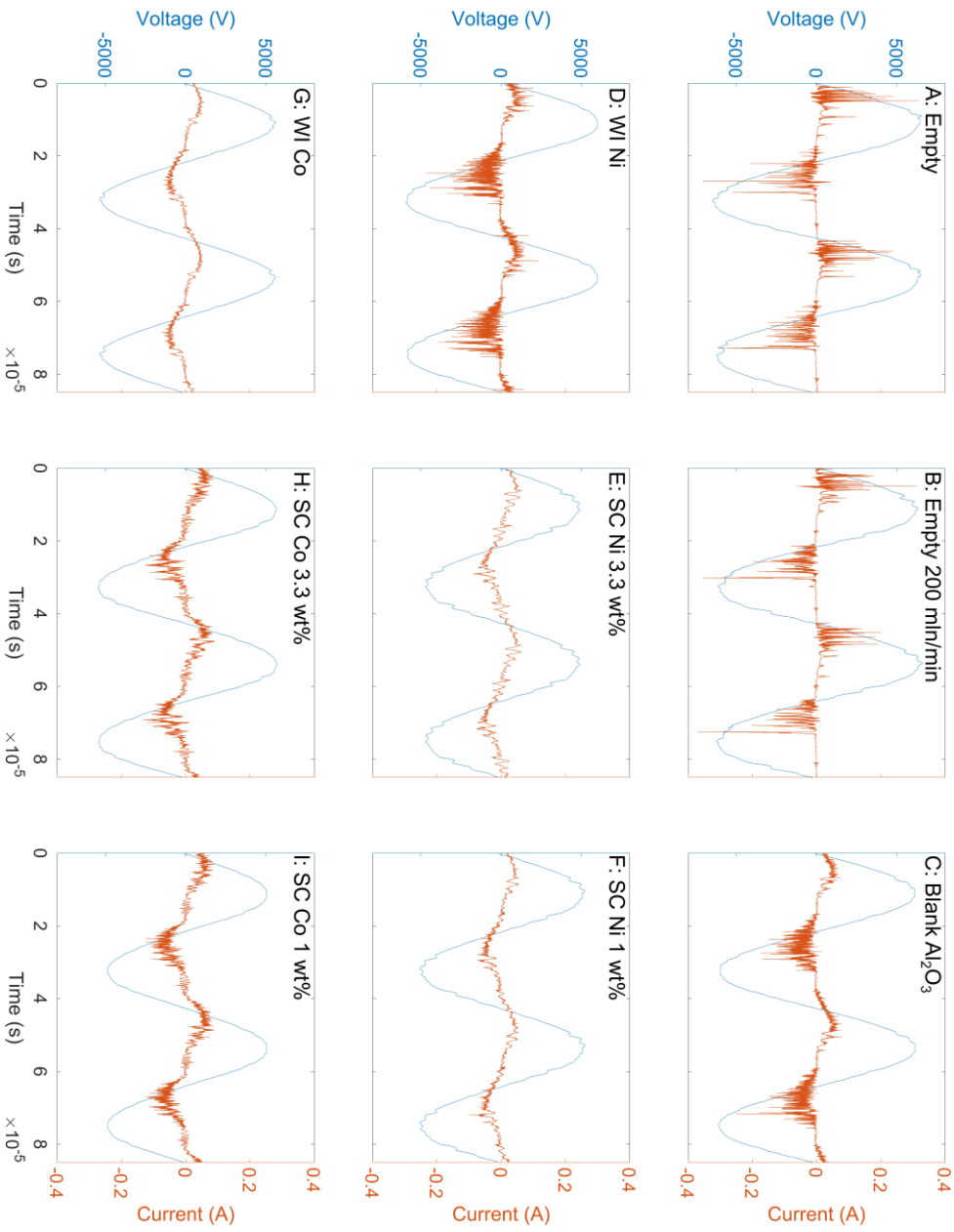

Figure 3-17: Representative I-V curves of the calculated discharge current $I_{discharge}$ for all experimental sets of DRM for a CO_2/CH_4 ratio of 1:1, illustrating the clear filamentary regime for the empty reactor, the reactor with blank Al_2O_3 packing and with WI Ni catalyst, whereas these filaments virtually disappear for the WI Co and the various SC catalysts.

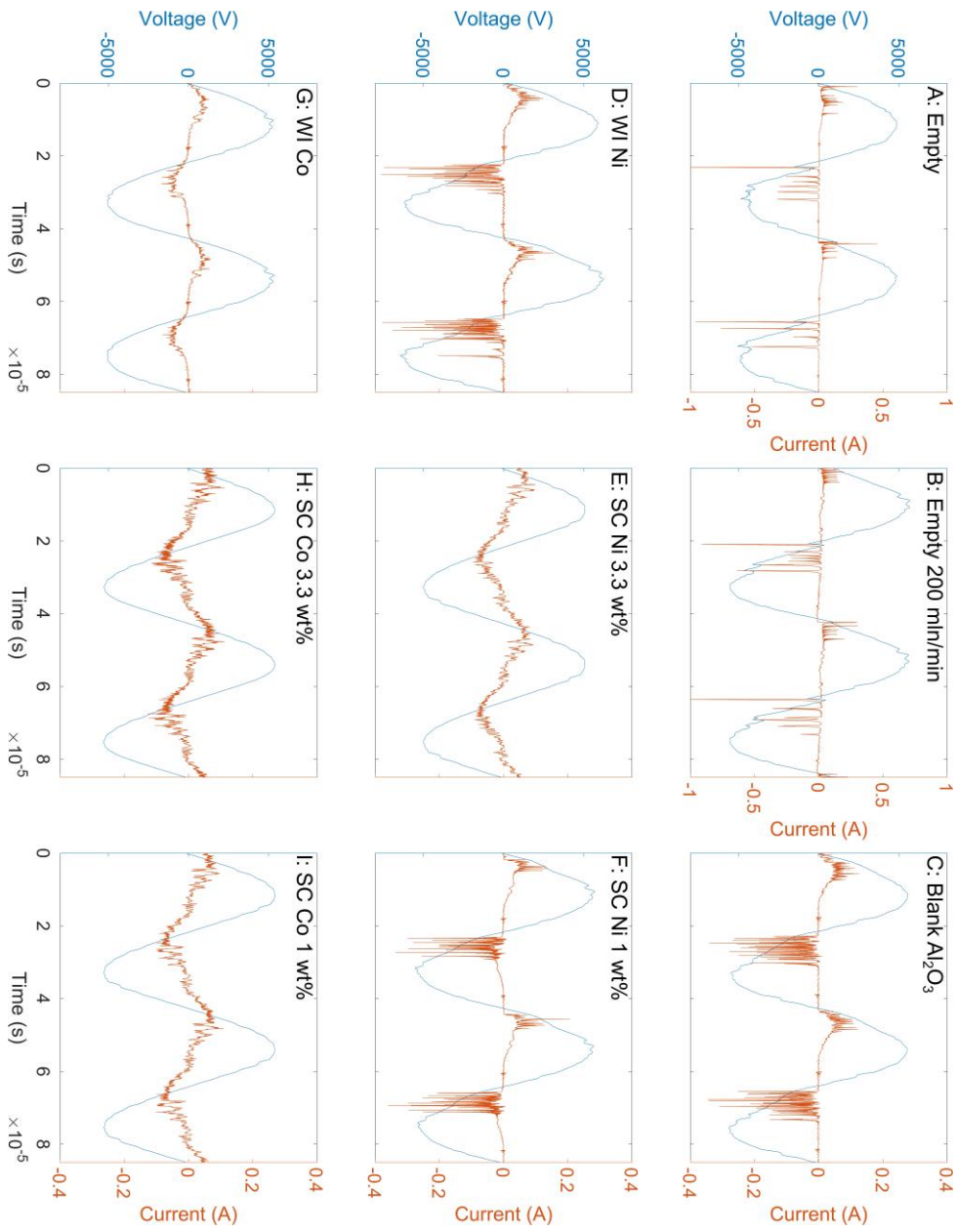

Figure 3-18: Representative I-V curves of the calculated discharge current $I_{discharge}$ for all experimental sets of NH_3 synthesis for a N_2/H_2 ratio of 1:1. Note that the y-axes of the current are wider for the empty reactor at both 100 and 200 mln/min (A,B) compared to the other graphs to prevent clipping the signal while still giving a clear representation of the signal for the other graphs. This figure again illustrates the clear filamentary regime for the empty reactor, the reactor with blank Al_2O_3 packing and with WI Ni catalyst, whereas these filaments virtually disappear for the WI Co and the various SC catalysts (with the exception of SC Ni 1wt%, probably due to instability of the catalyst; see text).

Further, the metal present at the surface is also expected to significantly affect the formation and propagation of surface ionization waves, which typically play an important role in packed-bed DBD plasma reactors [107,108].

Note that these effects can be very sensitive to physical and chemical differences, such as particle size and surface oxidation, which implies that minor changes in the catalyst properties can affect the plasma discharge, which in turn can alter the chemistry of the gas phase. However, these hypotheses remain somewhat speculative, since the precise mechanisms that enable a diffuse discharge in a DBD are not yet fully understood (not in the least for packed-bed systems) [19]. Recently, Bajon et al. were able to achieve a diffuse CO_2 plasma in a non-packed DBD, yet even for this less complicated system, the precise underlying mechanisms remain unclear [26]. Therefore, further fundamental research is necessary to fully elucidate the relevant processes in a DBD to enable a complete understanding of how (packing) materials can affect the plasma discharge, which will be the subject of Chapter 5.

Similar to the I-V characteristics, the voltage-charge diagrams show great variance depending on the catalyst material (or empty reactor), as shown in Figure 3-19 for DRM and in Figure 3-20 for NH_3 synthesis. Especially the SC (Co) catalysts yield an elongated voltage-charge diagram, which is more inclined upwards compared to, e.g., the empty reactor. This indicates an increase of the effective dielectric capacitance ζ_{diel} (cf. Figure 3-7 above), as more charge is stored by the dielectric for the same applied voltage [86]. Since the actual dielectric layer is identical for all experiments, this increased capacitance ζ_{diel} indicates a higher discharging areal fraction β, since a larger fraction of the dielectric now actually participates in the plasma discharge. In practice, this means that a larger part of the reactor volume is filled with plasma. This will be illustrated in Section 3.3 of this chapter, namely in Figure 3-22 B, D for DRM and in Figure 3-24 B, D, F for NH_3 synthesis, where especially for the SC Co catalysts the values of β are close to 1. The same is true for the SC Ni 3.3 wt% catalyst in case of NH_3 synthesis, also in line with the voltage-charge diagrams of Figure 3-20. When comparing the voltage-charge diagrams from the different reactions, the dissimilarity between the shapes corresponding to the empty reactors stands out. The voltage-charge diagrams from the empty reactor during NH_3 syntheses are notably less regular, exhibiting significant dips in the voltage. This is caused by the very high intensity of the microdischarges during this reaction in an empty reactor (as also visible in Figure 3-18, note the deviant y-scale for the empty reactors) which very quickly add/remove charge from the dielectric, briefly affecting the measured voltage.

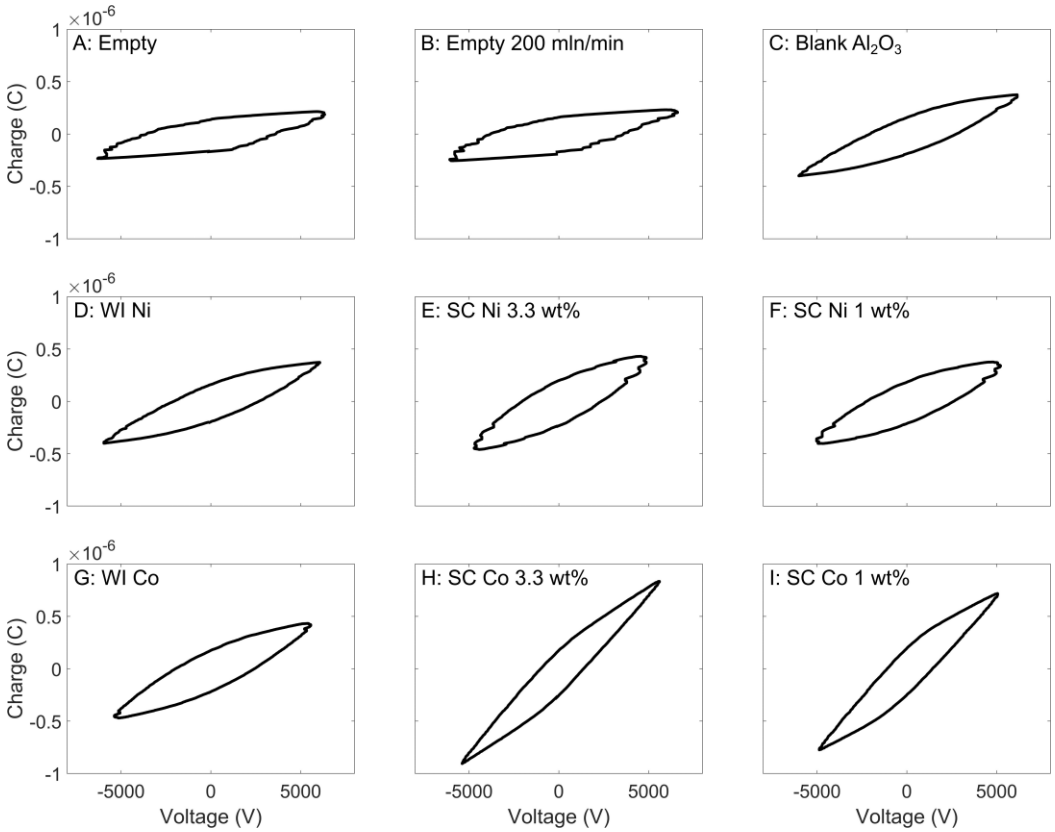

Figure 3-19: Representative voltage-charge diagrams for all experimental sets of DRM for a CO_2/CH_4 ratio of 1:1, illustrating the clear difference in discharge characteristics for the empty reactor and the reactor with blank Al_2O_3 packing and WI Ni or Co catalyst, on the one hand, and with the various SC catalysts (most significant for Co), on the other hand. Especially the SC Co catalysts yield a significantly deformed voltage-charge diagram, indicating an increased effective dielectric capacitance ζ_{diel}.

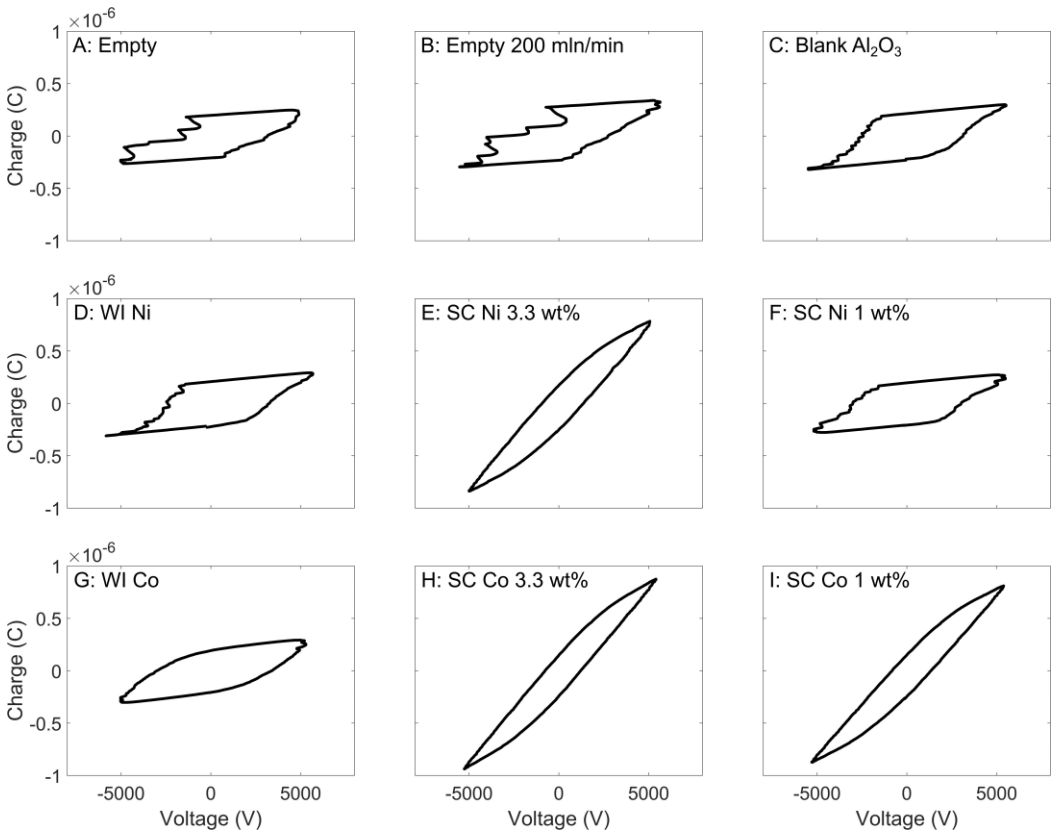

Figure 3-20: Representative voltage-charge diagrams for all experimental sets of NH_3 synthesis for a N_2/H_2 ratio of 1:1, illustrating the clear difference in discharge characteristics for the empty reactor and the reactor with blank Al_2O_3 packing and WI Ni or Co catalyst, on the one hand, and with the various SC catalysts, on the other hand. Especially the SC Co and SC Ni 3.3 wt% catalysts yield a significantly deformed voltage-charge diagram, indicating an increased effective dielectric capacitance ζ_{diel}. The discrepancy for the SC Ni 1wt% catalyst is again attributed to instability of the catalyst; see text.

As already described in Section 2.4 of this chapter, these I-V curves and voltage-charge diagrams can be analyzed in detail to extract (semi-)quantitative information about the plasma discharge. The results for the microdischarge quantity and discharging areal fraction β are presented in Figure 3-22 B, D for DRM and in Figure 3-24 B, D, F for the NH_3 synthesis experiments, and will be discussed in Section 3.3 of this chapter, to correlate them with the performance metrics. In addition, the burning voltage U_b, peak-to-peak applied voltage $V_{pk\text{-}pk}$, conductively transferred charge ΔQ_{dis}, and cell capacitance C_{cell} are presented and discussed in Appendix A, Section 4. The peak-to-peak voltage varies little, whereas the other metrics exhibit similar correlations to the used catalysts as the observations discussed here.

An intriguing observation is the behavior of the WI Co catalysts. As described earlier, this catalyst completely eliminates the formation of microdischarges (without affecting the plasma power, which will be discussed in more detail in Section 3.3 of this chapter), as also confirmed by the microdischarge quantity (see Figure 3-22 B, D and Figure 3-24 B, D, F in Section 3.3 of this chapter). However, for all other discharge characteristics, such as the discharging areal fraction β, the burning voltage U_b or the conductively transferred charge ΔQ_{dis}, the WI Co catalyst performs seemingly identical to the WI Ni catalyst or even blank Al_2O_3, in stark contrast to especially the SC Co catalysts. This discrepancy between the microdischarge quantity and the other discharge characteristics for the WI Co catalysts suggests that the formation of microdischarges is governed by different mechanisms than those that affect the other discharge characteristics. The strongly affected voltage-charge diagrams and subsequent discharge characteristics in the SC (Co) case also indicate an increased cell capacitance C_{cell} (see Appendix A, Section 4). We attribute this to the metallic layer at the surface of the dielectric beads. This metal/dielectric combination appears to notably increase the capacitance of the packing material, and thus of the overall system. We hypothesize that this increased capacitance contributes to the altered plasma discharge, in particular the strong increase of the discharging areal fraction β and the characteristics that are connected to it. Further, this metallic layer enhances the conductivity of the packing, which could explain the higher conductively transferred charge at the lower burning voltages (see Appendix A, Section 4). The burning voltage represents the gap voltage at the places where discharges are occurring, and therefore impacts the local electric field and ion/electron energies, though determining the latter is not straightforward [86]. This would also explain the behavior of the WI Co catalysts compared to the SC ones, since the WI beads exhibit metal particles at the surface (strongly decreasing the microdischarge quantity), but the particles do not form a layer at the surface, preventing charges to spread across the surface (and thus limiting the capacitance). Given the different underlying physical mechanisms that affect the microdischarges and the other discharge characteristics (e.g., partial discharging), these characteristics should always be considered separately and one of them cannot act as a representative measure for the others.

Another interesting observation is the very similar behavior of the WI Ni catalysts compared to blank Al_2O_3. Despite having a 10 wt% metal loading (of which a part is not fully reduced, see Figure 3-14), the WI Ni catalysts do not seem to alter the plasma discharge in a meaningful way. The contrast with the WI Co is striking, and most likely

due to the lower surface coverage of the Ni particles on the WI Ni catalysts, compared to the Co samples (see Figure 3-11). On the one hand, this supports our hypothesis that metal particles exposed to the plasma can have a significant influence on the plasma discharge. On the other hand, this result implies that the effect of the catalyst on the plasma (compared to a support-only packing) can be reduced significantly, perhaps even eliminated, when the amount of metal particles at the outer surface of the support beads/pellets is sufficiently low. Furthermore, this illustrates that the total metal loading of the catalyst can be relatively nondescriptive, especially when the distribution of the metal varies. This is also why the WI and SC catalysts are not compared at the same loading, since decreasing the loading of the WI Ni catalyst which already has limited effects does not make sense, and the higher loading for the SC catalysts was not structurally stable, as already discussed in Section 2.1 of this chapter.

The clear change in discharge regime for the WI Co and the various SC catalysts, i.e., fewer and/or less intense microdischarge filaments (if any) than in the empty reactor or with blank Al_2O_3 packing, is also visualized by additional observations made using a quartz tube as the dielectric, illustrating the altered discharge behavior. The quartz tube enabled direct observation of the plasma, which is shown in Figure 3-21 for an empty reactor, one packed with blank Al_2O_3 and one with the SC Co 3.3 wt% catalyst. These images help illustrate the drastic change in discharge regime when comparing the empty and blank Al_2O_3 packed reactor to the reactor filled with SC catalyst. For the empty reactor, clear filamentary discharges are observed, which moved around freely as the plasma was ignited. For the blank Al_2O_3 packing, the discharge was still clearly filamentary, indicated by the bright spots in between the beads. In contrast, for the SC Co 3.3 wt% catalysts, the reactor was completely filled with a more uniform plasma.

It must be noted that due to the practical limitations (e.g., the diameter of the quartz tube, etc.), the tests with the quartz tube could not be used for quantitative measurements and were only conducted as an illustrative example of the change of the discharge regime. Further, these basic images cannot be interpreted in a scientifically relevant way, and are shared merely to make the changes in the discharge more tangible.

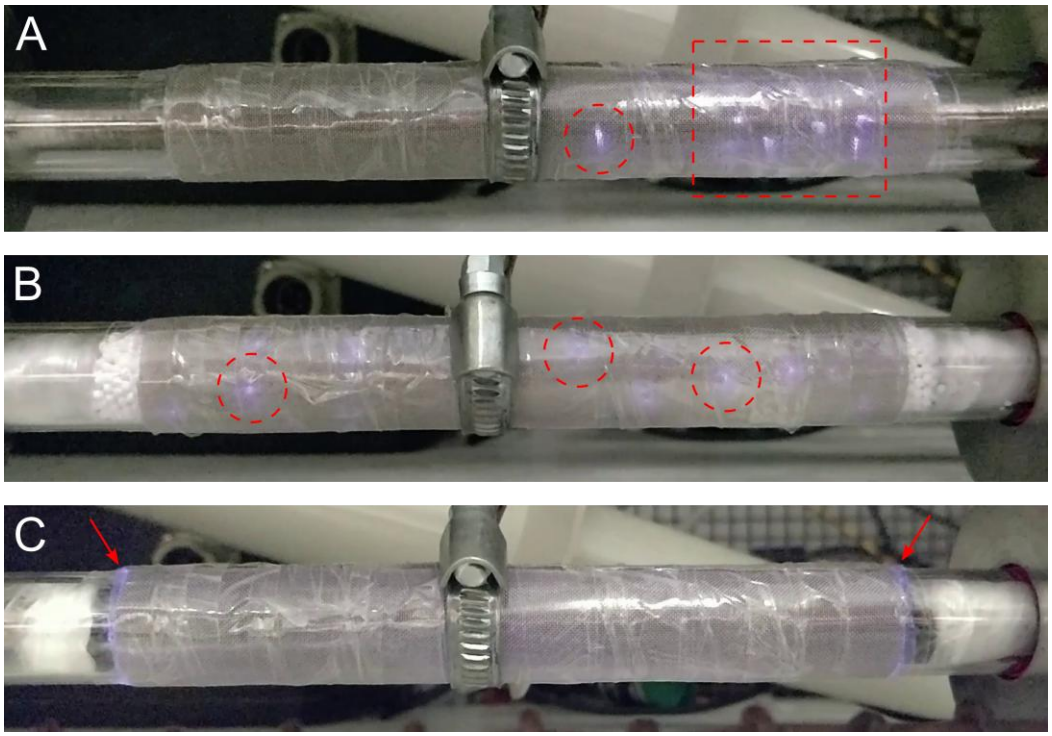

Figure 3-21: Images of a DBD reactor with quartz dielectric (so that the plasma can be visualized), discharging in a N_2/H_2 atmosphere (ratio 1:1). (A): empty reactor, (B): reactor packed with blank Al_2O_3, (C): reactor packed with SC Co 3wt% catalysts. In the empty reactor (A), the filaments moved around during the discharge, but remained in the same area of the reactor. The filaments are indicated by the dashed red circle and rectangle. In the reactor packed with blank Al_2O_3 (B), the discharge was still filamentary, but the filaments did not move around and were fixed in their location. Some of these locations are indicated by the dashed red circle. In the reactor packed with SC Co 3wt% catalysts (C), no filaments were observed, but rather a uniform purple hue throughout the whole packed bed was present. This uniform hue is most clearly visible at the edges of the electrode, indicated by the red arrows.

3.3 Plasma-Catalytic Performance and the Influence of the Discharge Characteristics

The effect of the catalysts on the plasma discharge was illustrated extensively. Next, the performance of the system for the desired gas conversion reactions is discussed and correlated to the discharge characteristics.

3.3.1 Dry Reforming of Methane

The total conversion of CO_2 and CH_4 is shown in Figure 3-22 A, C, together with the measured plasma power for an empty reactor, an empty reactor with a total flow rate

of 200 mln/min to mimic the residence time of a packed reactor, and for a packed reactor with blank Al_2O_3 and with the various catalysts.

The first striking observation is that for the CO_2/CH_4 ratio of 1:1 (Figure 3-22 A), the total conversion is the highest for the empty reactor, which performed nearly identical to the reactor with blank Al_2O_3 beads. The SC Co catalysts only have a slightly lower conversion, whereas all other catalysts show a clear decrease in conversion. Indeed, microdischarges are expected to contribute to the overall CO_2 and CH_4 conversion, as demonstrated by previous chemical kinetics modeling from PLASMANT [109], and the microdischarge quantity is the highest for the empty reactor and the reactor packed with blank Al_2O_3, whereas it drops significantly for all catalysts (except WI Ni); see Figure 3-22 B. Besides, the more intense microdischarges in the empty reactor (see also Figure 3-17 A) may also locally heat the gas to a higher temperature, which could further contribute to the increased conversion. On the other hand, the increased plasma volume for the SC Co catalysts (high β, see also Figure 3-22 B) could compensate for the lower microdischarge quantity, leading to a comparable overall conversion. The combination of a low microdischarge quantity with a low discharging areal fraction β generally leads to poor performance in DRM (e.g., SC Ni 1 wt%). In the 200 mln/min case, the higher flow rate corresponds to a lower SEI (since the plasma power remained constant). The lower total conversion at this higher flow rate corresponds roughly to the decrease in SEI (i.e., a factor of 2), which leads to a nearly identical energy cost (see Appendix A, Section 5). This quasi-linear dependence of the conversion to the SEI indicates that in the case of the empty reactor, the overall performance is limited by the amount of energy that can be used for the forward reactions. Further, the plasma power remains nearly constant over all experiments, thus it cannot explain the stark differences in total conversion.

For the CO_2/CH_4 ratio of 2:1 (Figure 3-22 C), the SC Co catalysts outperform the blank Al_2O_3 and perform similarly to the empty reactor at the same flow rate, but clearly better than the empty reactor at the same residence time (flow rate of 200 mln/min). It is, however, not clear whether this improvement is due to a chemical catalytic effect, or simply due to a plasma (physical) effect, as it may again be explained by the larger plasma volume (high β, see Figure 3-22 D).

Importantly, the plasma-deposited power remained virtually constant regardless of the quantity of microdischarges (see Figure 3-22 A, C). Therefore, the changes in the conversion cannot be (partially) attributed to possible changes in power, but instead should be related to the properties of plasma. Given the similar thermal properties for

all packed-bed experiments (i.e., the same gas flow rate, the same plasma power, the same reactor body through which heat can transfer and escape), we expect the overall temperature to be comparable for all experiments. However, the filamentary discharges are most likely creating hotspots on the catalyst, the dielectric, and in the gas, whereas the more homogeneous discharges will dissipate the heat more uniformly throughout the entire bed. Note that further insights can also be obtained from the temperature inside the plasma and the catalyst bed. However, measuring the temperature in plasma catalysis is very challenging. Introducing a temperature probe in the catalyst bed (i.e., the plasma discharge zone) would affect the plasma itself, which would then yield wrong results, and it could damage the temperature probe. Measuring the gas temperature downstream would only give a very approximate temperature, as the gas cools down as soon as it exits the plasma zone. Alternatively, measuring the exterior of the reactor provides little insight in the true temperature of the catalyst bed, because the dielectric barrier is typically a poor thermal conductor as well, making the correlation between the outer and the inner temperature of the reactor difficult. To determine the true temperature at the catalyst surface itself, advanced techniques and dedicated setups are required [110–112], which cannot readily be coupled with conventional packed-bed DBD plasma catalysis experiments.

Altogether, the highest conversion appears to be correlated to either a high microdischarge quantity (i.e., many microdischarge filaments, and/or with high intensity), or a high discharging areal fraction β (i.e., large fraction of reactor volume filled with plasma), and thus, plasma (physical) effects, whereas chemical catalytic effects are not clearly demonstrated. However, even though our results do not directly indicate chemical effects, a contribution of plasma-catalytic reactions cannot be excluded. As discussed by Loenders et al., plasma-catalytic reactions can be counterproductive in DRM [59]. Indeed, modeling predicts that the plasma-produced radicals may be quenched at a (transition metal) catalyst surface, and react back into the reactants, rather than into the products. This may add to the physical effects that were already discussed, leading to the poor overall performance as observed here [59]. In order to gain further insights into the contributions of plasma-catalytic reactions (metal surface reactions, specifically), a meticulous approach as presented by Barboun et al. would be required [32]. There, a distinction is made between plasma-phase and surface-catalytic reactions in plasma-assisted NH_3 synthesis. Despite offering valuable insights, their approach is not directly applicable here, since the plasma discharge differs significantly between the metal-loaded and blank supports. Furthermore, the

distribution of the metal particles on and throughout the support is complex, hindering the rational interpretation of accessible metal-site measurements (e.g., CO-chemisorption, as presented by Barboun et al.).

Nevertheless, we do not make a direct comparison between thermal and plasma catalysis in this work. Indeed, this has been often performed in literature, and can sometimes provide additional insights. However, it is also becoming increasingly clear that plasma catalysis cannot be simply described as "thermal catalysis with additional complexity" [31,37,59,81]. There is no direct correlation between the performance of certain catalysts in thermal versus plasma catalysis. Therefore, we believe our work challenges this conventional paradigm, stressing the complexity and uniqueness of plasma catalysis, requiring a dedicated approach, independent from thermal catalysis, to achieve novel insights.

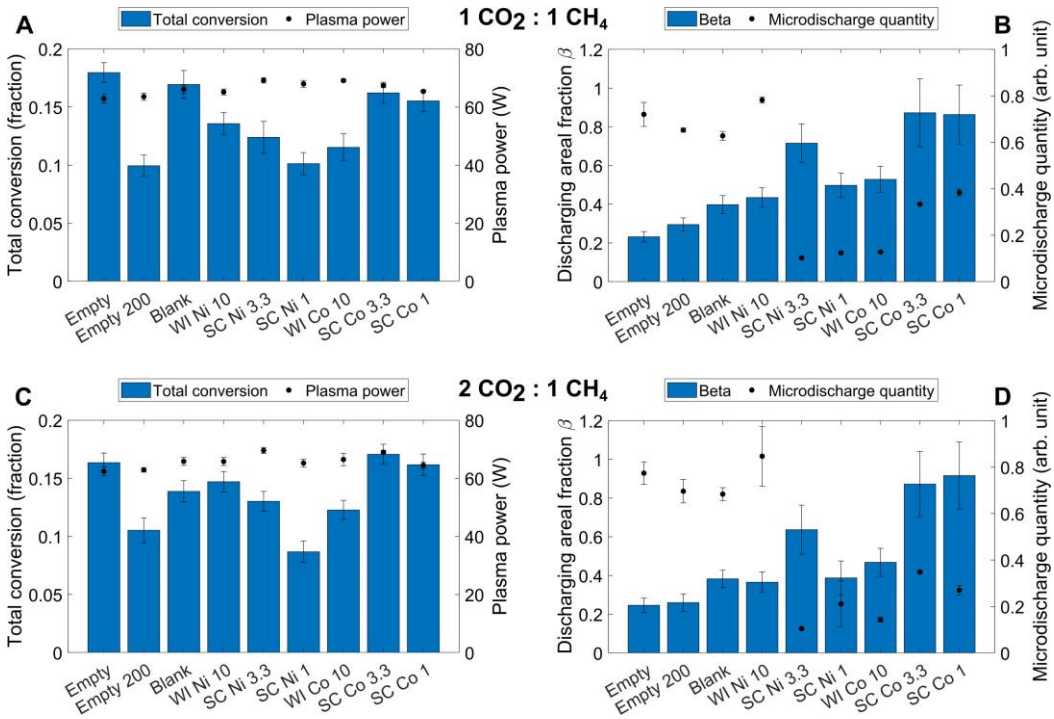

Figure 3-22: Total conversion and measured plasma power for the various catalysts used for DRM with a CO_2/CH_4 ratio of 1:1 (A) and 2:1 (C). Discharging areal fraction β and microdischarge quantity for DRM with a CO_2/CH_4 ratio of 1:1 (B), and 2:1 (D). Overall, the effect of the catalyst on the total conversion is relatively limited, though the catalyst never improves the overall performance. The relation between the overall performance and the discharge characteristics is not immediately obvious, though the conversion appears to benefit from a high discharging areal fraction and/or a high microdischarge quantity.

Despite the clear effects of the discharge characteristics on the overall performance, the selectivities may indicate that true plasma-catalytic reactions could also occur, since the various catalysts do affect the selectivities toward various products. All selectivities are presented in Appendix A, Section 5.1 , whereas the most relevant ones are shown in Figure 3-23. Firstly, the H_2 selectivity is either similar or increased for the metal-loaded beads compared to the blank Al_2O_3. Similar observations were made by Tu et al., where a drop in total conversion combined with a higher H_2 selectivity was observed for a Ni/Al_2O_3 catalyst in DRM compared to plasma-only [33]. Further, the changes in the selectivities toward C_2H_2, C_2H_4 and C_2H_6 are remarkable. For all Ni-containing catalysts, virtually no C_2H_2 was formed, whereas for the Co-containing catalysts, the C_2H_2 selectivity was higher than for the empty reactor or the one packed with blank Al_2O_3. This implies that the formation of C_2H_2 is less dependent on the discharge, but that indeed, a catalytic effect is dominant here, where Co clearly outperforms Ni. However, the underlying mechanism for this is still unclear and would require more detailed catalyst characterization or *in situ* diagnostics sensitive to the surface chemistry, which is outside the scope of this work. DFT simulations of the catalyst surface, combined with microkinetic modelling, could offer further fundamental insights into the underlying mechanisms of this apparent surface catalytic effect [113]. The C_2H_4 and C_2H_6 selectivities for the various catalysts are generally similar or lower compared to the empty reactor. This suggests a stronger dependence on the discharge, rather than any catalytic effects. In addition, the O-based selectivities (see Figure 3-23 E, F) show some variance as well. For the CO_2/CH_4 ratio of 1:1, the SC Ni 1wt% and Co catalysts show the highest combined O-based selectivity, implying that a lower amount of liquid components (mostly H_2O, see above) were formed (as they are not included in this (gas-phase) O-based selectivity). This suggests that the overall chemistry is affected compared to the other experiments, though given the relatively large error bars, it is hard to draw direct conclusions.

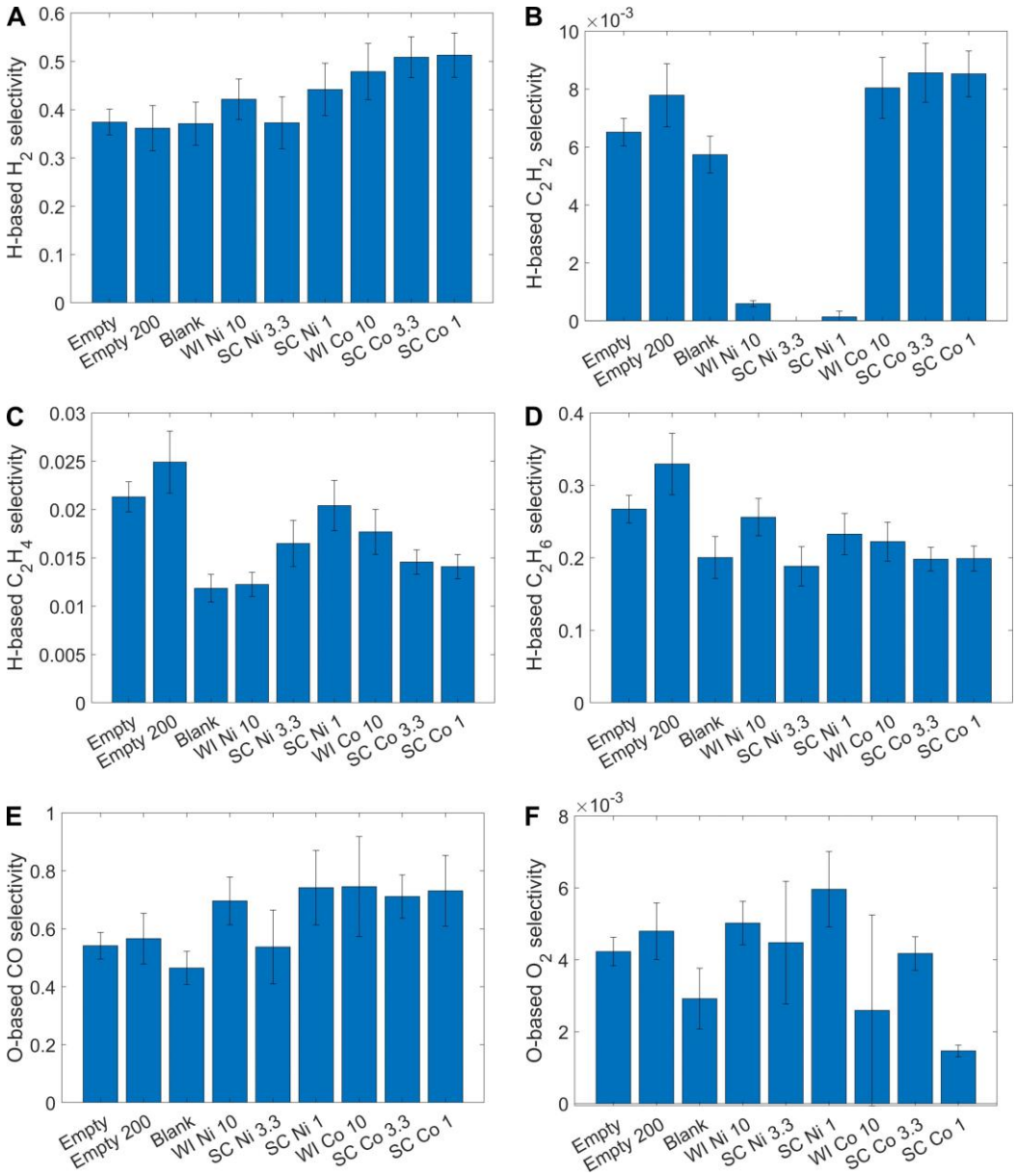

Figure 3-23: Selectivities based on DRM experiments with a CO_2/CH_4 ratio of 1:1. (A): H-based H_2 selectivity. (B): H-based C_2H_2 selectivity. (C): H-based C_2H_4 selectivity. (D): H-based C_2H_6 selectivity. (E): O-based CO selectivity. (F): O-based O_2 selectivity. The Co-based catalysts appear to yield higher selectivities toward H_2 and C_2H_2 and lower selectivities toward C_2H_4, though these differences tend to be small.

Despite the increasing number of works on plasma-catalytic DRM, the observations reveal discrepancies which make isolating any trends difficult. For example, similar to our observations, Tu et al. found that when introducing a Ni/Al_2O_3 catalyst, the total conversion decreases, which they also attributed to alterations of the plasma discharge [33]. Though, they also observed a dramatic increase in H_2 selectivity, which was less distinct in our experiments. Similarly, Brune et al. found little to no changes in conversion when introducing a Ni/Al_2O_3 or Co/Al_2O_3 catalyst, despite minor changes in the plasma discharge [34]. Contrastingly, Farshidrokh et al. did observe an increase of the total conversion, but the driving mechanisms remain unclear [35]. Similarly, Suttikul et al. observed a clear increase in total conversion when introducing Ni to the Al_2O_3 support, which they attributed to catalytic effects [36]. However, the relevant discharge characteristics were not reported, so it remains ambiguous as to what role the discharge plays in these seemingly catalytic effects. We believe that the discharge characteristics could indeed play an important role in these observations, and clear analyses and reporting are crucial to gain a complete understanding of the plasma-catalytic performance.

In short, while the DRM performance is clearly affected in different ways by the multiple catalysts, the observed differences in performance cannot be attributed simply to catalytic effects in the conventional sense. Various discharge characteristics, not in the least the microdischarges, will influence the gas-phase chemistry, which can have significant effects on the overall performance. It is therefore essential to always take discharge characteristics into account when comparing different catalysts or packing materials. Interpretation of data should be done with caution, making sure discharge effects are identical before attributing performance changes to precisely defined catalytic mechanisms.

3.3.2 NH_3 Synthesis

In contrast to DRM, the beneficial effect of the catalysts is much clearer in NH_3 synthesis; see Figure 3-24 A, C, E. In general, all SC catalysts (except SC Ni 1 wt%, most likely due to its instability, see earlier discussion) perform significantly better than the WI catalysts, the blank Al_2O_3 and the empty reactor. While for an N_2/H_2 ratio of 1:1 the Al_2O_3 packing already increases the NH_3 concentration by a factor of 2 compared to the empty reactor, and the WI catalysts perform even slightly better (WI Ni 2.5 times higher and WI Co 3 times higher), the SC Ni 3.3 wt% and the SC Co catalysts enhance the NH_3 concentration by a factor of over 5. The significant alteration of the plasma discharge by the SC catalysts (which makes it much more homogenous and expanded instead of filamentary, as

indicated by the nearly doubling of the discharging areal fraction β and by the microdischarge quantity decreasing by a factor of more than 2, see Figure 3-24), drastically improves the NH_3 synthesis. This is again in line with earlier chemical kinetics simulations by PLASMANT, which predicted that NH_3 is largely destroyed in the microdischarge filaments [61], as well as by previous experimental studies [37,62,82]. In other words, fewer (and/or less intense) microdischarges will improve the NH_3 synthesis. Potentially, the intense filaments in the empty reactor locally heat the gas volume of the filaments substantially, contributing to the decreased NH_3 production due to thermal decomposition of the formed NH_3. In addition, electron-impact dissociation in these intense microdischarges can contribute to the net destruction of NH_3. In the altered discharge, these fewer and/or less intense microdischarges may locally heat the gas less, rather spreading the heat uniformly across the reactor volume. The lack of hotspots could contribute to the increased overall performance due to the lower rate of thermal NH_3 decomposition, and the electron-impact dissociation of NH_3 may also be decreased in the more homogeneous discharge.

The case of the WI Co catalyst is again an intriguing one. For the N_2/H_2 ratio of 3:1 (and also the 1:1 ratio, although less pronounced), it performs somewhere in-between the SC catalysts and the blank Al_2O_3/WI Ni catalysts. As discussed earlier, the WI Co catalyst eliminated the microdischarges, which is an evident benefit for NH_3 synthesis, as explained above [61]. However, the lack of microdischarges cannot be the only parameter influencing the NH_3 production, since the SC Co and SC Ni 3.3 wt% still clearly outperform the WI Co, even though the microdischarge quantity is not lower when using these SC catalysts. Two other main mechanisms, besides the rather low microdischarge quantity, may cause this clear improvement by the SC catalysts. Firstly, the plasma is more expanded, filling the reactor entirely (as indicated by the discharging areal fraction β being close to 1, see Figure 3-24 B, D, F), thus increasing the overall plasma volume. This larger plasma volume increases the effective residence time, since the gas is exposed to plasma throughout the entire reactor volume, rather than just in the discrete filaments. At the same time, since the plasma power remains constant, the local power density will be lower. This should enable an overall larger NH_3 synthesis, because the higher power density facilitates the decomposition of the formed NH_3 more than its synthesis, as was predicted by modeling [61]. Secondly, the SC catalysts generally expose more metal surface to the plasma, potentially enabling a more pronounced catalytic effect in the conventional sense, although the latter would require further investigation to really prove this hypothesis.

Interestingly, the benefit of the WI Co catalyst over Al_2O_3 and WI Ni is no longer present at a N_2/H_2 ratio of 1:3. This implies that at this stoichiometric ratio, the destruction of NH_3 in the microdischarge filaments may no longer hinder the performance. Rather, the amount of activated N_2 is expected to be too low compared to the activated H_2, as the latter is much more readily activated by plasma given its much lower bond dissociation energy. The lower NH_3 production is expected to be a more dominant factor compared to the destruction of NH_3 for the N_2-richer ratios. The best performance being obtained with a N_2/H_2 ratio of 1:1 is again attributed to the higher activation energy of N_2 compared to H_2, making the stoichiometric gas mixture less effective [81]. Note that the highest performance of 14570 ppm NH_3 at 100 mln/min with a N_2/H_2 ratio of 1:1 corresponds to a N_2 conversion of 1.4%, and an energy cost of 60 MJ/mol. This is still far from competing with Haber-Bosch, which very well may never be achievable for direct plasma-catalytic NH_3 synthesis. Other options, e.g., based on NOx production by warm plasmas (which is much more energy-efficient), followed by the catalytic reduction into NH_3 [114] are more promising in this respect. However, reaching the best performance is not the aim of this work, as we rather aspire to better understand plasma catalysis on a fundamental level.

Indeed, we want to stress the importance of the gas-phase plasma reactions, and how the packing/catalyst can affect those, indirectly altering the overall performance. Also in literature, it was reported that catalysts do not always have a beneficial effect on the reaction. For DRM, for example, it was recently proposed [59] that transition metal catalysts could even have a negative effect on the overall performance, because they can quench the plasma radicals, and let them react back to the reactants instead of toward the desired products. Further, for plasma-catalytic NH_3 synthesis, modeling work [115] suggests that the actual catalyst metal has little effect on the overall performance, when radicals play a dominant role (as is mostly the case in DBD plasma), which was further supported by experimental work [31].

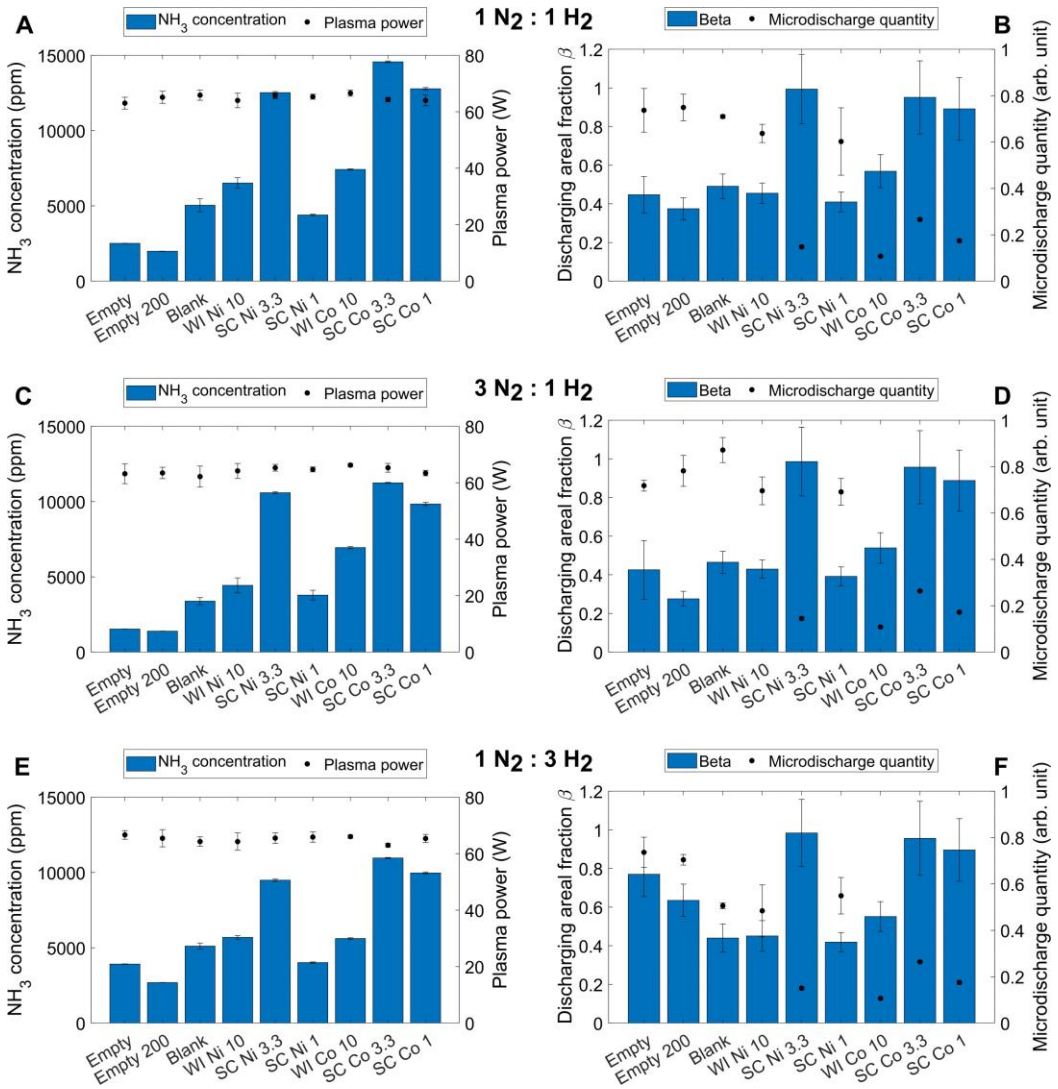

Figure 3-24: NH_3 outflow concentration and measured plasma power for a N_2:H_2 ratio of 1:1 (A), 3:1 (C), and 1:3 (E). Discharging areal fraction β and microdischarge quantity for a N_2:H_2 ratio of 1:1 (B), 3:1 (D), and 1:3 (F). The effect of the catalyst on the obtained NH_3 concentration can be dramatic, and a clear correlation with the discharge characteristics is apparent. In general, a lower microdischarge quantity and a higher discharging areal fraction are strongly beneficial for NH_3 synthesis.

3.3.3 Importance of the Discharge Characteristics

Inherently, plasma catalysis is complicated, with many aspects to take into account. In addition to the relevant parameters and mechanisms in more conventional heterogeneous catalysis, such as the physical and chemical properties of the catalyst (nano)particles and support materials, the plasma discharge cannot be neglected here. Not only is the plasma an indispensable part of the system, it is highly sensitive to many external factors, not in the least to the packing material (i.e., the catalyst). It is therefore impossible to treat the plasma discharge as an independent constant parameter in an experimental setup, without thorough analysis and comparison.

The complexity of these systems is also illustrated by seemingly contradictory results. For example, Andersen et al. found that microdischarges are detrimental for NH_3 synthesis, and are in fact beneficial for NH_3 decomposition [62,82]. These findings are in line with earlier model predictions from PLASMANT [61], and with our observations in this work, where a lower microdischarge quantity tends to correspond to a higher NH_3 yield. In contrast, Patil et al. reported that microdischarges are beneficial for NH_3 synthesis [76,81]. It is not straightforward to pinpoint the underlying cause of this discrepancy. However, it illustrates that many parameters need to be taken into account and further fundamental research is required to fully elucidate what mechanisms drive plasma catalysis in DBDs, especially in packed-bed configurations.

In practice, it is crucial to monitor the plasma discharge using the conventional electrical diagnostics. Further, a quantification of the discharge characteristics is highly advisable, since not all discharge characteristics are immediately visually obvious. Only when it is confirmed that the plasma discharge is identical for two different catalysts, it is possible to confidently attribute any changes in overall performance to catalytic effects. Whenever there are discrepancies in the discharge, even if they seem minor, caution is advised when interpreting the results, as gas phase chemistry can be dominant, even in so-called plasma catalysis.

An additional message of this work is that when studying different catalysts, simply applying the same synthesis protocol for different (metal) precursors may not suffice, as we illustrated here by the WI Ni and WI Co catalysts. A thorough, spatially resolved microscopic characterization of the catalysts is strongly advised. Ideally, this additional analysis goes beyond the conventional catalyst characterization techniques that are commonly applied for thermal catalysis, but lack spatial information on the support (such as XRD, N_2 sorption, etc.).

In short, we studied both DRM and NH_3 synthesis, showing vastly different responses to changes in the plasma discharge. DRM seems to benefit from the presence of (more, stronger) microdischarge filaments, as they give rise to higher CO_2 and CH_4 conversion (in line with model predictions [109]). For NH_3 synthesis, we observe the opposite effect, since a better performance is obtained with more uniform discharges, as created by the SC catalysts, because the microdischarge filaments destroy the formed NH_3, as also elucidated by model predictions [61]. Therefore, it is clear that every reaction or gas mixture will react differently to changes in the discharge properties. Thus, especially when studying lesser-known reactions, the effect of the discharge on the specific reaction should be studied in greater detail, in order to be able to separate gas-phase chemistry from the desired catalytic reactions.

4. Conclusion

In this chapter, we studied plasma catalysis in a packed-bed DBD reactor for DRM and NH_3 synthesis. We synthesized both Ni and Co on Al_2O_3 catalysts in two different ways, i.e., by wet impregnation (WI) and spray-coating (SC), yielding very different distributions of metal/metal oxide on and throughout the porous support beads. These changes in catalyst morphology had a drastic impact on the plasma discharge, in some cases eliminating the formation of microdischarges and forming a more homogeneous plasma, filling the entire reactor. We also found that not all characteristics are impacted by the same catalysts, indicating that different mechanisms govern the various properties of the plasma discharge. Specifically, the microdischarges were eliminated by the WI Co catalyst (exhibiting a relatively high coverage of nanoparticles at its surface), without displaying the fully expanded plasma that was observed for the SC catalysts (which have a µm-scale layer of metal nanoparticles at their surface).

Even when the same metal was deposited on the same support, but with a different synthesis method that distributed the metal differently on/throughout the support, the various catalysts showed great variety in overall performance. Especially for NH_3 synthesis, the benefit of the SC catalysts over the WI catalysts was tremendous. This strong improvement is attributed to the altered plasma discharge, which fills a larger part of the reactor volume, promoting the formation of NH_3, while at the same time limiting the destruction of the formed NH_3 due to the lower microdischarge quantity. For DRM, the influence of the discharge on the overall performance was more ambiguous, but also here the plasma discharge affects the performance. Especially the presence of

microdischarges and a larger plasma volume (larger discharging areal fraction) seem beneficial for the overall DRM reaction. By studying these dissimilar chemistries, we aim to illustrate how plasma properties and their effect on the performance do not translate well between various reactions.

Though the precise SC synthesis as described here needs further optimization, given the unstable nature of the metallic shell (as demonstrated for SC Ni 1 wt%), the general conclusions offer an interesting perspective. By deliberately designing the packing of the reactor in such a way, the plasma could be altered relatively easily to tune its properties toward the desired form (i.e., more filamentary or less, restricted or filling the entire reactor). Further optimization can be done to design a robust packing that resembles the presented beads, i.e., a dielectric core with a thin metallic shell. This can serve as a template to add further catalytically relevant materials, to aim for a desired combination of the altered plasma discharge and other proposed beneficial mechanisms. This core-shell structure could further serve as a simple and reliable plasma modifier to study the effect of the plasma discharge on other reactions of interest. Further, this could aid fundamental studies looking into the mechanisms that govern (packed-bed) dielectric barrier discharges, as the precise underlying mechanisms are still poorly understood.

Chapter 4

Contamination in Dielectric Barrier Discharges by Electrode Erosion

In this chapter, the same plasma reactor as in the previous chapter is employed. Here, the contamination of the packing material due to erosion of the uncovered electrode is described. By exposing blank oxide support beads to several hours of plasma, generated in Ar, He, and CO_2, and characterizing the materials with several electron microscopy techniques, we show that this erosion mechanism is persistent. Further, employing the electrical characterization introduced in the previous chapter, the dominant effect of the plasma discharge characteristics is revealed.

The content of this chapter is based on:

Contamination in Dielectric Barrier Discharge Plasmas by Electrode Erosion
Robin De Meyer, Jo Verbeeck, Sara Bals, and Annemie Bogaerts
ACS Materials Letters, 7, 52-58, 2025

1. Introduction

As introduced in Chapter 1, a dielectric barrier discharge (DBD) is a type of plasma ignited between two electrodes, and is characterized by the presence of a dielectric layer covering at least one of the electrodes, preventing persistent high current arcs from being formed. As a result, DBDs are non-equilibrium plasmas, meaning that the gas temperature is several orders of magnitude lower than the electron temperature [8]. These gentle conditions, combined with the reactive nature of the plasma, partially consisting of excited species, radicals, ions, and electrons, offer a great variety of applications, including surface treatment [116–118], (nano)material synthesis and functionalization [119–122], catalyst regeneration [123,124], biological and medical applications [125–128], and of course plasma catalysis for gas conversion and pollution control [16,18,28].

DBDs can operate in various geometries. For many applications, packed-bed DBDs are employed, in which the volume between the electrodes (where the plasma is generated) is filled with a packing material, as presented in the previous chapter. Indeed, this geometry offers direct contact between the plasma and the packing material which can be highly desirable for many applications.

As introduced in Chapter 1 and discussed extensively in Chapter 3, DBDs typically operate in a filamentary mode [19]. This means that generally, the gas volume is not filled with a homogeneous plasma, but rather with discrete filaments. These filaments are formed by microdischarges, i.e., short-lived but intense discharges, with relatively high current densities (up to 1000 A cm^{-2}). Microdischarges often majorly contribute to the chemistry in a DBD plasma, but given their short lifetime and discrete nature, gas heating remains limited [19].

The dielectric barrier, especially when employing relatively soft materials, such as polymers, can erode due to the plasma exposure [129,130]. In addition, erosion of the exposed electrode in surface DBDs was previously described [131–134]. For example, recently, Nguyen-Smith et al. observed the erosion of the exposed electrode of a surface DBD after operating in air for 60 minutes [132]. By tuning the pulse width of the applied voltage, the authors managed to operate the plasma both in a filamentary and a relatively uniform mode, while keeping other discharge parameters such as plasma power similar. Detailed scanning electron microscopy (SEM) and energy dispersive X-ray spectroscopy (EDX) measurements revealed that the electrode was measurably eroded

in both cases, though significant differences were observed between the electrodes exposed to a filamentary or a homogeneous plasma. The authors reported that a filamentary discharge locally melts the nickel electrode, with some nickel oxide particles being present, both on the electrode, as well as on the dielectric around the eroded area. In contrast, the electrode exposed to a homogeneous discharge did not show any local melting of the electrode. Whereas the oxidation is most likely due to the presence of oxygen, the plasma discharge clearly affects the electrode, and the precise discharge characteristics further determine the extent and nature of the erosion.

Given the demonstrated erosion of the electrode due to the plasma discharge and the apparent mobility of the eroded electrode material, the question arises whether a material inside a DBD could possibly be affected by the eroded electrode material. To answer this question, we employed the same coaxial DBD as the one that was presented in the previous chapter. This DBD reactor has an exposed stainless steel electrode passing through the center of an Al_2O_3 cylinder, and the second electrode is wrapped around the outside of the dielectric cylinder. The reactor was packed with pristine Al_2O_3 spheres, which were characterized by SEM and transmission electron microscopy (TEM) after exposure to the plasma.

2. Methods

2.1 DBD Reactor and Experiments

The experimental setup employed in this chapter is quasi identical to the one presented in Chapter 3, and its relevant components and dimensions are briefly summarized in Figure 4-1. The gases (Air Liquide; Ar ≥ 99.999 %, He ≥ 99.999 %, CO_2 ≥ 99.998 %) were controlled by a mass flow controller (Bronkhorst). The plasma was generated using the G10 S-V AFS GmbH power supply unit (PSU) set at 23.5 kHz, while the discharge was monitored using a high voltage probe (Tektronix P6015A), a current monitor (Pearson Electronics 4100, high-frequency 3 dB point approx. 35 MHz), and a low voltage probe (Pico Technology TA150) across a 10 nF monitoring capacitor. All probes were connected to a Picoscope 6402A (Pico Technology, bandwidth 250 MHz) oscilloscope that was used to save snapshots of the discharge for later analysis. The inner electrode of the reactor is made of 304 stainless steel (i.e., an alloy of Fe, Cr, Ni, C, and possibly other elements such as Mn), whereas the dielectric barrier consists of alumina (Al_2O_3). The reactor was packed with pristine γ-Al_2O_3 spheres (Sasol) with a diameter of 1.8 mm prior to each experiment.

The gas flow rate was set at 100 mls/min (standard ml per min) with a constant applied power, yielding a relatively stable plasma power of 45-50 W for Ar and He, and around 60-65 W for the CO_2 discharge. The same reactor and electrode were used for all experiments, and they were cleaned thoroughly prior to every new experiment.

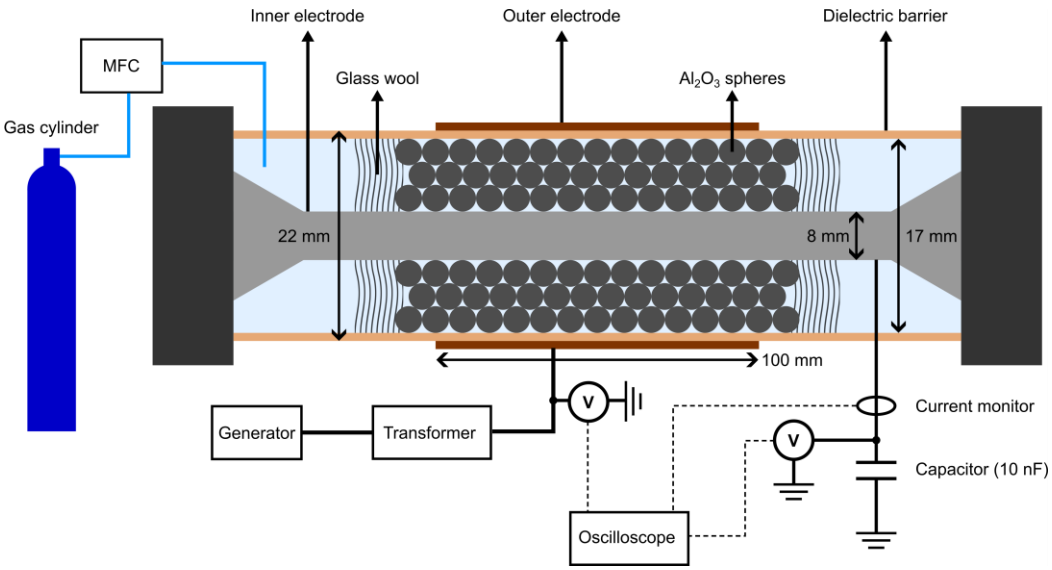

Figure 4-1: Schematic of the complete experimental setup including reaction dimensions. This figure is an adaption from a figure in Chapter 3, since the same system was used for these experiments.

To investigate the influence of the discharge characteristics, experiments were performed in pure Ar, He, and CO_2. Further, to isolate the effect of temperature on the plasma discharge from any potential changes to the packing material itself, every experiment was performed in two phases. First, the plasma was operated for 3 hours for Ar and He, and for 6 hours for CO_2, after which the plasma was stopped. The reactor was then left to cool down completely, while continuing the gas flow, without further disturbances. After reaching room temperature, the plasma was operated again for 2 hours in the case of Ar and He, and 3 hours using CO_2 as further discussed later.

2.2 SEM Characterization

For the SEM analyses, a Thermo Fisher Scientific Quanta 250 ESEM was employed. An acceleration voltage of 20 kV was used, with a working distance of 10 mm, while operating the microscope in its high vacuum mode. Both secondary electron (SE) and backscattered electron (BSE) imaging were used throughout this chapter. More

information on these imaging techniques is provided in Chapter 2. An Oxford Instruments energy dispersive (EDX) and wave dispersive (WDX) X-ray detector were used to identify three key elements in the particles of interest: Fe, Cr, Ni. Both detectors were used at some point, depending on technical operability of the detectors at the time of the various analyses.

Prior to the analyses, entire spheres were attached to a SEM stub using silver paint, after which the exposed surfaces of the spheres were coated with approximately 25 nm of carbon to improve surface conductivity.

2.3 TEM Characterization

The TEM analyses were performed using a Thermo Fisher Scientific Tecnai Osiris microscope operated at 200 kV, with a camera length of 115 mm. High-angle annular dark field scanning transmission electron microscopy (HAADF-STEM) imaging and EDX-STEM analyses were performed to identify and investigate the stainless steel particles. A beam current of approximately 125 pA was used. Prior to the TEM analyses, five of the used Al_2O_3 spheres were added to a vial with approximately 1 ml of acetone, after which the sample was vortexed and sonicated for around 30 seconds each. Next, a few drops of the resulting liquid were dropcast on a holey carbon TEM support grid, which was left to dry in ambient conditions.

For the bright field (BF) TEM analysis of the steel particles in a carbon matrix (Figure 4-12 later in this chapter), the same microscope was used, operated at 200 kV in conventional BF-TEM imaging mode. More details on the various TEM imaging modes are provided in Chapter 2. A small amount of the material formed in the reactor was added to a vial and sonicated together with a few drops of acetone. This suspension was then dropcast on a holey carbon grid, prior to TEM analysis.

2.4 A Note on Bias

For the SEM analyses, the spheres were manipulated minimally, ensuring a maximally representative sample in the SEM. However, the experimental conditions were challenging. Indeed, stainless steel particles, usually just hundreds of nm large, were scattered across an Al_2O_3 sphere of almost 2 mm in diameter. In addition, the concentration of particles was low. This meant that large areas of the sphere had to be searched for few and small particles. Due to the presence of impurities in the pristine Al_2O_3 spheres, automating this process proved challenging. Therefore, it is likely that the actual data acquired is slightly biased, most likely toward larger particles, as they would

stand out more against the lighter background. Furthermore, the SEM may also have been resolution-limited, especially when screening areas at a relatively low magnification, possibly further biasing the data. However, as all samples were treated and analyzed in the same way, we believe relative comparisons between the samples are still highly relevant. For the TEM analyses, a similar bias toward larger particles may be expected. However, in addition, the samples were manipulated quite drastically in order to be able to analyze the stainless steel particles themselves. It is plausible that in this process, a sort of pre-selection of stainless steel particles was made, as some particles may have stronger or weaker interactions with the support than others, thus potentially introducing another bias to the analyses. However, again, since all samples were manipulated and analyzed using an identical approach, a relative comparison should still be valid. Though, due to the differences in sample manipulation, a direct comparison between SEM and TEM data may be less justified.

3. Results and Discussion

In every sample from beads that were exposed to plasma, stainless steel particles were observed, as discussed in detail in the following. In addition, the discharge characteristics are studied and correlated with the observations of the erosion products.

3.1 Characterization of the Erosion Products

In Figure 4-2, backscattered electron (BSE) SEM images are shown of the surface of the Al_2O_3 spheres exposed to the Ar (A-B), He (C-D), and CO_2 (E-F) plasma. The BSE-SEM signal is proportional to the mass density of the sample, which allows to easily identify heavier (metallic) particles against the lighter Al_2O_3 background. It stands out that both the Ar sample (Figure 4-2 A) and the CO_2 sample (Figure 4-2 E) contain highly spherical stainless steel particles, whereas no such particles were found in the He sample. Further, all samples contain particles of various, seemingly arbitrary, morphology. Moreover, it is striking that the CO_2 sample has a significantly higher fraction of highly spherical particles compared to the Ar sample: 12 out of 19 for CO_2 and 4 out of 24 for Ar.

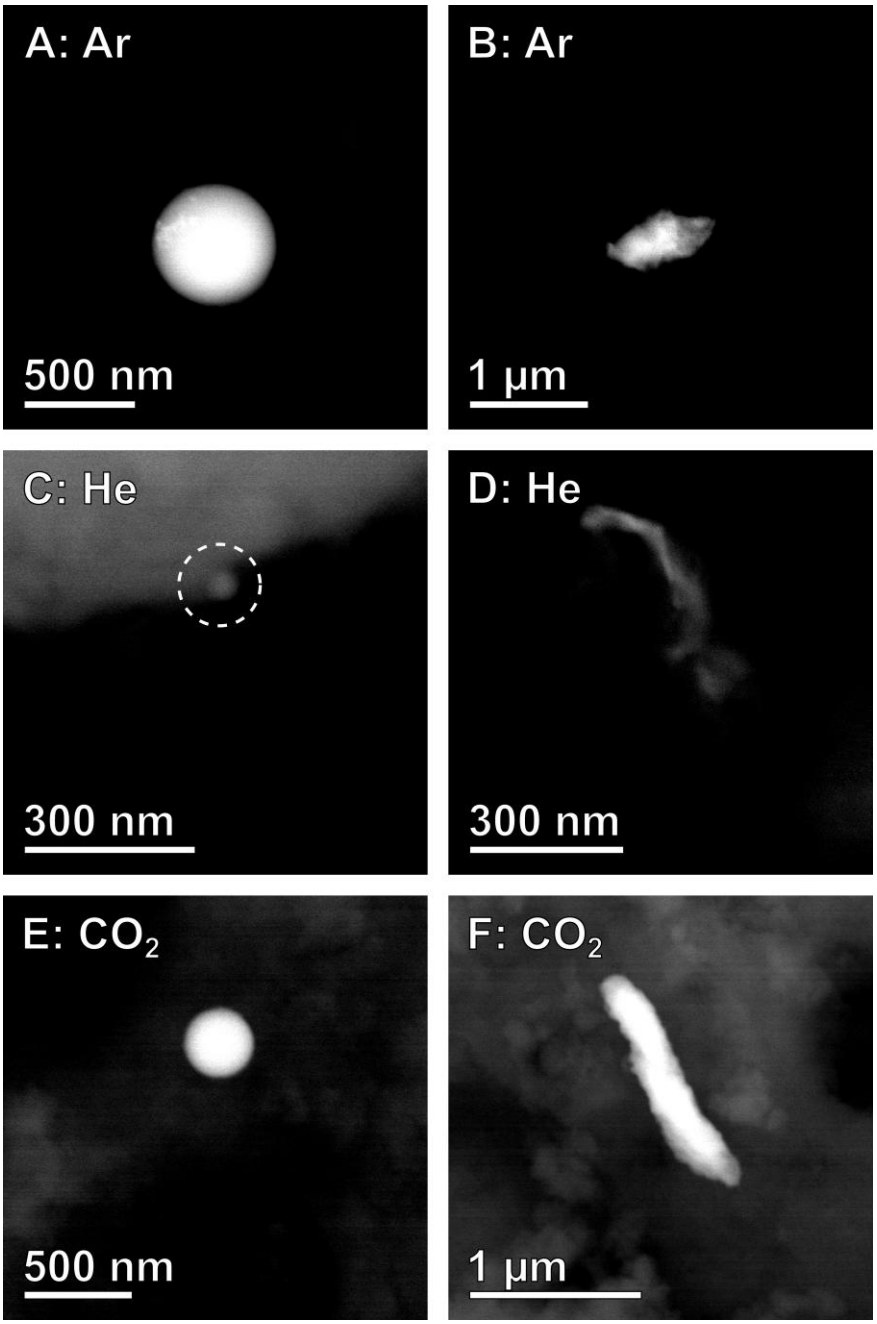

Figure 4-2: BSE-SEM images of the Ar (A-B), He (C-D), and CO_2 (E-F) samples. The BSE signal highlights the relatively heavy steel particles against the relatively light Al_2O_3 background. Particles with various morphologies were observed, though notably the Ar (A) and CO_2 (E) samples contained several highly spherical particles.

Note that every particle that is shown or included in further analyses was confirmed to contain Fe and Cr (and when a high signal to noise ratio was obtained, Ni and even Mn could also be identified) using X-ray based spectroscopy, indicating the particles are very likely stainless steel. An example of such an EDX spectrum is presented in Figure 4-3. The spectrum shows strong O and Al signals, which makes sense given that the particle was on an Al_2O_3 sphere during analysis. Indeed, when employing SEM-EDX for such relatively small particles, the primary electron beam interacts with a larger volume than just the particle of interest in this case, yielding the strong O and Al signals. However, when highlighting the relevant energy range, clear signals for Fe, Cr, Ni, and even Mn were also observed, thus confirming the composition of the stainless steel particle.

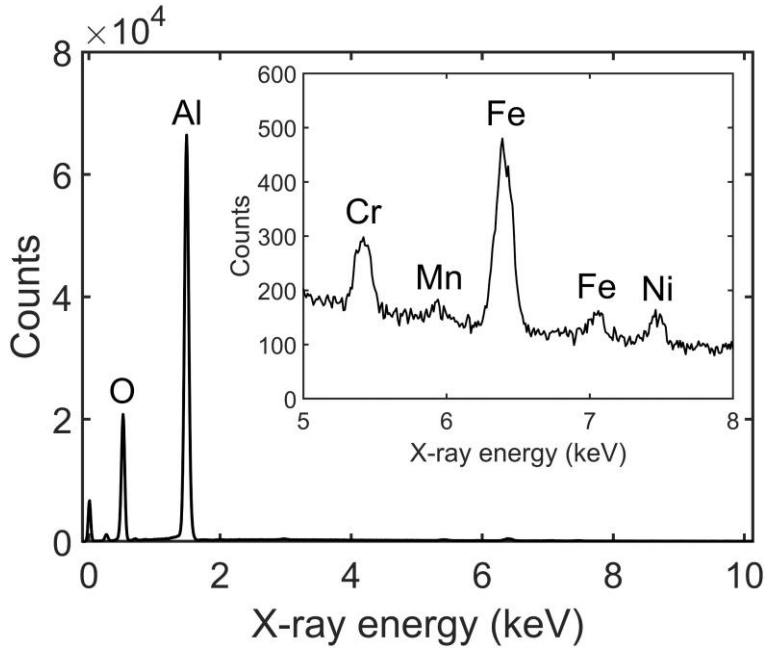

Figure 4-3: Representative SEM-EDX spectrum from a stainless steel particle on the surface of an Al_2O_3 sphere, used in the Ar plasma. Strong Al and O peaks are present due to the Al_2O_3 support, whereas Fe, Cr, and Ni could be observed, confirming the composition of the stainless steel particle.

The SEM analyses enable the investigation of the overall morphology and the composition of the stainless steel particles. However, the SEM lacks the spatial resolution to study the surface structure of the steel particles, and may also miss smaller particles. Therefore, HAADF-STEM was employed due to its superior spatial resolution compared to SEM. Furthermore, the HAADF signal scales with the projected density of the sample, highlighting the heavier steel particles against the lighter Al_2O_3 background.

The HAADF-STEM images in Figure 4-4 reveal particles that were observed in the Al_2O_3 samples exposed to the Ar (A-B), He (C-D), and CO_2 (E-F) plasma.

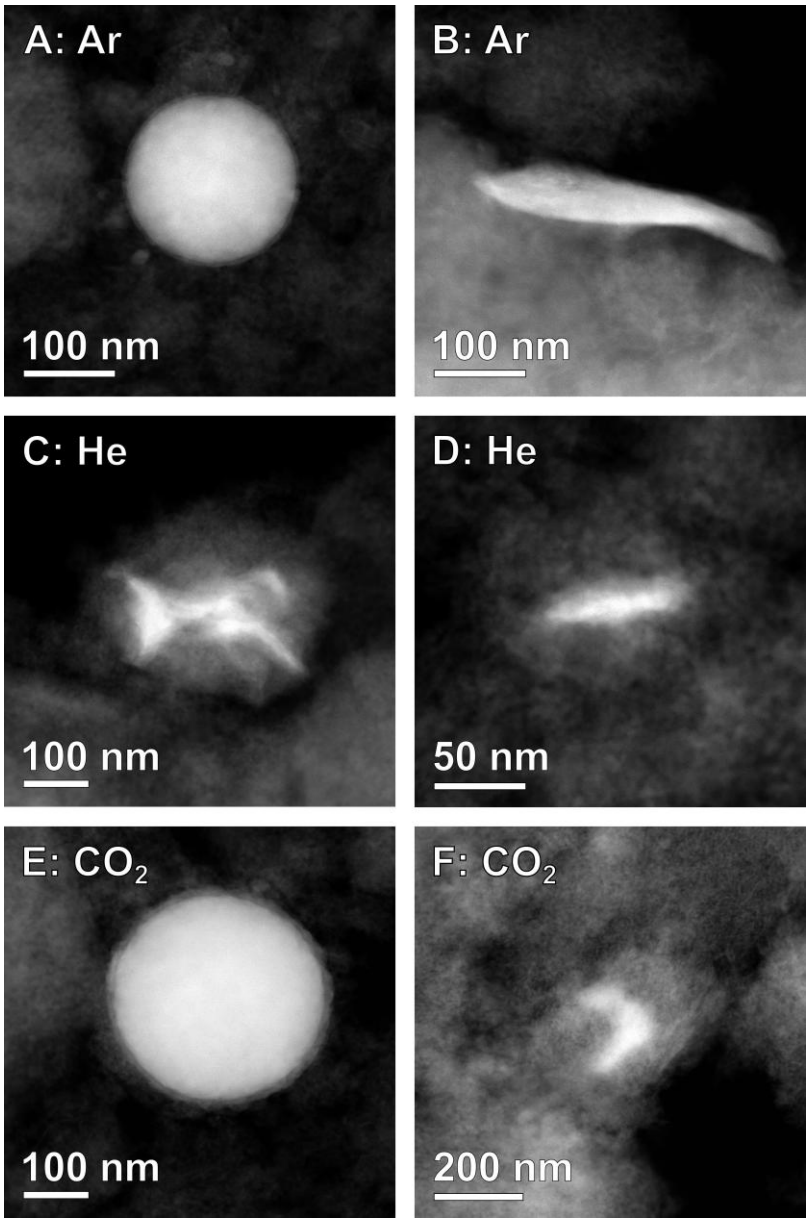

Figure 4-4: HAADF-STEM images of stainless steel particles in the Ar (A-B), He (C-D), and CO_2 (E-F) samples. The HAADF-STEM signal highlights the heavier steel particles against the lighter Al_2O_3 support. Highly spherical particles are observed for the Ar (A) and CO_2 (E) samples, but not for the He sample. Smaller particles with various morphologies were observed in all samples.

Note that, using EDX, all particles were confirmed to contain Fe, Cr, and Ni and are thus most likely stainless steel. In Figure 4-5, a representative EDX spectrum as obtained in the TEM is presented. The composition of the particles can again be confirmed by identifying the Fe, Cr, Ni, and Mn signals. In addition to these elements, Al and O were once more observed as they make up the Al_2O_3 support material that was still present during TEM analysis, though the peaks are not as dominant due to the different geometry compared to the SEM. Finally, also Cu and C signals were observed, but these can be attributed to the support on which the sample was deposited for TEM analysis.

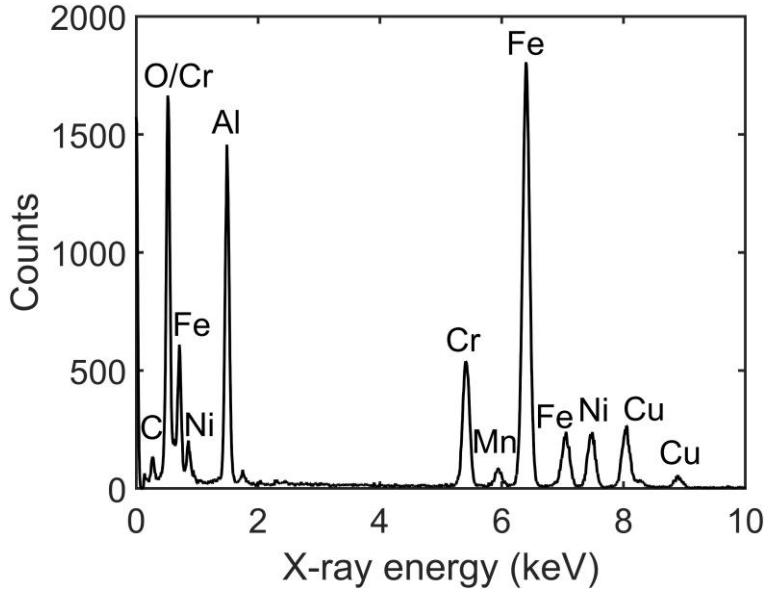

Figure 4-5: Representative TEM-EDX spectrum for a stainless steel particle, extracted from an Al_2O_3 sphere that was exposed to the CO_2 plasma. The identifying elements for stainless steel (Fe, Cr, Ni) are clearly present. In addition, Cu and C signals were also observed, but these can be attributed to the TEM support on which the sample was deposited.

Based on the TEM images, particle size distributions could be determined. The particle size was defined as the diameter of the smallest circle that encompasses the entire stainless steel particle in the image. The histograms of these particle sizes are provided in Figure 4-6 A-C, whereas the fitted lognormal distributions are presented in Figure 4-6 D. The stainless steel particles from the He sample are generally much smaller than the others, and more narrowly distributed. The CO_2 sample has the broadest distribution, with the largest particles overall, while the Ar particle size distribution sits somewhere in between He and CO_2.

To statistically support the differences between the presented datasets, a Lilliefors test for normality [135] was performed on the logarithms of the particle sizes of each sample. For every dataset, the Lilliefors test accepted the null hypothesis that the data comes from a normal distribution, justifying the lognormal fit. Furthermore, two-sample t-tests revealed significant differences between the different sets of logarithmic values, proving that there is a significant difference between the various particle size distributions.

In addition to the particle size distributions, the increased spatial resolution of the TEM enables a more detailed investigation of the individual particles. Higher magnification HAADF-STEM images in Figure 4-6 E (Ar) and F (CO_2) reveal that the spherical stainless steel particles have a lighter shell around their heavier core. Furthermore, the shell in the CO_2 sample is notable thicker compared to the Ar sample (10-15 nm versus 4-8 nm), which was observed for multiple spherical particles. EDX analyses revealed that the observed shell is an oxide layer on top of the metallic core, as presented in Figure 4-7.

Despite the clear observations presented here, it should be noted that the absolute deposition quantity of the eroded particles is low. Bulk characterization techniques were unable to capture an increase in Fe, Cr, or Ni content, as the impurities present in the pristine spheres were too high, thus no change after the plasma was observed. Furthermore, it was challenging to objectively quantify the number of deposited particles based on, e.g., the SEM measurements, as electron microscopy is inherently a local technique and the density of particles on the surface was low. In addition, the number of observed particles varied significantly between spheres, which is understandable as the plasma discharge is not homogeneous throughout the reactor and thus spheres in different locations will be affected differently. This prevents a reliable measurement of the extent of the erosion in our current system. Nevertheless, the current data offer various insights and do enable a comparison between the various discharges.

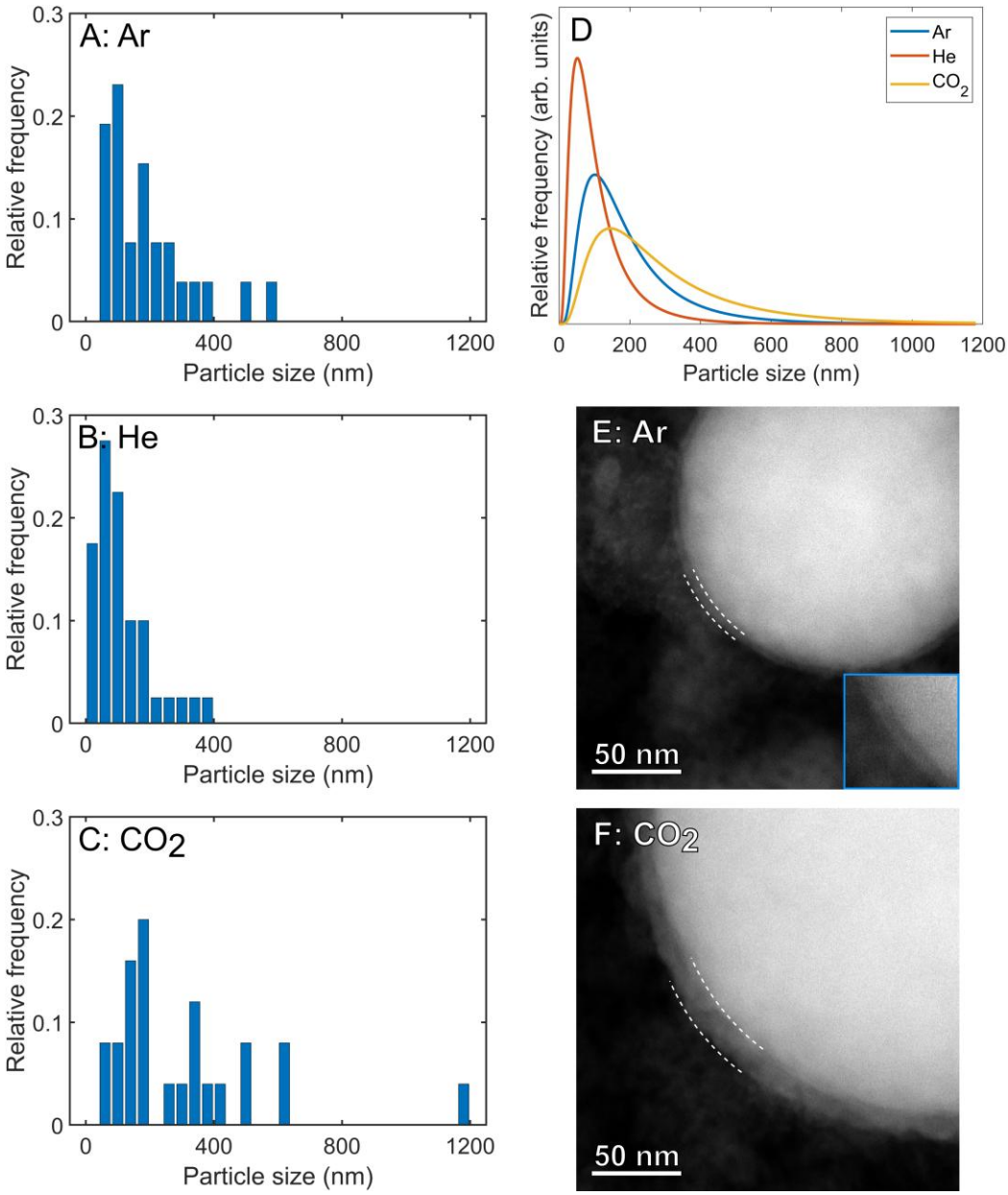

Figure 4-6: (A-D): Particle size distributions for the stainless steel particles formed in the discharges in various gases, based on TEM data: (A-C): Histograms of the particle sizes, for Ar (A: 26 particles), He (B: 40 particles) and CO_2 (C: 25 particles). (D): Lognormal distributions. The particles formed in the He plasma are clearly the smallest, whereas those formed in the CO_2 plasma exhibit a much broader particle size distribution with more larger particles. (E, F): Higher magnification images of stainless steel spheres with a thin oxide shell, indicated by the dashed white lines for the Ar (E) and CO_2 (F) samples. The inset in (E) shows the area indicated by the dashed lines at double the magnification to highlight the thin shell.

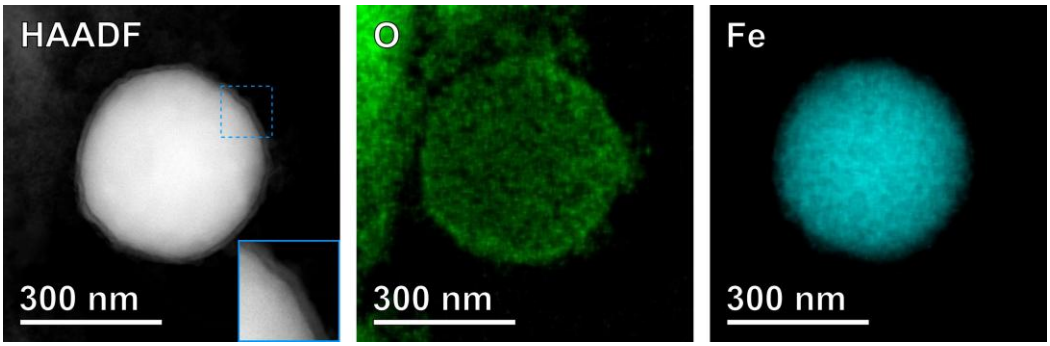

Figure 4-7: STEM-EDX characterization of a spherical steel particle generated in a CO_2 plasma. The HAADF-STEM image illustrates that the particle is covered by a lighter shell. The inset in the HAADF figure shows the indicated area at double the magnification. The oxygen EDX-map shows that the shell contains a clear oxygen signal, indicating that the shell is an oxide layer of the steel particle. The Fe map confirms that the particle contains Fe. The EDX characterization also yielded Ni and Cr signals (not shown), indicating that the particle is stainless steel.

3.2 Plasma Discharge Characterization

In order to understand what is causing the formation and deposition of these stainless steel particles, as well as which parameters influence the properties of these particles, the plasma discharge should be considered. Therefore, the plasma was electrically characterized, paying attention to two metrics we believe are highly relevant and representative for the discharge properties: the microdischarge quantity and the discharging areal fraction β, both explained in detail in Chapter 3. The microdischarge quantity is based on the Fourier transform of the discharge current signal, where the relevant frequency domain is integrated, yielding a value that includes contributions from both the number of microdischarges and their intensity. The discharging areal fraction β is the fraction of the dielectric barrier actually participating in the discharge, and can be calculated based on the theoretical value of the dielectric capacitance and the measured voltage-charge diagrams [86]. More details on these analyses can be found in Chapter 3.

As presented in Figure 4-8, the plasma discharges in the different gases yield varying discharge characteristics. Representative voltage and discharge current signals of the discharge after 1 hour of operation are shown in Figure 4-8 A-C, whereas the measured voltage-charge diagrams (also after 1 hour) are presented in Figure 4-8 D. Furthermore, the microdischarge quantity and discharging areal fraction were monitored over time, as presented in Figure 4-8 E and F, respectively. Both the visual inspection of the discharge current signal and the quantification of the microdischarges show that the CO_2

discharge is much more filamentary, with drastically more, and also more intense microdischarges. In addition, the voltage-charge diagram (in particular the inclination of the various edges, explained in detail in Chapter 3) can be analyzed to reveal various discharge properties, such as the discharging areal fraction, as mentioned earlier. A discharging areal fraction β of less than 0.3 for the CO_2 discharge indicates that barely a quarter of the dielectric barrier actually participates in the discharges. This implies that the power (which is slightly higher for the CO_2 discharge; see Figure 4-9) is dissipated in a smaller volume compared to the discharges in Ar or He, leading to higher local power densities, which can be expected for filamentary discharges. In contrast, the He discharge exhibits opposite properties, both for the microdischarges and the discharging areal fraction β. Indeed, the He plasma yields almost no microdischarges, whereas β approaches 1, indicating that nearly the entire dielectric participates in the discharge and thus that the reactor is completely filled with plasma. The Ar plasma has a similar discharging areal fraction β as the He discharge, and it exhibits a more filamentary discharge at the start. During the first 1-2 hours of operation, notably more microdischarges can be observed in the Ar discharge compared to the He discharge, though this behavior disappears over time. Note that although there are in fact changes in the discharge characteristics over time, they are not due to purely thermal effects. During the first ca. 30 minutes, the discharge characteristics can vary drastically, as can be expected due to heating of the system [136]. However, after again reaching the thermal steady state, the original trends of the discharge characteristics continue as before cooling down, indicating there must be an underlying, cumulative effect, discussed in more detail in the following. This is also why the CO_2 plasma was operated for a longer time than the Ar and He plasma. The discharging areal fraction for Ar and He was already high from the start, and increased even more during the first hours of operation. A similar effect was hypothesized for CO_2, as the introduction of metal particles to the outside of the packing can have this effect (discussed in detail in Chapter 3), but it was not observed immediately. Therefore, the plasma was operated for a longer time, to allow for the hypothesized cumulative effect to build up. However, even after these additional hours of plasma operation, this trend was not observed.

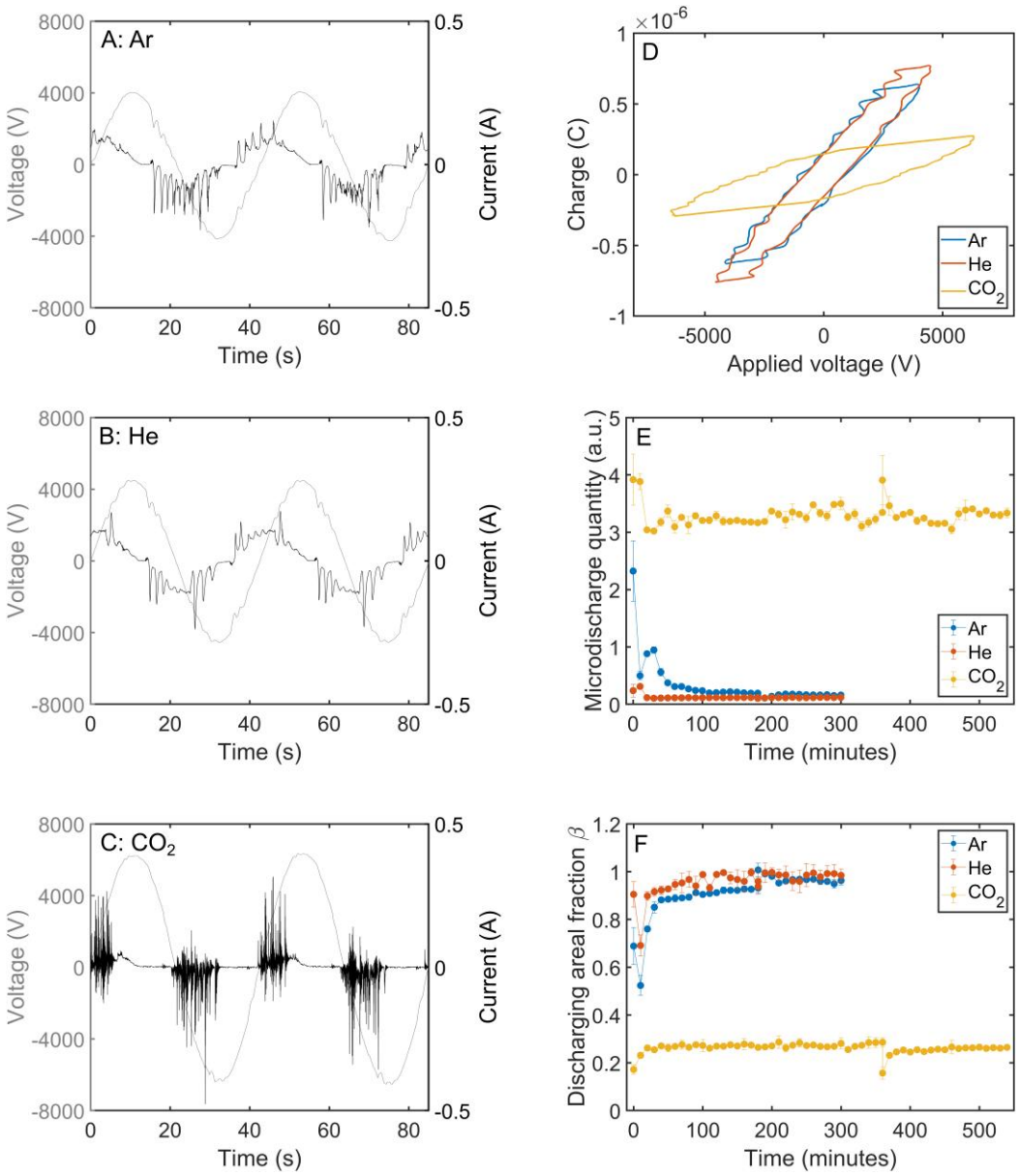

Figure 4-8: (A-C): Representative voltage and discharge current signals after operating the plasma for 1 hour in Ar (A), He (B), and CO_2 (C). (D): Representative voltage-charge diagrams after operating the plasma for 1 hour for all gases. (E): Microdischarge quantity over time for all gases. (F): Discharging areal fraction β over time for all gases. CO_2 exhibits the most explicit microdischarging behavior. The Ar discharge exhibits some microdischarging, though this decreased over time. The microdischarges in the He discharge are minimal. In addition, the Ar and He discharge yield a discharging areal fraction near 1, indicating that the plasma fills the entire reactor, whereas the CO_2 discharge is restricted to less than one third of the reactor.

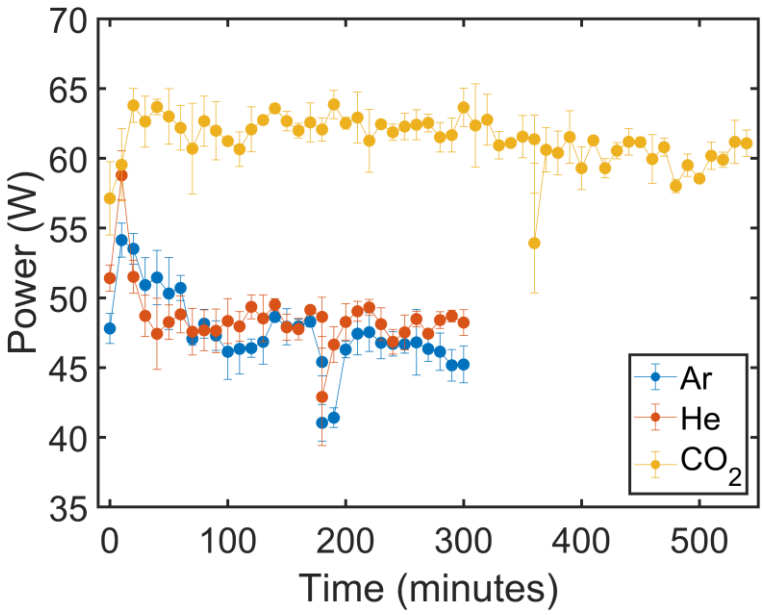

Figure 4-9: Plasma power over time for all gases. The plasma power in the CO_2 discharge was consistently higher than the powers in the Ar and He discharges.

The discharging areal fraction β and microdischarge quantity over time are presented in Figure 4-10 for the Ar (A, B), He (C, D), and CO_2 (E, F) discharges. Note that the y-axes are different to reveal the details of the data, though major difference may be present between the different gases. The orange data points indicate the second phase of each experiment, so after reignition once cooled down to room temperature. In most cases, the first half hour shows some additional variation of the values due to heating of the system, but after that, the trend from the end of the first phase continues. Only the discharging areal fraction during the CO_2 discharge appears to reach the previous value slightly slower, but is still very near those values. These results indicate that, especially for the Ar and He discharges, there is a cumulative effect independent of the temperature, i.e., something is changing in the system, that is causing the plasma discharge characteristics to vary slightly.

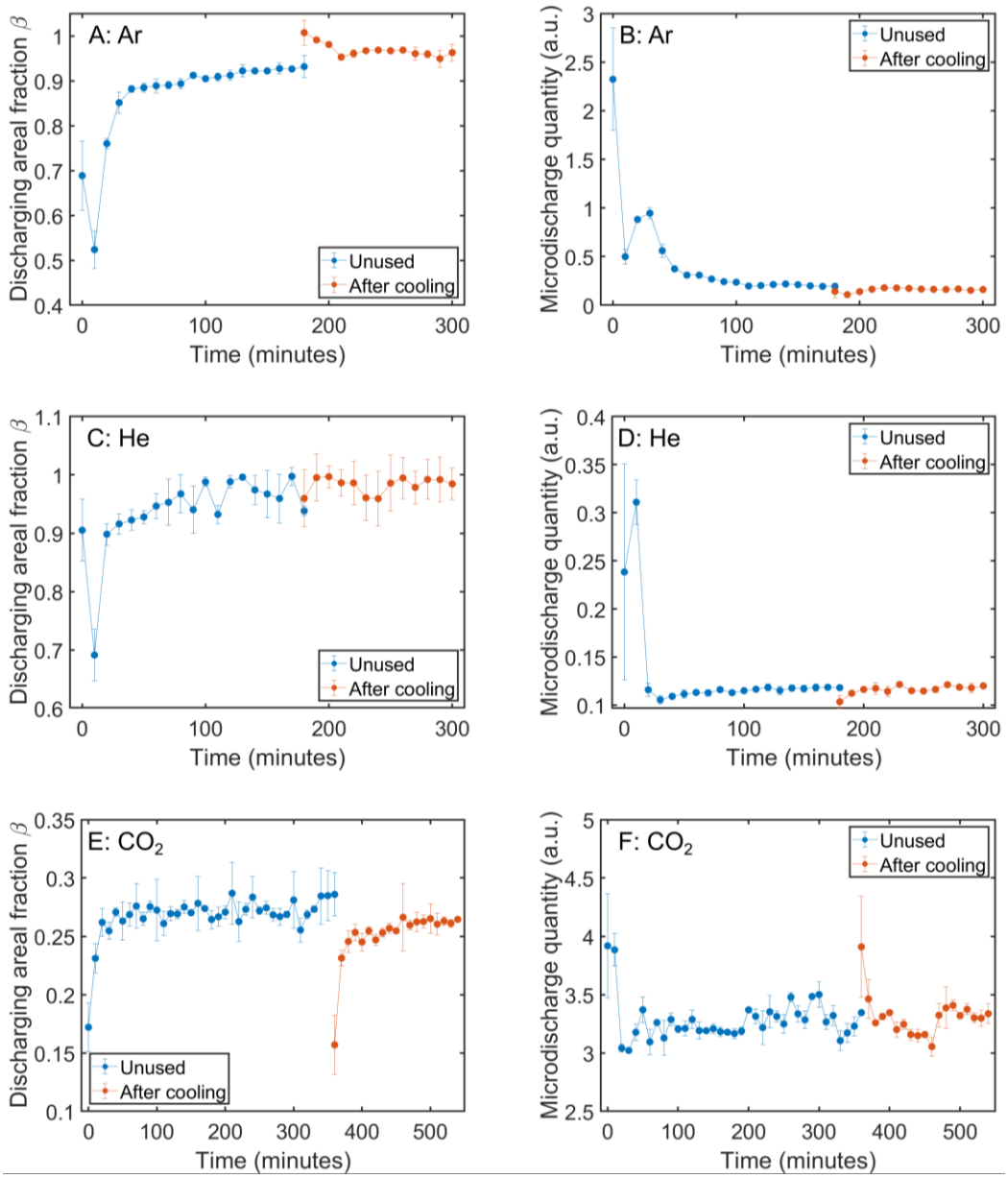

Figure 4-10: Discharging areal fraction β (A, C, E) and microdischarge quantity (B, D, F) during the Ar (A, B), He (C, D), and CO_2 (E, F) discharges. The orange data points indicate the data after cooling down. Note the different y-axes to illustrate the detail within the individual datasets. The increasing trend of the discharging areal fraction β for Ar (A) and He (C) continues after thermal stabilization upon reigniting the plasma. For the CO_2 discharge, the discharging areal fraction β (E) is slightly lower after reignition at room temperature, but is still very close (again not the different y-axis). For all gases, the observed trend of the microdischarge quantity continues after reignition at room temperature.

3.3 Particle Formation Mechanisms

The quantification of the plasma discharge can offer valuable insights in the underlying mechanisms that are responsible for the formation of these stainless steel particles. For example, we believe that the abundance of the highly spherical particles observed by SEM (see also Figure 4-2) is directly related to the abundance and intensity of the microdischarges. Indeed, it was already shown by Nguyen-Smith et al. that the microdischarges are able to locally melt the electrode [132]. When a small amount of the electrode melts locally, it is possible for a small droplet to be removed, after which it will quickly cool down and solidify (as it exits the high-intensity plasma region), thus forming these perfect spheres. This hypothesis is supported by our SEM observations, correlated with the plasma discharge characteristics. As demonstrated in Figure 4-8, the CO_2 plasma contained many intense microdischarges, leading to this high fraction of spherical steel particles. The Ar discharge was moderately filamentary, and only for a limited period of time, explaining why some spherical particles were found, but not many. Finally, the He discharge showed almost no microdischarges, which again corroborates with the lack of spherical particles. Note that the surface of the exposed electrode was also investigated by SEM, but even for the pristine electrode, the surface was found to contain many microscopic imperfections, making it impossible to reliably attribute any microscopic features to these erosion effects.

Regardless of the discharge characteristics, non-spherical stainless steel particles were also observed in every sample. The more randomly shaped particles are most likely formed by different mechanisms, such as sputtering, for example. Ion energies in atmospheric pressure DBDs tend to be rather low, but there may still be ions with sufficient energy to remove material from the exposed electrode surface [44,137,138]. While ion mass may have some effect on the sputtering of a material, its influence is not trivial [139,140]. Moreover, although the molecular weight of CO_2 is slightly higher than that of Ar (44 g/mol versus 40 g/mol), it is unlikely that this can explain the differences in particle size distributions, as presented in Figure 4-6 A, especially since CO_2 molecules might split in lighter ions. Rather, the plasma discharge again appears to play a significant role. Indeed, the higher microdischarge quantity, in addition to the higher local power density, is likely intensifying the erosion mechanisms, yielding larger eroded particles for the CO_2 plasma compared to the others. Note that also other discharge parameters, such as burning voltage, frequency, and temperature, may also influence the erosion processes. In addition to sputtering, alternative or additional formation mechanisms for

the steel particles caused by, e.g., local heating, oxidation, or even explosive electron emission [141,142] cannot be ruled out.

Besides the physical effects causing the formation of these particles, chemical effects were also observed, as demonstrated in Figure 4-6 E-F and Figure 4-7 by the stronger oxidation of the exterior of the steel spheres formed in the CO_2 plasma. Indeed, when the CO_2 plasma is sufficiently intense to locally melt the electrode, it is very likely that there will be reactive oxygen species present as well, causing oxidation of the outside layer of the stainless steel. In the Ar plasma, however, no oxygen should be present. Therefore, the lesser oxidation is attributed to oxidation in air during the manipulation of the spheres after plasma operation.

Although there is no direct evidence, oxidation of the steel particles in the CO_2 plasma may explain why the plasma discharge characteristics remained stable over the observed time, contrary to the Ar and He discharges. Indeed, the drop in microdischarge quantity and rise of the discharging areal fraction β is consistent with previous observations presented in Chapter 3 for the addition of metal particles to the exterior of the packing spheres, although the loading here is much lower. If the exposed stainless steel particles on the spheres would all have oxide surfaces, this may explain why their impact on the plasma discharge is minimal, as the exposed oxide can have very different properties and subsequent effects on the plasma than the metal. Though this is only a hypothesis, it does highlight the complexity of the system, making it very important to further our understanding of all processes taking place during the experiment.

3.4 Additional DBD Reactors

It should be noted that in addition to the materials described here, we also observed stainless steel particles on the packing material after plasma operation for other DBD reactors with very different specifications. These samples were analyzed by SEM and EDX to investigate whether they also contained stainless steel particles. While both additional samples were used in distinctly different reactors, they all have an exposed stainless steel central electrode in common. Our analyses revealed that both additional samples also contained stainless steel particles, and examples are presented in Figure 4-11. Their composition was again confirmed by EDX. The technical specifications of the reactors used are provided in Table 4-1. It is clear that they span a wide range of properties, highlighting that this phenomenon is not unique to a particular system.

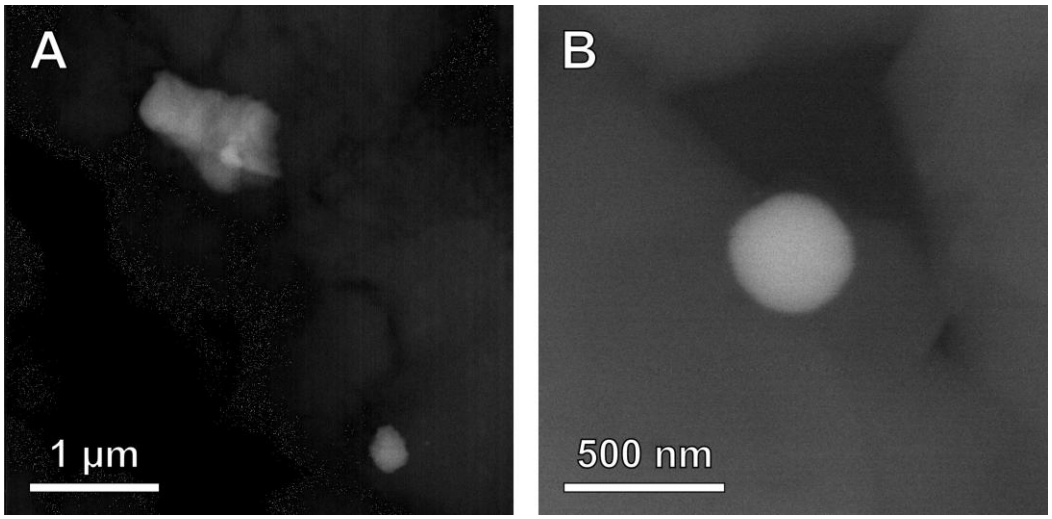

Figure 4-11: BSE-SEM images of stainless steel particles found on a silica (A) and zeolite 5A (B) support after being used in a packed-bed DBD experiment. Their composition was confirmed by EDX analyses.

Table 4-1: Specifications of the packed-bed DBD reactors in which the presented samples were used.

Packing material	**Al_2O_3 (this work)**	**SiO_2**	**zeolite 5A** [143]
Discharge gap (mm)	4.5	2.5	1
PSU frequency (kHz)	23.5	23.5	45
Plasma power (W)	45-65	ca. 25	ca. 30
Dielectric material	alumina	glass (water cooled)	alumina
Inner electrode	stainless steel	stainless steel	stainless steel
Discharge gas	Ar, He, or CO_2	$CO_2 + H_2$	$CO_2 + CH_4 + Ar$

Moreover, very small nanoparticles (down to 2-3 nm) were found in a carbon matrix after generating a CH_4 plasma in an empty DBD. The same reactor that was used for the silica sample from Figure 4-11 A and Table 4-1 was used empty to generate a pure CH_4 plasma. After operating the plasma continuously for 2 h with a plasma power of ca. 25 W, carbon deposits were collected and analyzed. The SEM and TEM data are presented in Figure 4-12. All data clearly illustrate the presence of steel particles on and throughout the carbon material. The BF-TEM analyses even revealed very small particles, down to 2-3 nm. The representative SEM-EDX spectrum again confirms that the particles are indeed stainless steel. Note that these very small particles of just a few nm in size are likely to be present on the Al_2O_3 spheres as well, but these are easily missed due to the stronger background signal of the Al_2O_3 compared to the very thin layer of carbon here.

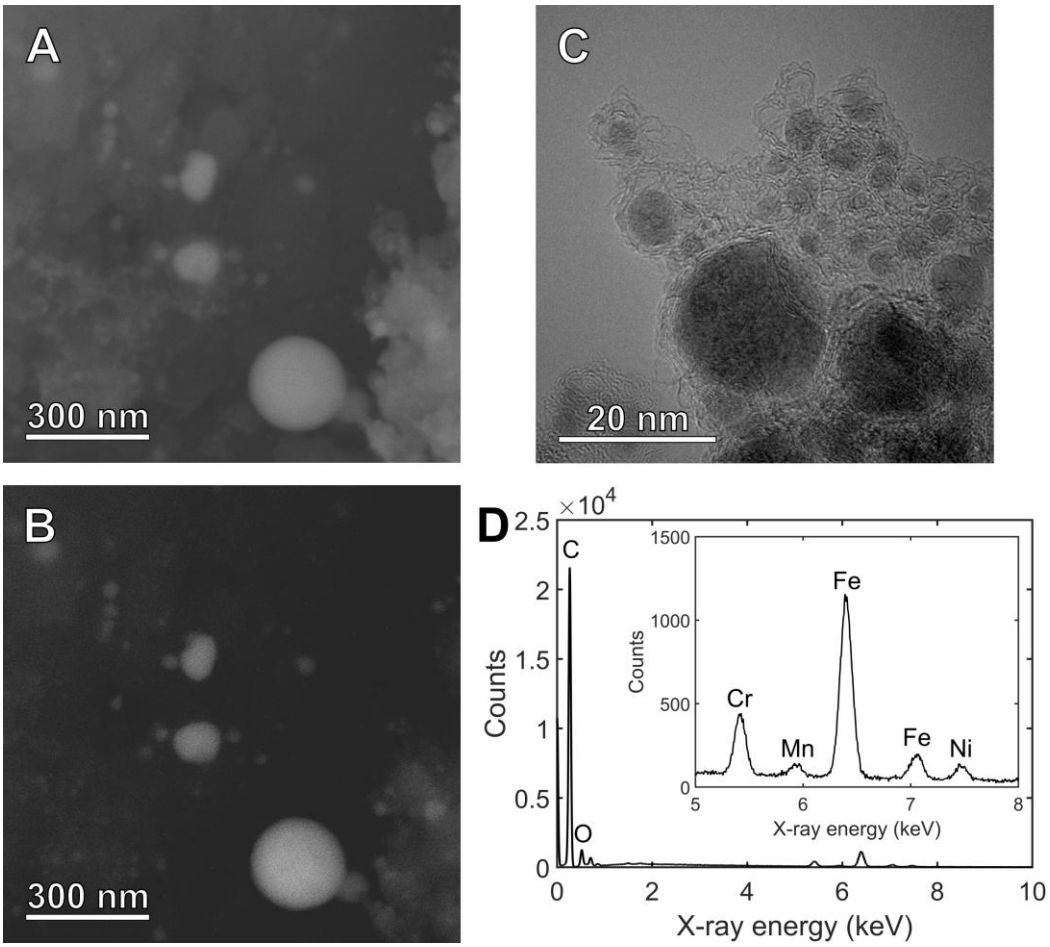

Figure 4-12: (A, B): SE- (A) and BSE- (B) SEM images of the carbon deposits that were generated in an empty DBD with a CH_4 plasma. Heavy (steel) particles are clearly present in the carbon material. (C): BF-TEM image of steel nanoparticles inside the carbon material. (D): Representative SEM-EDX spectrum of the heavy particles in the carbon material, clearly containing Fe, Cr, and Ni, identifying the particles as stainless steel.

Hence, despite the large variety in reactor geometries and operating conditions, the erosion and subsequent deposition of an exposed metal electrode in a DBD seems inevitable. Therefore, it is crucial that this phenomenon is known and understood. Whether this effect is problematic, or to what extent, depends heavily on the desired application. For example, when treating biological samples, such as seeds or even food, a small number of metal (nano)particles may already pose toxicity risks [144]. In addition, when treating or synthesizing materials using DBDs, the deposition of these particles may introduce undesired impurities. Also in plasma catalysis, this effect may be drastic, especially when considering long-term operation with the aim of further

upscaling and industrialization. Indeed, as discussed extensively in Chapter 3, the deposition of metal particles on the packing material is likely to have an effect on the discharge characteristics, which in turn will alter the overall performance. Moreover, the introduction of (overlooked) metal(oxide) particles may offer catalytically active sites, that could further steer the reactions in a different direction over time. Therefore, it is crucial that researchers are aware of this effect, so it can be taken into account when interpreting results and designing novel systems. Note that this issue could be addressed by employing a double DBD, where both electrodes are covered by a dielectric. Although this would prevent the formation and deposition of steel particles, the dielectric material may erode to some extent as well, as was recently shown by Wang et al. for surface DBDs [131]. Moreover, covering the second electrode will alter the plasma discharge, which may limit the overall performance of the system [73]. Whether the use of a double DBD is beneficial depends on the precise application, finding a balance between the deposition of the electrode material and the alteration of the discharge, with potential effects on the overall performance.

4. Conclusion

Although DBDs are generally regarded as gentle plasmas, the results in this chapter demonstrate that the exposed stainless steel electrodes undergo erosion. This erosion leads to the deposition of stainless steel particles on the packing material, becoming a significant source of contamination. Our analyses indicate that the plasma discharge parameters strongly influence the particles' size, shape, and surface oxidation, yet the formation of these particles occurs consistently across different operating conditions and reactors, suggesting this issue is widespread.

The presence of these particles must be considered in all potential applications, such as material synthesis or functionalization, and plasma catalysis. In catalytic applications, stainless steel particle contamination may obscure experimental results and ultimately affect the plasma discharge, thereby impacting overall performance. Additionally, when DBD plasmas are used for treating biological systems like seeds or food, the presence of stainless steel particles could pose serious health risks, emphasizing the importance of understanding and mitigating this effect in practical applications.

Chapter 5

Electrical Characterization of an Atmospheric Pressure Townsend Discharge Exposed to a Conductive Layer: an Update of the Equivalent Circuit

In this chapter, a simplified system is employed to investigate the influence of a catalytic material on the discharge in more detail. Specifically, an atmospheric pressure Townsend discharge in N_2 is exposed to a layer of Fe(oxide) on one of the dielectrics. When this layer is conductive, it affects the capacitances of the system, which clearly influence the discharge characteristics. Due to the altered capacitance, an update to the electrical characterization is required. Hereby, clear indications are found that the introduced material can decrease the discharge voltage, further highlighting the importance of understanding the interaction between the catalytic materials and the plasma discharge.

The content of this chapter is based on:

Electrical characterization of an atmospheric pressure Townsend discharge exposed to a conductive layer: an update of the equivalent circuit
Robin De Meyer, Philip Cimento, Ronny Brandenburg, Jo Verbeeck, Sylvain Coulombe, Annemie Bogaerts
Submitted to Plasma Sources Science & Technology

1. Introduction

As discussed in the previous chapters, dielectric barrier discharges (DBDs) were already adopted by several industries [10], and are further developed for a wide range of potential applications [21,28,122,125,145–147]. As explained in Chapter 1, and illustrated in Chapter 3 and Chapter 4, DBDs usually operate in a so-called filamentary mode. In this case, the gas gap between the electrodes is not completely filled with plasma, but rather discrete filaments bridge the gap. In addition to the filamentary discharge, the DBD can also be diffuse under certain conditions [22]. As introduced in Chapter 1, one of such diffuse discharges is the so-called atmospheric pressure Townsend discharge (APTD), where the breakdown in the gas takes place at relatively low voltages due to pre-ionization, preventing streamer formation [12]. APTDs are usually obtained in pure N_2 or N_2 with low admixtures of O_2 or NO_2, but recently also in air and pure CO_2 [24,26,27,148–150]. The APTD is of great interest compared to the more common filamentary discharges, due to the (more) uniform treatment of the gas or material exposed to the plasma and the well-characterized electric field strength in the gap. Therefore, the APTD enables reproducible gas and material processing conditions with a clear understanding of the discharge properties.

Regardless of the discharge mode and desired application, the electrical characterization of the discharge is crucial to understand its properties, which often have a major impact on the overall performance of the system, as described in detail in Chapter 3. The electrical characterization of the DBD was pioneered by Manley in 1943 [52], when it was first proposed to analyze the voltage-charge diagram and interpretations based on the capacitances of the system were suggested, as introduced in Chapter 2. Since then, the electrical characterization and physical interpretation of the discharge characteristics have been further developed. Nowadays, it is common practice to analyze these voltage-charge diagrams based on equivalent circuits, where the various parts of the DBD are represented by electrical components, as illustrated and implemented in Chapter 3. A major update of the equivalent circuit for volume DBDs was provided by Peeters and van de Sanden [86]. Herein, the authors introduced the concept of partial discharging, where the circuit is split in two sections: one that is discharging and one that is not. Based on the known values of the capacitances in the circuit and the measured voltage-charge diagram, the discharging areal fraction β can be calculated, and other metrics such as the gap voltage and the amount of transferred charge can be determined correctly.

In general, the surface properties of a material exposed to the plasma can significantly influence the discharge characteristics in DBDs [22,151], and this can strongly affect the applications, as plasma-surface interactions are highly relevant. For example, filamentary DBDs and APTDs are employed for thin film and nanocomposite deposition, where the discharge could be affected by the altered surface properties [152,153]. Further, in plasma catalysis, the interaction of the plasma with the catalyst is crucial [29], as also discussed in Chapter 3, but experimental investigations are often hampered by the complex geometry and discharge behavior of a packed-bed DBD [44,154]. Therefore, a simplified geometry and a more reproducible discharge could enable more detailed investigation of plasma-catalyst interactions. Several metal-based materials are commonly investigated in plasma catalysis, such as for example Fe(oxide) [31,155,156], but the effect of these metal-based particles on the discharge is poorly understood. Indeed, the results from Chapter 3 showed a clear effect of the catalyst on the discharge characteristics, but the precise underlying mechanisms remain ambiguous.

Hence, in this chapter, we investigate how the dynamics of a well-characterizable discharge are influenced by Fe nanoparticles deposited on one of the exposed dielectrics of a DBD with a simple geometry. In particular, an APTD is generated in atmospheric pressure N_2 in a parallel-plate, two-sided DBD using quartz disks as dielectric barriers, where one disk is coated with Fe nanoparticles. The discharge is electrically characterized and an adapted version of the equivalent circuit is introduced, enabling the physically relevant interpretation of the voltage-charge data.

The experiments described in this chapter were performed during a research stay at McGill University (Montreal, Canada) under the supervision of prof. Sylvain Coulombe. The syntheses by PLA and characterization of the coatings were performed by Philip Cimento.

2. Experimental Methods

2.1 Pulsed Laser Ablation

The central section of quartz disks (Technical Glass products, 1 inch (25.4 mm) diameter, 1/16 inch (ca. 1.59 mm) thickness) was coated with Fe nanoparticles using an in-house pulsed laser ablation (PLA) system, schematically presented in Figure 5-1 [157]. The Fe target (Kurt J. Lesker, 99.9% purity) was hand-polished using a 1-µm grit sandpaper prior to mounting on a linear displacement stage in the PLA chamber. The quartz disk was

mounted parallel to the Fe target (3 cm away) on a rotation substrate holder equipped with a mask to limit the deposition diameter to 19.8 mm. The chamber was flushed with argon (Praxair, 5.0 grade) for 3 min before evacuating down to a base pressure of approximately 10^{-5} Torr.

Ablation of Fe was performed using a 10 Hz Q-switch Nd:YAG laser (Quantel, Brilliant B10) operating at a frequency-tripled wavelength of 355 nm. The measured average laser power at the fixed Q-switch delay of 215 µs was measured to be 0.57 W by a single-channel laser power meter (Gentec-EO, SOLO model), which corresponds to a laser fluence per shot of 7.3 J cm^{-2}. The target was vertically oscillated at 1.4 cm min^{-1} to avoid local cratering on the metal target and to ensure uniform nanostructure deposition [158]. The coating structure and thickness were controlled through adjustment of the total number of laser shots fired at the target (250, 500, 1000, and 2000 laser shots).

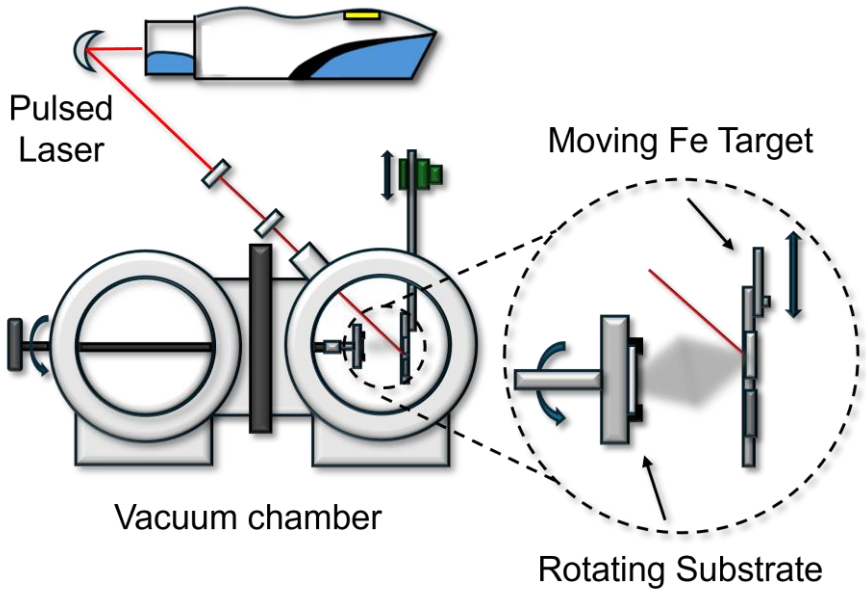

Figure 5-1: Schematic of the pulsed laser ablation (PLA) setup. The laser is directed at the Fe target inside the vacuum chamber. The Fe target oscillates vertically to prevent local cratering. A quartz disk is mounted on a rotating stage and placed parallel to the Fe target at a distance of 3 cm.

2.2 Coating Characterization

Sheet resistance measurements of the prepared samples were conducted using four-terminal sensing (Everbeing, C Series) based on the van der Pauw method, where the probes are arranged on the corners of a square along the perimeter of the coating [159].

Measurements were obtained using a 0.7 µm tungsten tipped probe with an open-circuit DC voltage of 1 V.

2.3 Plasma Experiments

The plasma experiments were performed inside a vacuum chamber equipped with a viewport for optical access. Prior to every experiment, the chamber was evacuated to base pressure (< 25 mTorr), after which the system was flushed with high-purity N_2 (Praxair, 5.0 grade) for 30 min at 5000 sccm (standard cubic centimeters per minute) to remove any remaining impurities. A continuous flow of N_2 of 500 sccm through the chamber was ensured during the experiments to prevent excessive heating or a buildup of impurities.

A schematic of the experiment setup is provided in Figure 5-2. The powered (top) electrode in the DBD assembly consists of an Al piece (12 mm diameter at the quartz surface) that is fixed to a quartz disk (Technical Glass products, 2.5" diameter, 1/16" or ca. 1.59 mm thickness) using an epoxy (Devcon, 2 Ton Epoxy). The Al electrode is powered by voltage- and power-amplified (Trek, 20/20C) 1 kHz sinusoidal signal (Siglent, SDG 1032X). The top electrode assembly rests on two quartz spacers (1.59 mm gap), centered above the lower quartz disk which is either blank or coated with Fe nanoparticles, and resting on a flat Al plate. This lower electrode is connected to the ground through a monitoring capacitor (10 nF) and resistor (25 Ω).

The applied voltage is measured by a high voltage probe (Tektronix, P6015A). Regular voltage probes (Pico Technology, TA386) are used to register the voltage across the resistor, as well as the voltage across both the capacitor and the resistor combined. All signals are acquired simultaneously by the oscilloscope (Pico Technology, 2408B, 18 MS/s sampling rate used, 100 MHz device bandwidth).

For every datapoint, up to 64 snapshots were acquired by the oscilloscope, which were averaged prior to further analysis. Note that the averaging of the signals is only justified because the atmospheric pressure Townsend discharge studied here is extremely reproducible. When investigating a filamentary discharge, such averaging is not justified, since the streamers in the filamentary discharge are stochastic in nature. Despite the averaging, the current signal is still quite noisy, given the generally very small currents. Therefore, it was smoothed by a moving average filter with a window size of 300 (1 timestep is 56 ns) prior to further analysis and interpretation.

Further, for calculating certain metrics, the time derivative of the applied voltage should be determined. Calculating the numerical derivative of an experimentally acquired signal can be challenging, since the oscilloscope translates the measured voltage to an 8 bit number. This limited vertical resolution poses significant issues when calculating the time derivative based on the voltage difference between subsequent timesteps. Therefore, when calculating the time derivative of the applied voltage, this signal is first smoothed by a moving average filter with a window size of 1000.

At every applied voltage, three datapoints were acquired to ensure consistency. Further, it was found that the parasitic capacitance caused by the probes, as well as their timing offset, varied slightly over time (possibly due to heating effects). Therefore, after every acquisition of the threefold datapoint, the voltage was decreased and a measurement with plasma-off was acquired to correct for this effect. More information is provided in Appendix B, Section 1.

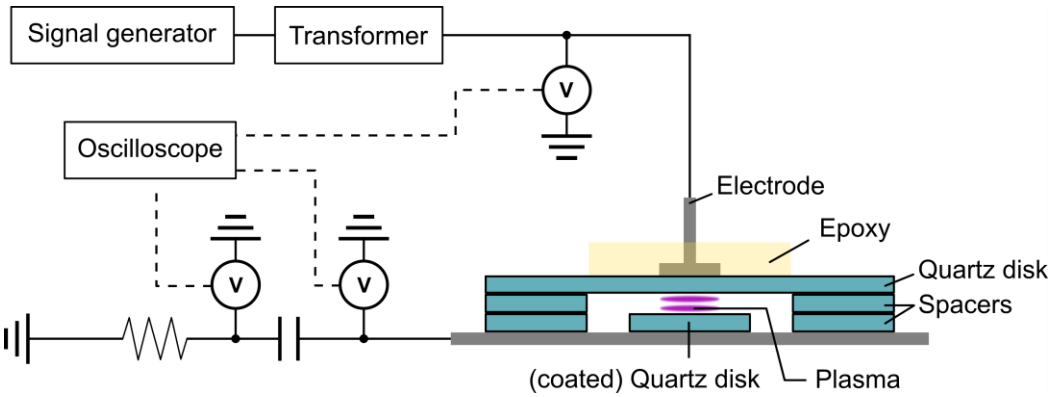

Figure 5-2: Schematic of the experimental setup with the various electrical components. The signal generator and transformer apply a high AC voltage to the top electrode that is embedded in epoxy and fixed to the top quartz disk. This assembly rests on spacers, creating a gap between the top and bottom quartz disks in which the plasma can be generated. Below the bottom quartz disk is an Al plate that is electrically connected to the monitoring capacitor, resistor, and ground.

3. Coating Characterization Results

The conductivity measurements using the 4-point probe revealed that the coatings produced with 1000 and 2000 laser shots were conductive. The average resistances as measured with the van der Pauw method [159] for the 1000 and 2000 shots samples were 535 ± 44 MΩ and 413 ± 160 kΩ, respectively. Measurements by the 4-point probe of the lower shot count samples prepared with 250 and 500 laser shots did not reveal a

detectable signal and thus, these coatings are considered to be non-conductive. This PLA synthesis method yields very small and highly dispersed nanoparticles [157,160,161]. It can be expected that at these lower laser shot counts, the coating is too sparse to result in a macroscopic conductivity. In addition, since the disks were stored in air, partial (or even complete) oxidation of the Fe nanoparticles is expected to take place [157], further hindering the electrical conductivity of the coating. The conductivity of the coatings synthesized with 1000 and 2000 laser shots implies that the deposition of nanoparticles is sufficiently dense to provide the macroscopic electrical conductivity.

4. Equivalent Circuit and Electrical Characterization

The electrical characterization of the DBD is an invaluable tool to investigate the discharge properties. This electrical characterization is based on an electrical model of the DBD, the so-called equivalent circuit [162]. Several modifications to this equivalent circuit have been proposed, and a brief overview of the state of the art is provided. Then, the model will be applied to the experimental data, and its limitations will be highlighted. Finally, an update to the equivalent circuit is proposed, and its applicability is illustrated with the experimental data.

4.1 Conventional Equivalent Circuit

In the simplest equivalent circuit, briefly introduced in Chapter 2 and presented in Figure 5-3 A, the DBD is represented by two capacitors in series, the dielectric capacitance C_{diel}, and the gap capacitance C_{gap}. When the plasma ignites, a conductive channel appears in the gap, bypassing the gap capacitance. The values of these capacitances are (in principle) fixed and determined by purely geometrical and material properties of the dielectric (the type of gas typically has a negligible effect on the gap capacitance). For simple geometries, such as parallel plane or coaxial, these values can be calculated accurately. In addition, the cell capacitance C_{cell} (being the capacitance of the whole system formed by C_{diel} and C_{gap}) and the dielectric capacitance can be determined from the voltage-charge diagram. Indeed, when the plasma is off, the charge variation in function of the applied voltage directly relates to the cell capacitance ($C = \mathrm{d}Q/\mathrm{d}V$). Based on this ideal equivalent circuit, several discharge characteristics can be determined such as the gap voltage, mean discharge current, and dissipated plasma power [163].

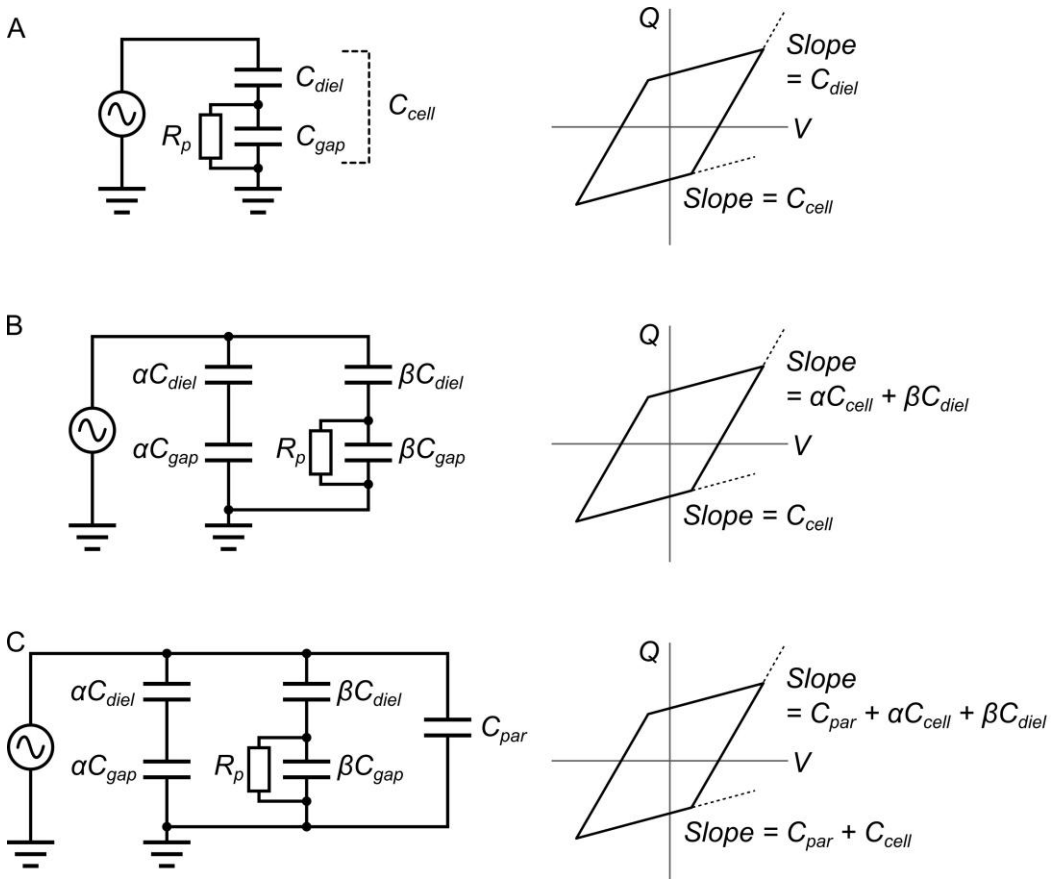

Figure 5-3: Equivalent circuits and their corresponding interpretation of the capacitances in the voltage-charge diagrams. (A): simplest circuit, that assumes the DBD can be treated as a single dielectric capacitor and a single gap capacitor which can be shorted by the plasma discharge. (B): circuit including partial discharging, which splits the circuit in a discharging (β) and non-discharging (α) fraction. (C): circuit including partial discharging and parasitic capacitances, where an additional constant capacitance is added to the circuit.

Over a decade ago, Peeters and van de Sanden introduced a significant update to this equivalent circuit (Figure 5-3 B [86]). They showed that in many cases, the plasma discharge is not permeating the entire electrode cross-section, i.e., only a fraction of the gap is truly shorted by a conductive path. In practice, this means that the measured dielectric capacitance (i.e., the effective dielectric capacitance, ζ_{diel}) is often lower than expected based on the geometry of the arrangement. To understand and quantify this effect, an extended equivalent circuit was introduced, where the system is split in two sections: the discharging and non-discharging fractions. When the plasma is on, only a part of the reactor participates in the discharge, and thus only a part of the gap

capacitance is eliminated from the measured capacitance. This fraction is called the discharging areal fraction β (between 0 and 1). The other fraction is then naturally the non-discharging areal fraction α, with $\alpha + \beta = 1$. Based on this new equivalent circuit, the authors updated the equations to determine quantitative discharge characteristics, and they showed that this partial discharging can significantly affect the final results when not properly accounted for [86].

In addition to this fundamental update of the equivalent circuit, a more practical consideration was proposed to take into account the effect of parasitic capacitances, as illustrated in Figure 5-3 C [164,165]. These parasitic capacitances are unavoidable in any system, and can be very significant, especially when dealing with DBD systems with small capacitances. Although parasitic capacitances do not affect the power measurements, they can notably influence other metrics, such as the gap voltage and the transferred charge. In addition, the measured capacitances can deviate significantly from the expected geometrical values.

Employing the most extensive equivalent circuit, including both partial discharging and parasitic capacitances, several metrics can be calculated. First, the parasitic capacitance C_{par} has to be determined. This is done using a plasma-off measurement (i.e., applied voltage amplitude below the discharge ignition threshold V_{min}). In this case, the system acts as a single capacitor with capacitance $C_{cell} + C_{par}$, which can be directly calculated from these measurements (since $C = \mathrm{d}Q/\mathrm{d}V$). Given the simple geometry of the system and the known material properties, the cell capacitance can be accurately calculated from the dielectric capacitance C_{diel} and gap capacitance C_{gap} in series:

$$C_{diel,geom} = \frac{1}{2}\frac{A\varepsilon_0\varepsilon_d}{d} \tag{17}$$

$$C_{gap,geom} = \frac{A\varepsilon_0\varepsilon_g}{d_g} \tag{18}$$

$$C_{cell,geom} = \frac{C_{diel,geom}C_{gap,geom}}{C_{diel,geom} + C_{gap,geom}} \tag{19}$$

With A the electrode area (here 113 mm^2), ε_0 the permittivity of vacuum (approximately 8.854 * 10^{-12} F/m), ε_d the dielectric constant (or relative permittivity) of the dielectric (3.75), ε_g the dielectric constant of the gas (1.0006), d the thickness of the dielectric (1.59 mm), and d_g the gap distance (1.59 mm). In the equation for $C_{diel,geom}$, the factor 1/2 is added because the overall dielectric capacitance consists of the two separate dielectric capacitances (i.e., the top and bottom quartz pieces) in series. These equations yield the following values for our arrangement: $C_{diel,geom}$ = 1.180 pF, $C_{gap,geom}$ = 0.630 pF, and $C_{cell,geom}$ = 0.411 pF. Based on these geometric capacitances and the measured capacitance during the plasma-off measurements, the parasitic capacitance can be determined.

In Figure 5-4, the capacitances are presented as directly extracted from the plasma off measurements after every threefold datapoint acquisition. This means that for a datapoint at, e.g., 30 kV, the value shown here is the total measured capacitance (i.e., C_{cell} + C_{par}) at a low voltage, after acquiring the threefold datapoint at 30 kV.

Firstly, a rising trend can be observed for all experiments. Since the experiment is performed by stepwise increasing the voltage, the increasing trend is attributed to a cumulative effect, such as heating of the high voltage probe, contributing to a slow rise of the parasitic capacitance.

Secondly, there are minor differences between the experiments with the different disks, but no correlation between the deposition amount is found. This is likely due to minor variations in alignment of the disks and spacers, again slightly influencing the parasitic capacitance. Therefore, it seems justified to assume that the actual C_{cell} value is constant for all disks and experiments, and that the only variable observed here is the parasitic capacitance, which is found to vary slightly with a value around 1.8 pF.

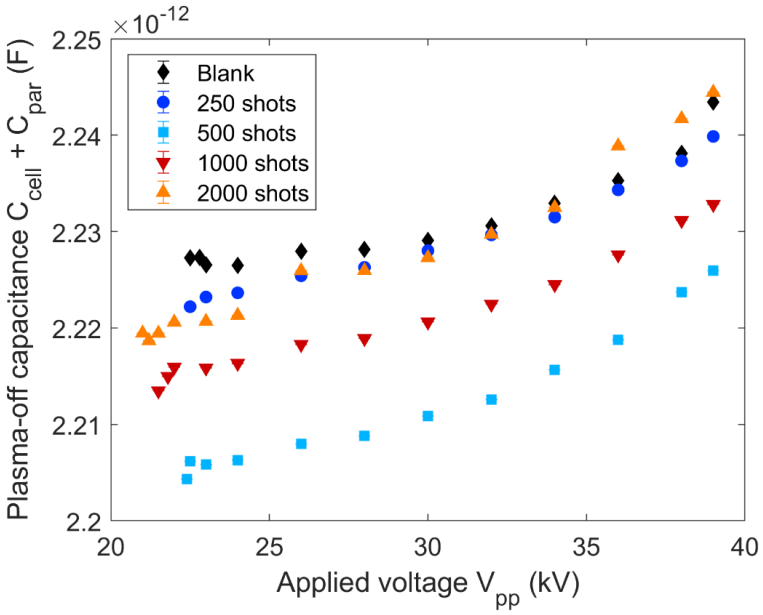

Figure 5-4: Measured capacitances during plasma off measurements (i.e., C_{cell} + C_{par}) after every threefold datapoint. For every sample, an increasing trend is observed, where the parasitic capacitance increases slowly during the course of the experiment (the datapoints at the different voltages were acquired in ascending order). The values between the datasets also vary slightly, but this is not correlated with the coating and likely due to slight differences in alignment of the components.

Then, the discharging areal fraction β can be determined based on the measured effective dielectric capacitance ζ_{diel}, and the theoretical (i.e., geometrical) dielectric and cell capacitances:

$$\beta = \frac{\zeta_{diel} - C_{cell,geom}}{C_{diel,geom} - C_{cell,geom}} \tag{20}$$

These calculations are done for all samples (i.e., blank quartz disk, and coated quartz disks with 250, 500, 1000, or 2000 laser shots), and for a wide range of applied voltage amplitudes. The effective dielectric capacitances ζ_{diel} as extracted from the voltage-charge diagram (after subtracting the parasitic capacitance), as well as the resulting values for β, are presented in Figure 5-5.

Note that the errors on all threefold datapoints (in this figure and throughout the entire chapter) are based only on the standard deviation. The errors on the geometrical capacitances are not propagated since the true values are constant for all experiments and we are mostly interested in the relative differences between the various disks. The

errors in the presented graphs tend to be very small (often not visible) because the APTD is highly stable and reproducible, and thus variations are minimal.

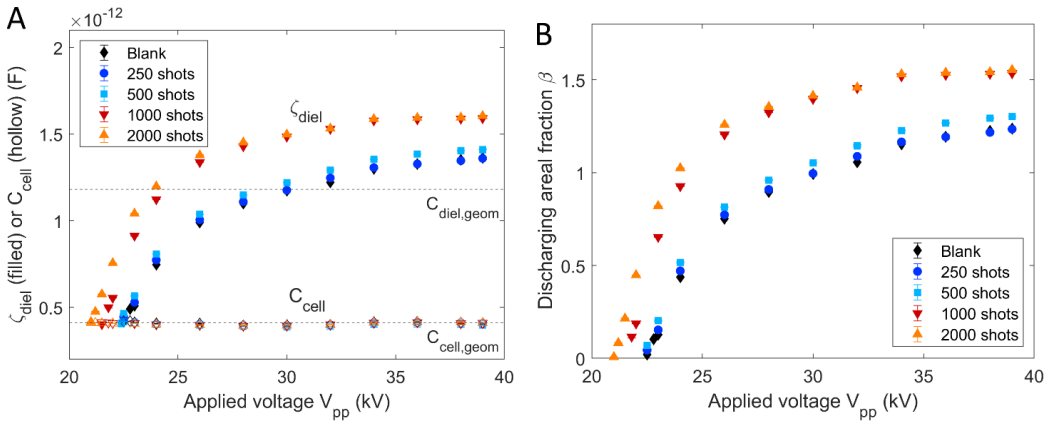

Figure 5-5: (A): Measured effective dielectric capacitances and cell capacitances from the voltage-charge diagrams (after subtracting the parasitic capacitance) for the various disks and at a range of applied voltages. The theoretical cell and dielectric capacitance are indicated by dashed horizontal lines. (B): Discharging areal fraction β as calculated based on the conventional equivalent circuit for the various samples and applied voltages. The measured effective dielectric capacitances are notably higher than the theoretical values, especially for the conductive (1000/2000 shots) disks, leading to values of β that exceed the theoretical maximum of 1.

The measured effective dielectric capacitances ζ_{diel} exhibit an increasing trend with increasing applied voltage, which is indeed expected [86]. However, the values exceed the theoretical dielectric capacitance. This directly results in discharging areal fractions increasing above 1. It is important to remember that by definition, the discharging and non-discharging areal fractions are bound between 0 and 1, and their sum must be equal to 1. This is due to the geometrical interpretation of the model, where the discharge is assumed to be bound by the areas of the electrodes, and thus a negative non-discharging areal fraction is not physical.

The slight increase beyond theoretical maximal values in measured capacitance and β for the non-conductive disks (blank, 250 shots, and 500 shots) can be understood as an "over-discharging", i.e., a moderate expansion of the plasma outside the electrode area due to the fringe fields being sufficiently strong to generate a discharge at the edge of the electrode area. This is often observed in volume DBDs with significant over-voltages [165,166]. Although strictly speaking the conventional model is no longer valid in this case, the results can still be interpreted intuitively. Indeed, when the discharge extends slightly beyond the dimensions of the electrode, a larger area of the dielectric will

charge, contributing to the measured effective dielectric capacitance ζ_{diel}. β then increases above 1, which can be interpreted qualitatively as an increase in the area of the dielectrics participating in the discharge.

However, this interpretation of the "unphysical" results is no longer true for the conductive disks (prepared with 1000 and 2000 laser shots). The increase in measured capacitance is significant, even at relatively low applied voltage amplitudes. Furthermore, images of the discharge do not indicate an increase of the plasma volume compared to the non-conductive disks.

The plasma could be observed through the window on the vacuum chamber. For qualitative visual characterization, we were able to acquire long exposure (relative to the period of the applied voltage) images using a smartphone, giving a general impression of the discharge (see Figure 5-6 and Figure 5-7). For all experiments, two distinct discharge volumes could be observed. This is in line with what is expected for atmospheric pressure Townsend discharges [148,167]. Indeed, the light emission tends to be strongest near the anode, and since the images are acquired with an exposure time well above the half period of the discharge, the plasma appears as two bright areas near the dielectrics, since every half cycle the discharge is brightest on one of the dielectrics.

Although these images are flawed due to the limited sensitivity of the camera and automatic on-device processing, they can give a general impression on the dimensions of the discharge, and may provide hints to the presence or absence of over-discharging, where the plasma extends beyond the dimensions of the electrode. In Figure 5-6 and Figure 5-7, images of the discharge are shown for the blank disk and 2000 shots disk, respectively. Note that due to variations in the exposure, focus, and processing settings of the camera, differences in color, brightness, and sharpness should be interpreted with caution. However, an estimate of the dimensions of the plasma can be made, using the bottom quartz disk as a scale bar. This analysis indicates an over-discharging of the plasma at an applied voltage amplitude of 35 kV (peak-to-peak) for the blank disk (the area of the plasma is estimated to be 1.2 times the electrode area). However, for the 2000 shots disk, the plasma appears to adhere to the dimensions of the electrode (the plasma is estimated to cover the same area as the electrode).

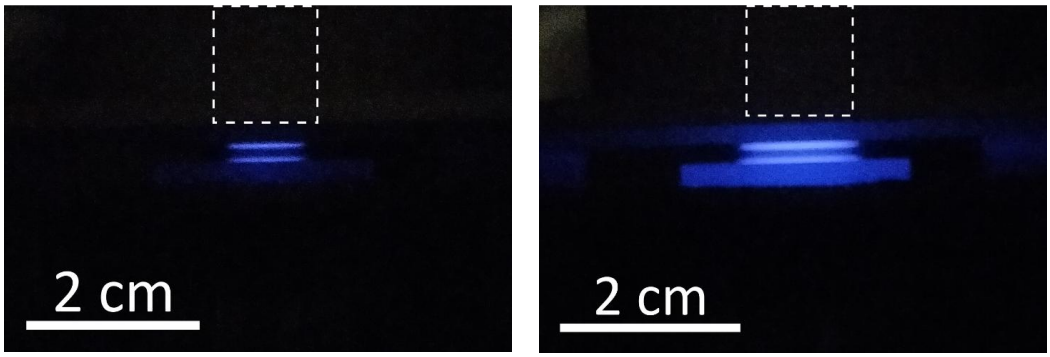

Figure 5-6: Images of the discharge with a blank disk at an applied voltage of 25 kV (left) and 35 kV (right). The dimension of the top electrode is indicated by the dashed rectangle. The discharge clearly expands when increasing the applied voltage. In addition, at an applied voltage of 35 kV, the discharge appears to extend slightly beyond the dimensions of the top electrode.

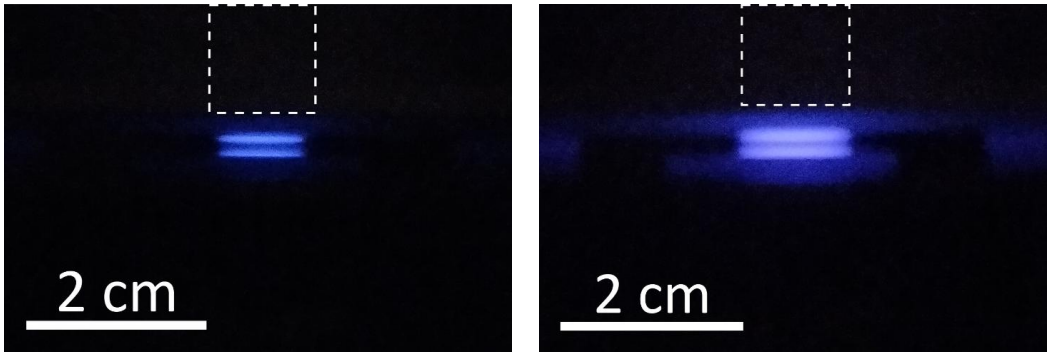

Figure 5-7: Images of the discharge with the 2000 shots disk at an applied voltage of 25 kV (left) and 35 kV (right). The dimension of the top electrode is indicated by the dashed rectangle. The discharge again expands with increasing applied voltage, but the plasma appears to remain within the dimensions of the top electrode.

4.2 Updated Equivalent Circuit

Rather than an enhanced over-discharging, the strong increase in measured effective capacitance and decrease of the threshold voltage V_{min} (illustrated in Figure 5-5 by the datapoints at lower applied voltage amplitudes) are correlated with the conductivity of the additional layer at the surface of the bottom dielectric barrier. The coated surface area is larger than the area of the top electrode. Thus, when the plasma is ignited and current flows through the gap, the charge is not just stored locally on the surface of the dielectric directly exposed to the plasma, but can be distributed across the entire coated surface. This effectively enhances the dielectric capacitance, but only when the plasma is on (i.e., when a current flows through the gap). Note that this additional capacitance

cannot be treated as a parasitic capacitance, since its presence directly affects the discharge current.

The contribution of the coating on the dielectric capacitance can be calculated theoretically, by increasing the area of the bottom dielectric to 308 mm^2 (instead of the 113 mm^2 from the top electrode). The theoretical dielectric capacitance C_{diel}^{coated} can then also be adapted, as the combination of the regular dielectric capacitance of the top electrode C_{diel}^{top}, with the increased capacitance of the bottom dielectric $C_{diel}^{bottom,coated}$ (the latter two are calculated using Equation (17), without the factor 1/2).

$$C_{diel}^{coated} = \frac{C_{diel}^{top} C_{diel}^{bottom,coated}}{C_{diel}^{top} + C_{diel}^{bottom,coated}} \tag{21}$$

This calculation yields a theoretical total dielectric capacitance including the coating C_{diel}^{coated} of 1.747 pF, notably higher than the value without coating of 1.180 pF.

As a hypothetical consideration, the cell capacitance can also be re-calculated (see Equation (19)). In Figure 5-8, this value (0.463 pF), as well as the theoretical dielectric capacitance including the coating, are now added to the same graph that was presented in Figure 5-5 A.

First of all, the data presented in Figure 5-8 show that the coated disk only affects the capacitance when the plasma is on and the charges from the discharge current are distributed. This is illustrated by the effective capacitances of the conductive disks at low applied voltages. The measured effective capacitance must always be larger than C_{cell} (or approaching C_{cell} at very low discharge currents). Thus, since the measured effective capacitances of the conductive disks at low voltage amplitudes are almost equal to the geometrical C_{cell} values (not including the coating), and below the theoretical value C_{cell} that includes the coated area, this shows that C_{cell} should not include the enhancement due to the conductive coating. This also makes sense, since the coating can only contribute to a measured capacitance by distributing charges conductively transferred through the plasma. C_{cell} is thus only determined by the geometry of the electrodes, although fringe fields may affect these values as well [168]. So, it can be stated that even when a conductive layer is present on the dielectrics, the cell capacitance C_{cell} is unaffected. This is also confirmed by the C_{cell} measurements, as illustrated in Figure 5-4.

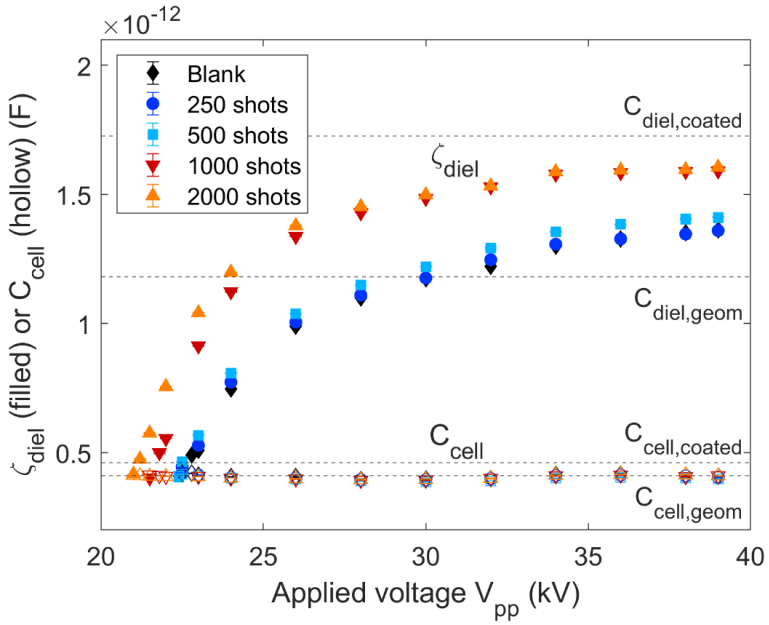

Figure 5-8: Measured effective dielectric capacitances ζ_{diel} (filled) and cell capacitances C_{cell} (hollow) for all samples at a range of applied voltages (after subtracting the parasitic capacitance). In addition to the theoretical cell and dielectric capacitances ("geom"), the ones calculated with the coating are added as well ("coated"). For the conductive coatings (1000 and 2000 shots), the theoretical dielectric capacitance that includes the coatings is a much better estimate of the true measured values, whereas the cell capacitance remains unaffected by the coating and thus the theoretical value including the coating does not seem appropriate.

A comparison of the measured effective capacitances with the theoretical values for the coated dielectric reveals a significantly improved agreement. In essence, the theoretical dielectric capacitance, including the coating, represents the upper limit for the effective dielectric capacitance.

As an additional generalization of the model, to account for possible over-discharging, the maximum measured dielectric capacitance C_{diel}^{max} can be used as the "true" dielectric capacitance of the system. This makes the equations more generally applicable, while largely maintaining its physical interpretability.

To summarize, the adapted equivalent circuit is presented in Figure 5-9 and contains the following aspects. The conductive layer enhances the dielectric capacitance, but only during the actual plasma discharge, and thus C_{cell} remains unaffected. In addition, and as a generalization of the model, the maximum measured capacitance C_{diel}^{max} can be considered as the "true" dielectric capacitance of the system. This ensures that the discharging fractions remain bound between 0 and 1. Applying this model, the

discharging and non-discharging fractions can still be calculated. However, the new circuit is mainly intended to describe the two limiting cases, namely non-discharging (α = 1), and (nearly) full discharging ($\beta \cong 1$). Indeed, then these fractions maintain their electrical interpretation, i.e., the weights of C_{cell} and C_{diel} in the measured effective dielectric capacitance ζ_{diel}, though their direct geometrical interpretation is lost. This maintained electrical interpretation is also reflected in the equation for β_{new} (note that the parasitic capacitance C_{par} is subtracted from the measured effective capacitance before this calculation is performed):

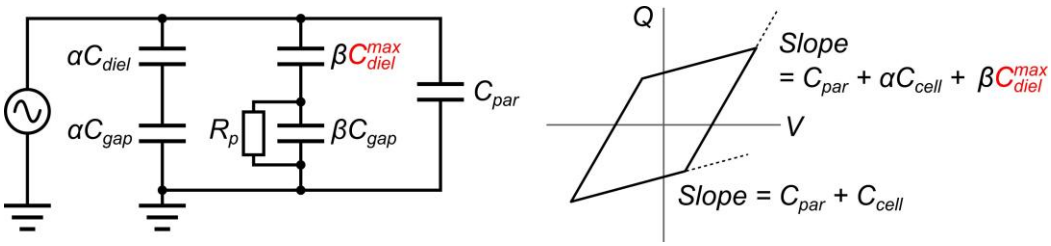

Figure 5-9: Proposed update to the equivalent circuit (left), and the corresponding interpretation of the capacitances in the voltage-charge diagram (right). Instead of using the theoretical dielectric capacitance that is based on the geometry of the reactor, the maximum measured dielectric capacitance is used in the equivalent circuit.

$$\beta_{new} = \frac{\zeta_{diel} - C_{cell}}{C_{diel}^{max} - C_{cell}} \tag{22}$$

The geometrical value of the discharging areal fraction can still be determined, which can be useful when calculating, e.g., the effective current density. For example, for a non-conductive disk, the original equation for β can be employed (see Equation (20)), using the geometrical C_{diel}, which will directly lead to a geometrical discharging areal fraction. This way, the value can exceed 1, possibly indicating some amount of over-discharging. For the conductive disks, the contribution of the bottom dielectric to the overall dielectric capacitance can be treated as a constant, having the value determined by the coated area. Indeed, regardless of the dimensions of the plasma volume, the charges can always be distributed across the entire coated area on the conductive disks. Then, the dielectric capacitance effectively contributing to the discharge (i.e., $\beta_{new} * C_{diel}^{max}$) can be interpreted as the combination of the fixed coated dielectric capacitance $C_{diel}^{bottom,coated}$, and a fraction (i.e., the new "areal fraction" β_{areal}) of the uncoated top dielectric capacitance C_{diel}^{top}. Rewriting this equation yields an expression for the effective areal fraction of the plasma when exposed to a conductive layer:

$$(\beta_{new} C_{diel}^{max})^{-1} = (C_{diel}^{bottom,coated})^{-1} + (\beta_{areal} C_{diel}^{top})^{-1} \quad (23)$$

$$\beta_{areal} = \frac{1}{C_{diel}^{top}} \frac{\beta_{new} C_{diel}^{max} C_{diel}^{bottom,coated}}{C_{diel}^{bottom,coated} - \beta_{new} C_{diel}^{max}} \quad (24)$$

The values for β_{new} are presented in Figure 5-10 (A).They are now below or equal to 1. It is noteworthy that the conductive disks reach the maximal discharging fraction at much lower voltage amplitudes compared to the non-conductive disks. This can also be observed and further understood by investigating the areal fraction, shown in Figure 5-10 (B). Indeed, the areal fraction of the non-conductive disks exceeds 1, due to some over-discharging. The increase of the areal fraction with increasing applied voltage slows down, but it appears to keep rising gently. For the conductive disks, however, no over-discharging is observed, as the areal fraction does not exceed 1. Moreover, the areal fraction appears to reach a plateau around an applied voltage amplitude of 34 kV (peak-to-peak), after which the value does not increase further. Visual observations of the plasma (see Figure 5-6 and Figure 5-7) qualitatively agree with these observations, i.e., moderate over-discharging for the blank disk, and none for the conductive ones, though these images should be interpreted with caution.

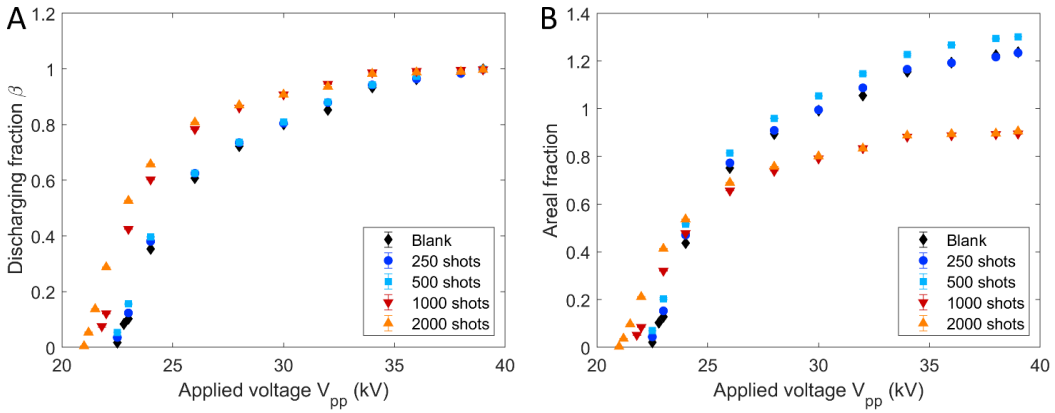

Figure 5-10: (A): Discharging fraction β, calculated with the updated circuit, which now remains bound below or equal to the theoretical upper limit of 1. (B): Areal fractions of the plasma, as calculated based on the theoretical and measured capacitances. For the non-conductive disks (blank or 250/500 shots), this value exceeds 1, indicating there could be some over-discharging, where the plasma extends beyond the dimensions of the electrode. For the conductive disks (1000/2000 shots), the areal fraction remains below 1, indicating the dimensions of the plasma remain bound by the electrode dimensions.

Based on this new, adapted equivalent circuit, the equations for other relevant metrics, such as the discharge current, gap voltage, or transferred charge, can be determined. In general, this approach requires an updated expression for the discharging fractions (see earlier), and employing the maximal measured dielectric capacitance rather than the geometrical value is necessary. However, the cell capacitance should remain the geometrical value (or when the geometry doesn't allow for accurate calculation, the measured value, though minor differences may occur due to, e.g., parasitic capacitances). In addition to the updated equations for the discharging fractions, the expressions for the discharge current $I_{discharge}$, transferred charge Q_{trans}, and gap voltage U_{gap} are now the following:

$$I_{discharge}^{new}(t) = \left(\frac{C_{diel}^{max}}{C_{diel}^{max} - C_{cell}}\right) * \left(I_{meas}(t) - (C_{cell} + C_{par}) * \frac{dV_{appl}(t)}{dt}\right) \quad (25)$$

$$Q_{trans}^{new}(t) = \left(\frac{C_{diel}^{max}}{C_{diel}^{max} - C_{cell}}\right) * \left(Q_{meas}(t) - (C_{cell} + C_{par}) * V_{appl}(t)\right) \quad (26)$$

$$U_{gap}^{new}(t) = \left(1 + \frac{\alpha_{new} * C_{cell} + C_{par}}{\beta_{new} * C_{diel}^{max}}\right) V_{appl}(t) - \frac{1}{\beta_{new} * C_{diel}^{max}} Q_{meas}(t) \quad (27)$$

With I_{meas} the measured current, Q_{meas} the measured charge on the monitoring capacitor, and V_{appl} the measured applied voltage. Note that in the original derivation of these equations by Peeters and van de Sanden [86], starting from Kirchoff's laws applied to the equivalent circuit, the relation between C_{cell}, C_{gap}, and C_{diel}, as expressed in Equation (19), is employed to determine the final expressions used. However, in our approach, this relation is more complicated, since the value for C_{cell} is determined by a C_{diel} that is different from the one used in these equations. This is motivated by the different physical interpretations in the different phases of the discharge. Therefore, it is important to understand the physical meaning of the various terms in the equations. For example, in the equation for the discharge current (Equation (25)), the capacitive current

((C_{cell} + C_{par}) * dV/dt) is subtracted from the measured current. It makes sense to use C_{cell} in this case, because the capacitive displacement current (when there is no plasma) is determined by the (de)charging of the entire cell. The scaling factor in this equation ($C_{diel}^{max}/(C_{diel}^{max} - C_{cell})$) is compensating for the energy stored in the gap by the charge on the dielectrics. Since this value is indeed affected by the altered dielectric capacitance, it is important to use the scaling factor including both C_{diel}^{max} and C_{cell}. Since transferred charge is obtained by integrating the equation for the discharge current, the same arguments remain for this formula. For determining the expression for the gap voltage U_{gap}, the above-mentioned issue with the definition of C_{cell} does not arise, and therefore the expression can readily be updated to include β_{new} and C_{diel}^{max}. Note that using a different scaling factor in the expressions for the discharge current or transferred charge (e.g., C_{gap}/C_{cell}, which would in principle be correct in the original approach) yields incorrect results, as discussed in Appendix B, Section 2, further validating this approach.

5. Results and Discussion of Discharge Characteristics

Voltage-charge diagrams as measured for the various disks are presented in Figure 5-11 A, acquired at an applied peak-to-peak voltage (V_{pp}) of 38 kV. The capacitances extracted from the voltage-charge diagrams and discussed earlier are confirmed. Indeed, the "plasma-off" sections of the voltage-charge diagrams (i.e., C_{cell} + C_{par}) are parallel for all disks. Furthermore, the "plasma-on" sections (i.e., ζ_{diel} + C_{par}) of the conductive disks are visibly more inclined compared to the non-conductive disks. An additional observation that can be made directly from the voltage-charge diagrams is regarding the plasma power. As introduced by Manley [52], the surface area of the plot represents the energy dissipated in the plasma per period. Since the frequency is constant for all experiments (1 kHz) and the plasma is operated continuously, this surface area directly relates to the plasma power P, which is larger for the conductive disks than for the non-conductive disks. The obtained values for the plasma power at various applied voltages are also presented in Figure 5-11 B.

Furthermore, based on the theory of Manley, a theoretical relation for the plasma power can be calculated (assuming full discharging, i.e., β = 1), based on the cell and dielectric capacitance, the frequency f, the minimum sustaining voltage V_{min}, and the applied voltage V_{pp} [169]. The minimum sustaining voltage V_{min} is determined from the voltage-charge diagrams as well [169], and will be discussed in more detail in this section. In this

new model, the maximal dielectric capacitance C_{diel}^{max} is used, as well as the geometrical value for C_{cell}:

$$P_{Manley} = 4fV_{min}(C_{diel}^{max} - C_{cell})(0.5 * V_{pp} - V_{min}) \quad (28)$$

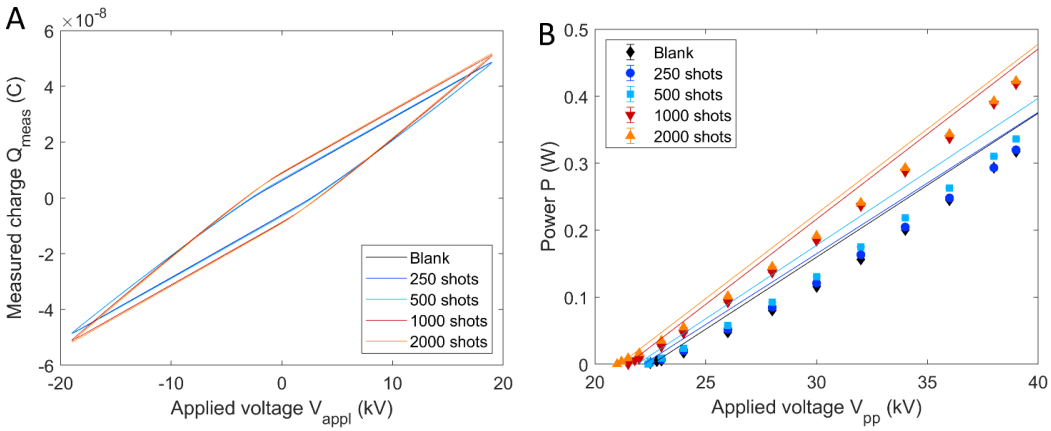

Figure 5-11: (A): Voltage-charge diagrams acquired at 38 kV (peak-to-peak) for the various disks. For the conductive disks (1000/2000 shots), the voltage-charge diagram appears larger and the steepest slopes appear stronger compared to the non-conductive disks. (B): Plasma power at various applied voltages calculated from the voltage-charge diagrams for the different disks (symbols). In addition, the theoretical expected power based on the Manley equation is plotted (lines). The plasma power is larger for the conductive disks than for the non-conductive disks, which is captured well by the Manley equation.

The experimentally determined plasma powers match closely with the calculated values, as illustrated in Figure 5-11 B. The slight overestimation of the plasma power by the Manley-equation is in line with previous observations [165], and could be due to incomplete discharging (i.e., $\beta < 1$) or a slight overestimation of V_{min}. More importantly, Equation (28) captures the difference in power between the conductive and non-conductive disks. This good agreement between the observed metrics and the theoretical values indicates that the effects of the conductive coating on the plasma discharge characteristics can be captured well by the updated equivalent circuit with the corresponding capacitances. It is also interesting to note that the difference between the conductive disks (1000 and 2000 shots), or the difference between the non-conductive disks (blank, 250, and 500 shots) is rather small. The power when using the 500 shots sample is slightly higher than for the other non-conductive disks, but overall the effect of the altered surface properties (not related to conductivity/capacitance) appears limited.

Next, the discharge current $I_{discharge}$ can be calculated. The physical interpretation of equation (25), as well as its applicability to these experiments, is illustrated in Figure 5-12. The high voltage applied to the DBD causes a current to flow through the circuit, even when there is no plasma, due to the capacitive displacement of charges. This current can be calculated by taking the derivative of the applied voltage, and multiplying it by the sum of the cell and parasitic capacitance, as also illustrated in Equation (25). This term is presented in in Figure 5-12, along with the measured current and the discharge current.

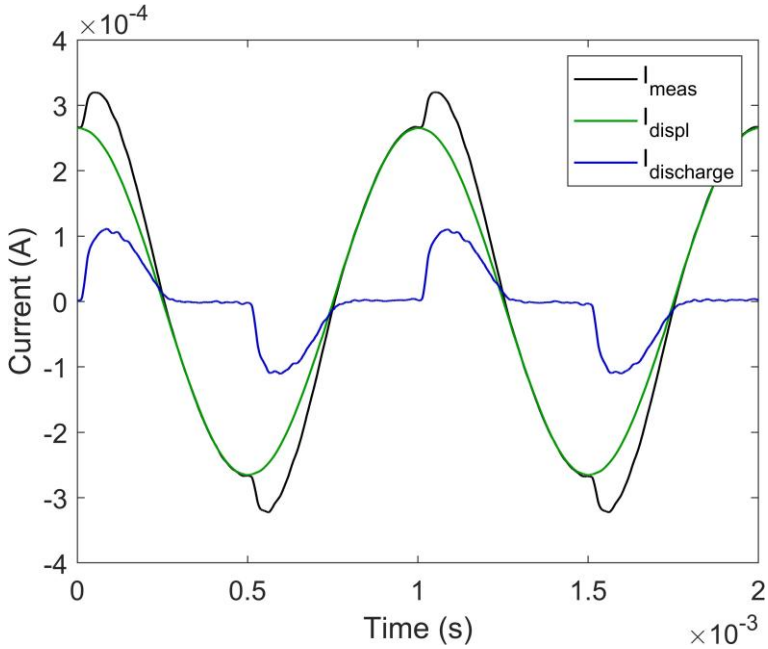

Figure 5-12: Illustration of how the discharge current $I_{disharge}$ is determined. The term in Equation (25) based on the derivative of the applied voltage is here called I_{displ}, as it represents the current that is caused by the capacitive displacement of charges due to the (varying) applied voltage. This I_{displ} is subtracted from the measured current to reveal the true discharge current (after rescaling, as indicated in Equation (25)).

The discharge current $I_{discharge}$, gap voltage U_{gap}, and transferred charge Q_{trans} as calculated with Equations (25)-(27) are presented in Figure 5-13. The discharge current is plotted for a full period at an applied voltage amplitude of 38 kV (peak-to-peak) and for the various disks in Figure 5-13 A. Here, again a clear distinction between the conductive and the non-conductive disks is obtained. When the plasma is exposed to a conductive disk, the plasma ignites at a slightly lower applied voltage, whereas the discharge current is notably higher, compared to the non-conductive disks. Again, the differences within the groups of conductive and non-conductive disks are small.

Further, the transferred charge Q_{trans} is plotted against the gap voltage U_{gap} in Figure 5-13 B, also acquired at an applied voltage amplitude of 38 kV (peak-to-peak). This plot can be understood as a "corrected" voltage-charge diagram, offering an intuitive insight in the plasma discharge [165]. Indeed, during the "plasma-off" phases (horizontal sections in this plot), there is no discharge current and thus, the transferred charge remains constant. At the same time, the gap voltage increases, until the electric field becomes sufficiently strong for a discharge to occur. At this point, the plasma-on phase starts (vertical sections in this plot), and the gap voltage remains (more or less) constant while the plasma is conductively transferring charges across the gap. The gap voltage increases slightly during the discharge, which is attributed to an expansion of the plasma, eventually discharging slightly beyond the exact electrode dimensions, thus requiring a slightly larger gap voltage.

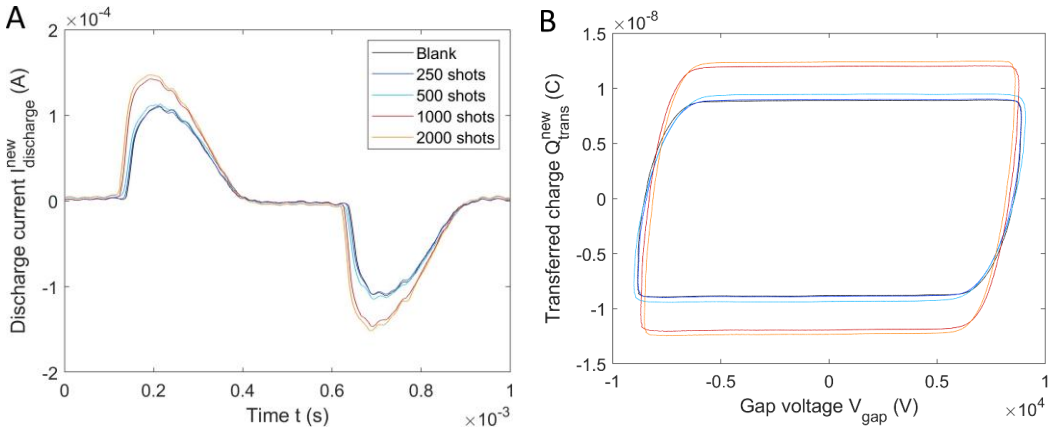

Figure 5-13: (A): Discharge current for an applied voltage amplitude of 38 kV (peak-to-peak) for the various disks. (B): Transferred charge plotted against the gap voltage at an applied voltage of 38 kV for the various disks. A clear separation between the conductive (1000/2000 shots) and the non-conductive disks is observed, where the discharge current and the transferred charge are higher for the conductive disks. The same legend applies for both panels of the figure.

The same plots, but acquired at V_{pp} = 24 kV, are presented in Figure 5-14, where indeed the vertical sections are straighter. This indicates a constant gap voltage during the discharge, likely due to a lesser expansion of the plasma with an almost uniform discharge gap. Furthermore, the signals are notably weaker (as expected due to the lower applied voltage), but the overall trends remain the same.

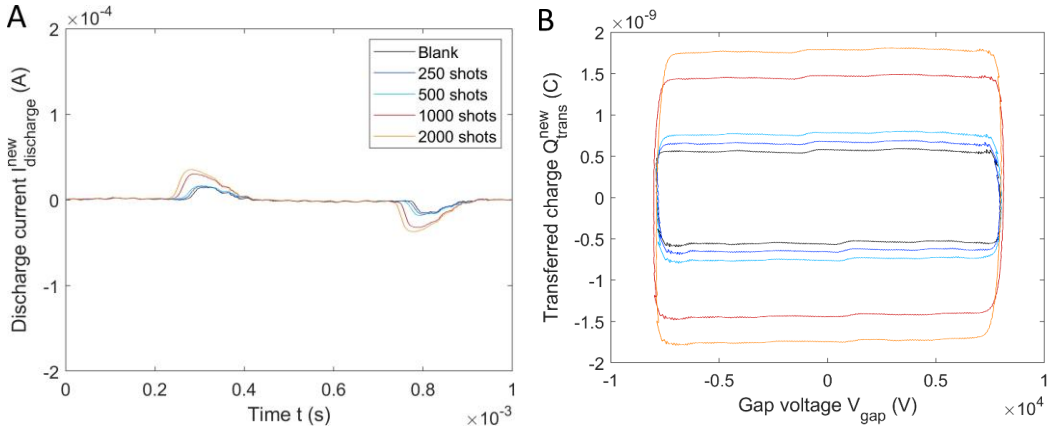

Figure 5-14: (A): Discharge current for an applied voltage of 24 kV (peak-to-peak) for the various disks. (B): Transferred charge plotted against the gap voltage at an applied voltage of 24 kV for the various disks. A clear separation between the conductive (1000/2000 shots) and the non-conductive disks is observed. The same legend applies for both panels of the figure.

In Figure 5-15, the discharge current is again presented, together with the applied voltage V_{appl}, the gap voltage U_{gap}, and the voltage across the dielectric U_{diel} (with V_{appl} = U_{gap} + U_{diel}). The different phases of the discharge are clearly described. As the applied voltage increases when there is no plasma, both the gap voltage and voltage across the dielectric increase. When the gap voltage reaches the discharge voltage, the plasma ignites and the discharge current suddenly increases. During the discharge, the gap voltage remains constant, and the voltage across the dielectric increases more rapidly. When the applied voltage reaches its maximum, the discharge extinguishes and the gap voltage decreases while the dielectric (= memory) voltage remains more stable. The discharge is symmetrical for both half periods. Qualitatively, the discharge is independent of the coating on the quartz disk, as these phases are present for all discharges.

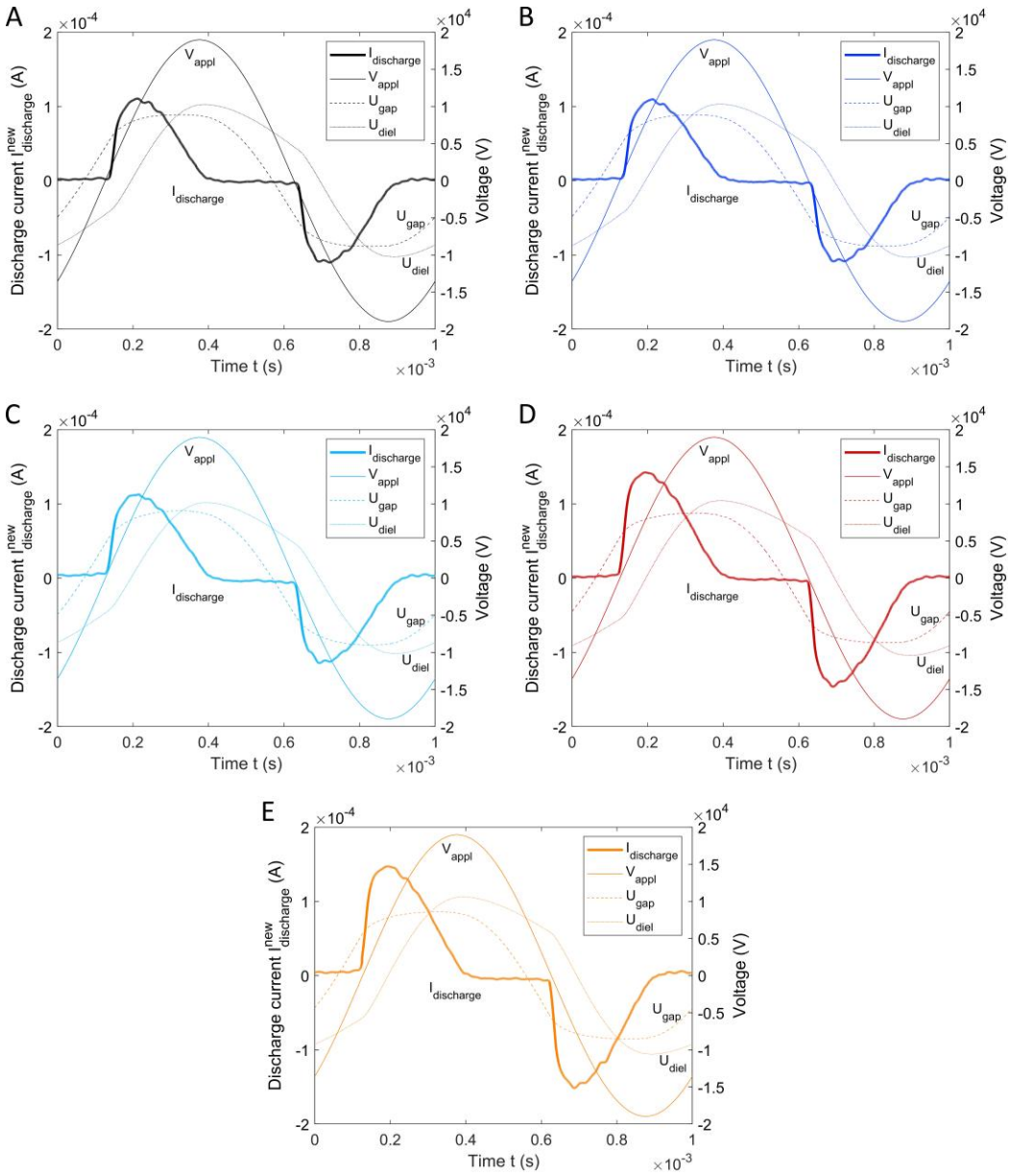

Figure 5-15: Discharge current (left y-axis), applied voltage, gap voltage, and dielectric voltage (right y-axis) for the blank disk (A), and disks with a coating by 250 shots (B), 500 shots (C), 1000 shots (D), and 2000 shots (E). Qualitatively, the discharge behavior and the presented signals all the same regardless of the used disk. The absolute values (e.g., discharge current) do vary, most notable between the conductive (D-E) and the non-conductive (A-C) disks.

These signals can be further quantified to enable objective comparisons between the different disks at various applied voltages. The peak-to-peak discharge current is plotted as a function of applied voltage in Figure 5-16, which shows the expected relation of increasing discharge current amplitude with applied voltage amplitude. As already illustrated in Figure 5-13, the conductive disks consistently show a higher discharge current amplitude compared to the non-conductive disks. Naturally, the same trend is observed for the conductively transferred charge, calculated as the peak-to-peak value of the $Q_{trans}^{new}(t)$ signal (ΔQ_{dis}), presented in Figure 5-16 B.

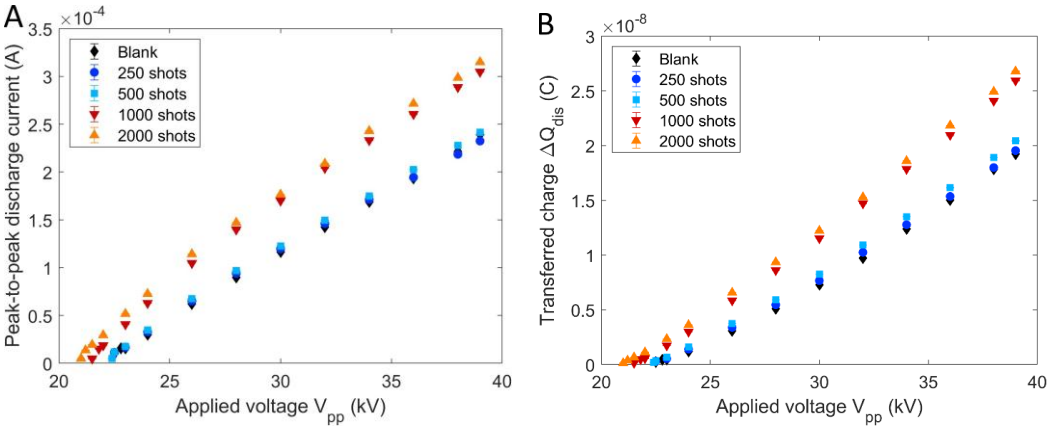

Figure 5-16: (A): Peak-to-peak discharge current and (B): Transferred charge for the different disks at various applied voltages. The conductive disks (1000/2000 shots) yield notably higher peak-to-peak discharge currents and transferred charge.

The enhanced discharge current and transferred charge for the dielectric barriers with conductive layers are related to the increased dielectric capacitance introduced by the conductive coating. Indeed, the discharge current is expected to be related to the dielectric capacitance, and thus the transferred charge will also be increased [25].

Next, the measured minimum sustaining voltage V_{min} is presented in Figure 5-17 A. This is determined by calculating the intersection between the lines fitted to the plasma-on and plasma-off sections of the voltage-charge diagrams [169]. The data at low applied voltage amplitudes should be interpreted with caution, due to their poor signal-to-noise ratio. Because of this calculation method and a somewhat gentle transition from the plasma-off to the plasma-on phase in the voltage-charge diagrams, specifically at higher applied voltages, a slight overestimation of V_{min} occurs, as illustrated in Appendix B, Section 2. Therefore, the values obtained at an applied voltage amplitude of 26 kV (peak-to-peak) were used in Equation (28), as a balance between good signal-to-noise ratio,

and limited overestimation. Interestingly, at moderate applied voltage amplitudes (V_{pp} of 24 – 30 kV), the minimum sustaining voltage drops consistently with an increasing deposition amount (i.e., number of laser shots). In this voltage range, the distinction between the conductive and non-conductive disks does not appear dominant, and a clear (albeit minor) difference between the blank and 250 shots disk is observed, contrary to most other metrics where no differences between these disks are apparent. This might be an indication that there are other surface effects influencing the plasma, enabling a discharge at lower voltages for higher deposition rates, though capacitive effects cannot be ruled out here. At higher applied voltages, this trend remains the same, though now the division between the conductive and non-conductive disks becomes more pronounced. This may be due to the over-discharging present with the non-conductive disks (but absent with the conductive disks; see Figure 5-10 B), where the effective dielectric capacitance increases during the discharge, requiring higher voltages to reach the maximal dielectric capacitance. Additionally, due to the enhanced dielectric capacitance, the true gap voltage is affected, also at a constant applied voltage.

Therefore, the discharging voltage V_{dis} (i.e., the height of the "plateau" in $U_{gap}(t)$ during the plasma-on phase) is a relevant metric to analyze, since this is based solely on the gap voltage and it is often used to determine a mean reduced electric field (E/N). These values are presented in Figure 5-17 B for the different disks. At very low applied voltages, the data should again be interpreted with caution. Although there is certainly a plasma, the signals are weak and the noise present in the signals makes them hard to interpret quantitatively. At higher applied voltages, however, the signal-to-noise ratio improves significantly and the metrics can be analyzed more unequivocally. For example, for all disks, an increase in the discharge voltage is observed with increasing applied voltage amplitude, whereas the absolute values are similar between the disks. This can again be understood through an expansion of the discharge, where the plasma bridges non-ideal gaps (i.e., regions with slightly larger gaps), thus requiring slightly higher discharge voltages. Interestingly, at the higher applied voltages, a clear separation between the conductive and non-conductive disks is apparent. The conductive disks reach a plateau in the discharge voltage, whereas the discharge voltage for the non-conductive disks keeps rising with increasing applied voltage. The lower discharge voltage for the conductive disks is also apparent in Figure 5-13 B. There is no direct explanation for this behavior based solely on the different capacitances. This may be an indication of a different mechanism enhancing the discharge ignition, for example, enhanced electron emission (whether or not secondary) from the more conductive surface.

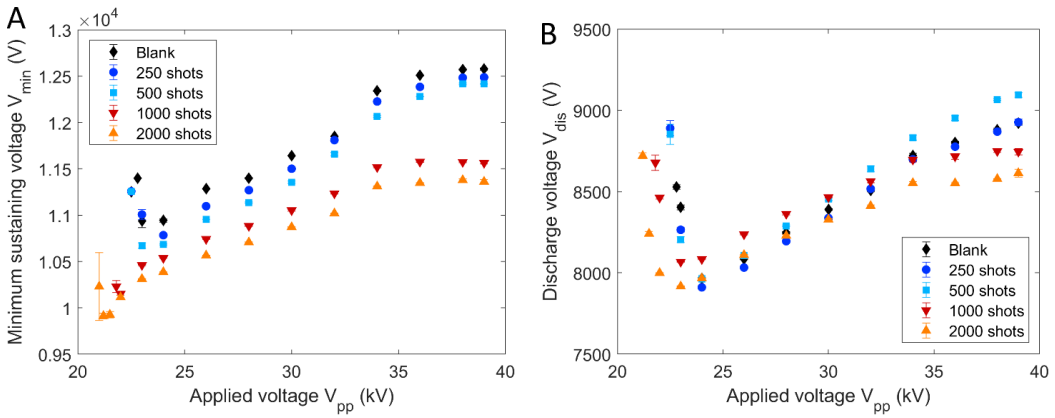

Figure 5-17: (A): Minimum sustaining voltage and (B): Discharge voltage for the different disks at various applied voltages. Note that for both figures, some outliers at very low applied voltage amplitudes are not shown to improve the clarity of the figures. The minimum sustaining voltage is notably lower for the conductive disks (1000/2000 shots) compared to the non-conductive disks, especially at higher applied voltage amplitudes. At higher applied voltage, the discharge voltage also appears to be slightly lower for the conductive disks.

The presented results further support the applicability of the updated equivalent circuit. Indeed, using the proposed equations, quantitative comparisons between the discharge characteristics for the various disks can be made. These results show a clear separation between the barriers with and without conductive layers. Interestingly, despite a difference in conductivity of three orders of magnitude, most of the discharge metrics obtained with the 1000 shots and 2000 shots disks are similar, especially compared to the non-conductive layered barriers. This implies that the effect of the conductive layer on the dielectric capacitance is dominant, confirmed by the similar measured capacitances. Although the conductivities are different, the charges can still spread uniformly across the coating, altering the capacitance, and this isn't notably affected by the enhanced conductivity of the 2000 laser shots sample. As is typical with DBDs, the capacitances of the system can drastically affect the discharge characteristics, which is also demonstrated here.

Another indication for the overall limited influence of the surface properties is the lack of asymmetry in the discharge. During the experiments and analyses, no asymmetry between the positive and negative half periods of the applied voltage were observed, whereas in certain circumstances, notable asymmetries are reported [151].

Despite the seemingly dominant effect of the capacitance, the surface properties of the dielectrics are known to play a major role in APTD formation and operation [41].

Although this influence is less obvious in these results, there are still indications that the discharge is indeed affected by the altered surface. For example, the discharge voltage V_{dis} is lower for the conductive disks compared to the non-conductive disks. In addition, contrary to most other metrics, the difference between the 1000 and 2000 laser shots is notable. This may further indicate that this effect is due to something else than (just) the altered capacitance. Furthermore, the minimum sustaining voltage V_{min} suggests that effects other than purely capacitive contribute to the discharge characteristics as well, since it decreases notably, also for the non-conductive disks. This may also explain why the plasma ignites at slightly lower applied voltage amplitudes with the conductive disks, as illustrated in Figure 5-13 A.

6. Conclusion

In this chapter, an atmospheric pressure Townsend discharge in N_2 was studied in a planar DBD arrangement. One of the dielectrics was coated with varying amounts of Fe nanoparticles by pulsed laser ablation to obtain surfaces with different, but defined surface electrical conductivities. Electrically conductive layers were obtained above a laser ablation shots threshold. When conductive, the nanoparticle coating causes the dielectric capacitance of the assembly to increase significantly when the plasma is active. The enhanced capacitance requires an update to the existing equivalent circuit. Its applicability was illustrated, and it revealed that the enhanced dielectric capacitance has a measurable effect on the discharge properties, such as the discharge current, deposited power, and amount of transferred charge. Other effects due to the altered surface properties were less obvious, though there are indications that they may also contribute. For example, at high applied voltage amplitudes, the discharge voltage appears to decrease as the conductivity of the barrier layers increases, which cannot be explained by purely capacitive effects. Rather, this could be an indication for an enhanced electron emission mechanism enabling a plasma to be formed and sustained at lower voltages.

The updated equivalent circuit and related equations can expand the applicability of the model used to analyze and interpret the electrical data from dielectric barrier discharges. This is crucial, since the electrical characterization enables a quantitative analysis of the discharge characteristics, which dominantly regulate the properties of the plasma, being relevant for most applications.

Chapter 6

In situ Plasma Studies Using a Direct Current Microplasma in a Scanning Electron Microscope

In this chapter, a setup is developed to generate a plasma inside a scanning electron microscope, enabling *in situ* characterization of a material while it is exposed to a plasma. As illustrated throughout the previous chapters, scanning electron microscopy is a powerful characterization technique, revealing crucial microscopic properties of the investigated materials. In addition, many processes in plasma systems take place at a microscopic scale, requiring diagnostics with high spatial resolution. Therefore, this system was developed and thoroughly characterized, highlighting the capabilities of such a setup and its potential value for plasma catalysis and other fields where plasmas and materials interact.

The content of this chapter is based on:

In situ Plasma Studies Using a Direct Current Microplasma in a Scanning Electron Microscope
Lukas Grünewald*, Dmitry Chezganov*, **Robin De Meyer***, Andrey Orekhov, Sandra Van Aert, Annemie Bogaerts, Sara Bals, Jo Verbeeck
Advanced Materials Technologies, 9, 2301632, 2024

* Shared first author: My contributions to this project were mainly in designing and performing the experiments, interpreting the data, and validating the results.

1. Introduction

As explained in Chapter 1, plasma is a complex and versatile state of matter with many established applications, e.g., in the semiconductor industry [11], as well as promising emerging technologies [170–172]. Many different types of plasma exist [8], but the simplest geometry consists of two electrodes separated by a gas (at low, atmospheric, or elevated pressure), with a voltage being applied between the electrodes [173]. More recently, so-called microplasmas have received a rising interest in the scientific community [174–178]. Microplasmas have at least one dimension in the sub-mm range [175]. Besides the practical aspect of reduced operation cost of microplasma setups compared to large plasma reactors for laboratory-scale experiments and a general trend toward miniaturization of devices in plasma-application areas, microplasmas also have interesting properties. For example, the large surface-to-volume ratio and short gap distances between the electrodes (typically a few 100 µm) lead to a non-equilibrium state where the ion/gas temperature is lower than the electron temperature [171], resulting in a "cold" plasma with gas temperatures close to room temperature [174–176]. These non-equilibrium plasmas show great promise, e.g., in nanomaterial and nanoparticle fabrication [171], but also for plasma catalysis, as discussed throughout this work and introduced in Chapter 1. In addition, microplasmas are not confined to vacuum operation. Paschen's law relates the breakdown voltage of a gas with the product *pd* of the pressure *p* and the gap distance *d* between two parallel electrode plates. For many gases, the smallest breakdown voltages lie in the range of 10 Pa cm to 1000 Pa cm [176]. Reducing *d* to 100 µm or less enables plasma operation at or near atmospheric pressure (p = 101 kPa).

The interaction of plasmas with flat surfaces or nanoparticles is highly relevant in the field of plasma catalysis, but is also of interest for technical applications and a better understanding of plasma physics and chemistry in general. Often, *ex situ* material characterization on the mm- to nm-scale is performed after plasma treatment of a sample. For these length scales, scanning electron microscopy (SEM) is a valuable technique, enabling microstructural and chemical investigations (typically using energy-dispersive X-ray spectroscopy, EDX), as demonstrated in Chapter 3 and Chapter 4. However, *ex situ* investigations have several limitations, as they can be labor intensive (especially when studying changes over time, and many back and forth operations are required) and the sample may change due to exposure to ambient conditions. Therefore, *in situ* characterization techniques could be highly valuable. A plasma-in-SEM setup

would not only reduce the time between plasma treatment and subsequent SEM analyses compared to a separate plasma setup, but it would also prevent exposure of the sample surface to ambient air. The latter aspect can enable studies of plasma-treated surfaces where subsequent contact with oxygen, humidity, or contamination must be avoided.

Recently, the first (micro)plasmas were generated inside SEMs [179–183]. Different approaches to generate plasmas in SEMs were demonstrated in earlier studies. For example, local sputter etching was achieved by Mulders and Trompenaars [180] by introducing a small gas nozzle into a SEM and using the electron beam for ionization. In the setup by these authors, the electron beam is scanned in a small slit in the nozzle near the orifice to generate ions in the gas stream. The generated ions flow out of the orifice with the gas flow and are then accelerated toward the sample using an applied voltage between the nozzle and the stage. Modern SEMs often have a built-in option to apply the required negative voltage to the sample stage, typically used for beam-deceleration SEM imaging [184,185]. This approach does not require reaching the breakdown voltage of the gas, hence leading to a low-energy ion bombardment of the sample. With this setup, low-energy Ar^+ ions with energies ranging from 20 eV to 500 eV were used to remove amorphous surface layers [186,187].

Massone et al. [183] investigated the effect of H-charging on the mechanical properties of a Ni-based alloy by exposing the sample to a radio frequency (RF) hydrogen plasma. However, in the presented setup, the RF plasma is generated below the sample, whereas the SEM can only investigate the top of the sample. Therefore, only bulk effects of the plasma on the material can be observed, severely limiting the applicability of this geometry.

Another plasma setup consists of a micro hollow cathode (or anode) direct current (DC) plasma configuration in an environmental SEM (ESEM) [181]. In the latter, the chamber pressure and gas type (in this case Ar) is directly controlled by the microscope, as introduced in Chapter 2. A supplied high voltage (in this case ±1 kV) generates the plasma, and the plasma-surface interaction subsequently can be analyzed within the ESEM. Depending on the electrode polarity, either redeposition of sputtered material from the counter electrode onto the sample surface, or direct sputtering of the sample surface with positive ions was observed. The sputtered area had a relatively large width of ca. 2 mm [181]. A benefit of this experimental setup is that the gas-flow controls of the ESEM are used, which reduces the requirements for the hardware modifications to

a SEM. However, a drawback is that using the low-vacuum mode reduces the image quality due to electron-beam scattering in the gas, resulting in a so-called electron-beam skirt [50,188]. This aspect impedes *in situ* SEM imaging of the plasma-sample interactions, limiting high-quality imaging to the normal high-vacuum mode of the ESEM. To optimize image quality in gaseous environments, the distance between the end of the microscope's pole piece and the sample, i.e., the gas-path length, is typically minimized to reduce the beam skirt. However, the gas-path length cannot be reduced too much for plasma experiments due to the risk of unwanted arcing to the microscope hardware. Indeed, arcing from the micro hollow cathode to the microscope hardware over a relatively large distance of approximately 25 mm was reported for this setup using the low-vacuum mode [181].

Matra et al. [179,189,190] and Tomatsu et al. [182] demonstrated a working jet-like microplasma setup inside a SEM. This approach combines the properties of a jet (enabling a comparably high pressure in the gas jet compared to its environment) with the small dimensions of a microplasma for local plasma application (typically within a few ten µm). The gas flows from a gas nozzle with a small orifice (nominal diameter of a few ten µm) toward a (flat) sample surface, whereas the chamber is continuously pumped to maintain a low overall pressure. A plasma is generated by applying a voltage, here denoted as source voltage V_S, between the nozzle and the sample, somewhat similar to a plasma reactor with two electrode plates [173]. However, the non-uniform pressure profile between the nozzle and the sample makes this plasma configuration unique, complicating the characterization of the plasma discharge. The gap distance can be adjusted by using SEM imaging for alignment. The pressure profile between the nozzle and the sample can be modified by changing the gas flow, though it will also be heavily affected by the distance between the orifice and the sample. A plasma is generated by applying at least the breakdown voltage between the nozzle and the sample (although the electron beam can be used to aid plasma ignition). Depending on the gas, material removal by Ar^+ sputtering [179] and growth of an C-rich thin film [191] on a Si surface were observed. This proof-of-principle study [179] showed that a jet-like microplasma can be generated in the evacuated SEM chamber.

However, the (desired) DC glow discharge was reported not to be fully stable, resulting in arcing to the sample [179] and a self-pulsing plasma mode for discharge currents in the range of 3 µA to 30 µA (depending on voltage, gas flow rate, and gap distance) [189]. This arcing led to strong local heating and pronounced damaged spots on the sample [179]. Furthermore, these previous studies did not investigate the possibility of "true" *in*

situ SEM imaging, i.e., live SEM imaging during plasma operation. Instead, SEM images were taken before and after the plasma-treatment steps (also in ref. [181]), or the discharge was pulsed where only the SEM signal acquired between the pulses was usable [182], which will be denoted as "quasi *in situ*" operation in this work. Still, these studies prove that a microplasma can be generated in a SEM and used for surface treatment. This provides the opportunity to observe *in situ* changes of a sample's morphology and chemistry on the mm to nm scale during plasma treatment using a SEM, ultimately leading to a better understanding of plasma-surface interactions and fundamental plasma properties.

Nevertheless, the availability of more studies is hampered by the required non-trivial modifications of a SEM and the lack of commercial solutions. In this chapter, a plasma setup built inside a modern ESEM based on the work of Matra et al. [179] is presented. This configuration consists of a DC microplasma where one of the electrodes is a nozzle with a small orifice through which gas is supplied. Whereas the geometry closely resembles that of a jet, the setup isn't technically defined as a plasma jet since the plasma is generated in the gap between the nozzle and the grounded electrode/sample [192]. A stable operation of a DC discharge without arcing is realized. Further, we present real-time *in situ* SEM imaging during plasma operation and show exemplary applications of our plasma-in-SEM setup for sputtering and local surface oxidation. Finally, experimental challenges and potential upgrades of the setup are discussed.

2. Methods

2.1 SEM Operation with the Plasma Setup

Plasma experiments were performed using an FEI Quanta 250 ESEM equipped with an Oxford Instruments X-Max EDX detector. Figure 6-1 a schematically shows the main parts of the plasma setup that was built in-house. A horizontally aligned steel nozzle with a small orifice (SS-1/8-TUBE-CAL-20, 20 µm nominal orifice diameter, Lenox Laser) is fixed opposite to a nearly vertically aligned sample surface. The sample surface is slightly tilted with an angle α of approximately 10° toward the electron beam for better SEM imaging conditions. The sample-nozzle distance ("Gap" in Figure 6-1) determines the plasma gap distance and can be adjusted by moving the sample with SEM microscope stage controls. A gas flows from the nozzle into the gap toward the sample surface. The nozzle can be biased with a DC voltage V_S in the range of −1.25 kV to 2 kV, i.e., with a positive or negative polarity relative to the sample. A ballast resistance R_B = 4.3 MΩ is

used to limit the discharge current. The discharge current $I_D = V_M/R_M$ is measured by the voltage drop V_M across a R_M = 1 kΩ resistor.

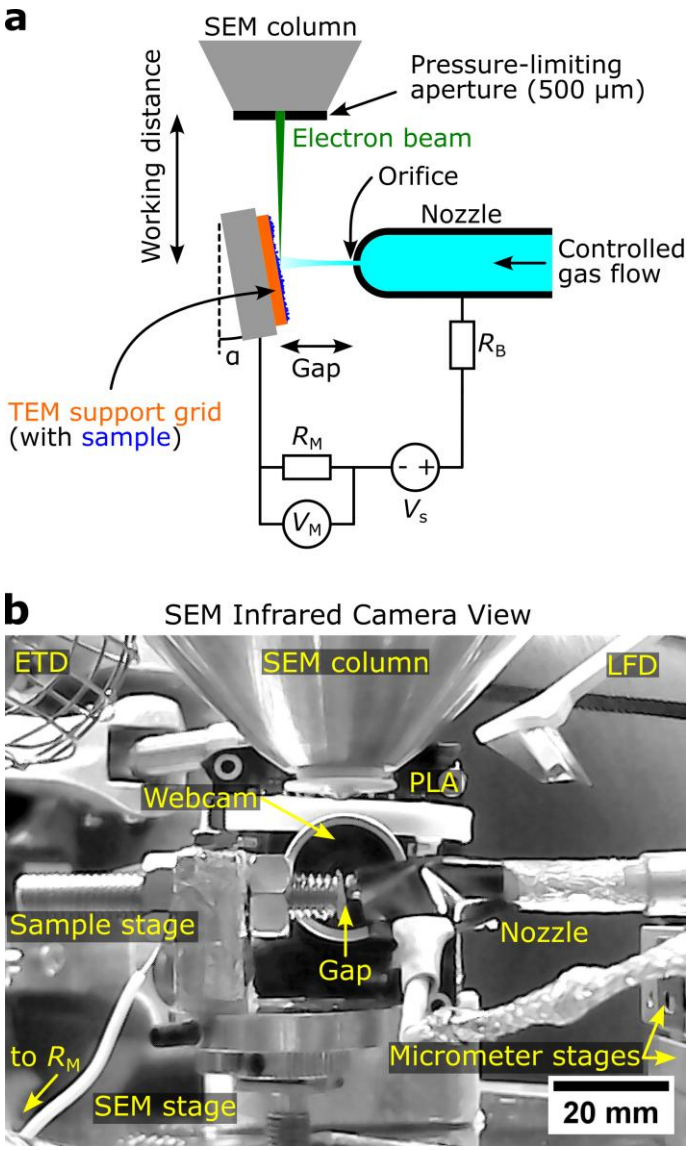

Figure 6-1: Schematic and image of the plasma-in-SEM setup. (a): Schematic showing the experimental setup and the most important components. Gas flows from a nozzle orifice over an adjustable gap distance toward a sample surface. A high voltage V_S is applied to ignite the plasma. The sample surface is slightly tilted at an angle α toward the incident electron beam, allowing for *in situ* SEM imaging. (b): Image of the setup taken with the built-in infrared camera of the SEM showing the setup. A few additional components are shown compared to (a), such as a webcam and the electron detectors, ETD and LFD.

Figure 6-1 b displays the experimental setup with an image taken with the microscope's built-in infrared (IR) camera. A few additional components compared to the schematic in Figure 6-1 a are visible, which are explained from top to bottom in the following. The Everhart-Thornley detector (ETD) and the large-field detector (LFD) are used for SEM imaging in high-vacuum and low-vacuum modes, respectively. The shown images in this work are mainly SE-SEM images. Selected BSE-SEM images are mentioned explicitly in the text. A pressure-limiting aperture (PLA) with a 500 µm diameter is mounted on the SEM pole piece to restrict gas flow into the microscope column. An IR-USB webcam (Arducam B0205) is mounted in addition to the microscope's built-in IR camera to improve imaging conditions of the plasma and control the gap distance. The sample stage consists of a threaded metal rod that is rigidly fixed with two nuts to a Teflon piece. The Teflon piece isolates the sample from the microscope stage to prevent current flow through the latter and possible damage to the microscope. Instead, the current flows via a cable to the measurement resistor R_M. The sample stage with the threaded metal rod and the Teflon block are fixed on a SEM stub, which itself is fixed on the moveable SEM stage. Two micrometer stages (Thorlabs MS3/M) are used to laterally position the nozzle close to the optical axis (below the SEM pole piece) before closing the SEM chamber. The nozzle and the webcam are mounted on a Al platform that is fixed above the moving microscope stage. The height of the Al platform can be adjusted to change the working distance between the SEM column and the sample (typically 15 mm). The gas line and electrical connections are routed through a custom-made feedthrough flange.

A detailed image of the plasma gap is shown in the webcam view in Figure 6-2. Commercially available grids or apertures made for transmission electron microscopy (TEM) with 3 mm diameter (Gilder Grids GA50 Cu apertures) were typically used as sample or sample support for nanoparticles. The sample is mounted on an Al wedge with conductive Ag paste (EM-Tec AG15). The Al wedge was ground at an angle α and fixed to the threaded metal rod's end with conductive Ag paste. The right image in Figure 6-2 shows the working setup with a glowing DC microplasma. More details regarding the experimental setup can be found in Appendix C, Section 1.

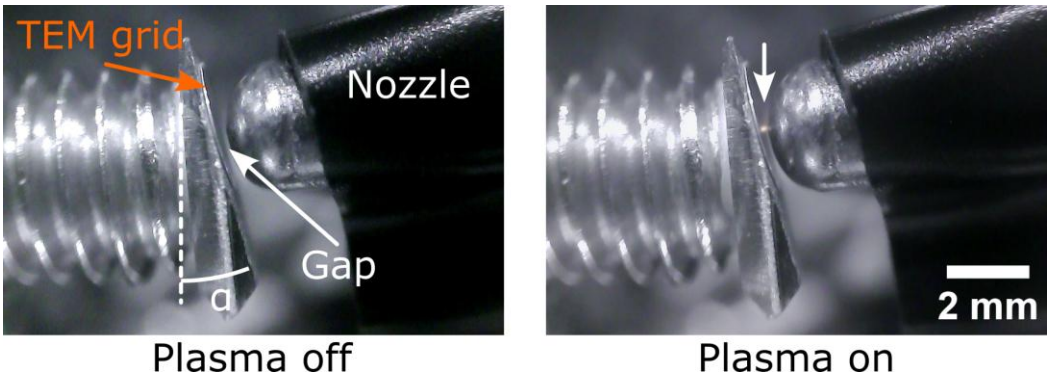

Figure 6-2: Higher-magnification side-view of the plasma region using the webcam without plasma (left) and with ignited plasma (right, the microplasma is marked with an arrow). The plasma is generated outside the nozzle, in the gap between the sample (grounded) and the nozzle.

2.2 Plasma Operation

Plasma experiments were performed in the high-vacuum mode of the microscope since undesired discharges in the SEM chamber in low-vacuum mode were observed when applying high voltage between the nozzle and the sample. The high-vacuum mode reached a stable chamber pressure of around 2×10^{-2} Pa while providing a gas flow of ca. 2 sccm (standard cubic centimeters per minute) to 8 sccm through the nozzle (20 µm nominal orifice diameter as per the manufacturer) into the microscope chamber. The gas flow was monitored using an Alicat flow meter (M-200SCCM-D/5M). We used CO_2 (purity 99.995 %), Ar (99.9999 %), and N_2 (99.9999 %) gases, and a 75 % Ar/25 % O_2 gas mixture (measured: 74.88 %/25.12 %) in this work (bought from Air Products).

The plasma was operated by applying and controlling the voltage difference on the nozzle relative to the sample. A DC-DC converter with a 1 MΩ output resistor (CA20P or CA12N depending on polarity, XP Power) was powered by an RS PRO IPS-3303 power supply. The 1 MΩ output resistor limits the output current of the DC-DC converter in standalone usage for user safety. The output resistor is in series with a 3.3 MΩ resistor, resulting in a total ballast resistance R_B = 4.3 MΩ. The output high voltage V_S of the DC-DC converter was adjusted with a control voltage between 0 V to 5 V using a Keysight E36106B power supply. After plasma ignition, the discharge current was regulated by adjusting V_S with the control voltage. Voltage-current characteristics of the plasma were measured with a Keithley 2400 source measurement unit. The highest source voltage of 2 kV was applied, after which the source voltage was gradually reduced while registering the current until no discharge current was measurable. The discharge voltage of the DC plasma V_D is calculated as $V_D = V_S - I_D (R_B + R_M)$ [173].

2.3 Sample Preparation

A Cu TEM aperture (50 µm, Gilder Grids GA50) with a diameter of 3 mm and a thickness of approximately 30 µm was used in most experiments to ensure a well-defined, flat electrode opposing the nozzle. For experiments with nanoparticles, commercial Ni particles (nanopowder, 99 % purity, Sigma-Aldrich, CAS number 7440-02-0) were mixed with acetone and then drop cast on the Cu disc. After solvent evaporation, a thin layer of Ni particles is left on the Cu surface. Drop casting was repeated multiple times until the TEM aperture was fully covered with Ni particles.

3. Results and Discussion

The first part of this section presents results related to the microplasma and *in situ* SEM imaging. The second part discusses some exemplary results when applying the microplasma to materials. Finally, the third part reviews the limitations of this setup and proposes potential solutions to overcome these limitations.

3.1 Microplasma Characterization

The physical properties of the microplasma setup and operation are discussed. First, the gas flow from the nozzle to the sample is studied. Next, the electrical characteristics of the plasma are investigated, after which the practical operation of the plasma inside the SEM is discussed.

3.1.1 Gas-Pressure Profile

The used plasma setup has a non-uniform gas pressure along the plasma gap. The gas density profile can be visualized by SEM imaging (Figure 6-3 a) by using a low primary electron energy (here 2 keV) to increase the electron-scattering probability and secondary electron (SE) generation within the gas cloud [193]. As a result, the SE-SEM image presumably shows higher intensity in regions with higher gas densities (Figure 6-3 a). Here, the gas cloud in Figure 6-3 a flows into the microscope vacuum without obstruction. The contrast variations in the background result from out-of-focus imaging of the sample stage a few mm below the nozzle along the electron-beam direction. The gas density is highest close to the orifice and gradually decreases away from it. This monotonic decrease is in accordance with calculated gas density profiles of restricted gas flows, e.g., in references [194–196]. More explicitly, Salehi et al. [197] report an exponential decay of the gas density away from an orifice from a simulation of gas jets for different pressure differences between the inside of the nozzle and the chamber.

Experimental measurements of the pressure gradient away from the nozzle by Patel et al. [198] reveal a continuous pressure decrease away from the nozzle for a distance of approximately 20 orifice diameters (in their experiment ca. 20 mm for a 0.8 mm orifice diameter), which would correspond to a continuous pressure decrease away from the orifice of ca. 400 µm for a nominal 20 µm orifice diameter. From comparison with these results, we suspect a monotonic decrease in gas density and pressure across the microplasma gap in our experimental setup.

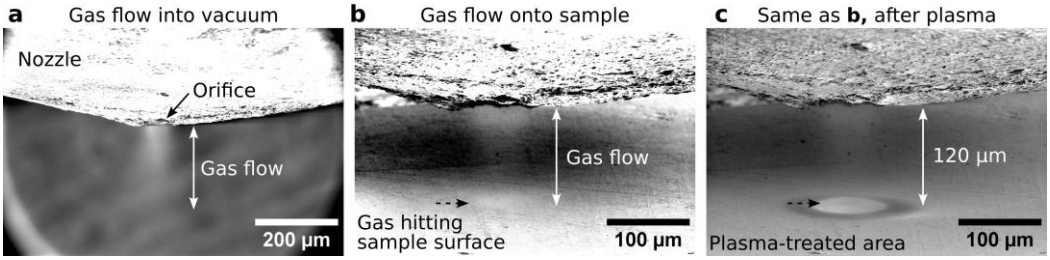

Figure 6-3: Investigation of the gas density profile in the plasma gap. (a): SE-SEM image of the gas flow into vacuum acquired with a primary electron energy of 2 keV. (b): A spot with a slightly increased SE signal is visible on the sample surface (marked with a dashed arrow) when a sample is brought into proximity, probably due to an increased gas density when the gas jet hits the sample surface. (c): After plasma treatment, the bright spot coincides with the plasma-treated region, indicating that the gas spot in (b) can be used for aiming the microplasma at the desired region of interest.

However, if the gap distance is reduced by bringing the sample close to the orifice (here ca. 120 µm), an increase in SE signal is visible on the sample surface as well (Figure 6-3 b, dashed arrow). The increased SE signal at the sample indicates an increased gas density at the sample surface. From these observations, it becomes clear that the gas density profile in the gap also depends, among other parameters, on the gap distance. This non-uniform gas pressure impedes predictions and comparison with conventional plasma reactors with a constant pressure between the electrodes. As a beneficial side aspect, the visible gas spot on the sample surface can be used to predict the plasma-spot region. This can be seen by comparing the images before and after plasma operation in Figure 6-3 b and c, respectively, where the pit due to plasma sputtering forms in the region predicted in Figure 6-3 b.

3.1.2 Voltage-Current Characteristics of the Plasma

Next, the voltage-current characteristics (i.e., the dependence of discharge voltage V_D and discharge current I_D) of a N_2 microplasma were investigated for three gap distances (75 µm, 100 µm, and 125 µm) and three gas flow rates (2.5 sccm, 5.0 sccm, and 7.5 sccm). Nitrogen was chosen over Ar because it resulted in lower chamber pressures for the same gas flow rate, allowing for higher gas flow rates (up to 8 sccm) into the high-vacuum microscope chamber. The pumping speed of different gases is discussed in more detail in Appendix C, Section 1. For each gas-flow/gap-distance pair, two measurements were taken for repeatability (here denoted in the brackets in the figure legends). Figure 6-4 a–c show the values sorted with decreasing gap distance from left to right. The same axis limits were used for easier comparison.

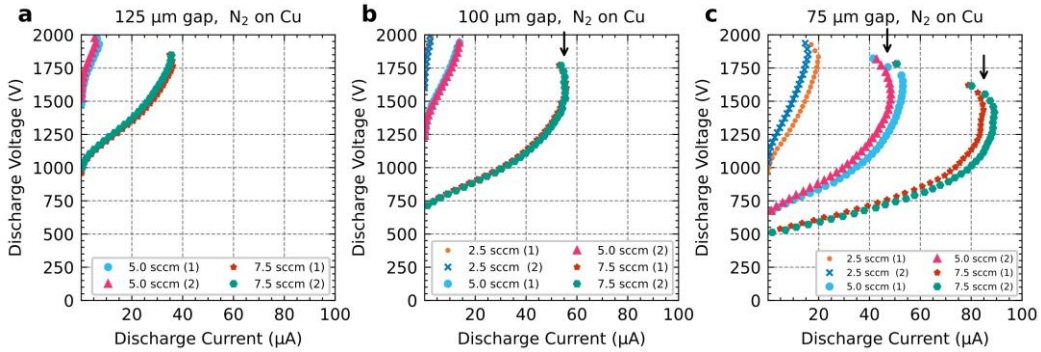

Figure 6-4: Voltage-current characteristics of a N_2 microplasma for different gas flow rates and gap distances. All axis limits are equal for easier comparison. The data is shown for decreasing gap distance from left to right. Two measurements were performed for each gas flow rate and gap distance. No discharge was observed for 125 µm/2.5 sccm. Slight deviations between these measurements are mainly caused by uncertainties in gap distance. The apparent drop in current for higher voltages (marked with arrows in (b) and (c)) is a measurement artifact caused by sample-surface sputtering or heating. In general, larger discharge currents are observed for higher gas flow rates and smaller gap distances. A positive slope for all curves indicates a so-called abnormal glow discharge behavior.

In general, a positive slope is visible for all curves, indicative of a so-called abnormal glow discharge plasma [173]. This was also observed by Matra et al. [189], but not in all of their measurements. After this initial positive increase of discharge current with discharge voltage, nearly all curves show a maximum current followed by a current decrease (cf. arrows in Figure 6-4 b and c). The last aspect is a measurement artifact, probably caused by rapid sputtering or heating of the electrode, and should not be interpreted as an actual voltage-current characteristic of the microplasma. This artifact is discussed in more detail in Appendix C, Section 2.

Next, the ordinate intercepts of the curves in Figure 6-4 are discussed. These points correspond to the lowest discharge voltage at which a plasma discharge can be sustained. Note that this isn't equal to the breakdown voltage, as the voltage required to initiate a breakdown is often (significantly) higher than the voltage required to sustain one [8]. The actual breakdown voltages were not measured since our setup does not produce the necessary uniform gas pressure for a given gap distance for a controlled measurement [199]. Figure 6-4 a–c show a decreasing minimum discharge voltage for increasing gas flow rates for the same gap distance. Since an increase in gas flow rate for a constant gap distance is assumed to result in an increasing gas density, this decreasing minimum discharge voltage offers an interesting insight into the plasma discharge. As described by the Paschen curve for simple parallel-plate and uniform-pressure DC plasma systems, an increased pressure heavily affects the discharge properties.

On the one hand, if the gas density is higher than the optimum (i.e., the point with the lowest minimum discharge voltage, similar to the minimum in the Paschen curve), the electrons undergo many collisions, which limit their possibility to gain enough energy to ionize a molecule. This ionization is required to create an avalanche effect, which is needed to sustain a discharge. In this case, a higher voltage is required to sustain the discharge to ensure the electrons can gain sufficient energy to cause subsequent ionization.

On the other hand, if the gas density is lower than the optimum, the electrons can easily gain sufficient energy, but they may not collide frequently enough to cause the further ionization required to sustain the discharge. Then, again, a higher voltage is required to ensure that the collisions will cause ionization. As the minimum voltage required to sustain a discharge decreases with increasing gas density, it is implied that the gas density is lower than the optimal case overall. This is analogous to being on the left side of the minimum in the Paschen curve. It should be noted, though, that given the strong pressure gradient in this setup, the discharge mechanisms are not as straightforward as they are assumed by the Paschen curve, so a direct comparison is difficult. This behavior of the minimum discharge voltage implies that the plasma could be categorized as a so-called obstructed abnormal glow discharge [8,173]. When comparing the curves for the same gas flow rate and different gap distances in Figure 6-4 a-c, both the gas density and the gap distance are varied since the former is affected by the latter. Assuming that the gas density at a constant gas flow rate increases for a decreasing gap distance, the changes in minimum discharge voltage in Figure 6-4 a-c indicate that the gas density is increasing non-linearly (in contrast to linearly decreasing distance) and more substantial

than the gap distance. An additional complication affecting the interpretation of the data is the setup geometry. The shown setup with a rounded nozzle with an orifice as one electrode and a possibly textured sample surface as another electrode is different from earlier publications studying various electrode geometries [199–202]. Microplasmas are especially sensitive to surface effects due to the small spatial scale in the sub-mm range, as the electric field can be strongly altered by small morphological changes in the electrode surfaces [202]. In addition, due to the high pressure-gradient, it is impossible to accurately control the pressure in the discharge gap using this setup.

3.1.3 Plasma Generation and Stability in a SEM

The plasma-in-SEM setup enables studying the interplay between the electron beam of the SEM and the plasma. Different aspects of this interaction are discussed in the following.

Firstly, an electron beam can be used to ignite the plasma at lower voltages than required for the self-ignition when reaching the breakdown voltage [179] (Figure 6-5 a). For example, in one case a plasma discharge could not be achieved, even when applying a maximum source voltage V_S = 2 kV to the nozzle without an electron beam. However, scanning with the electron beam caused a plasma discharge already at V_S = 920 V for the same gap distance and gas flow rate. This can be explained by the generation of SE, backscattered electrons (BSE), and X-rays upon the interaction of the electron beam with the sample, which then triggers the plasma ignition. Notably, the electron beam ignites the plasma even if not directly scanning in the gap region. No changes in plasma discharge current or plasma behavior were observed between the electron beam scanning inside or outside the central plasma-spot region, i.e., the plasma was unaffected by the exact electron-beam position during discharge. This shows that the generated signals (SE, BSE, X-rays) serve as the ionization source for the plasma. However, small effects may still be present and could be below the detection limit of our setup. For example, sample sputtering during plasma operation led to continuous changes in discharge current which might overshadow small changes in plasma behavior when the electron beam is scanning the plasma cloud.

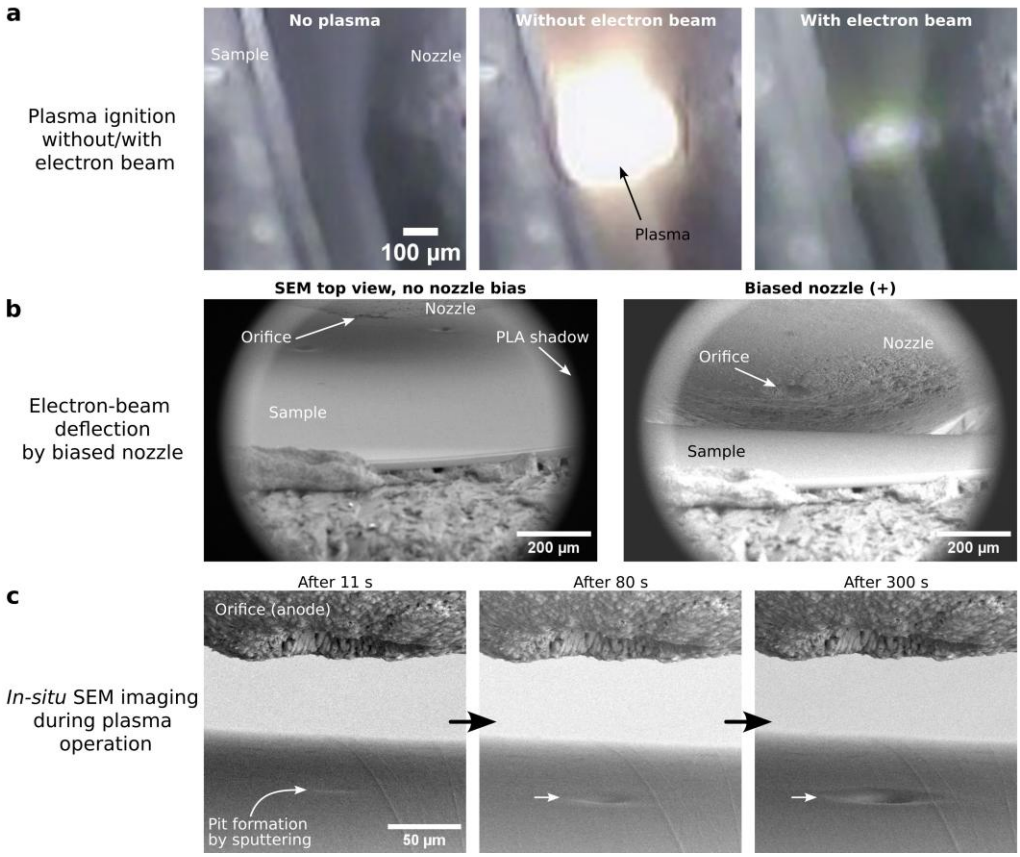

Figure 6-5: Aspects of microplasma operation in a scanning electron microscope. (a): Webcam images of plasma operation. The electron beam can be used to ignite the plasma at a lower applied source voltage to generate a less intense plasma (right) compared to self-ignition by reaching the breakdown voltage (middle). The shown plasma images correspond to the plasma conditions right after plasma ignition. (b): Top-view SE-SEM images (10 keV) of the nozzle and sample (left) without and (right) with applied voltage on the nozzle (V_S = 920 V). In this example, the electrons are attracted to the positive potential on the nozzle, which enables imaging of the orifice area. (c): True *in situ* SE-SEM imaging during plasma operation is possible and shows the formation of a pit in the sample due to sputtering.

A webcam video comparing plasma ignition by reaching breakdown voltage (the conventional way), or by using the electron beam is found in the supplementary information of [203] (Breakdown-vs-SEM-Plasma.mp4). In this video, the SEM-triggered plasma shows a less intense plasma cloud than the self-ignited plasma. Therefore, the electron beam can be advantageously employed to ignite a less intense plasma at lower voltages (also illustrated in the middle and right images in Figure 6-5 a). In addition, for conditions where a plasma is not self-sustainable, i.e., with a large gap distance and/or low gas flow rate, a plasma discharge was observed that was only active during active

electron-beam scanning (see Appendix C, Section 2). Secondly, applying an electric potential to the nozzle will create an electric field that deflects the incoming electron beam, e.g., toward the positive potential on the nozzle (Figure 6-5 b). The deflection depends on the electron energy (less deflection for higher keV) and possibly also on the extent of the exposed metal part of the steel nozzle. In our setup, insulating tape was used to cover most of the steel nozzle, excluding the tip (see black tape in Figure 6-1 and Figure 6-2). The deflection may be minimized by shielding the open metallic surface of the nozzle tip and using a higher primary electron energy. However, the deflection can also be used advantageously. For example, the deflection can be strong enough so that the SE-SEM image is formed from the nozzle-tip surface, e.g., at V_S = 920 V for a primary beam energy of 10 keV (Figure 6-5 b, right). In this way, the tip region of the nozzle can be imaged with the SEM even though it is aligned parallel to the electron beam, i.e., without a direct line of sight. This effect is more pronounced at lower electron energies. A movie in the supplementary information of [203] (SEM Plasma Ignition.mp4) shows correlative imaging of the webcam and SEM images during a gradual increase in the source voltage V_S and subsequent SEM-induced plasma ignition. The SEM image is increasingly "tilted" toward the nozzle with increasing V_S.

Thirdly, it was observed that *in situ* SEM imaging during plasma operation is indeed possible, opening up the opportunity for time-resolved studies. In SE-SEM imaging, a working plasma leads to an increase in signal (brightness) using the ETD. For imaging, this effect can be compensated by reducing the ETD bias setting. For a CO_2 plasma, this method proved effective for discharge currents up to ca. 7 µA, after which the ETD was saturated (i.e., no further reduction in bias possible), and no SE-SEM imaging was possible. It is remarkable that *in situ* SE-SEM imaging during plasma operation is feasible, despite several challenges. Indeed, the total electron-beam current used (few nA) is approximately a thousand times lower than the measured discharge current (few µA), many spurious SE are likely generated in the plasma region [8,173], and the positive suction voltage on the ETD of 250 V to attract SE is comparatively low compared to the nozzle voltage (typically >1 kV). A potential explanation for why SE-SEM imaging is possible during plasma operation, is that it may have BSE contributing as well. The BSE generated at the sample are highly energetic and can therefore escape the potential between the nozzle and the sample more easily. As these energetic BSE then strike a surface inside the SEM chamber, they generate additional SE (so-called SE_3 [50]), enabling the visualization of the sample, even when operating the detector in SE-mode.

Three SE-SEM images taken during continuous microplasma operation are shown in Figure 6-5 c. The plasma duration increases from left to right, leading to increasing pit diameter and depth due to surface sputtering. The most notable distortion in the SE-SEM image is caused by the applied nozzle voltage, resulting in an electron-beam deflection (Figure 6-5 b). Similarly, BSE-SEM imaging was tested by negatively biasing the ETD with −150 V to suppress (mainly) SE from the image signal. In contrast to SE-SEM imaging, the BSE-SEM image brightness is not affected by the discharge current during plasma operation, meaning that BSE-SEM imaging is still possible even when the SE signal becomes saturated at high discharge currents (e.g., >7 µA for CO_2). A video comparing BSE- and SE-SEM imaging is found in the supplementary information of [203] (*In-situ*-SEM SEvs-BSE.mp4). Since the ETD covers only a relatively small solid angle, it is inefficient for BSE detection. This results in a lower signal yield than for SE-SEM imaging. However, the low BSE signal may be increased by using a more efficient and low-vacuum compatible BSE detector [204,205], but this was not tested in this work. Since both SE- and BSE-SEM imaging is possible and similar to conventional SEM imaging, the signals can be chosen depending on the experiment, or both signals can be collected with two different detectors. This enables more surface-sensitive imaging with SE and Z-dependent imaging with BSE [50]. Overall, these results demonstrate that *in situ* SEM imaging during plasma treatment is possible, which opens the possibility for time-resolved *in situ* studies. The quality of SEM imaging during plasma treatment is hampered by beam deflection and additional SE signal from the plasma, but these aspects may be improved. For cases where highest spatial resolution of the SEM is required, intermittent switching between SEM imaging and plasma treatment can alternatively be applied so that SEM imaging is not deteriorated by the plasma cloud and the applied voltage on the electrodes.

An application-relevant observation from the demonstrated setup is the absence of undesired high-current and high-frequency discharges, which were reported by Matra et al. [189] as a self-pulsating plasma mode. Instead, we observed stable DC glow discharges with discharge currents ranging from 0.1 µA to 175 µA, which can be controlled by adjusting V_S. This corresponds to current densities ranging from 5 mA cm^{-2} to 9 A cm^{-2} for an assumed plasma-spot diameter of 50 µm. The latter can vary depending on the gap distance. We did not investigate higher currents than 175 µA since the 30 µm thick Cu target is sputtered away in a few (ten) seconds at the plasma spot. Conversely, the plasma could not be sustained below the lower limit of approximately 0.1 µA.

The absence of arcing may be explained by the lower chamber pressure in our used SEM (ca. 2×10^{-2} Pa) compared to the reported values "below 1 Pa" [189]. Notably, a self-pulsing plasma was observed for the shown setup when powering it in ambient air during prototyping. The high-frequency arcing in this self-pulsing mode (a few ten kHz) causes significant electromagnetic interference to surrounding electronic devices, including the SEM. In addition, powering the setup in the low-vacuum mode of the SEM at a chamber pressure of 40 Pa leads to undesired discharges in the SEM chamber, similarly as observed by Pardinas [181]. This restricts the plasma operation to the high-vacuum mode (below 3.3×10^{-2} Pa for the used SEM). Here, only occasional higher current discharges during plasma operation were observed when non-flat samples with surface protrusions were used. It may be possible to fully mitigate the self-pulsing plasma mode by an optimal choice of electronic components in the circuit. Still, in our case, the reduced chamber pressure (ca. 2 × 10−2 Pa) is the most likely reason for a stable DC plasma operation compared to Matra et al. [189]. The reduction of arcing in our setup is an important step toward better control and optimization of the plasma conditions for plasma-in-SEM studies.

3.2 Microplasma Applications

The effect of the plasma on the sample is discussed next. On the one hand, physical effects on the morphology of the sample are described. On the other hand, chemical changes in the sample due to exposure to the plasma are observed.

3.2.1 Sputtering and Cone Formation

Sputtering is the process of removing atoms of the target material by impinging ions. Sample material was removed by this process in all experiments where the sample was used as the cathode. The positively charged ions are accelerated toward the cathode and cause sputtering, as is common in glow discharges. This results in changes in surface morphology in the plasma-spot regions, with diameters ranging from 50 µm to 150 µm (depending on the gap distance, pressure, discharge voltage/current, and plasma duration). In the following, results for sputtering on a polished or a Ni nanoparticle covered Cu surface are shown.

The formation of a pit under CO_2 and Ar-containing plasma was observed for a polished Cu surface. An example is shown in Figure 6-6 a, which was created with Ar plasma. Experimentally, this pit formed after 1.2 keV Ar exposure with a discharge current of ca. 15 µA (current density of 1.2 A cm^{-2} for a plasma-spot pit diameter of 40 µm) for approximately 10 s. The rapid pit formation is indicative of the high sputter rates of the

setup. The pit surfaces are rougher than the original polished surface. A comparably small conical structure is visible at the edge of the pit, which is magnified in Figure 6-6 b. This may have been an impurity or other contamination present in or on the Cu surface, which deformed to the shown conical structure during sputtering. Its bright appearance in the SE-SEM images may be explained by the penetration depth of primary electrons, here at an energy of 15 keV. For relatively thin structures such as the shown impurity in Figure 6-6 b, SE are emitted not only on the entrance surface of the beam but also on the exit surface of the cone (and also the sample material behind the cone). The additional SE emission from the exit surface (relative to the incoming electron-beam direction) leads to higher SE-SEM image intensity for thinner sample regions.

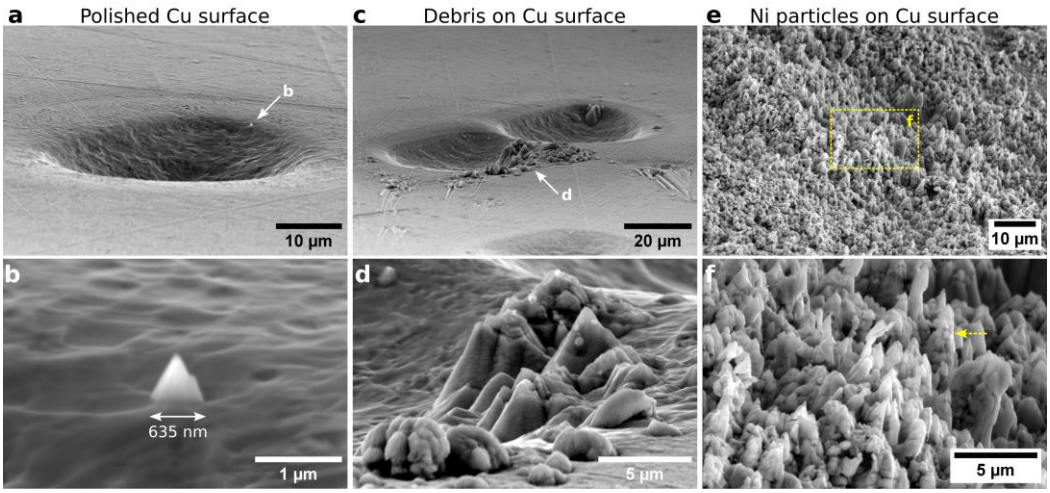

Figure 6-6: Cone formation after Ar^+-ion sputtering for different concentrations of surface particles. The lower row shows higher magnification SEM images of the upper row. (a): Cone formation is not visible in the shown region of a polished Cu surface. A small cone is visible on the edge (b), probably due to a small contaminating particle on the sample surface. (c, d): Debris on the Cu surface forms cones under plasma treatment. (e): Ni particles deposited on a Cu substrate show clear cone formation in the plasma-treated region. In the early stages of sputtering, the Ni particles locally agglomerate to form a cone (see the example in (f) marked with a dashed arrow).

Cone formation is observed for random debris (Figure 6-6 c and d) or full coverage with Ni nanoparticles (Figure 6-6 e and f). For the latter, the nanoparticles seem first to cluster together (see region marked with an arrow in Figure 6-6 f) and then tend toward a conical shape during prolonged sputtering. The latter aspect was studied in more detail by monitoring the same area after a certain plasma duration with SEM imaging (Figure 6-7). Between each plasma treatment, the sample area was moved onto the optical axis of the SEM to allow for high-magnification imaging.

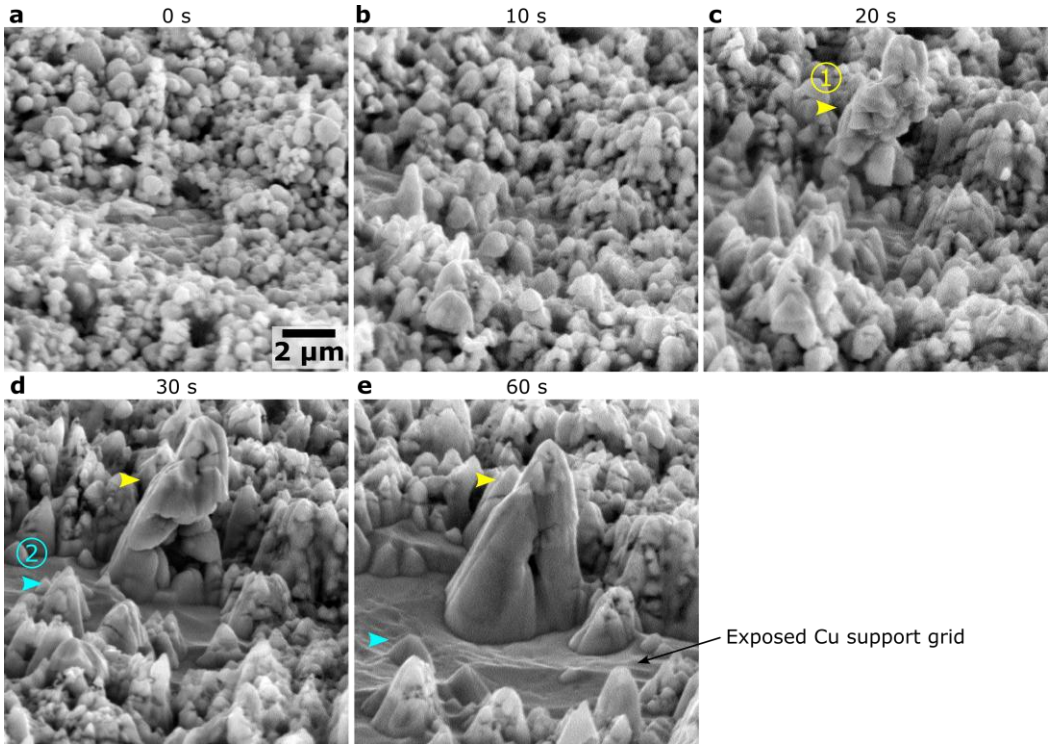

Figure 6-7: Quasi *in situ* observation of Ni nanoparticle agglomeration and subsequent cone formation during Ar^+-ion sputtering (5 µA, 1.32 keV) for the given duration shown above the SE-SEM images. The images were acquired using the LFD in the low-vacuum mode (40 Pa) after each plasma operation in high-vacuum mode. Already after 10 seconds, originally spherical particles are starting to become conical. The region indicated by arrow (1) shows the sudden agglomeration of a few nanoparticles in (c). A larger cone is forming from this agglomeration (d, e). Region (2) exemplifies that, after initial formation, the cones are sputtered away under further Ar^+-ion bombardment (d, e).

Figure 6-7 shows the shape evolution of Ni particles under Ar plasma. Between 0 s to 30 s, the shape gradually changes from round nanoparticles (Figure 6-7 a) toward a conical shape (Figure 6-7 d). After reaching the final conical shape, the cones are gradually removed during further sputtering. For region (1), a few Ni nanoparticles agglomerate between 10 s to 20 s. It is unclear from the images if these particular particles result from the present particles in the shown region or were redeposited from remote sample areas. Further plasma exposure leads to a merging of the individual nanoparticles and the formation of a larger cone with smooth surfaces (region (1) for Figure 6-7 d and e). Overall, after 60 s, the underlying Cu surface is partly exposed (Figure 6-7 e). Similarly, region (2) shows the removal of smaller cones between 30 s to 60 s of sputtering.

The observed formation of cones is a commonly observed modification of metal surfaces under ion bombardment [206–208]. The cone shape is commonly thought of as a combined result of varying sputter yield depending on the ion-incidence angle and material. The sputter yield typically increases with increasing ion-incidence angle up until a maximum value, and then decreases rapidly toward grazing incidence (i.e., the ion direction being parallel to the sample surface) [207]. This results in a cone shape of impurities and surface particles before complete removal by sputtering. The seeds for the cones can be intrinsic elemental impurities in an otherwise flat surface or particles on the surface with lower sputter yield. The latter correlates with the melting temperature of a material. Wehner [208] has tested numerous surface/seed combinations of metals with different melting temperatures and found that cone formation requires seed materials with higher melting temperatures than the surface material. This is the case for Ni particles (T_{melt} = 1728 K) on a Cu substrate (T_{melt} = 1358 K) observed in Figure 6-7. Note that the used nanoparticles are large enough (around 100 nm) so that a reduction in melting points is assumed to be negligible [209,210].

3.2.2 Local Oxidation

Plasma finds applications in both the oxidation and reduction of materials [120,211]. Here, we investigate the possibilities of local plasma-induced sample oxidation in the SEM. As a first example, a polished Cu surface was exposed to a CO_2 plasma (Figure 6-8). The gap distance was approximately 130 µm (Figure 6-8 a). In Figure 6-8 a, a sputtered hole from a previous experiment is visible in the top right corner, and the nozzle is visible in the bottom right corner. The applied source voltage was V_S = 2 kV and discharge currents between 70 µA to 120 µA were measured. After 10 s of plasma operation, Figure 6-8 b, a pit starts forming with a diameter of approximately 70 µm. Elemental analysis by EDX shows increased Cu and decreased O signals in the pit region, indicating a removal of the native Cu oxide by sputtering. This exposes the underlying Cu metal, leading to a higher Cu Lα signal. After 50 s, the pit is widened to approximately 100 µm diameter (Figure 6-8 c). The sputtered pit area still shows a higher Cu signal than the unaffected Cu surface around it, similar to Figure 6-8 b. The reduction in Cu Lα signal in the top part of the Cu elemental map in Figure 6-8 c results from shadowing of the generated Cu Lα signal X-rays from the inside of the pit toward the EDX detector. An increase in O Kα signal is visible at the pit's edge (Figure 6-8 c). This observation indicates the oxidation of Cu in this region. The O signal increases under prolonged CO_2-plasma exposure (not shown here), which we attribute to the continuous growth of this Cu-oxide layer.

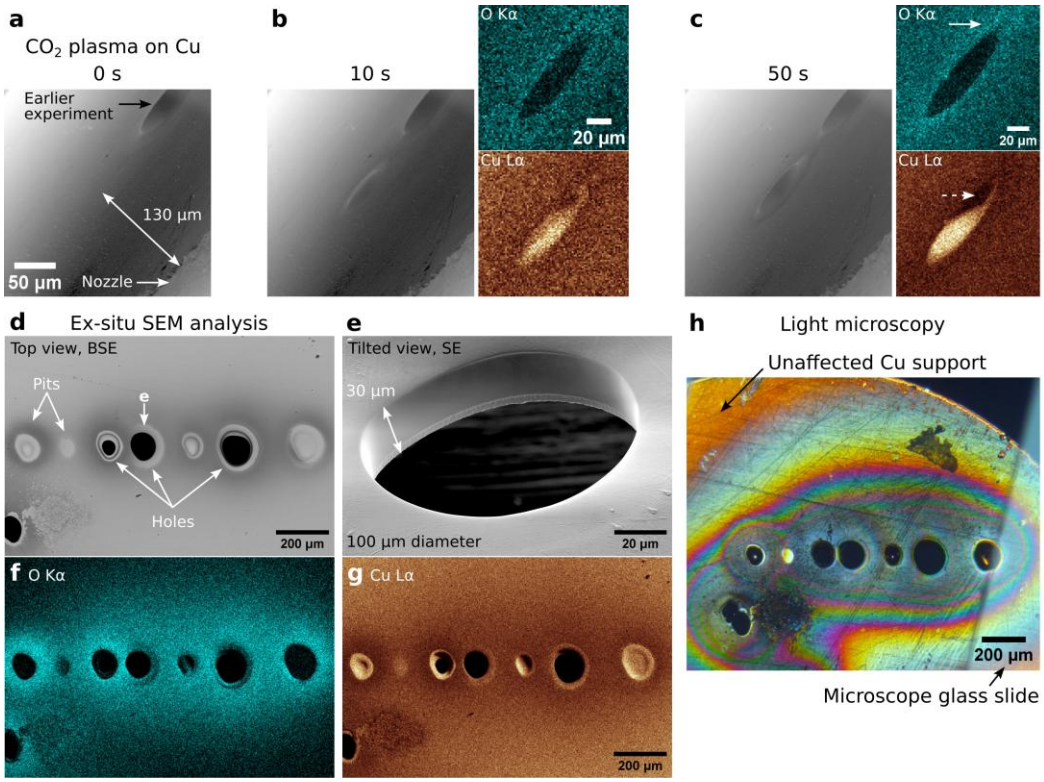

Figure 6-8: Sputtering and oxidation of a polished Cu surface under CO_2 plasma. (a): SE-SEM image showing the sample surface opposite to the nozzle with a 130 µm gap. The hole in the top-right corner is from an earlier experiment. (b, c): Images and O/Cu elemental maps after 10 s and 50 s plasma treatment. A pit forms due to sputtering. A higher Cu signal in the pit indicates the removal of the native oxide in the plasma spot. (c): Enhanced O signal is visible at the pit's edge (marked with a solid arrow). The depletion of Cu signal is due to the shadowing of the X-ray signal toward the detector. (d): Top-view BSE-SEM image of various pits and holes in the Cu foil after plasma treatment. (e): Side-view SE-SEM image of a hole showing vertical side walls. (f, g): The elemental maps reveal enhanced oxidation around the plasma spots and higher Cu signal in the pits similar to (b, c). (h): Light-microscopy image showing interference effects in the oxidized regions around the plasma spots.

After the *in situ* experiments, the sample was investigated again in the SEM and using light microscopy (Figure 6-8 d–h). The top-view BSE-SEM image acquired at 20 keV shows different experimental sites of local CO_2 plasma treatment (Figure 6-8 d). The black areas show regions where the total thickness (ca. 30 µm) of the Cu support was sputtered away, leaving holes behind. One of the holes is also displayed in the SE-SEM image in Figure 6-8 e. The tilted view reveals the high aspect ratio of the sputtering process, resulting in vertical sidewalls. The elemental map of O shows an increased O signal around the plasma spots, similar to Figure 6-8 c, which is decreasing in radial direction away from the spots. For the pits, the removal of the native oxide layer of Cu leads to an

increased Cu Lα signal. The increased O concentration around the holes reduces the effective atomic number relative to metallic Cu. This results in a reduced BSE intensity in Figure 6-8 d in the oxidized regions due to the BSE signal's atomic number Z dependence [50]. Interestingly, the oxidation of the Cu surface reaches a few hundred µm away from the initial plasma spots. This phenomenon is more clearly visible in the light-microscopy image (Figure 6-8 h), which shows interference effects related to the gradually changing thickness of the grown Cu-oxide film (Newton rings). In the top left corner of the image, there is an unaffected (i.e., without plasma-induced oxidation) area of the sample (marked with an arrow in Figure 6-8 h). Overall, the polished Cu surface is sputtered away under CO_2 plasma. A local CO_2 plasma causes oxidation around the plasma spot, probably forming a Cu-oxide film with decreasing thickness away from the plasma spot. This oxidation is most likely caused by oxygen species (such as atomic or ionized O) generated in the plasma. These species can be transported out of the plasma (so-called afterglow) by the gas flow, explaining why the oxidation of the Cu is observed away from the plasma spot as well. However, the sample temperature was not measured in our experiments and local sample heating with CO_2 flow might also contribute to Cu oxidation.

Next, similar experiments with CO_2 plasma on Ni nanoparticles were performed (Figure 6-9 a, left column). The Ni particles were deposited on a Cu support film and formed a layer with a (varying) thickness of a few µm (Figure 6-6 e). The gap distance was 250 µm, and the discharge current was 5 µA. Local oxidation was observed inside the plasma spot, as marked by the arrow in the elemental map acquired after 10 s plasma exposure. The O signal increases with increasing plasma duration from 0 s to 60 s. This aspect is not as evident in the noisy elemental maps but more clearly visible in the summed-up and normalized EDX spectra from the plasma-spot region as an increasing O Kα peak, presented in Figure 6-9 b, left. More details on this method are provided in Appendix C, Section 3. This observation is different from the oxidation outside the plasma spots observed for a flat Cu sample (Figure 6-8). This may be caused by a more pronounced sputtering of Cu compared to Ni, where any oxidized Cu in the central plasma spot is immediately removed by ion bombardment. In addition, the ion dose applied to the Ni nanoparticles (Figure 6-9, 5 µA) was lower than for bare Cu (Figure 6-8, 70 µA to 120 µA), resulting in more sputtering for the latter. In addition to the reduced sputtering effects, many other aspects can affect the oxidation rate and it is not fully clear from our experiments what exactly causes the observed differences between flat Cu and Ni nanoparticles. One aspect is the differences in surface morphology (flat Cu surface vs.

rounded Ni nanoparticles) affecting the oxidation rates [212]. In addition, considering a possible heating of the sample during plasma, Cu typically oxidizes at lower temperatures than Ni [212], even though nanoparticles oxidize at lower temperatures than a bulk material [213,214]. For the lower discharge current of 5 µA and the Ni nanoparticles, the local sample heating for oxidation might be only high enough in the central plasma-spot area. In contrast, for Cu and 50 µA to 70 µA discharge current, the stronger heating (and maybe a better heat transfer for flat Cu bulk compared to Ni nanoparticles) may result in a sufficiently high sample temperature for oxidation outside of the central plasma spot. Furthermore, the amount of reactive species (e.g., atomic O) formed inside the plasma will also be higher in the higher-current experiments, which may also contribute to the more extensive oxidation. Plasma-induced oxidation is another aspect, which is likely different for a flat Cu surface [215,216] and Ni nanoparticles. In plasma-based oxidation, many parameters affect the oxidation rate (pressure, ion energy, incident angle, plasma temperature, ionization degree, exposed facets, ...), further complicating a detailed comparison between the observed differences in Cu and Ni oxidation. Overall, a clear explanation is not possible based on our experimental results.

Besides oxidation, the sputtering during CO_2 plasma changed the morphology of the Ni particles inside the plasma spot from round shapes toward conical shapes, as discussed earlier (Figure 6-6). Overall, the EDX signals for Ni and Cu (from the underlying substrate) are nearly unchanged for CO_2 plasma for this ion dose (Figure 6-9 b, right).

Besides using CO_2, oxidation and sputtering of Ni nanoparticles was also studied for a 25 % O_2 -75 % Ar gas mixture (denoted as Ar/O_2 in the following). The plasma parameters were kept the same as for CO_2 (gap distance of 250 µm and an approximate discharge current of 5 µA). The oxidation of the Ni particles by Ar/O_2 plasma is similar to CO_2 plasma; the oxidation is localized to the plasma region (Figure 6-9 a, right column), and the oxidation gradually increases with plasma duration (see O Kα signal in Figure 6-9 c, left). It is noteworthy, that the oxygen-rich spot at 0 s in Figure 6-9 a for Ar/O_2 (marked with a dashed arrow) results from a previous experiment. Overall, the sputter rate of Ni particles for Ar/O_2 plasma is higher than for CO_2. The enhanced sputter yield for Ar/O_2 plasma is evident from the change in Ni and Cu Kα signals in the right plot in Figure 6-9 c, where the Ni/Cu signal decreases/increases due to the continuous removal of Ni particles and subsequent exposure of the underlying Cu support. This aspect is also slightly visible as a reduction of O signal in the central part of the plasma spot in the O elemental map after 60 s (Figure 6-9 a). After the removal of the oxidized Ni particles in

this area, the underlying Cu support is not oxidized inside the plasma-spot region, leading to the observed O depletion (in line with O maps in Figure 6-8 f).

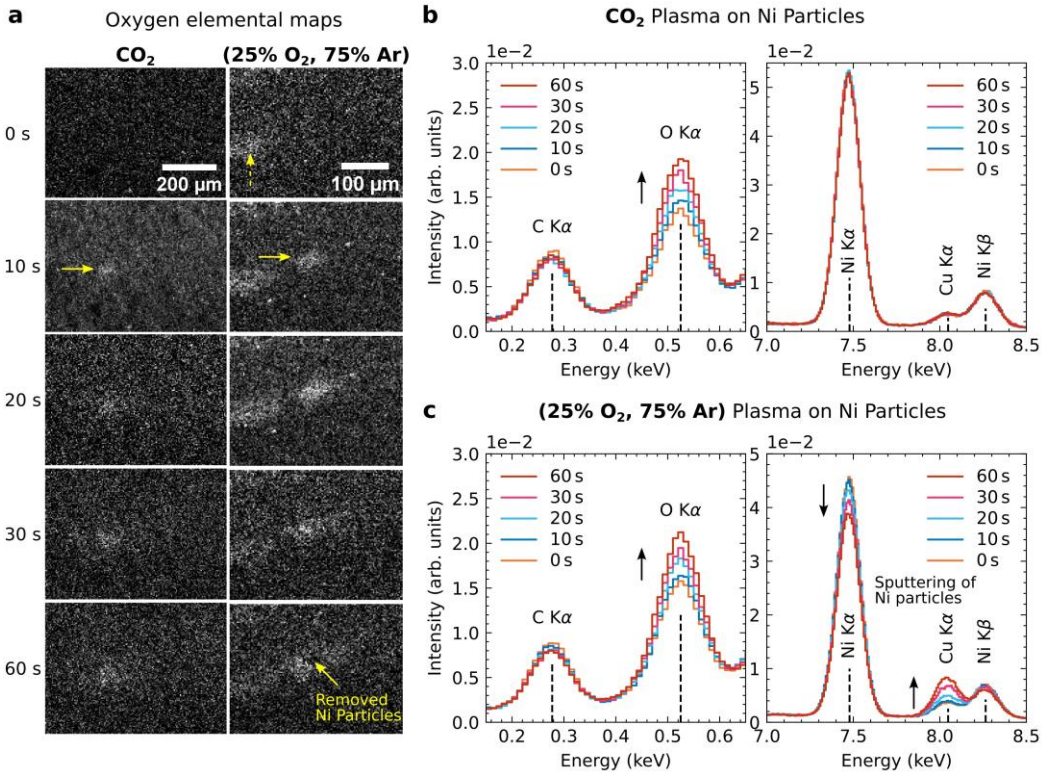

Figure 6-9: Local oxidation of Ni particles under CO_2 and O_2/Ar plasma treatment. (a): Elemental maps showing the O Kα intensity for increasing plasma duration between 0 s to 60 s (top to bottom) for CO_2 plasma (left column) and O_2/Ar plasma (right column) for similar discharge current (ca. 5 µA) and gap distance (ca. 250 µm). A spot of local oxidation is visible after 10 s (marked with horizontal arrows). The O-rich spot at 0 s for O_2/Ar is from a previous experiment (dashed vertical arrow). (b, c): Comparison of extracted EDX signals in selected energy region for the O (left), and Ni and Cu energy regions (right). The increase in O signal for increasing plasma duration is visible. (c): For O_2/Ar plasma, sputtering of Ni particles and subsequent exposition of the underlying Cu support reduces the Ni Kα signal and increases the Cu Kα signal. This effect is absent in (b), indicating a significantly reduced sputter yield for CO_2 plasma. For comparison, the EDX spectra in (b, c) were normalized to the integrated signals in the energy intervals [2 keV, 5 keV] and [10 keV, 14 keV] containing only bremsstrahlung background signal.

Since the sputtering is primarily caused by the bombardment of the grounded sample surface (relative to a positively biased nozzle) with positively charged ions, switching the polarity between the nozzle and the sample can mitigate sputtering. This aspect was verified experimentally by switching the polarity upon using another DC-DC converter (XP Power, CA12N) than the previously used one (XP Power, CA20P). The experiment

was then repeated using again CO_2 gas and a Cu target. The experimental setup is shown in Figure 6-10 a with the EDX acquisition area marked with a dashed line. The polarity between the nozzle and the sample is reversed compared to all other conducted measurements in this chapter. Comparison of the O elemental maps before and after plasma treatment (Figure 6-10 b) reveals a pronounced oxidation of the surface in a comparatively wide area (ca. 400 µm diameter), i.e., larger than the actual plasma spot. The latter is not clearly visible in the highly tilted view onto the Cu target's surface in Figure 6-10 b, but it is visible in the top-view BSE-SEM image in Figure 6-10 c. This BSE-SEM image was captured during the investigation of the same sample after the plasma experiments using standard SEM imaging parameters. The top-view BSE-SEM image in Figure 6-10 c reveals the plasma spot with a higher image intensity relative to the surrounding dark area related to the oxidized Cu surface. Note that a low primary electron energy of 5 keV was used for BSE imaging to increase surface sensitivity. Based on the increasing BSE-SEM image intensity away from the plasma-spot region toward the unaffected Cu surface, Figure 6-10 c, the O signal seems to gradually decrease away from the central plasma spot. This gradient in O signal is not clearly visible in the O elemental map in Figure 6-10 b due to the highly tilted sample setup, but can be seen in top-view EDX analysis (see Figure 6-12). The increased BSE image intensity of the bright plasma spot (Figure 6-10 c) can be explained by mild sputtering in this region by negatively charged ions bombarding the positively charged Cu surface. This removes the oxide layer and reveals metallic Cu, ultimately leading to higher BSE image intensity due to a higher average Z than the surrounding oxidized Cu surface. Even though mild sputtering is present, no large pit or hole is visible in the plasma-spot region (Figure 6-10 d and e) compared to the initially used negative sample polarity (Figure 6-8 d). The plasma spot area has a diameter of ca. 25 µm (qualitatively marked with a dashed circle in Figure 6-10 d) and shows the formation of small pits with 200 nm to 300 nm (surface) diameter (Figure 6-10 e). The pit shape was confirmed by additional SEM imaging of the tilted sample for better visibility of the topography (not shown here). Note that the dashed circle only qualitatively shows the plasma-spot region as a guide for the eye. Small pits can also be observed outside of the marked region in Figure 6-10 d but with a lower number density. These pits are likely caused by the sputtering process and may show its initial stage. Overall, the sputtering of the sample surface is highly reduced when the sample surface is positively biased relative to the nozzle.

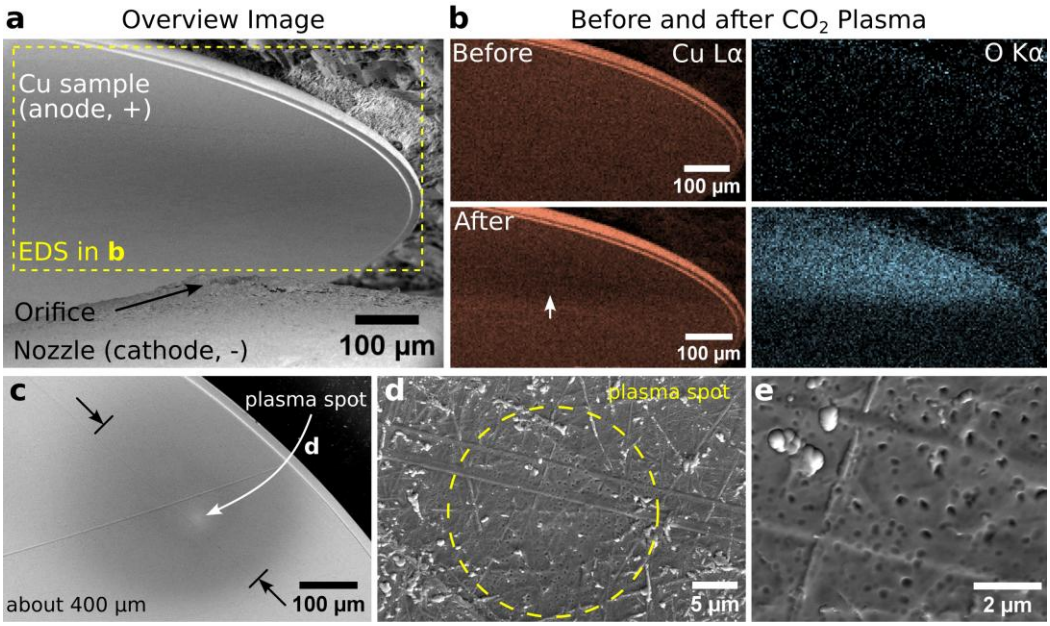

Figure 6-10: Local oxidation of a polished Cu surface under CO_2 plasma treatment with reversed electrode polarity. (a): Overview SEM image of the plasma gap with the EDX region for (b) marked with a dashed rectangle. Note the reversed nozzle/sample polarities. (b): Quasi *in situ* EDX measurements before (upper row) and after (lower row) CO_2 plasma treatment. The increased O signal is caused by oxidation and re-deposition of oxidized Cu from the nozzle. (c): BSE-SEM image (5 keV) of the plasma treated after plasma experiments. (d): Higher magnification SE-SEM image of the central plasma spot (qualitatively marked by the dashed circle). (e): Pits formed in the central plasma spot, probably caused by sputtering.

In the configuration shown in Figure 6-10 a, the mainly positively charged ions are accelerated toward the negatively biased nozzle, resulting in sputtering of the nozzle surface. Therefore, the nozzle was characterized before use, after use as the anode, and after using the nozzle as the cathode. These results are summarized in Figure 6-11. The unused, fresh nozzle in the left column of Figure 6-11 shows some contamination near the orifice (Figure 6-11 d), but the inner walls of the laser-cut orifice are well-defined. The outer diameter is approximately 87 µm, which is substantially larger than the nominal 20 µm. Since the measured gas flow rate was close to the nominal value, we suspect that the orifice diameter gets gradually smaller toward the inside of the nozzle. The EDX elemental map of Fe Kα resulting from the steel nozzle is used to show the absence of debris (Figure 6-11 g). The lack of signal from the lower left corner of the EDX map is caused by shadowing effects toward the EDX detector (no direct line of sight for emerging X-rays).

When the nozzle is used as an anode with a positive bias, most of the positively charged ions are hitting the sample surface, and the sputtered material is redeposited on the nozzle tip. Since mostly Cu apertures were used as sample material, a pronounced Cu Kα signal is visible around the orifice (Figure 6-11 h). The deposited material reduces the outer diameter of the orifice (here to ca. 80 µm).

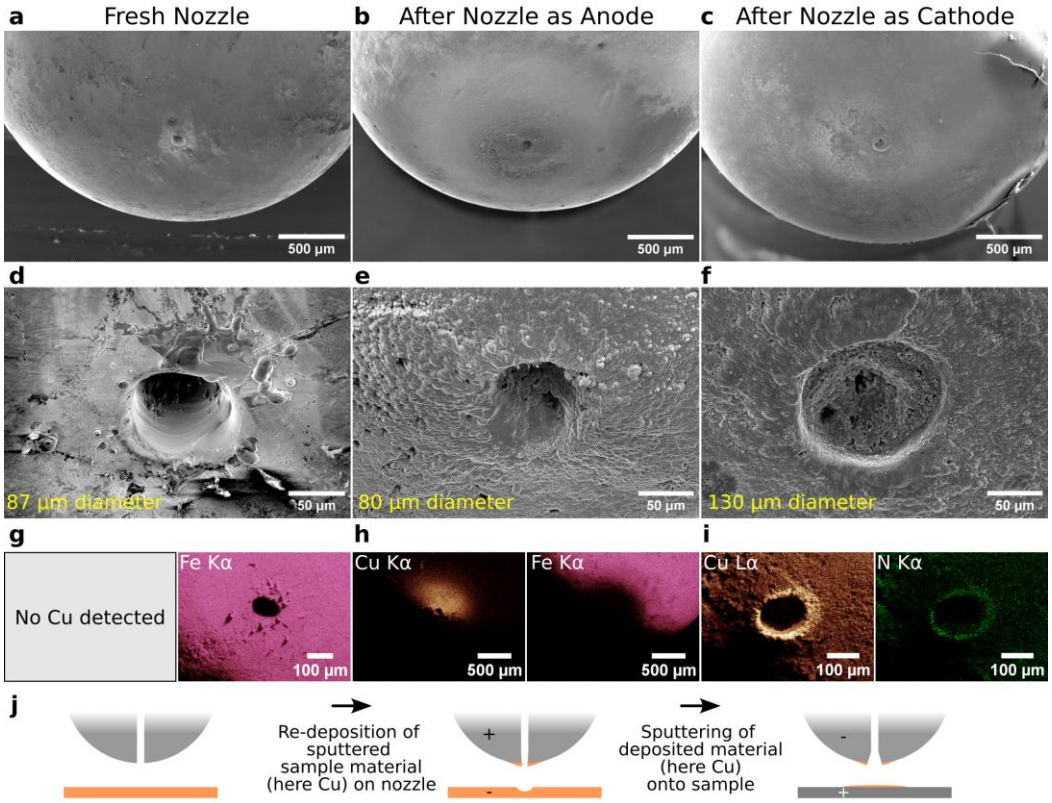

Figure 6-11: Low magnification (upper row) and high magnification (middle row) SEM images of the fresh (left column, below (a)) nozzle and after it was used as anode (middle column, below (b)) and cathode (right column, below (c)). EDX maps of the orifice are shown in the lower middle row starting from (g). Note that the absence of X-ray signals from the lower left corner in the maps is caused by the shadowing of X-rays by the nozzle. Fe signal stems from the steel nozzle, Cu and N signals from material redeposition/sputtering. The last row depicts the situation of the nozzle when used as an anode or a cathode.

Afterward, the nozzle was used as a cathode and the ions are now mostly bombarding the nozzle instead of the sample. Sputtering of the orifice region leads to the removal of the previously-deposited Cu. The sputtered Cu is now deposited on the sample instead. The orifice is widened after sputtering (here ca. 130 µm diameter) and filled with redeposited material. The EDX maps reveal a higher signal for Cu at the orifice edges,

probably due to pronounced sputtering, which may have removed the native or CO_2 - plasma-induced Cu oxide. Since N_2 was mostly used as a gas with the nozzle as a cathode, N is implanted at the orifice edge. The lower row (Figure 6-11 j) schematically shows the described deposition/removal of material on the nozzle depending on its polarity.

To confirm the redeposition of material from the nozzle when it is used as the cathode, the gas was switched from CO_2 to N_2. Still, the plasma-treated area showed a N and O signal, illustrated in Figure 6-12.

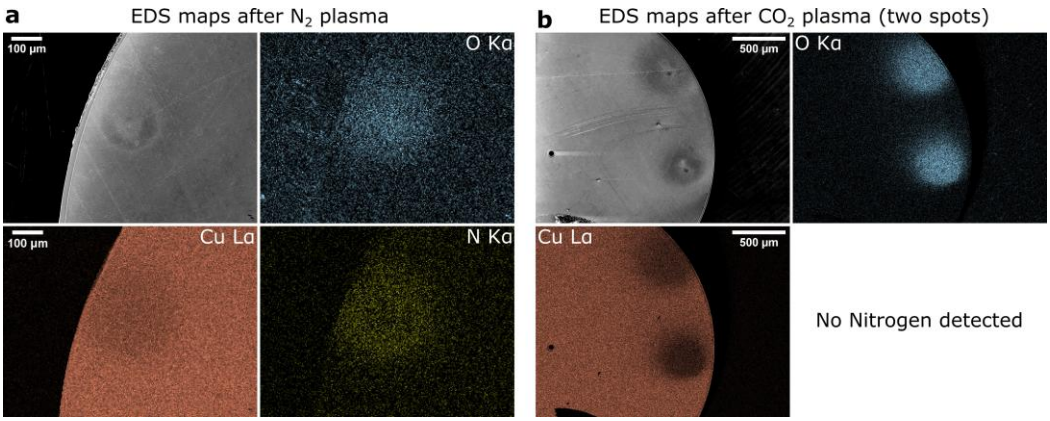

Figure 6-12: Comparison of N_2 and CO_2 plasma interactions on a Cu surface with reversed polarity (nozzle as a cathode). (a): EDX elemental maps reveal an O signal besides N after N_2 plasma treatment, probably caused by Cu oxide redeposition. (b): EDX elemental maps reveal the oxidized spots diameters of ca. 400 µm on the Cu foil for CO_2 plasma.

For a N_2 plasma on a Cu surface, an O signal is unexpected and should not be present without considering the aforementioned re-deposition effects. Our results suggest that part of the O signal in Figure 6-10 b is caused by re-deposited oxidized Cu from the nozzle from previous experiments. Even though this effect is undesired for pure oxidation with plasma-generated radicals, it may be interesting to study film growth during sputtering. In this explanation, mainly two simultaneous effects lead to oxidation of the Cu surface. Firstly, reactive O-containing species such as atomic O or O_2 molecules oxidize Cu even far away from the central plasma-spot region since some of these reactive species are long-lived and can thus be transported in the gas flow outside of the plasma volume. The same effect also oxidized the Cu surface for the initial electrode setup (negative sample polarity), where no sputtering (or only mild sputtering) of the nozzle is present (Figure 6-8). Secondly, there is the redeposition of previously oxidized material (here mostly Cu oxide) from the nozzle, thus adding O-containing Cu to the sample. Finally, it is also possible that O-containing gas molecules (e.g., water) are present in the SEM chamber

during plasma treatment. Such impurity species may also contribute to the observed oxidation during plasma treatment with O-free gases such as N_2.

In summary, oxidation of Ni nanoparticles was observed for CO_2 and Ar/O_2. Oxidation is limited to the central plasma-spot region. For the same ion dose, Ar/O_2 sputtering of Ni nanoparticles is more pronounced than for CO_2. In contrast, oxidation of a flat Cu surface occurs around the central plasma-spot region, which is mostly sputtered rather than oxidized. Sputtering with positively charged ions causes rapid removal of sample material when the nozzle is used as an anode (positive polarity). This results in pits and holes in the central plasma region.

Sputtering of the sample can be strongly reduced by reversing the polarity between the sample and the nozzle, leading to less damage during oxidation. However, sputtering of the nozzle material in this configuration causes damage to the tip of the nozzle and redeposition of this material onto the sample surface. Pure sample oxidation without sputtering or redeposition of material requires other plasma configurations.

3.3 Current Limitations and Outlook

The current setup presented here demonstrates significant advances compared to the state of the art, including a stable DC discharge, no undesired arcing, and true *in situ* SEM imaging while the plasma is active. This enables further research regarding plasma-surface interactions, plasma physics, sputtering, and even provides the future potential to study the plasma constituents with both spatial and time resolution. For example, the investigated processes regarding sputtering, material deposition, and surface oxidation are highly relevant for materials science, nanotechnology and the semiconductor industry.

Despite these advances and the unique possibilities they offer, certain limitations remain, particularly in terms of expanding the scope of potential research areas and making the plasma conditions more directly representative of relevant plasma systems. For example, for plasma catalysis research, the persistent sputtering and redeposition of the sample (or the nozzle) is undesirable and prevents studying the samples under relevant conditions. In order to study plasma catalysis in more appropriate conditions, the sputtering behavior of the plasma should be eliminated. In principle, the current setup could be optimized further to reduce the discharge voltage to decrease the ion energy, lowering the sputtering rates. One potential approach would be to increase the ballast resistor in the system, to limit the current and lower the discharge voltage.

Another approach would be to further increase the pressure, as it is expected that the current setup operates below the optimum value. However, increasing the gas flow rate would require an upgrade to the pumping system of the SEM since the current experiments were performed at the limit of the microscope when operating in high-vacuum mode. The pressure could also be increased by decreasing the gap distance, but this would then also increase the probability of unwanted higher-current discharges, as was also observed in our experiments.

Depending on the precise desired application or experiment, a fundamentally different plasma type may be considered. A number of plasma types could be of interest, each with their potential applications and limitations, as well as practical drawbacks. We hereby present a non-exhaustive list of plasma types with their advantages, disadvantages, and potential for *in situ* SEM applications.

A common type of plasma plasma, especially for plasma catalysis, is the dielectric barrier discharge (DBD), which was described extensively throughout this work [8]. This alternating current (AC, or pulsed) discharge is characterized by a dielectric layer covering one or both electrodes, limiting the current and thus preventing arc formation. In addition to plasma catalysis, this non-thermal plasma is also often used for biomedical research [217]. However, as introduced in Chapter 1 and discussed in detail in Chapter 3 and Chapter 4, DBD plasmas are generally filamentary, where the filaments consist of microdischarges (short duration, high current discharges). These filaments make the plasma treatment of the sample heterogeneous, complicating the analysis, and cause issues with electromagnetic interference. As shown in Chapter 5, DBDs can also be operated in a uniform mode, but this requires precise tuning of all relevant parameters (including the dielectric material, voltage, frequency, discharge gas, and pressure) further impeding rapid development of such an experimental setup.

An alternative discharge based on the DBD is the so-called surface discharge. This plasma is similar to the DBD, but one of the electrodes is embedded or below the dielectric, whereas the other electrode is placed on the surface of the dielectric. With this, the discharge will be generated at the surface of the dielectric. This plasma still requires AC or pulsed power, but is generally more convenient to operate in a uniform mode [8].

Another approach could be using a plasma jet. Many geometries exist, driven by DC, pulsed, or AC power, but they all have in common that the plasma is generated within a device, after which it flows outwards, e.g., to a sample [192]. The main difference with the setup presented here is that in the current setup, the plasma is generated in the gap

between the nozzle and the sample rather than inside the nozzle and sent to the sample. A main advantage of such a plasma jet could be the elimination of the sputtering behavior, as charged species are not predominant (or even absent) in the so-called afterglow. Based on this geometry, an electron beam plasma can be generated [8], of which a variation was previously introduced in a SEM [180]. In such plasmas, a high-energy electron beam is sent through a neutral gas, where the electrons ionize gas molecules. The plasma can then be sent to a sample through a gas flow, or the ions/electrons could be selectively attracted by biasing the sample. An external AC or DC circuit can also be added to further sustain and alter the plasma discharge, depending on the desired properties. Having access to a high-energy electron beam makes a SEM promising to further explore such plasmas.

Note that all AC or pulsed-powered plasmas are very likely to interfere with the true *in situ* imaging capabilities of the SEM since the electron beam will be deflected periodically during scanning, drastically decreasing the image resolution. However, these limitations can often be overcome by employing stroboscopic imaging, where the plasma is momentarily switched off during SEM imaging. Such quasi *in situ* experiments can offer a combination of excellent spatial and temporal resolution.

Despite the remaining challenges, this developing technology is exciting, since introducing a microplasma may enable very different experiments and applications. On the one hand, the *in situ* plasma may lead to new analytical techniques in a SEM, such as glow discharge optical emission spectroscopy [218,219], where the emission from sputtered material in a plasma is studied while ablating the sample material for depth profiling (similar to secondary ion mass spectroscopy in focused ion beam instruments) [220]. On the other hand, established (e.g., EDX or wavelength dispersive X-ray spectroscopy, WDX) [221] or more recently available (e.g., electron energy loss spectroscopy) [222] analytical methods in SEMs may have the potential to probe the ionic species in the plasma cloud. This would provide essential and direct *in situ* feedback for plasma simulation codes and holds promise for improved control over plasma setups.

4. Conclusion

A custom-built microplasma setup was realized inside a SEM based on the design by Matra et al. [179]. A nozzle with a small orifice feeds a gas into the evacuated SEM chamber, from which a plasma can be generated by applying a certain electrical potential. Stable DC glow discharge plasmas with Ar, Ar/O_2, CO_2, and N_2 gases were successfully generated inside the SEM's vacuum chamber. In general, larger discharge currents were measured for higher gas flow rates and smaller gap distances. A non-uniform gas pressure profile was observed in the plasma gap, which (in addition to a non-uniform electric field due to the electrode geometry) complicates a direct comparison of the shown setup with conventional plasma systems. Simultaneous SEM imaging with SE and BSE during plasma operation was demonstrated, enabling *in situ* studies of sample-plasma interactions in the SEM.

A few exemplary plasma-sample interactions were studied. Sputtering of Cu surfaces and Ni nanoparticles under different gases was observed. The lower sputter yield of the Ni particles compared to the Cu support, as well as the incidence-angle dependence of the sputter yield, results in the local formation of cones in the plasma-treated area. The same phenomenon was studied with conventional plasma reactors, which shows that our setup can replicate such experimental conditions on the local scale of several tens of µm. Local plasma-induced oxidation of Cu and Ni was observed for CO_2 and an Ar/O_2 mixture. At the same time, however, the sample was either simultaneously sputtered away by ion bombardment on the sample, or nozzle material was redeposited on the sample by sputtering of the nozzle. These limitations might be overcome by further optimizations of the setup, though for applications where sputtering is detrimental, other types of plasma are to be considered.

In conclusion, we have demonstrated that *in situ* studies of plasma-sample interactions in a modern SEM are possible. This approach provides direct insight into morphological and chemical changes of the sample during and after plasma treatment. Overall, the detailed description and characterization of this *in situ* system serves as a foundation for further development of this technology, which may lead to a better understanding of plasma physics and plasma-surface interactions, which are of great interest in the field of plasma catalysis.

Chapter 7

General Conclusions and Outlook

1. General Conclusion

This thesis employed a multidisciplinary approach to address several challenges in plasma catalysis. One of the main factors preventing the optimization and implementation of this technology, is a lack of fundamental understanding of the underlying processes. By combining detailed electrical characterization of the dielectric barrier discharge (DBD) with several electron microscopy techniques, this work aimed to gain insights in relevant mechanisms of plasma catalysis.

It was shown that the plasma discharge characteristics can have a dominant role in determining the overall performance of the plasma-catalytic experiment. Moreover, we found that the packing material (i.e., catalysts) inside the DBD can have a major influence on these discharge characteristics. Specifically, metal nanoparticles exposed directly to the plasma have a clear and potentially dramatic influence on the plasma discharge characteristics. We believe these findings are relevant, not only for the plasma catalysis field, but also the entire catalysis community. Indeed, plasma catalysis is gaining interest, also in (classical) catalysis groups, due to the large potential benefits of plasma (catalysis) for electrifying chemical reactions. It is important to realize that plasma catalysis is more complex than thermal catalysis, because introducing a (catalytic) packing in the reactor inevitably affects the plasma. As presented in this work, small changes in that packing can sometimes have drastic implications with regard to the plasma behavior. When studying and comparing different catalysts, it is therefore crucial to measure, analyze, and report the discharge characteristics for all experiments. Only when it is clear that certain changes in performance cannot be attributed to differences in plasma behavior, it is possible to hypothesize purely catalytic mechanisms to understand the observed results.

Furthermore, we showed that exposed metal electrode of the DBD erodes, which subsequently contaminates the catalyst (or any other material) inside the DBD. In addition, by combining electron microscopy characterization and electrical discharge analyses, we found that the discharge properties can significantly influence the erosion mechanisms and the properties of the formed erosion products. However, the erosion of the electrode and subsequent contamination was found to be persistent. This could cause notable complications when operating DBDs at larger scales for longer times, as we also showed that metallic particles on the packing material can influence the discharge properties. Also for other applications, the contamination could have major consequences, for example with regard to toxicity.

Since metal nanoparticles were found to dramatically affect the plasma, the influence of a (catalyst) material on the discharge characteristics was studied in more detail with a simplified geometry. These results show that several discharge characteristics are highly sensitive to the capacitances of the system, and that these capacitances can be affected by the catalyst. Moreover, the data indicate that additional effects induced by the catalyst decrease the discharge voltage. This is likely caused by an enhanced electron emission mechanism providing electrons to the system, enabling a sustained discharge at lower voltages. These results show that when introducing a catalytic material to a DBD, its material properties (beyond the envisioned catalytic effects) have to be considered, as they will affect the discharge as well.

Finally, we developed and characterized a setup that enables true *in situ* SEM investigation of a material while it is exposed to a plasma. Both physical and chemical changes in the sample caused by the plasma could be observed. Due to the DC nature of this system, sputtering of the sample was significant, whereas oxidation of the sample was observed after exposure to an O-containing plasma. Although this system is not directly representative of plasma-catalytic experiments, it provides a clear improvement of the state of the art and allows for the further development of this technology toward gaining more insights in plasma catalysis and potentially other plasma-based technologies.

2. Outlook

A clear takeaway from this work should be the necessity of electrical characterization of the DBD in any plasma catalysis experiment. Both analyses based on the voltage-charge diagram, and the investigation of the current signal, are indispensable in this field. When studying various catalysts, true catalytic effects can only be deduced when the discharge is thoroughly characterized and found to be unaffected by the introduction of the catalyst. Whenever changes in the discharge properties are observed, it is very likely that they (at least in part) contribute to the changes in performance of the system.

Although the effect of the discharge characteristics on the chemical conversion is clearly present, the underlying processes are not always obvious. For example, for NH_3 synthesis, the intense microdischarges contribute to a net destruction of NH_3, thus explaining the poor performance of highly filamentary discharges as discussed in Chapter 3. However, this understanding is not necessarily transferable to other reactions. Indeed, the relevant chemical pathways, and thus their dependency on the discharge properties, vary for every individual reaction. Achieving this comprehensive understanding is not straightforward, and will require a multidisciplinary approach. On the one hand, further dedicated experiments could reveal insights into the dependency of the overall performance on the discharge characteristics. In addition to electrical characterization of the discharge and monitoring the composition of the reacted gases, spectroscopic techniques could provide valuable information on the processes taking place inside the plasma. On the other hand, plasma-chemical modeling studies may provide further fundamental insights into the effects of various discharge properties on the chemistry in the plasma. In this regard, Townsend discharges may also be of great interest. These discharges provide a notably more homogeneous treatment of the gas (and the catalyst) compared to typical filamentary discharges, while also exhibiting different discharge properties. However, generating Townsend discharges is not straightforward and was so far only achieved in a limited number of gases. Therefore, further developing this field could prove valuable for plasma catalysis as well.

Furthermore, the influence of the catalyst material on the discharge characteristics, which can be dramatic as illustrated in Chapter 3 and additionally studied in Chapter 5, should be investigated further. Fundamental studies in relevant conditions can reveal critical insights into how certain material properties and plasma conditions influence the electron emission mechanisms. However, as indicated in this work, macroscopic aspects of the system such as the capacitance, and how these aspects may be affected by the

catalyst, should also be considered. All these investigations are further complicated by the fact that often, packed-bed DBD reactors are used, in which the electric fields can be very inhomogeneous, which may be the subject of dedicated further investigation. Moreover, although the electrical diagnostics employed here were found to be very valuable, they are a global diagnostic that only provides insights into the average behavior of the DBD, and thus lacks local details. Simplified reactor geometries with electrical diagnostics and detailed optical (and spectroscopic) characterization of the discharge may provide further valuable information regarding the local discharge behavior.

In addition to understanding the role of the catalytic material on the plasma discharge and the effect of the discharge properties on the overall chemistry, the effect of the actual catalyst on the chemistry needs to be investigated. Specialized surface-sensitive experiments may provide information on the adsorption and surface reactions that may take place between the surface and plasma-generated species. For example, *in situ* spectroscopic techniques that have been developed for thermal catalysis, could be adapted to study the surface of a sample when it is exposed to plasma.

The *in situ* plasma in SEM setup presented in this work may also contribute to a further understanding of plasma catalysis, for example by investigating the oxidation and reduction of catalysts exposed to a plasma, though several challenges remain. For example, due to the geometry of the nozzle inside the vacuum chamber, the pressure at the surface is difficult to define and control. Further, the current setup employs a DC glow discharge, but the reactive environment created by this plasma is not necessarily representative of the environment in a DBD, which is the most commonly used plasma for plasma catalysis. In order to be directly applicable to plasma catalysis, this setup could be adapted to generate a DBD plasma, though due to the AC (or pulsed) operation of these discharges, the *in situ* character of the setup is likely to be lost. Note that the current setup may be more directly applicable to other fields, for example for material synthesis and functionalization.

A related approach that could potentially reveal several fundamental insights of plasma-catalyst interactions, is the incorporation of a plasma inside a transmission electron microscope (TEM). Although this was reported for a DC microplasma [223], there is a lot of room for improvement toward true *in situ*, or even *operando* plasma catalysis experiments inside the TEM. In this previous report, the resolution of the system was limited, and only inert gases were employed. However, it is possible to achieve

atmospheric pressure in a microscopic gas cell and generate a plasma, while analyzing the sample by TEM. When such a setup would be developed that allows the investigation of materials under a variety of gases and with sufficient resolution, this could prove highly impactful for the field. However, as with the plasma in SEM system, it would be most representative to generate a DBD inside the TEM when investigating plasma catalysis, and this poses even more challenges compared to the existing DC system.

Finally, I would like to end with some general notes and questions on the field of plasma catalysis as a whole, based on the experiences obtained throughout this PhD. A fundamental challenge I see for plasma catalysis is that of dimensionality. Whenever a plasma is generated with the aim of converting certain gases, there will always be chemistry taking place inside the 3D volume that is plasma, due to its highly reactive nature. Alternatively, catalytic reactions can only take place on the 2D surface of the active sites of the catalyst. Is it possible for the surface of the catalyst to dominantly contribute to the overall chemistry, when there will always be the active plasma volume before and after species interact with the surface? In thermal catalysis, the temperature is typically sufficiently low such that chemical reactions in the gas phase can be neglected, whereas the dimensionality issue of limited available active sites on 2D surfaces is overcome by using nano-scale particles and highly porous materials, resulting in large (active) surface areas per mass of catalyst. However, this approach is less likely to be applicable to plasma catalysts, since plasma cannot be generated inside nano-scale pores, and due to the short lifetime of many plasma-generated species, their diffusion into the pores is restricted. A potential solution to this dimensionality issue could be the use of microplasmas, surface DBDs, or packed-bed DBDs with small void spaces, where the ratio of the volume of the plasma compared to the available surface area is minimized. However, this may still have its limitations regarding throughput and energy efficiency. Alternatively, an entirely different plasma than the DBD may be considered.

In general, plasma catalysis has not yet proven to be an energy efficient technology for potentially electrifying the chemical industry. In addition, this work highlights the lack of understanding that severely limits the optimization of this technology. Therefore, I believe continued fundamental research is crucial for the further understanding and development of this field. Due to the long road ahead toward this deeper understanding, optimization, and implementation of plasma catalysis, we must be realistic as to what role it may play in the current transition to a sustainable industry. However, this transition will be long and complex, and when plasma catalysis can be developed further, it may still find its place in the sustainable society of the future.

Appendix

A. Appendix to Chapter 3

1. Comparison of Power Determination Techniques

In Chapter 3, the discharge is characterized based on the measurement of the applied voltage and the measured current. These analyses include the plasma power, determined by multiplying the applied voltage with the measured current. A common technique to monitor the plasma power in a DBD is by calculating the area of the voltage-charge diagram, based on the measured voltage on a monitoring capacitor. The charge on the monitoring capacitor is calculated by multiplying the measured voltage and the capacitance of the capacitor. In this section, we discuss the different techniques and show that in our case, the various techniques yield identical results.

Three techniques to calculate the plasma power are discussed.

(i) Based on applied voltage and measured current ("current1" in Figure A-1)

Here, the current measured by the Rogowski coil is multiplied by the applied voltage, to yield a power for every sampling point. These power values are then averaged over one full cycle of the applied voltage (23.5 kHz frequency, i.e., 42.55 µs period). Due to the stochastic nature of the plasma discharge, the calculated plasma power will vary slightly from one power supply unit (PSU) cycle to the next.

(ii) Based on the area of the voltage-charge diagram, as calculated from the measured current ("current2" in Figure A-1)

The measured current is numerically integrated to yield the charge moving through the system (the best straight fit is subtracted from the integrated signal to ensure an oscillation around zero charge). This charge can then be plotted against the applied voltage to yield a voltage-charge diagram. The area within the voltage-charge diagram corresponds to the energy dissipated by the plasma in one cycle. By integrating this area and dividing it by the period of the PSU (23.5 kHz, i.e., 42.55 µs), the power dissipated by the plasma in that cycle can be calculated.

(iii) Based on the area of the voltage-charge diagram, as measured over the monitoring capacitor ("capacitor" in Figure A-1)

The charge moving through the system can also be measured directly by measuring the voltage over a monitoring capacitor. This again forms a voltage-charge diagram when plotted against the applied voltage, which is integrated and divided by the period to yield the power.

In one snapshot of the oscilloscope, 11 full cycles are measured, each of which is analyzed separately. The results of the different calculation techniques (based on the same data) are shown in Figure A-1. Firstly, it is clear that the power values based on the current data ("current1" and "current2") are very close to each other, showing the accuracy of either calculation method. The power as calculated with "current2" is consistently slightly higher than with "current1", possibly due to a minor error introduced by the different numerical approach. The power values based on the measurements over the capacitor are consistently slightly higher than the ones calculated using the signal generated by the current monitor. However, it is important to note that the cycle-by-cycle variation of the power is much greater than the systematic deviation between these values. This systematic difference could be caused by a tolerance of the capacitance value, meaning a slightly different capacitance than specified by the manufacturer. Indeed, the used capacitor has a capacitance of 10 nF with a tolerance of 1%, which could explain the systematic deviation here (ca. 0.7 %).

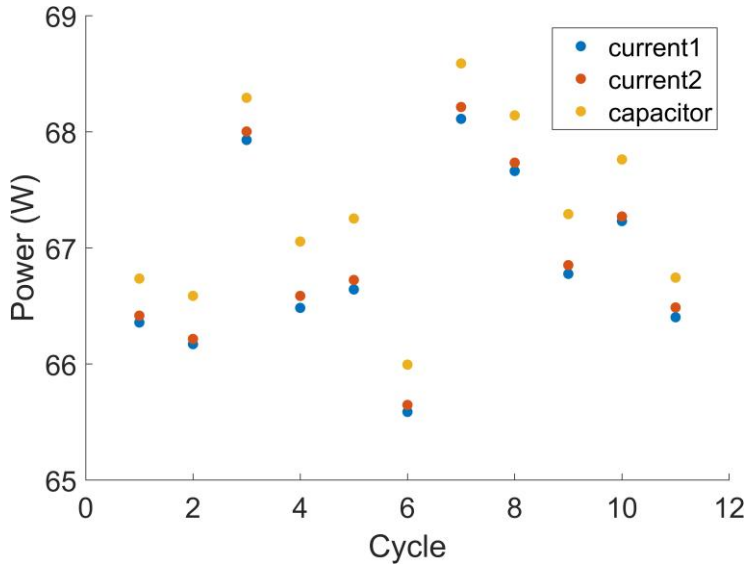

Figure A-1: Dissipated power per cycle in one snapshot, calculated using different methods. The cycle-to-cycle variation (due to inherent variation of the plasma discharge) is much larger than the deviation between different calculation techniques. The capacitor technique always yields a slightly higher power than the other techniques, which could be due to a small inaccuracy of the capacitance.

2. Comparison of Voltage-Charge Diagram Analyses

As mentioned in Chapter 3, the voltage-charge diagrams are analyzed individually (i.e., corresponding to a single PSU cycle), after which the extracted parameters are averaged ("cycle-by-cycle" analysis). The extracted parameters are then further processed to determine all physical properties, as described in the main text. It should be noted that the interpretation of the voltage-charge diagrams is based on equivalent circuits, which implies a macroscopic approach. However, the extracted values based on the cycle-by-cycle analyses were found to be practically identical to analyzing a single averaged voltage-charge diagram (average based on all full PSU cycles in one oscilloscope snapshot).

Three illustrative examples are presented here (Figure A-2 and Table A-1), where the values obtained using the cycle-by-cycle analysis are compared with the values from the averaged voltage-charge diagram. These data are all acquired during experiments with a 1:1 gas ratio (CO_2:CH_4 for DRM, and N_2:H_2 for NH_3 synthesis). Visually, the averaged voltage-charge diagrams (Figure A-2 A, C, E) are highly similar to the single "raw" voltage-charge diagrams (Figure A-2 B, D, F), with only minor smoothing observed for the empty NH_3 case. More importantly, the quantitative extracted characteristics are practically identical, as evidenced by the relative errors in Table A-1. Since the errors are all well below 1%, we conclude it is a fair approach to analyze the individual voltage-charge diagrams and average the extracted parameters per experiment. Note that this isn't necessarily true in all cases, since stochastic microscopic events can alter the observed voltage-charge diagrams. However, it seems that in our case, the system is large enough to naturally "average" these microscopic processes, which allows us to interpret and analyze the individual voltage-charge diagrams as well. If this would not be the case, the voltage-charge diagrams should be averaged prior to analysis.

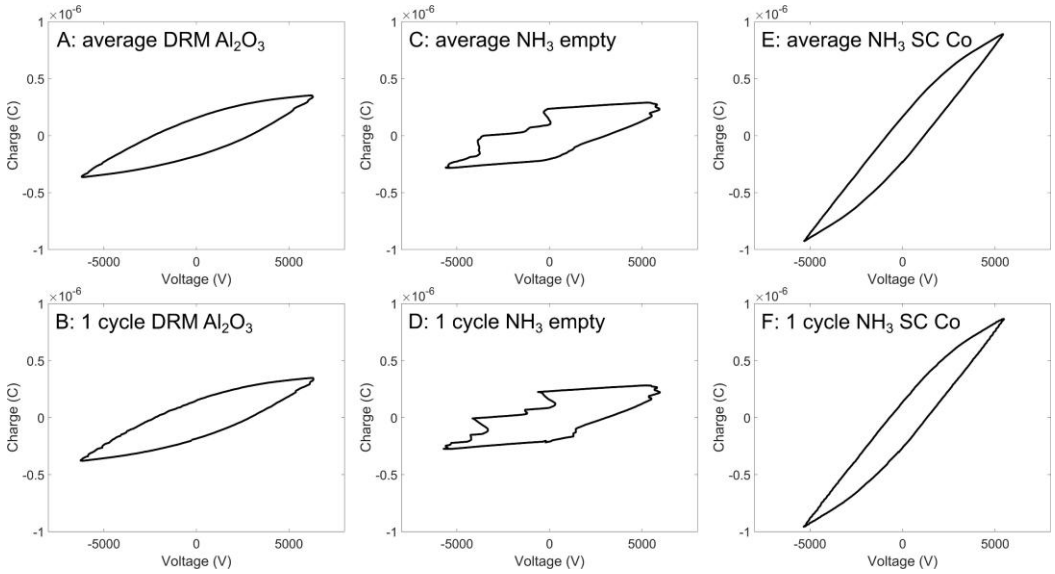

Figure A-2: Comparison between averaged voltage-charge diagrams (A, C, E) and single "raw" voltage-charge diagrams (B, D, F). Note that all experiments were performed with a 1:1 feed gas ratio. The extracted parameters from these voltage-charge diagrams are very similar and are presented in Table A-1.

Table A-1: Extracted values from voltage-charge diagrams, either based on the average voltage-charge diagram, or analyzed cycle-by-cycle. The relative error is dimensionless, and the examples provided here were all from experiments using a 1:1 gas ratio (either CO_2 + CH_4 or N_2 + H_2). The corresponding voltage-charge diagrams are shown in Figure A-2.

DRM blank Al_2O_3	**Averaged**	**Cycle-by-cycle**	**Rel. error**
ζ_{diel} (F)	1.00×10^{-10}	9.95×10^{-11}	0.0070
C_{cell} (F)	2.36×10^{-11}	2.36×10^{-11}	-0.0028
C_{gap} (F)	3.08×10^{-11}	3.10×10^{-11}	-0.0063
$V_{pk\text{-}pk}$ (V)	1.25×10^{4}	1.25×10^{4}	-0.0012
ΔU (V)	2.61×10^{3}	2.60×10^{3}	0.0018

NH_3 empty	**Averaged**	**Cycle-by-cycle**	**Rel. error**
ζ_{diel} (F)	7.18×10^{-11}	7.20×10^{-11}	-0.0026
C_{cell} (F)	1.30×10^{-11}	1.30×10^{-11}	-0.0007
C_{gap} (F)	1.58×10^{-11}	1.58×10^{-11}	-0.0003
$V_{pk\text{-}pk}$ (V)	1.16×10^{4}	1.16×10^{4}	0.0006
ΔU (V)	3.13×10^{3}	3.15×10^{3}	-0.0046

NH_3 SC Co 3.3 wt%	**Averaged**	**Cycle-by-cycle**	**Rel. error**
ζ_{diel} (F)	2.12×10^{-10}	2.12×10^{-10}	0.0003
C_{cell} (F)	1.08×10^{-10}	1.08×10^{-10}	-0.0004
C_{gap} (F)	2.18×10^{-10}	2.19×10^{-10}	-0.0012
$V_{pk\text{-}pk}$ (V)	1.08×10^{4}	1.08×10^{4}	-0.0001
ΔU (V)	1.01×10^{3}	1.01×10^{3}	-0.0009

3. Determining the Discharge Current

In order to obtain the true discharge current $I_{discharge}$, the measured current I has to be corrected by subtracting the capacitive displacement current $I_{displacement}$ (in principle this obtained signal should also be scaled as is done in Chapter 5, but since this signal is only quantified in arbitrary units, this step was omitted). Since the DBD is effectively a large capacitor, applying an AC voltage will cause the system to charge and discharge, inducing a consequential current that is also picked up by the current monitor and thus contributing to the measured current I. By assuming the measured applied voltage is indicative of the charge on the capacitor, the change of that voltage over time represents

the amount of charge moving around, corresponding to a current. As shown in the main text, this capacitive displacement current is calculated using the following equation:

$$I_{displacement}(t) = C_{cell} \frac{dV(t)}{dt} \tag{29}$$

The C_{diel} value was calculated theoretically, as described in the main text, whereas the C_{cell} value was extracted from the voltage-charge diagrams. The resulting discharge current $I_{discharge}$ was then analyzed further, as described in the main text in section 2.4 of Chapter 3, to yield the so-called microdischarge quantity.

Note that numerically calculating the derivative of the voltage, which is required here, is not straightforward. A high sampling rate (1.25 GHz) was used during the acquisition of the oscillograms, which is required to capture the microdischarges as accurately as possible. However, the variation of the voltage happens on a much longer timescale than the timestep of these oscillograms. Given the limited bitrate of the oscilloscope (despite some on-device upscaling), this means in practice that there are quite some "plateaus" present in the signal, i.e., tens or even hundreds of subsequent timesteps having identical voltage values. This isn't uncommon, and in most cases doesn't lead to any issues, but it becomes problematic when we attempt to differentiate this signal. Indeed, when calculating the derivative of the raw signal, the points at these plateaus yield a derivative (and thus $I_{displacement}$) of 0, whereas the points at the edges of the plateaus yield relatively high values for the derivative. This effect is not physical and clearly an artifact of the digital treatment of the analog signal. Therefore, we first apply a moving average filter to the voltage signal to smooth out the plateaus, enabling us to differentiate this smoothed signal which yields a much more sensible result. The window size of this moving average filter was chosen based on the maximum size of the plateaus. All oscillograms were analyzed, storing the maximal plateau widths, which yielded a histogram of all maximal values, shown in Figure A-3. Based on this, we decided to apply a window size of 275 timesteps (equivalent to 0.22 µs), to make sure none of the artificial zeros would remain present in the differentiated signal. This smoothing is effectively low pass filtering the signal, which introduces a certain error. However, we assume that given the high capacitance of the system, the momentary dips in voltage due to the microdischarges are still relatively slow (compared to the actual microdischarges) and therefore accurately described despite the smoothed signal. A zoomed-in plot of the raw data, as well as the smoothed signal, is shown in Figure A-4. The raw data clearly exhibits the plateaus, which are fully eliminated in the smoothed signal. Further, the smoothed

signal only deviates a few V from the raw data, which is negligible on the scale of this signal (peak-to-peak in the order of 10^4 V).

Oscillograms of the measured current and the derived capacitive displacement current for all catalysts are shown in Figure A-5 and Figure A-7 for DRM and in Figure A-6 and Figure A-8 for NH_3 synthesis (1:1 ratios), respectively. The calculated discharge current is presented in the main text (Figure 3-17 and Figure 3-18).

The correction by subtracting the displacement current sometimes changes the overall shape of the current trace, but the microdischarge behavior (very high frequency components) remains unaffected.

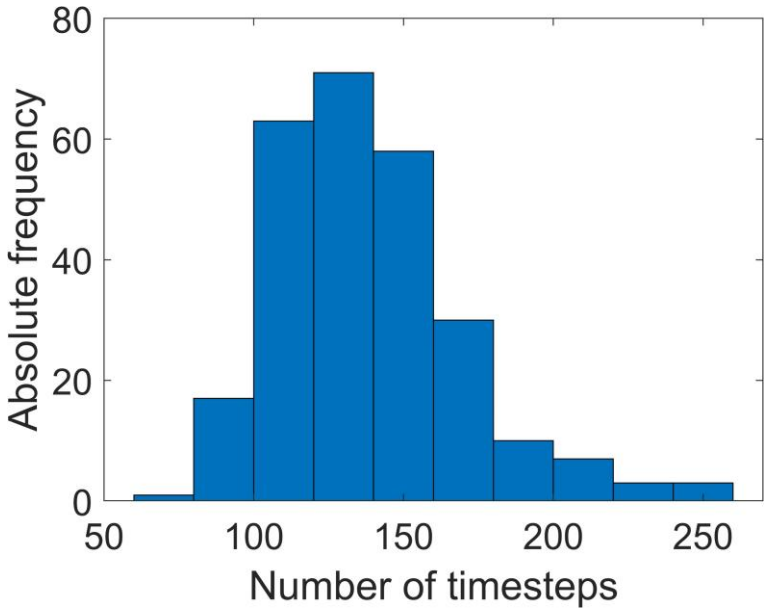

Figure A-3: Histogram of all maximal plateau widths. The maximal plateau widths in the various datasets never exceeded 256 timesteps, justifying the window size of the moving average filter of 275 timesteps.

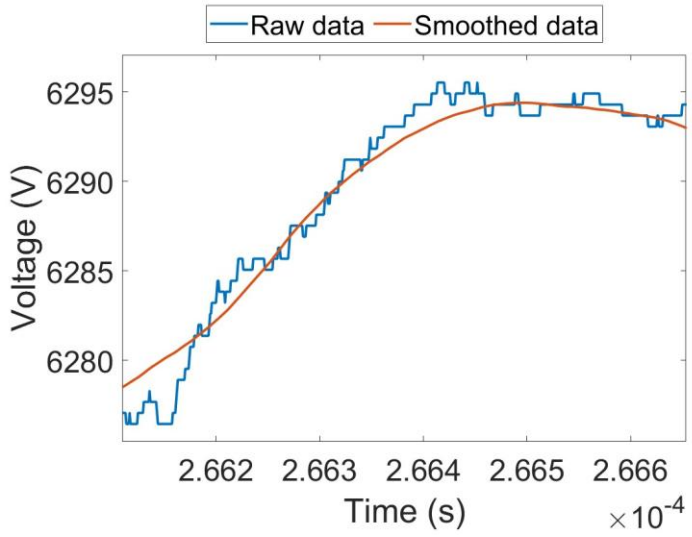

Figure A-4: Raw voltage signal and smoothed signal. The raw data exhibits plateaus in the signal, whereas these flat sections in the signal are eliminated in the smoothed signal.

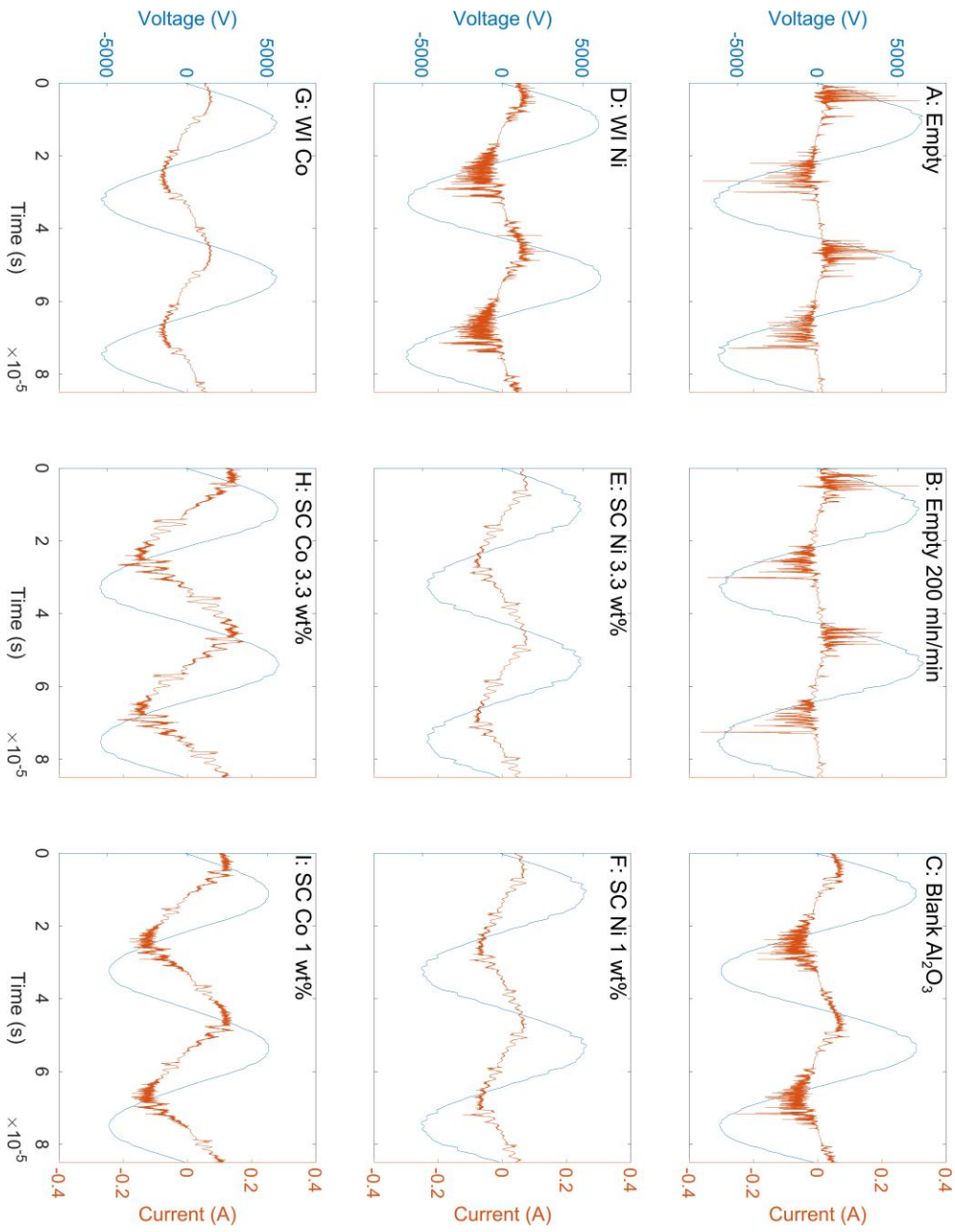

Figure A-5: Representative I-V curves of the measured current I for all experimental sets of DRM for a CO_2/CH_4 ratio of 1:1. As with the discharge current (shown in the main text), clear differences in discharge behavior can be observed, most notably in the microdischarge prevalence and intensity.

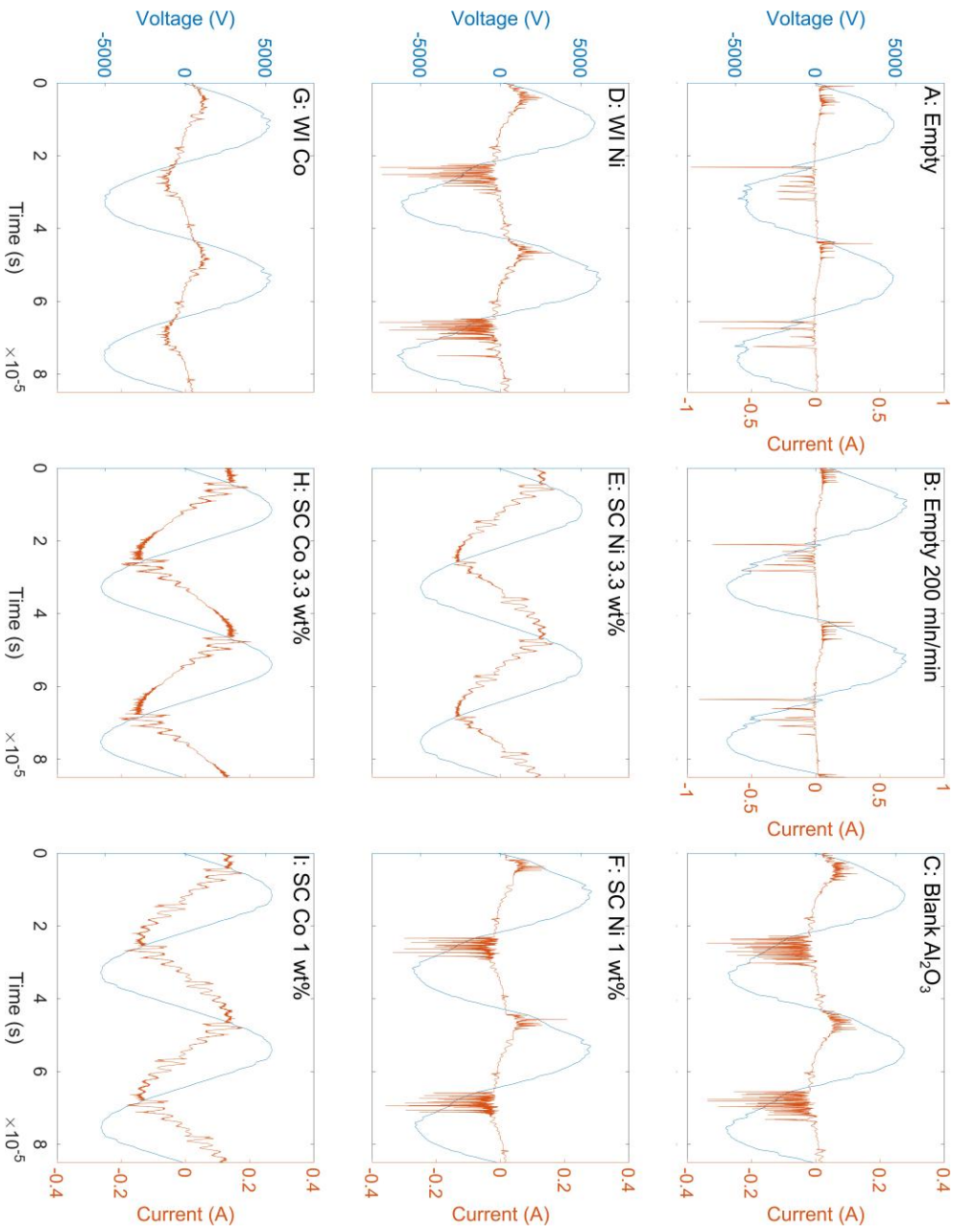

Figure A-6: Representative I-V curves of the measured current I for all experimental sets of NH_3 synthesis for a N_2/H_2 ratio of 1:1. Note that the y-axes of the current are wider for the empty reactor at both 100 and 200 mln/min (A,B) compared to the other graphs to prevent clipping the signal while still giving a clear representation of the signal for the other graphs. As with the discharge current (shown in the main text), clear differences in discharge behavior can be observed, most notably in the microdischarge prevalence and intensity.

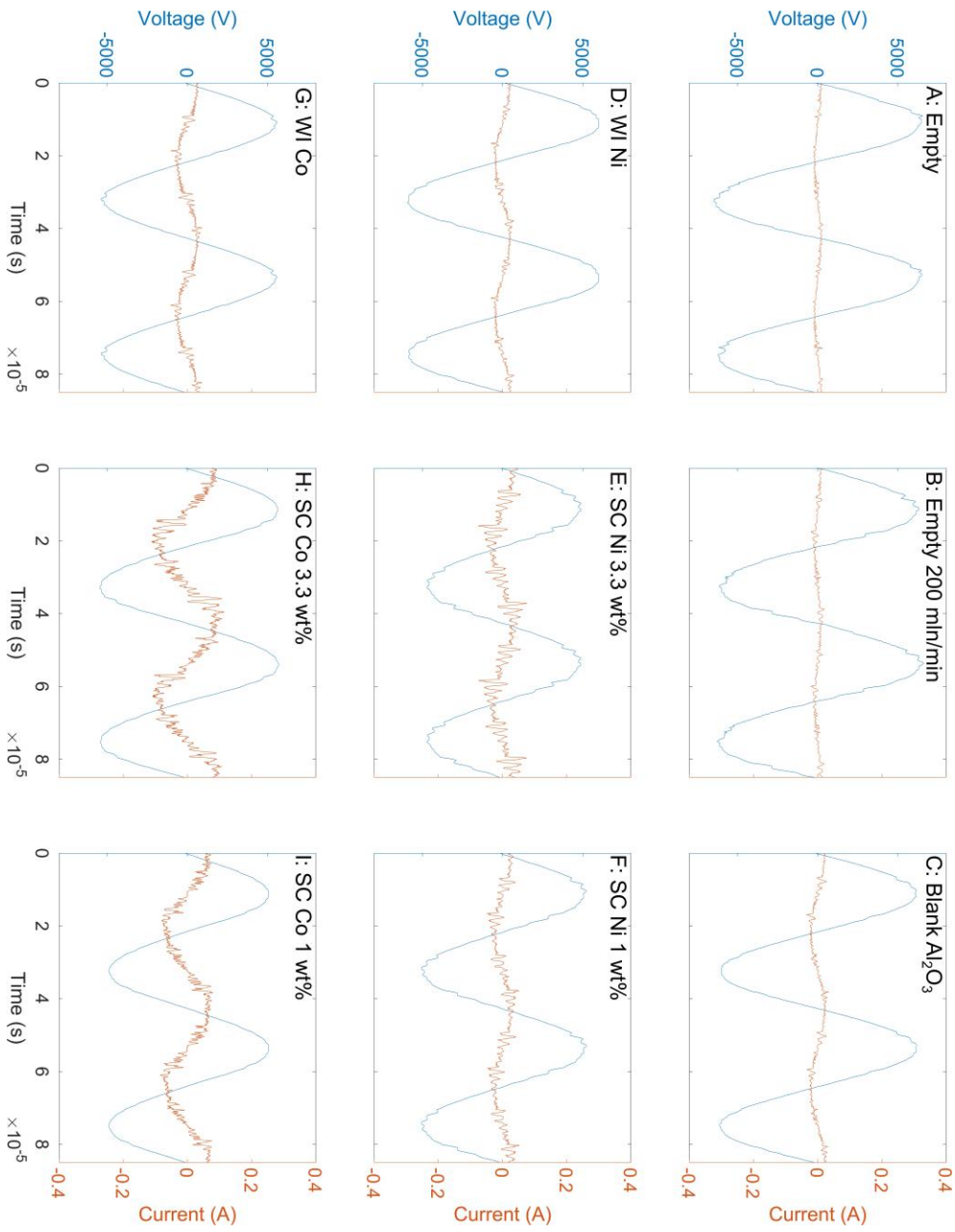

Figure A-7: Representative I-V curves of the calculated capacitive displacement current $I_{displacement}$ for all experimental sets of DRM for a CO_2/CH_4 ratio of 1:1. The displacement currents mostly adhere to the sinusoidal signal as determined based on the derivative of the (sinusoidal) applied voltage. The amplitude of the displacement current is notably higher for the catalysts exhibiting larger discharging areal fractions, due to the enhanced capacitance.

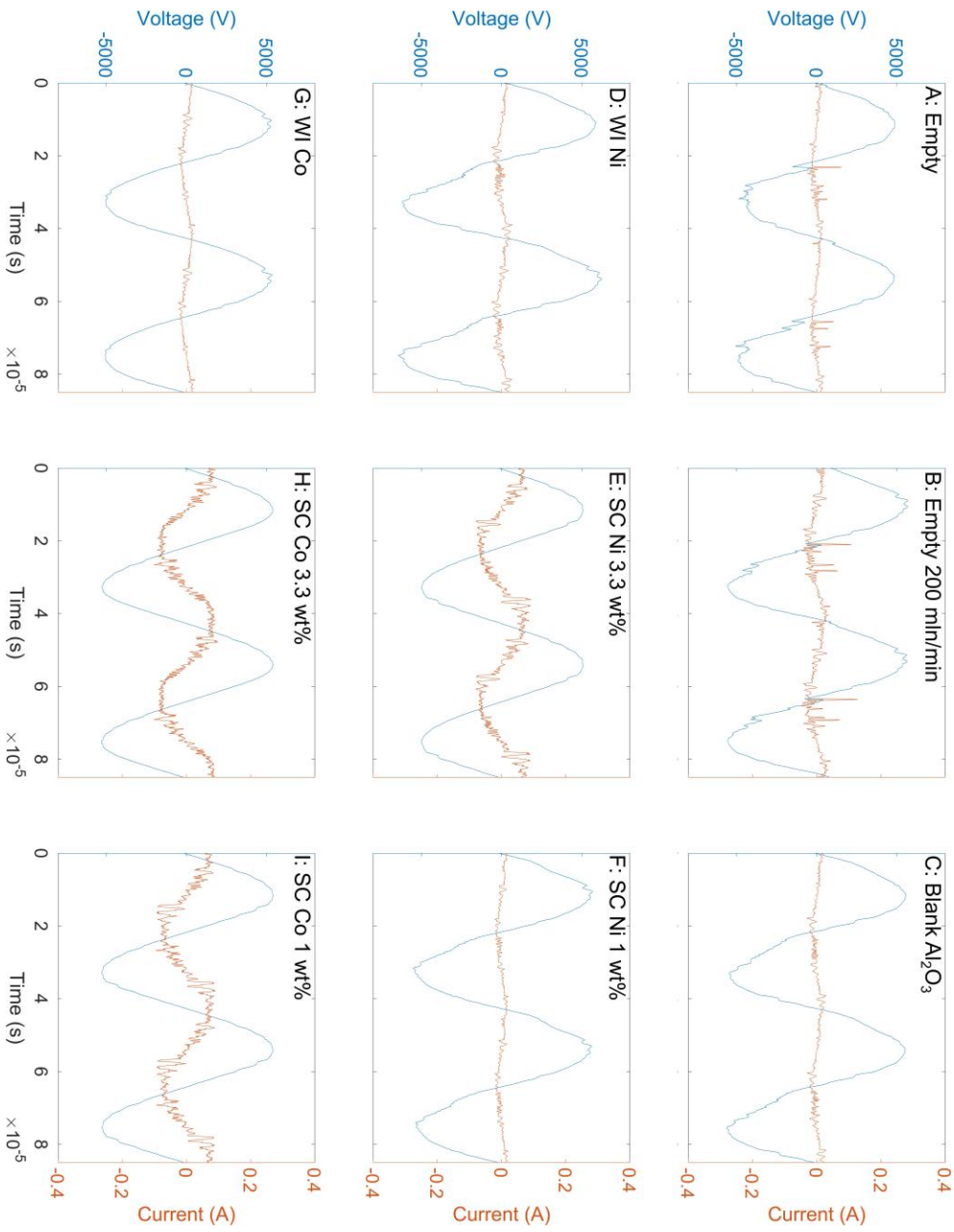

Figure A-8: Representative I-V curves of the calculated displacement current $I_{displacement}$ for all experimental sets of NH_3 synthesis for a N_2/H_2 ratio of 1:1. The displacement currents mostly adhere to the sinusoidal signal as determined based on the derivative of the (sinusoidal) applied voltage. The amplitude of the displacement current is notably higher for the catalysts exhibiting larger discharging areal fractions, due to the enhanced capacitance.

4. Discharge Characteristics

Next, various discharge characteristics can be extracted from the current-voltage (I-V) characteristics and voltage-charge diagrams, in addition to those presented in the main text. Here, the peak-to-peak voltage $V_{pk\text{-}pk}$, burning voltage U_b (representing the gap-voltage at the places where discharges occur), cell capacitance C_{cell}, and the conductively transferred charge ΔQ_{dis} are presented for all gas ratios, for both dry reforming of methane (DRM) and NH_3 synthesis (For DRM: see Figure A-9, Figure A-10, Figure A-11, and Figure A-12. For NH_3 synthesis: see Figure A-13, Figure A-14, Figure A-15, Figure A-16, Figure A-17, and Figure A-18). Since we aimed for a constant plasma power across the various catalytic experiments, the applied peak-to-peak voltage varies slightly. The applied voltage is the highest for the empty reactor, but this is expected since a higher breakdown voltage is required when no packing is present. The burning voltage U_b, however, does vary significantly between the different catalysts. Especially for the NH_3 synthesis experiments, a high discharging areal fraction β corresponds to a low U_b. This means that while the plasma fills the entire volume of the reactor, the voltage across the gap is relatively low. This will impact, e.g., the electron energy, which in turn strongly affects the gas phase chemistry inside the plasma. This is a likely explanation for the good performance in NH_3 synthesis, since the plasma will be less energy-dense, promoting the synthesis of NH_3 rather than its destruction, which is common in the very intense filamentary discharges. Similarly, these catalysts yielding a low U_b also present a high amount of conductively transferred charge ΔQ_{dis}. This makes sense since at lower voltages, a higher current is needed to achieve the same power. This further ties in well with the higher cell capacitance C_{cell} for these "high-β catalysts", since that indicates that the entire system can store more charge at the same applied voltage. Interestingly, these trends observed for U_b, ΔQ_{dis}, and C_{cell}, correspond very well with the discharging areal fraction β, indicating that these characteristics are strongly connected and one can likely not be changed without affecting the other. As discussed in the main text, the microdischarges seem to be governed by a different mechanism (illustrated by the WI Co catalyst).

4.1 Dry Reforming of Methane

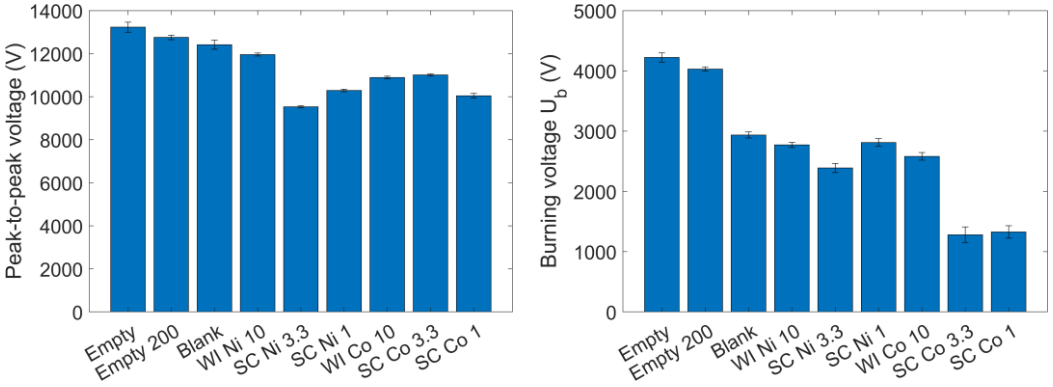

Figure A-9: Peak-to-peak voltage (left) and burning voltage U_b (right) for DRM with a CO_2/CH_4 ratio of 1:1. The burning voltage decreases significantly when catalysts are introduced, most notably for the SC Co catalysts.

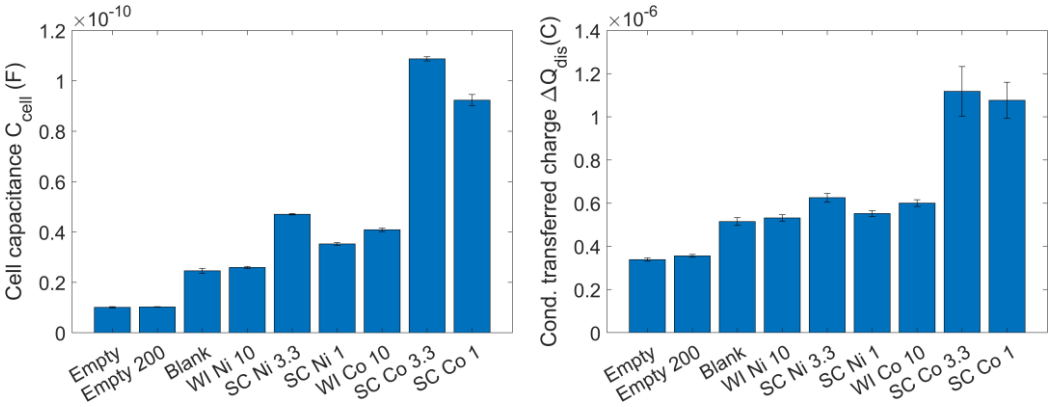

Figure A-10: Cell capacitance C_{cell} (left) and conductively transferred charge ΔQ_{dis} (right) for DRM with a CO_2/CH_4 ratio of 1:1. The cell capacitance and transferred charge vary significantly when catalysts are introduced, with the biggest effects observed for the SC Co catalysts.

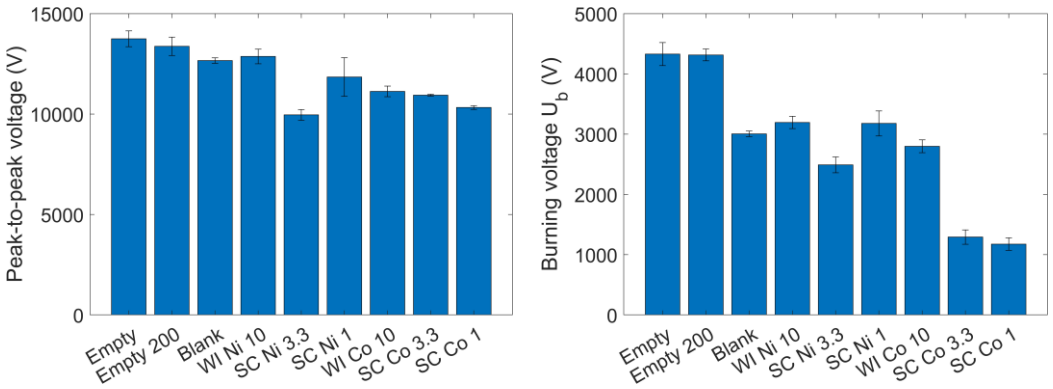

Figure A-11: Peak-to-peak voltage (left) and burning voltage U_b (right) for DRM with a CO_2/CH_4 ratio of 2:1. The burning voltage decreases significantly when catalysts are introduced, most notably for the SC Co catalysts.

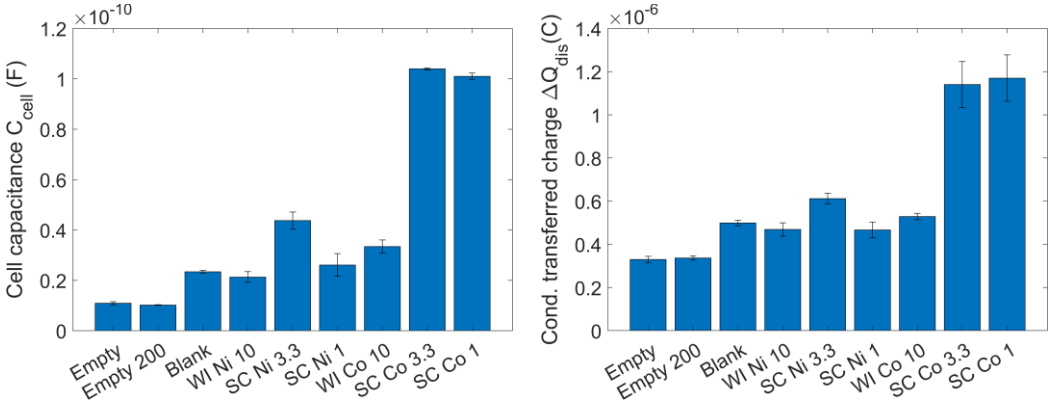

Figure A-12: Cell capacitance C_{cell} (left) and conductively transferred charge ΔQ_{dis} (right) for DRM with a CO_2/CH_4 ratio of 2:1. The cell capacitance and transferred charge vary significantly when catalysts are introduced, with the biggest effects observed for the SC Co catalysts.

4.2 NH_3 Synthesis

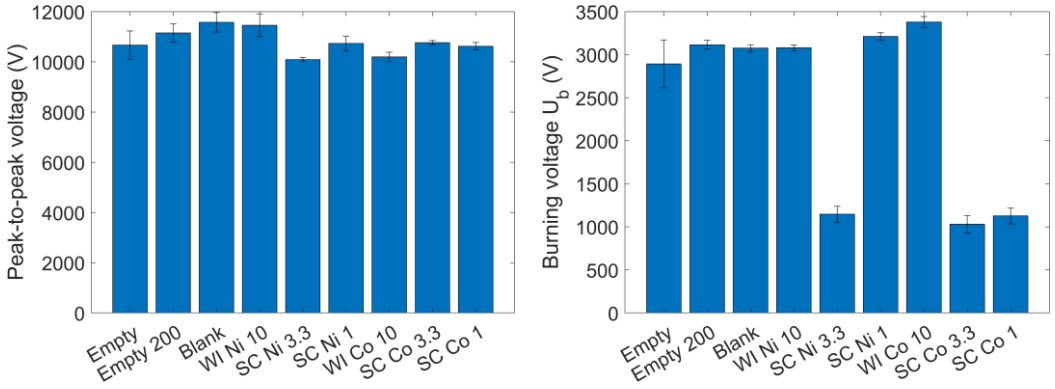

Figure A-13: Peak-to-peak voltage (left) and burning voltage U_b (right) for NH_3 synthesis with a N_2/H_2 ratio of 1:1. The burning voltage decreases significantly for the SC Co and SC Ni 3.3 wt% catalysts.

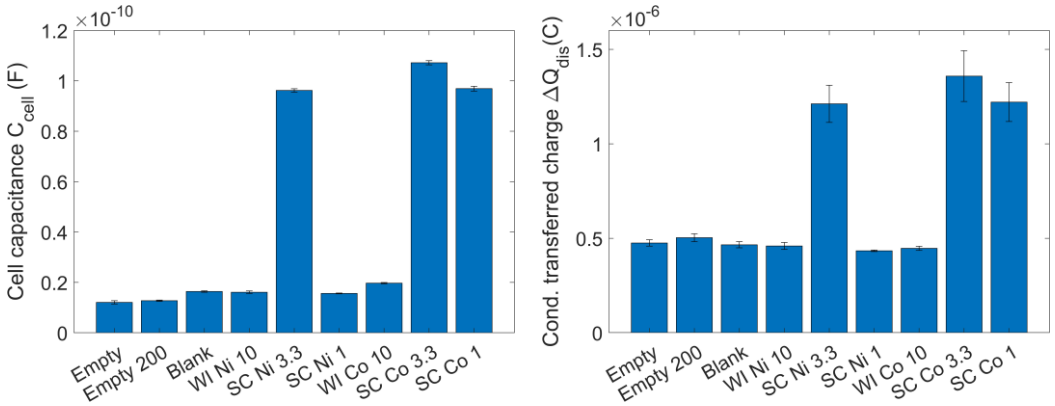

Figure A-14: Cell capacitance C_{cell} (left) and conductively transferred charge ΔQ_{dis} (right) for NH_3 synthesis with a N_2/H_2 ratio of 1:1. The cell capacitance and transferred charge increase significantly when the SC Co and SC Ni 3.3 wt% catalysts are introduced.

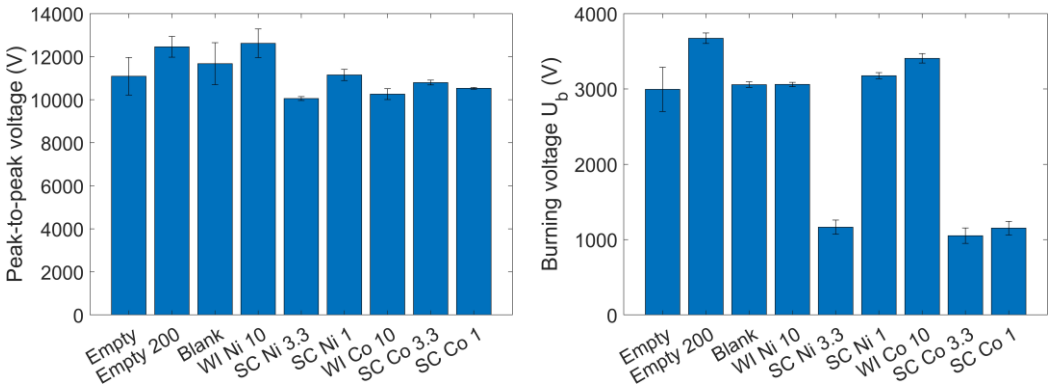

Figure A-15: Peak-to-peak voltage (left) and burning voltage U_b (right) for NH_3 synthesis with a N_2/H_2 ratio of 3:1. The burning voltage decreases significantly for the SC Co and SC Ni 3.3 wt% catalysts.

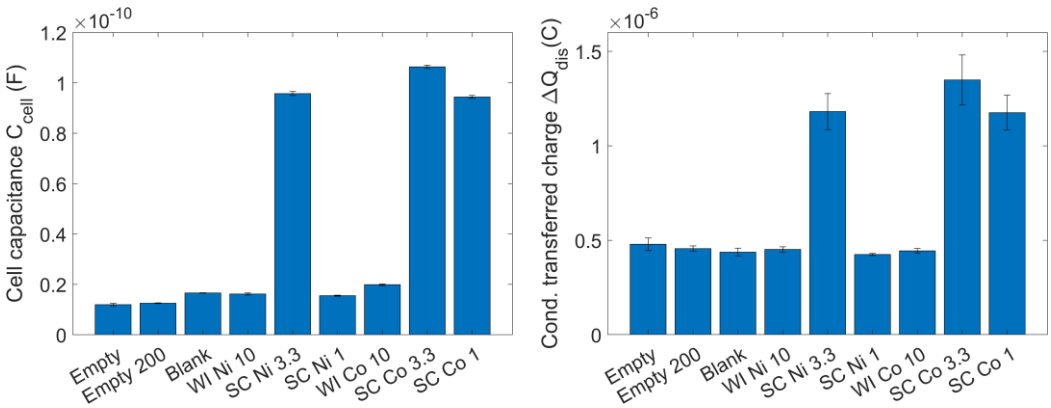

Figure A-16: Cell capacitance C_{cell} (left) and conductively transferred charge ΔQ_{dis} (right) for NH_3 synthesis with a N_2/H_2 ratio of 3:1. The cell capacitance and transferred charge increase significantly when the SC Co and SC Ni 3.3 wt% catalysts are introduced.

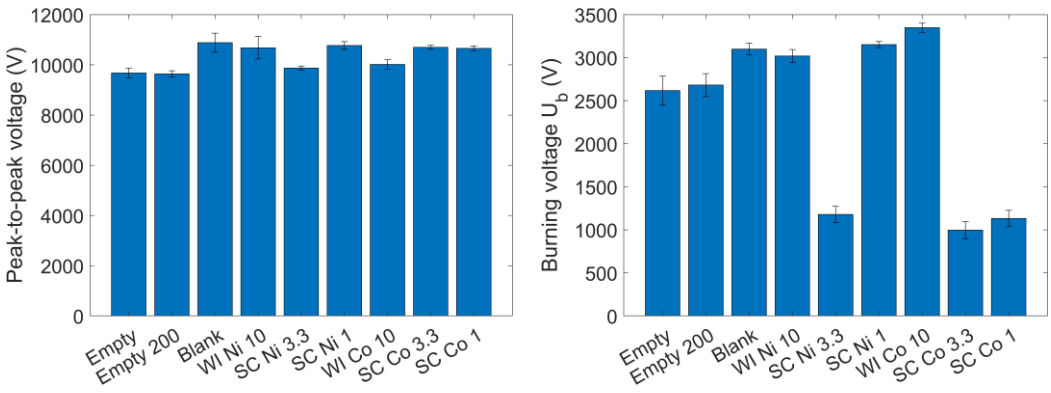

Figure A-17: Peak-to-peak voltage (left) and burning voltage U_b (right) for NH_3 synthesis with a N_2/H_2 ratio of 1:3. The burning voltage decreases significantly for the SC Co and SC Ni 3.3 wt% catalysts.

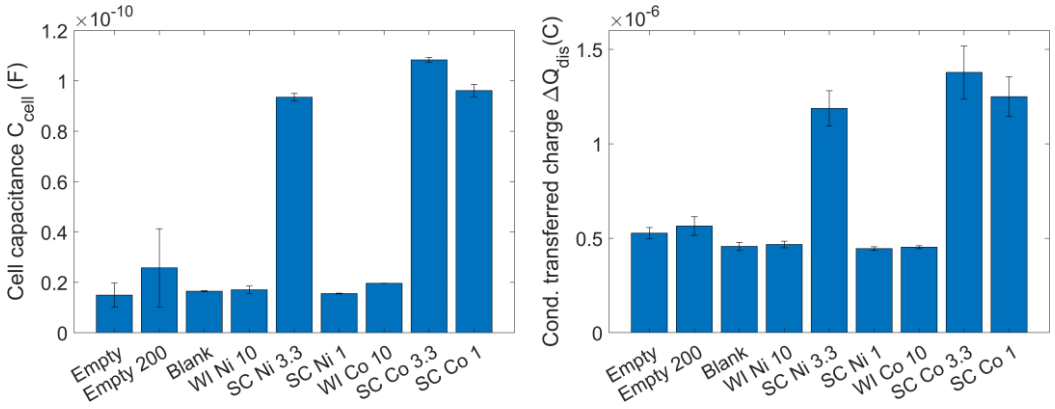

Figure A-18: Cell capacitance C_{cell} (left) and conductively transferred charge ΔQ_{dis} (right) for NH_3 synthesis with a N_2/H_2 ratio of 1:3. The cell capacitance and transferred charge increase significantly when the SC Co and SC Ni 3.3 wt% catalysts are introduced.

5. Additional Performance Metrics

A number of metrics can be used to describe the performance of the plasma-catalytic experiment. For example, the conversion can be combined with the specific energy input to the system to yield an energy cost (EC, see eq. (12) in the main text). The EC for DRM is shown in Figure A-19 and should be interpreted as the amount of energy used for the conversion of CO_2 and CH_4. Figure A-25 and Figure A-26 show the EC for NH_3 synthesis, which should be interpreted as the amount of energy used for the production of NH_3. As the plasma power for all experiments was very similar, the same trends can be observed as for the total conversion or NH_3 concentration, which are discussed in detail in the main text.

As the chemistry in DRM is much more complicated compared to NH_3 synthesis, a number of additional metrics can be used to analyze the overall performance of this reaction. Firstly, the CO_2 and CH_4 conversions can be considered separately, as presented in Figure A-20 and Figure A-21 for both CO_2/CH_4 ratios. Again, very similar trends are observed when compared to the total conversion discussed in the main text, with the CH_4 conversion being consistently higher than the CO_2 conversion, attributed to the lower C-H vs C=O binding energy.

Further, the O-based (Figure A-22, CO_2/CH_4 ratio of 2:1), H-based (Figure A-23, CO_2/CH_4 ratio of 2:1), and C-based (Figure A-24, both CO_2/CH_4 ratios) selectivities are presented. The most striking observation here, is that the C_2H_2 selectivities are close to zero for all

Ni-based catalysts. This is a clear indication of a chemically-catalytic effect taking place at the metal surface, where Ni has different effects compared to Co, as the discharge characteristics cannot explain this difference. This demonstrates that conventional catalytic effects also exist in plasma catalysis, though, as discussed in the main text, they are certainly not the only reactions taking place, and the gas-phase chemistry determined by the overall plasma discharge cannot be neglected.

5.1 Dry Reforming of Methane

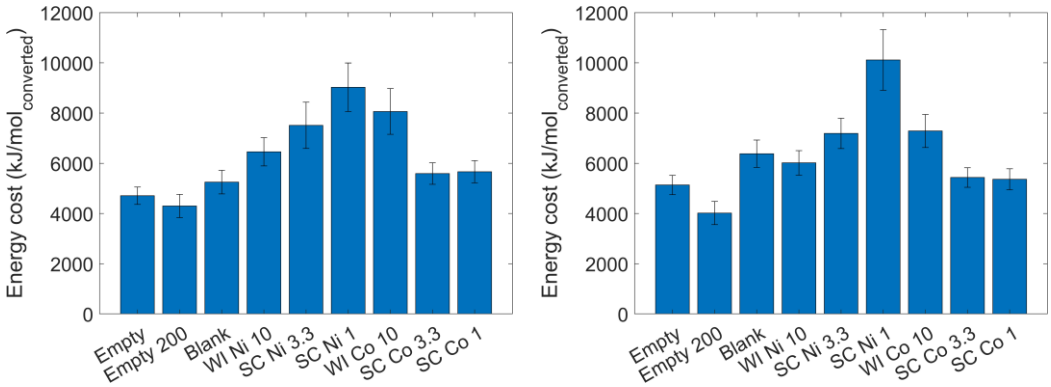

Figure A-19: Energy cost ($kJ/mol_{converted}$) for DRM with a CO_2/CH_4 ratio of 1:1 (left) and 2:1 (right). The catalyst do not improve (decrease) the energy cost compared to the empty reactor.

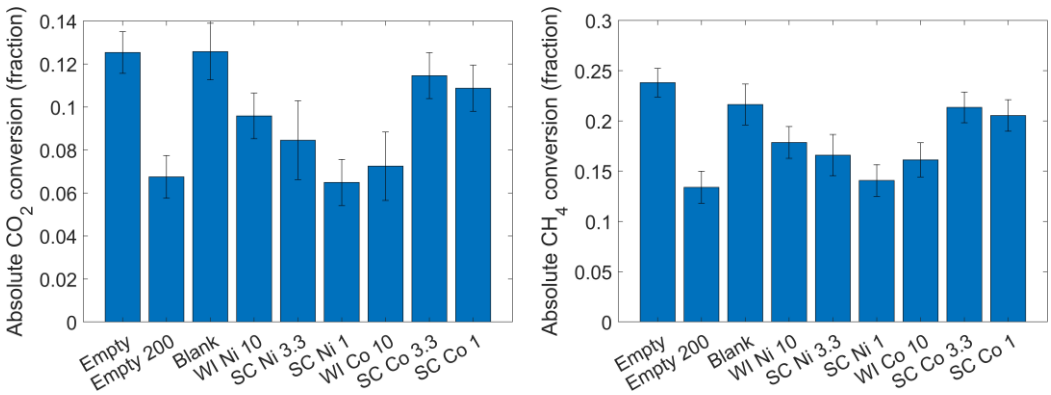

Figure A-20: Absolute CO_2 conversion (left) and CH_4 conversion (right) for DRM with a CO_2/CH_4 ratio of 1:1. The catalysts do not increase (and in some cases notably decrease) the conversion compared to the empty reactor.

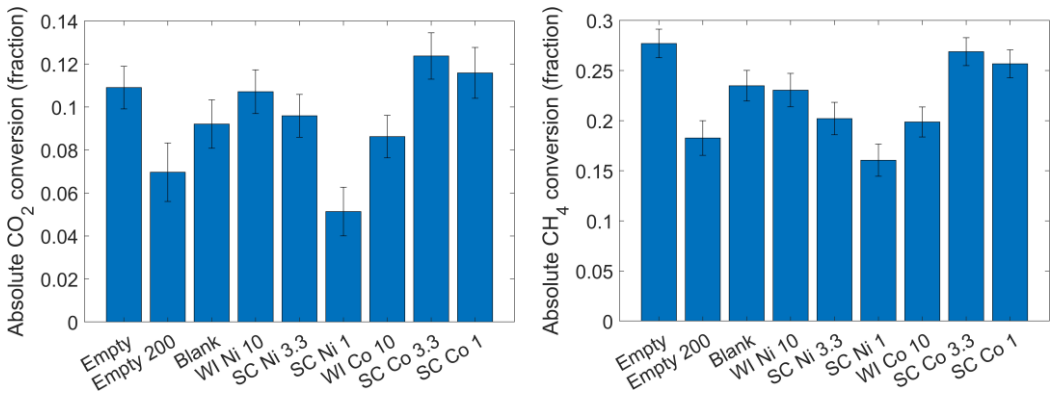

Figure A-21: Absolute CO_2 conversion (left) and CH_4 conversion (right) for DRM with a CO_2/CH_4 ratio of 2:1. The catalysts do not increase (and in some cases notably decrease) the conversion compared to the empty reactor.

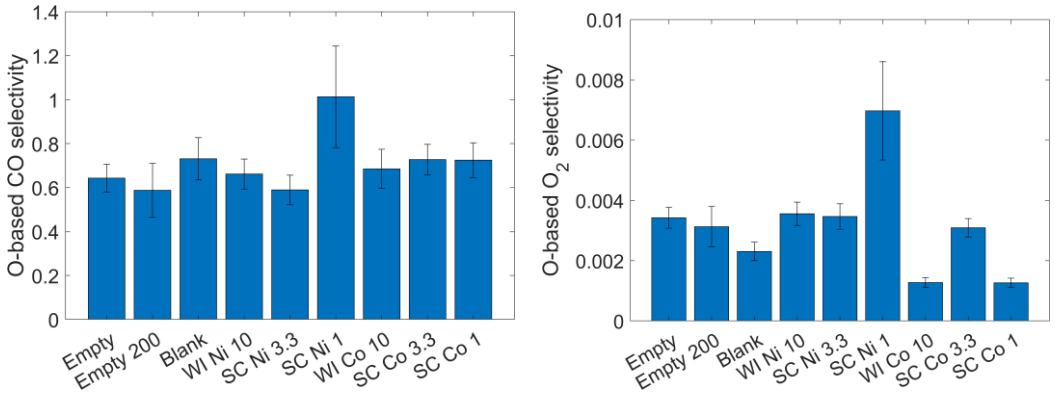

Figure A-22: O-based CO (left) and O_2 selectivity (right) for DRM with a CO_2/CH_4 ratio of 2:1. The CO selectivity only deviates from the other experiments for the SC Ni 1 wt% catalyst. The O_2 selectivity increases slightly for the SC Ni 1 wt% catalyst and decreases slightly for the WI Co and SC Co 1 wt% catalysts, but the values remain low.

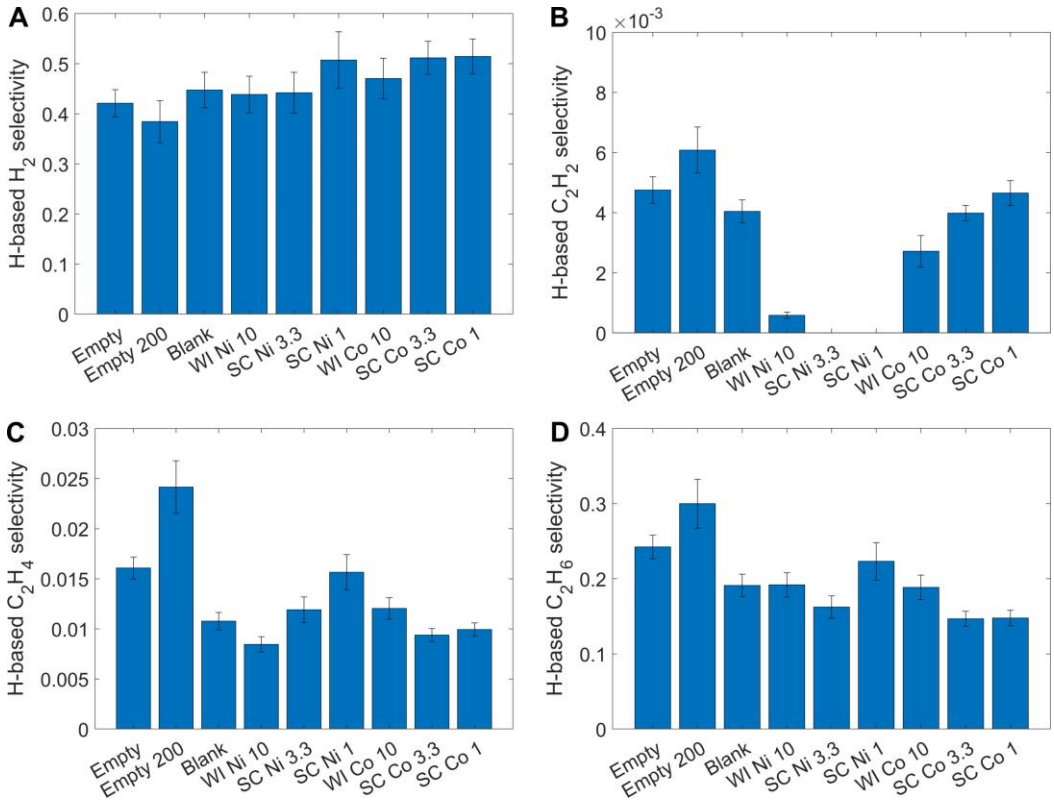

Figure A-23: H-based selectivities for DRM with a CO_2/CH_4 ratio of 2:1. The H-based selectivities vary slightly for the various catalysts, but the differences are mostly small. Only for the C_2H_2 selectivity, it is striking that the selectivity drops to (near) zero for the Ni-based catalysts.

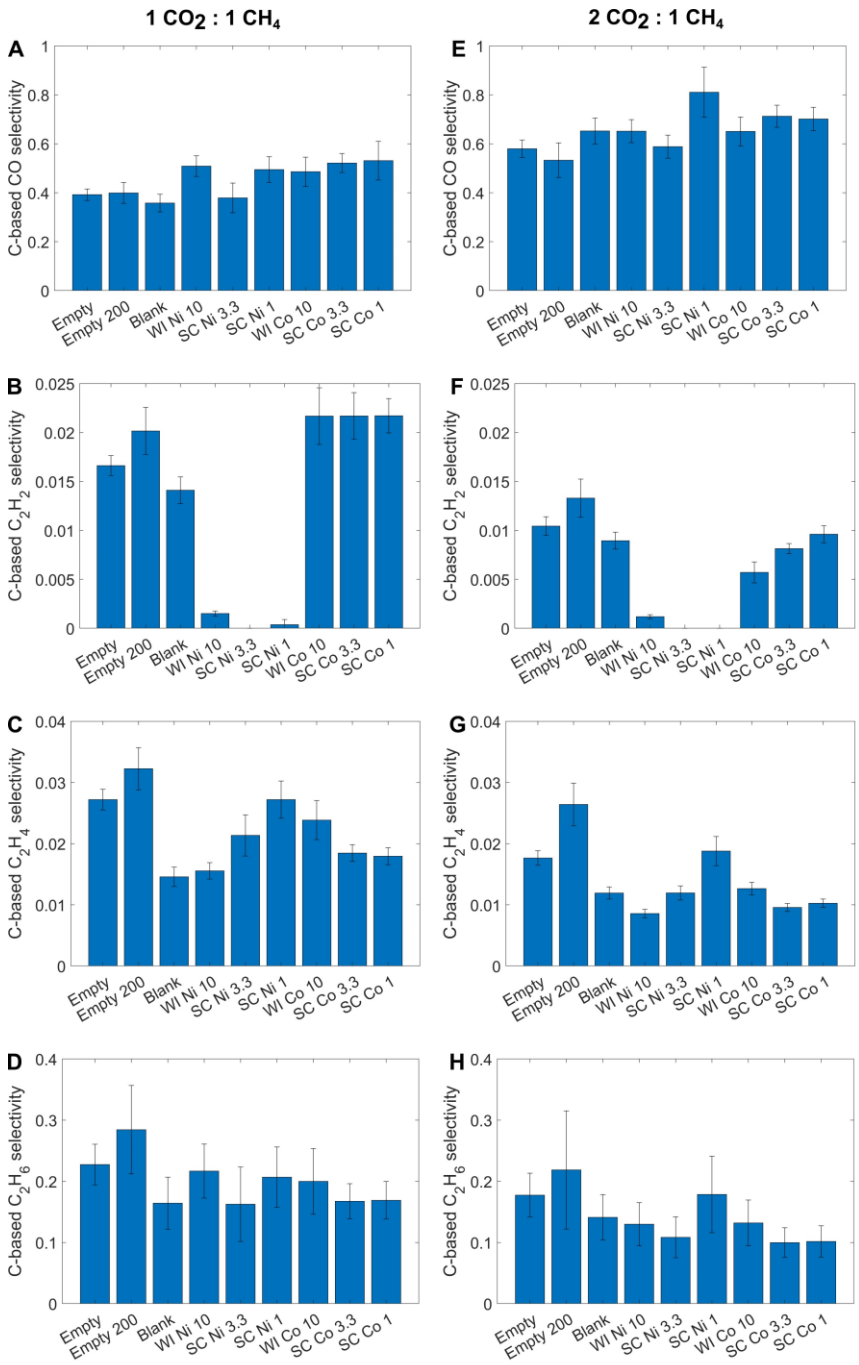

Figure A-24: C-based selectivities for DRM with a CO_2/CH_4 ratio of 1:1 (left) and 2:1 (right). The effects of the catalysts on the C-based selectivities are usually relatively small, except for the C_2H_2 selectivity, where the values for the Ni-based catalysts are notably lower compared to the other experiments.

5.2 NH_3 Synthesis

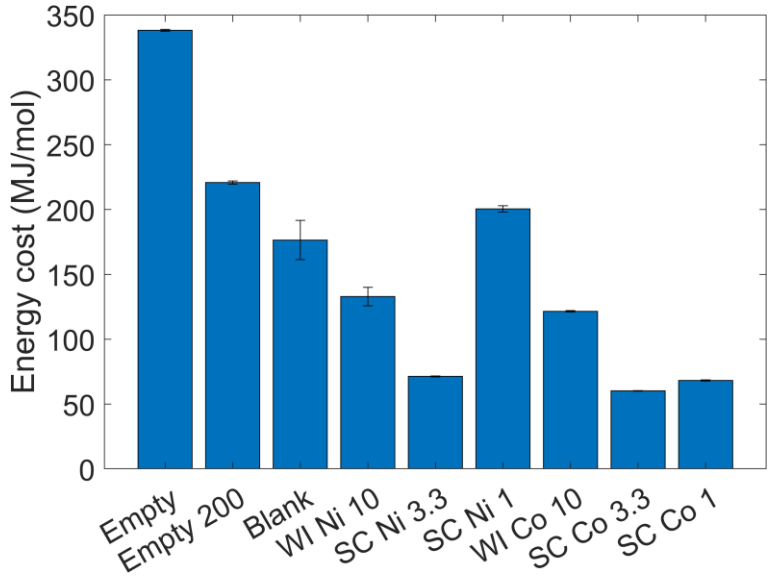

Figure A-25: Energy cost (EC) in MJ/mol NH_3 synthesized with a N_2/H_2 ratio of 1:1. The energy cost decreases significantly upon introducing a catalyst compared to the empty reactor, most notably for the SC Co and SC Ni 3.3 wt% catalysts.

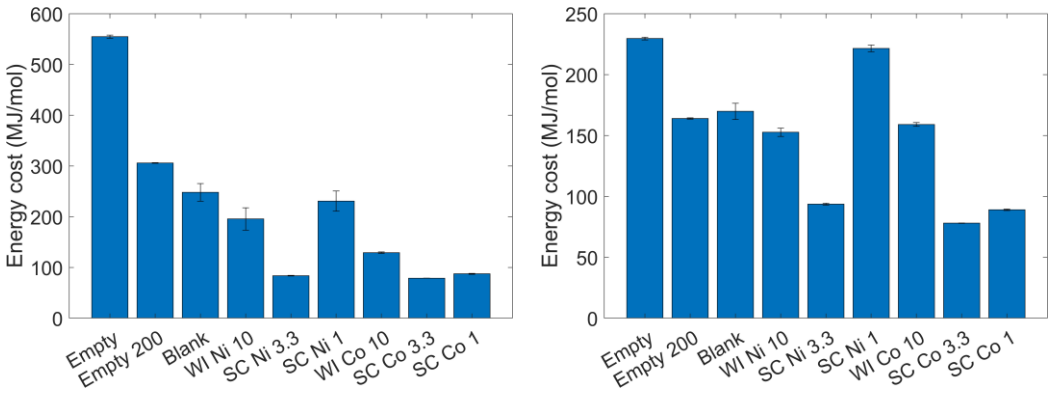

Figure A-26: Energy cost (EC) in MJ/mol NH3 synthesized with a N2/H2 ratio of 3:1 (left) and 1:3 (right). The catalysts again notably improve (decrease) the energy cost, though these differences are less pronounced for the 1:3 ratio (right).

B. Appendix to Chapter 5

1. Signal Alignment and Parasitic Capacitance

During each experiment described in Chapter 5, three electrical signals were acquired simultaneously: the applied voltage, the voltage across both the capacitor and resistor, and the voltage across just the resistor. To obtain the charge on the capacitor, the voltage across the resistor is subtracted from the signal containing the voltage across both the capacitor and the resistor, and the remaining voltage is multiplied by the known capacitance of the monitoring capacitor (10 nF). The current can be obtained by directly dividing the measured voltage by the known resistance (25 Ω).

Since in our experiments the signals are generally small (discharge current, deposited charge, plasma power, …), the measurements are very sensitive to small misalignments in the signals. In addition, variations in the parasitic capacitance would further hinder data analysis and interpretation. It was found that the timing of the signals was slightly misaligned (in particular the applied voltage signal versus the two other signals), and that this misalignment varied slightly over time. In addition, the parasitic capacitance was found to vary as well, and a correlation between the time-shift and the parasitic capacitance increasing/decreasing was observed. Therefore, we believe the source of these transient effects is the high-voltage probe, in which slight changes may occur due to heating by the high applied voltage. This phenomenon was found to be consistent across multiple probes of the same type.

To account for these effects, a plasma off measurement was acquired after each acquisition of the threefold datapoint, as described in the main text. For such a plasma off measurement, there is no plasma, and the deposited power should be zero (dielectric losses are assumed to be negligible). Therefore, the charge on the capacitor should be perfectly in phase with the applied voltage, and the current signal should be precisely $\pi/2$ out of phase with the two other signals. By calculating the FFT of each signal, the phase is determined at the frequency of the applied voltage (1000 Hz), and appropriate time shifts are applied to correct for any phase mismatch in the signals of the corresponding threefold datapoints.

In addition, the relation between the applied voltage and the charge on the capacitor reveals the total capacitance of the system, i.e., $\mathrm{d}Q/\mathrm{d}V = C_{cell} + C_{par}$. By imposing that C_{cell}

should be constant and equal to the geometric value, this calculation directly yields the parasitic capacitance C_{par} at that time. This capacitance is then used in the corresponding threefold datapoints to determine the true capacitances from the voltage-charge plots, as well as in other equations for discharge characteristics, as discussed in the main text.

2. Incorrect Power when Using Wrong Q_{trans} Scaling Factor

To illustrate the effect of using an incorrect scaling factor in the equations of the discharge current and the conductively transferred charge, an example is presented based on the data for the 2000 shots disk, at an applied voltage amplitude of 38 kV. Just like the area of the voltage-charge plot, as measured directly during the experiment, the area of the U_{gap} - Q_{trans} diagram represents the energy dissipated in the system in one period. Therefore, the power can be calculated from these signals as well, to validate their absolute values compared to the power from the voltage-charge diagram. In this example, the power determined based on the voltage-charge plot equals 0.392 W, and so does the method based on the U_{gap} - Q_{trans} diagram using the correct scaling factor as discussed in the main text. The corresponding plot using the correct scaling factor is presented in Figure B-1 A.

When using an incorrect scaling factor for the transferred charge, such as C_{gap}/C_{cell}, the transferred charge and thus the calculated power is incorrect. In this case, the power determined using this incorrect scaling factor is equal to 0.448 W, representing a significant overestimation of the true value. This erroneous value highlights the importance of using the correct scaling factor, as discussed in the main text, and the U_{gap} - Q_{trans} diagram using the incorrect scaling is presented in Figure B-1 B.

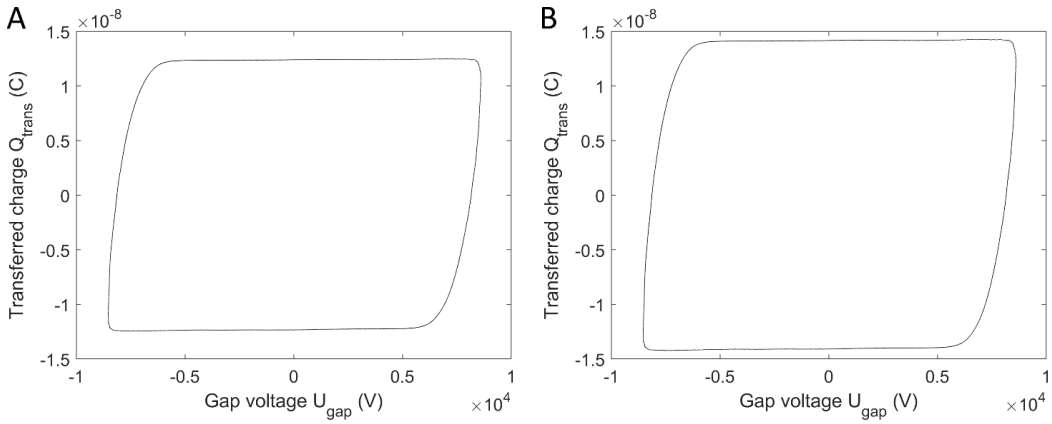

Figure B-1: U_{gap} - Q_{trans} diagram using the correct scaling factor (A), or the incorrect scaling factor (B) for calculating the transferred charge. The corresponding plasma powers are 0.392 W (A) and 0.448 W (B), the latter being incorrect.

3. Overestimation of V_{min} at Higher Applied Voltages

The minimum sustaining voltage is typically determined by calculating the crossing point between the lines fitted to the plasma on and plasma off edges of the voltage-charge diagram [169]. This method usually yields a point at or close to the point in the diagram where the plasma ignites, accurately providing the experimental value for the minimum sustaining voltage V_{min}. However, when the transition of the plasma off to the plasma on phase happens more slowly, and the true effective dielectric capacitance is only reached at relatively high applied voltages, this calculation method may overestimate the true value of V_{min}. This overestimation is illustrated in Figure B-2 for an applied voltage amplitude of 38 kV, where it becomes apparent that at these high applied voltages, the crossing point overestimates the voltage at which the discharge ignites. However, especially for these more gradual ignitions, it is difficult to accurately and objectively describe this ignition point. Therefore, we decided to use the value of V_{min} obtained at an applied voltage amplitude of 26 kV, as this offers a balance between minimal overestimation, and a reasonable signal to noise ratio.

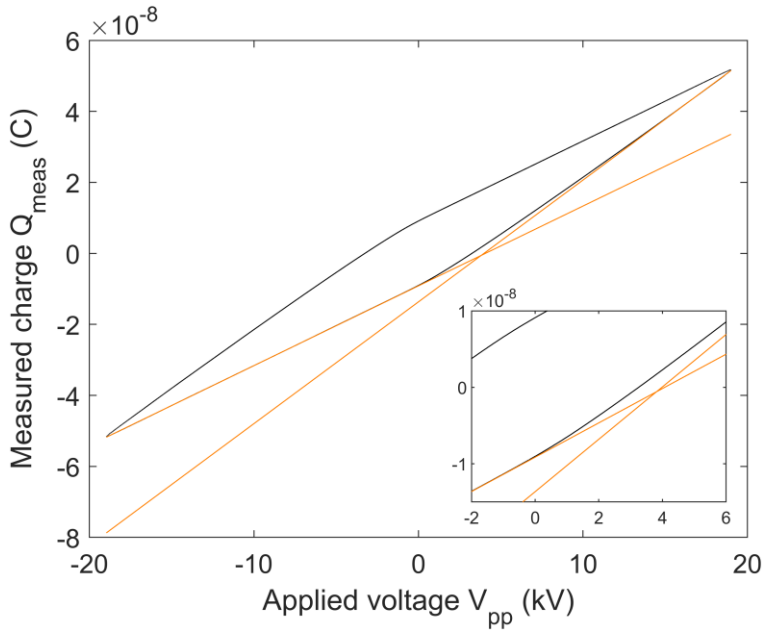

Figure B-2: Voltage-charge diagram and lines fitted to the plasma on/off edges for the blank disk at an applied voltage of 38 kV. The intersection point is slightly further away than the point at which the plasma ignites, as further highlighted in the inset.

C. Appendix to Chapter 6

1. Details on the Experimental Setup

Figure C-1 shows images of the assembled microplasma setup with opened SEM chamber. The subfigures are explained in detail in the following, and the parts are listed in Table C-1.

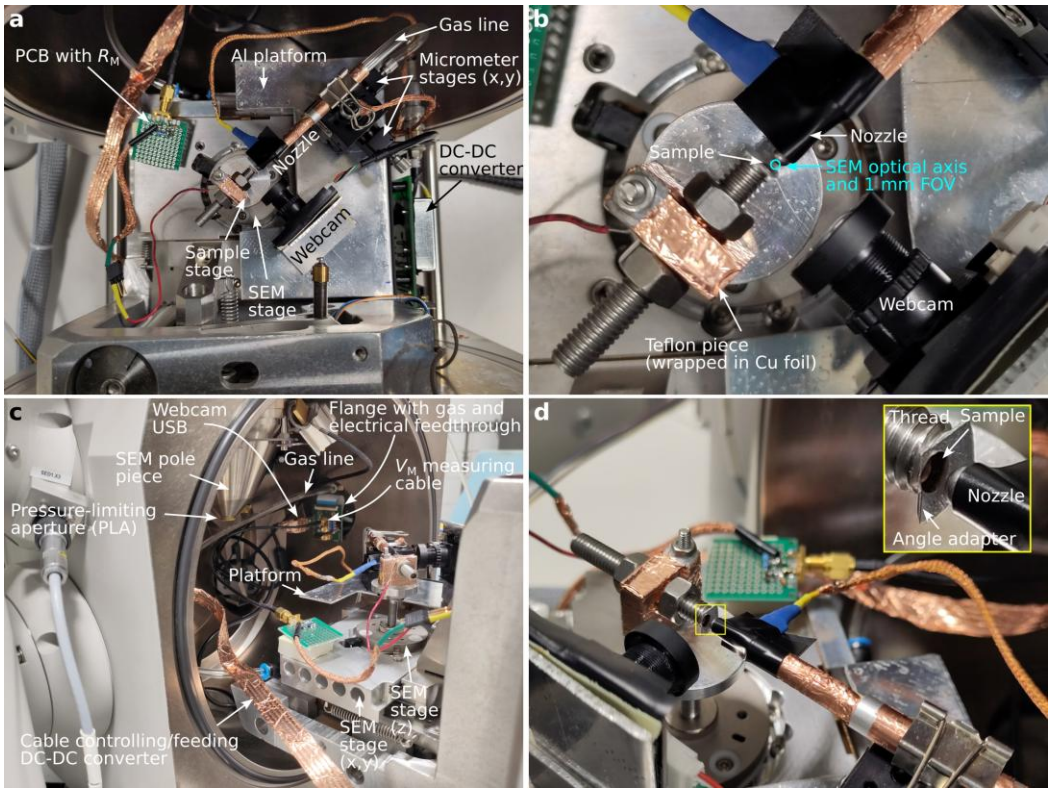

Figure C-1: Images of the experimental setup with opened SEM chamber. See the text for a detailed discussion.

Table C-1: Table of used components with their part number/stock-keeping unit (SKU).

Component	Manufacturer	Part number
Gas nozzle	LenoxLaser	S-1/8-TUBE-CAL-20
Micrometer stages	Thorlabs	MS3/M
DC-DC converter (+2 kV)	XP Power	CA20P
DC-DC converter (-1.25 kV)	XP Power	CA12N
Power supply 1	Keysight	E36106B
Power supply 2	RS PRO	IPS-3303
USB Webcam	Arducam	B0205
Flow meter	Alicat	M-200SCCM-D/5M
Voltage measurement	Keithley	2400
Cu-aperture targets	Gilder Grids	GA50

Figure C-1 (a, top view): Some components (gas nozzle, webcam, DC-DC converter) are mounted on an Al platform to isolate them from the movements of the sample stage of the SEM. The gas nozzle is fixed with a binder clip to two micrometer stages. The high-voltage cable (starting at the BNC connection of the DC-DC converter, here visible below the gas line) is fixed close to the end of the nozzle and here hidden below the black insulating tape. The DC-DC converter was mounted on the side of the Al platform to save space on the top. The sample is positioned in the center of the image opposite to the nozzle (Figure C-1 b and d). The printed circuit board (PCB, made according to the data sheet of the DC-DC converter, with an output resistor of 1 MΩ) with the measurement resistor R_M is fixed directly on the moveable part of the SEM stage. Its SMA connector and the cable go directly to the vacuum flange (Figure C-1 c).

Figure C-1 (b, top view): Close-up view of the nozzle-sample configuration. An adapter made of Teflon is used to isolate the sample from the SEM stage. This choice was made to protect the SEM electronics from possible current bursts (e.g., arcing). The discharge current runs through the red cable, then through R_M (see Figure C-1 a), and finally through the flange to the electronics outside the SEM chamber (not shown here). The Cu foil on the top part of this Teflon piece is used to minimize charging. Since a 500 µm diameter pressure-limiting aperture (PLA) was used, the field-of-view (FOV) for SEM imaging is significantly reduced. The actual visible area is around 1 mm and is exemplarily marked in the image with a circle. The center of the circle is given by the optical axis of the SEM as manufacturer-calibrated to the x = y = 0 position of the SEM stage. After setting the stage to x = y = 0 without a mounted sample, the orifice of the nozzle is

positioned as close as possible to the optical axis using the two micrometer stages. The nozzle position is fixed after closing the SEM chamber. In case the nozzle is out of the SEMs FOV after pumping the chamber, its position has to be realigned after venting the chamber. When the nozzle is positioned within the SEMs FOV, the sample can be brought closer to/moved away from the nozzle using the SEM stage controls to change the gap distance.

Figure C-1 (c, side view): The PLA is visible on the bottom of the SEM pole piece. It reduces gas flow into the SEM column to keep it at higher vacuum levels compared to the plasma-gap region. A self-made flange with gas and electronic feedthroughs is mounted on one of the free chamber ports (here visible in the back). Notably, the gas line does a 90° bend in the feedthrough to account for X-ray safety. The cable of the DC-DC converter goes on the flange on the opposite side (not visible here, but in the top part of Figure C-1 d), where a DB9 connector is present. This connector and the corresponding feedthrough are typically used for cooling/heating SEM stages provided by the microscope manufacturer. The pin layout was measured, and the shown custom cable with a DB9 connector was made to control the DC-DC converter.

Figure C-1 (d, side view): The image from this angle reveals the sample stage made of an "angle adapter" to tilt the sample surface slightly toward the incident electron beam for analyses. Different angle adapters were ground with angles from 5° to 20°. These are fixed to the threaded metal rod with conductive Ag paste. The sample used here is a 3 mm Cu disc with a small aperture in the center (50 µm diameter, Gilder Grids GA50), which is glued onto the angle adapter with conductive Ag paste.

The default vacuum system of the SEM (FEI Quanta 250 FEG) was used, consisting of a pre-vacuum rotary pump, a turbo molecular pump, and ion getter pumps (IGPs) for the electron-gun area. Without gas flow, the SEM-chamber pressure was able to reach the 4×10^{-4} Pa range after a few hours of pumping. Especially, the residual air inside the gas line takes this time to get pumped through the nozzle orifice. The gas lines were flushed with the process gas before experiments to reduce contamination with air. With gas flow, the chamber pressure for a given gas flow rate depends on the gas type. The pressure is typically around 2×10^{-2} Pa for gas flow rates of ca. 5 sccm, which is just below the threshold value of the microscope software for the high-vacuum mode (ca. 3.3×10^{-2} Pa). If the chamber pressure exceeds the threshold value, the gas flow rate must be reduced to allow for microscope and plasma operation in high-vacuum mode.

It was observed that the use of Ar leads to higher chamber pressures than for N_2 or CO_2 and, thus, Ar-containing gas mixtures must be used more carefully. The SEM chamber is mainly pumped by the turbo molecular pump, so a higher pumping speed for gases with smaller molecular weight is expected [224], i.e., higher pumping speed for N_2 (28 Da), followed by Ar (40 Da), and finally CO_2 (44 Da). In practice, Ar is probably less efficiently pumped than CO_2 because the IGP of the electron column might contribute to the total pumping speed as well. As indicated by the microscope manufacturer in the microscope's manual, "the argon use should be minimized to a short time, because the IGPs are not optimized for pumping of it at all.", meaning that N_2 and CO_2 are likely to be more efficiently pumped by the IGP.

2. Details on Voltage-Current characteristic measurements

The main text shows voltage-current characteristics of the generated microplasma in the scanning electron microscope's (SEM's) chamber. A problem during measurements was the continuous sputtering of the sample surface when using the nozzle as an anode with positive bias. Typical measurements of the voltage drop across the measurement resistor R_M versus the measurement duration are shown in Figure C-2. All measurements were started by first applying the highest possible source voltage V_S with the DC-DC converter (2 kV, visible as strong onset in the plots) and then gradually decreasing the source voltage with 40 V steps until no voltage across the measurement resistor R_M was measurable anymore. A small parasitic offset voltage was measured and subtracted from a reference region (e.g., the shaded area in Figure C-2 a). Ideally, the voltage steps in the measured curve should be horizontal plateaus, whereby each step corresponds to a defined step in the applied source voltage (here in steps of 40 V). However, as visible in the inset in Figure C-2 a, the discharge current was not stable but instead steadily increasing, especially in the first few seconds of plasma operation and at high currents. We attribute this to sputtering and heating of the electrodes, which may decreased the resistance and thus increase the discharge current (given the constant applied voltage). Even though it is, in principle, possible to correct the slope of the V_M-time curve, we opted to simply calculate the average value of each voltage step by manual extraction (see Jupyter notebook on Zenodo [225]). Figure C-2 b shows a more extreme example of higher discharge currents, resulting in faster surface sputtering and an even more pronounced discharge-current increase over time. A strong slope is visible in the inset figure for the first few seconds of plasma operation. The voltage steps become horizontal at around 20 s in the plot.

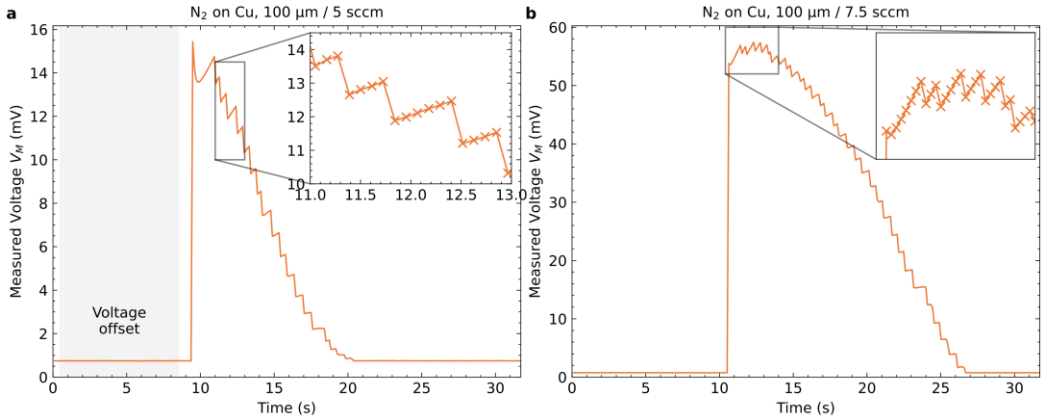

Figure C-2: Measurement problems of voltage-current characteristics, shown for two different measurements. (a): The shaded area marks a reference region without actual microplasma operation, which was used to determine and subtract the voltage offset. The sharp onset shows the plasma ignition for the highest source voltage of 2 kV, followed by subsequent reduction in 40 V steps. The ideally-horizontal steps show a positive slope due to a continuous discharge current increase, especially in the first few seconds of plasma operation. This is attributed to rapid sputtering of the sample surface. (b): Another example of higher gas flow rate, resulting in higher discharge currents. The sputtering is faster, and the slope is more pronounced than in (a).

No continuous plasma discharges were observed for specific combinations of (large) gap distances, (low) gas flow rates, and (low) source voltages. In such cases, the electron beam may be able to ignite the plasma and initiate a continuous discharge. In other cases, a discharge current was only measured when the electron beam was on and immediately vanished after the beam was switched off (Figure C-3). Two examples for the latter are shown in Figure C-3 a and b, where each step in the signal corresponds to the electron beam being switched on or off. A smoothed signal is plotted as well for better visibility of the steps. The signal was smoothed using locally weighted regression (LOWESS) with HyperSpy [226] with smoothing parameter = 0.03 and number of iterations = 1. The calculated current is in the nA-range, which is typical for SEM measurements, but was not explicitly measured here. However, these steps in the current signal were only observed when a bias was applied to the nozzle (either positive or negative). This implies that there was indeed a discharge present in the gap, but it could only be sustained by the external ionization of the SEM electron beam. The beam conditions were 15 keV, 30 µm objective aperture, and spot size 5. Interestingly, some steps show an initial current spike in the non-smooth signal (40 nA to 100 nA for Figure C-3 a or 20 nA to 50 nA Figure C-3 b) and then the reduction to the lower value.

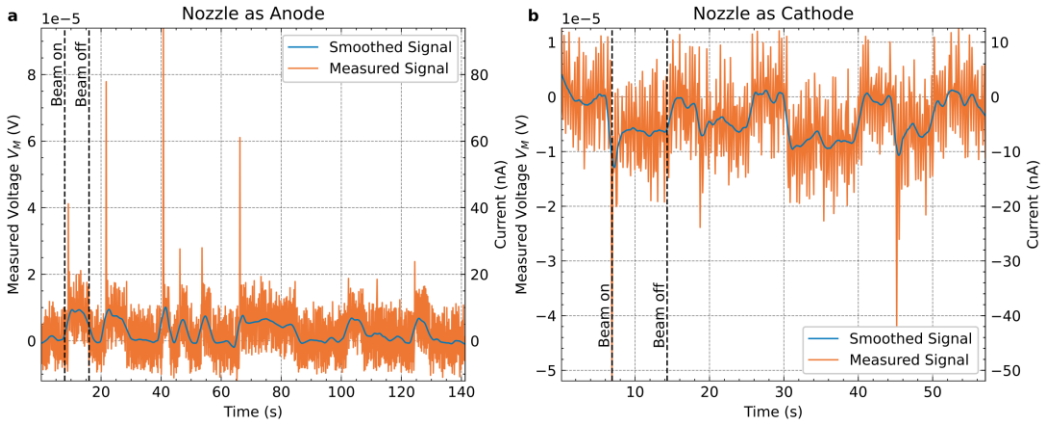

Figure C-3: Measured voltage across a 1 kΩ resistor (left abscissa, note the 1×10^{-5} factor) and corresponding discharge current (right abscissa) for experimental conditions that did not result in a continuous plasma for two different nozzle-sample polarities. Raw and smoothed signals are displayed. Each step corresponds to the time the electron beam was on and scanning. The measured current of a few nA is within the range of typical electron-beam currents for the used beam parameters. (a): Nozzle as the anode, and (b) nozzle as the cathode.

3. Spectrum Normalization in EDX

Figure C-4 a–c show energy-dispersive X-ray spectroscopy (EDX) spectra without normalization and varying total electron dose, resulting in different total X-ray counts. The upper plot shows the full energy range from 0 keV to 15 keV (Figure C-4 a). The insets in the lower row (Figure C-4 b and c) show selected energy ranges for energy windows containing the C and O signals (Figure C-4 b), and the Ni and Cu signals (Figure C-4 c). For these spectra, a direct comparison is impeded by the difference in total X-ray counts, resulting in varying peak heights even without relative changes between spectra. After normalization (Figure C-4 d–f), the increasing O signal is revealed (Figure C-4 e), and the signals for Ni and Cu are unchanged (Figure C-4 f). The shaded areas in Figure C-4 d mark the regions used for spectrum normalization. These contain no elemental peaks and only bremsstrahlung background. The sum of the X-ray counts in these two areas was used for normalization of the spectra.

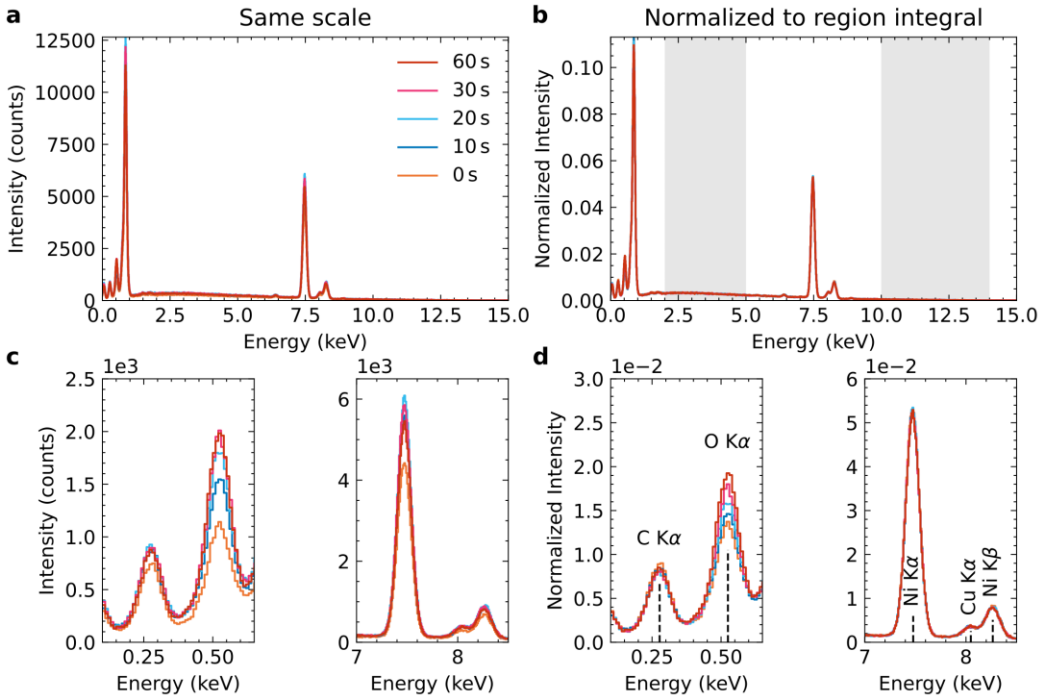

Figure C-4: Comparison of EDX spectra without (left) and with (right) normalization with respect to the summed intensity in a given energy interval (shaded in gray). The upper row shows the full energy range from 0 keV to 15 keV, and the lower row shows exemplary energy windows containing the C and O signal, and the Ni and Cu signals. The normalization accounts for varying total X-rays in the EDX spectra, impeding a direct comparison.

List of Scientific Contributions

1. Peer-Reviewed Publications

First Author Publications:

1. Electrical characterization of an atmospheric pressure Townsend discharge exposed to a conductive layer: an update of the equivalent circuit
   De Meyer R., Cimento P., Brandenburg R., Verbeeck J., Coulombe S., Bogaerts A.
   Submitted to Plasma Sources Science & Technology

2. Contamination in Dielectric Barrier Discharge Plasmas by Electrode Erosion
   De Meyer R., Verbeeck J., Bals S., Bogaerts A.
   ACS Materials Letters 7, 52 (2025)

3. Importance of plasma discharge characteristics in plasma catalysis: Dry reforming of methane vs. ammonia synthesis
   De Meyer R., Gorbanev Y., Ciocarlan R.-G., Cool P., Bals S., Bogaerts A.
   Chemical Engineering Journal 488, 150838 (2024)

4. *In situ* Plasma Studies Using a Direct Current Microplasma in a Scanning Electron Microscope
   Grünewald L.*, Chezganov D.*, **De Meyer R.***, Orekhov A., Van Aert S., Bogaerts A., Bals S., Verbeeck J. (*shared first author)
   Advanced Materials Technologies 9, 2301632 (2024)

5. Effectiveness of reducing the influence of CTAB at the surface of metal nanoparticles during *in situ* heating studies by TEM
   De Meyer R., Albrecht W., Bals S.
   Micron 144, 103036 (2021)

Co-Author Publications:

6. Comparing the Two Perspectives of Reactive Quenching: Enhancing CO_2 Conversion and Dry Reforming of Methane
   Mercer E., Albrecht M., **De Meyer R.**, Fedirchyk I., Morais E., Bals S., Bogaerts A.
   Submitted to Chemical Engineering Journal

7. Direct visualization of ligands on gold nanoparticles in a liquid environment
   Pedrazo Tardajos A., Claes N., Wang D., Sánchez-Iglesias A., Nandi P., Jenkinson K., **De Meyer R.**, Liz Marzán L.M., Bals S.
   Nature Chemistry 16, 1278 (2024)

8. Effect of O_2 on Plasma-Based Dry Reforming of Methane: Revealing the Optimal Gas Composition via Experiments and Modeling of an Atmospheric Pressure Glow Discharge
   Maerivoet S., Wanten B., **De Meyer R.**, Van Hove M., Van Alphen S., Bogaerts A.
   ACS Sustainable Chemistry and Engineering 12, 11419 (2024)

9. Microwave plasma-based dry reforming of methane: Reaction performance and carbon formation
   Kelly S., Mercer E., **De Meyer R.**, Ciocarlan R.-G., Bals S., Bogaerts A.
   Journal of CO2 utilization 75, 102564 (2023)

10. Plasma-based CO2 conversion: How to correctly analyze the performance?
    Wanten B., Vertongen R., **De Meyer R.**, Bogaerts A.
    Journal of Energy Chemistry 86, 180 (2023)

11. Plasma-catalytic ammonia synthesis : packed catalysts act as plasma modifiers
    Ndayirinde C., Gorbanev Y., Ciocarlan R.-G., **De Meyer R.**, Smets A., Vlasov E., Bals S., Cool P., Bogaerts A.
    Catalysis Today 419, 114156 (2023)

2. Conference Contributions

Invited Talks:

1. CHEMampere colloquium, “We need to talk about plasma catalysis…”, January 2025, University of Stuttgart, Stuttgart, Germany

Oral Presentations:

2. iPlasmaNano, “*In situ* Plasma Studies using a DC Microplasma in a Scanning Electron Microscope”, September 2024, Hamburg, Germany

3. International Symposium on Plasmas for Catalysis and Energy Materials (ISPCEM), “Deposition of eroded electrode particles on packing material in packed-bed DBD”, July 2024, Eindhoven, The Netherlands.
   Best oral presentation award

4. International Symposium on Plasma Chemistry (ISPC), “Importance of plasma discharge characteristics in plasma-catalytic DRM and NH_3 synthesis”, May 2023, Kyoto, Japan

5. NANOLab day, “Towards a better understanding of plasma-catalyst interactions”, September 2022, Antwerp, Belgium

6. International Symposium on Plasma Catalysis for CO_2 Recycling (PIONEER), “Plasma catalysis for DRM and NH3 synthesis: Influence of catalyst morphology”, September 2022, Krakow, Poland

Poster Presentations:

7. Plasma Rolduc, "*In situ* Plasma Studies using a DC Microplasma in an SEM", April 2025, Kerkrade, The Netherlands

8. European Microscopy Congress (EMC), "*In situ* Plasma Studies using a DC Microplasma in an SEM", August 2024, Copenhagen, Denmark

9. Faculty Research Day, "*In situ* Plasma Studies using a DC Microplasma in an SEM", February 2024, Antwerp, Belgium.
   Best poster presentation award

10. NANOLab day, "*In situ* Plasma Studies using a DC Microplasma in an SEM", September 2023, Antwerp, Belgium

References

[1] World Meteorological Organization (WMO), State of the Global Climate 2024, (n.d.). https://library.wmo.int/records/item/69455-state-of-the-global-climate-2024 (accessed April 7, 2025).

[2] United Nations, Causes and Effects of Climate Change, (n.d.). https://www.un.org/en/climatechange/science/causes-effects-climate-change (accessed April 22, 2025).

[3] Net Zero by 2050 - A Roadmap for the Global Energy Sector, (2021). https://www.iea.org/reports/net-zero-by-2050.

[4] Greenhouse Gas Emissions from Energy Data Explorer – Data Tools, IEA (n.d.). https://www.iea.org/data-and-statistics/data-tools/greenhouse-gas-emissions-from-energy-data-explorer (accessed May 9, 2025).

[5] D.S. Mallapragada, Y. Dvorkin, M.A. Modestino, D.V. Esposito, W.A. Smith, B.-M. Hodge, M.P. Harold, V.M. Donnelly, A. Nuz, C. Bloomquist, K. Baker, L.C. Grabow, Y. Yan, N.N. Rajput, R.L. Hartman, E.J. Biddinger, E.S. Aydil, A.D. Taylor, Decarbonization of the chemical industry through electrification: Barriers and opportunities, Joule 7 (2023) 23–41. https://doi.org/10.1016/j.joule.2022.12.008.

[6] T. Nozaki, D.-Y. Kim, X. Chen, Plasma-enabled electrification of chemical processes toward decarbonization of society, Jpn. J. Appl. Phys. 63 (2024) 030101. https://doi.org/10.35848/1347-4065/ad280f.

[7] A. Fridman, Plasma Chemistry, Cambridge University Press, Cambridge, 2008. https://doi.org/10.1017/CBO9780511546075.

[8] A. Fridman, L. Kennedy, Plasma Physics and Engineering, 2nd ed, CRC Press, Boca Raton, FL, 2011. https://doi.org/10.1201/b11728.

[9] Maher I. Boulos, Pierre L. Fauchais, Emil Pfender, Handbook of Thermal Plasmas, 1st ed., Springer Cham, 2023. https://doi.org/10.1007/978-3-030-84936-8.

[10] U. Kogelschatz, Dielectric-Barrier Discharges: Their History, Discharge Physics, and Industrial Applications, Plasma Chem. Plasma Process. 23 (2003) 1–46. https://doi.org/10.1023/A:1022470901385.

[11] K.J. Kanarik, Inside the Mysterious World of Plasma: A Process Engineer's Perspective, J. Vac. Sci. Technol. 38 (2020) 031004. https://doi.org/10.1116/1.5141863.

[12] P.J. Bruggeman, F. Iza, R. Brandenburg, Foundations of atmospheric pressure non-equilibrium plasmas, Plasma Sources Sci. Technol. 26 (2017) 123002. https://doi.org/10.1088/1361-6595/aa97af.

[13] M. Kushner, M. Kong, Fundamentals of non-equilibrium plasmas, in: M. Laroussi, M.G. Kong, G. Morfill, W. Stolz (Eds.), Plasma Medicine, 1st ed., Cambridge University Press, 2012: pp. 7–27. https://doi.org/10.1017/CBO9780511902598.004.

[14] M.S. Cha, R. Snoeckx, Plasma Technology–Preparing for the Electrified Future, Front. Mech. Eng. 8 (2022) 903379. https://doi.org/10.3389/fmech.2022.903379.

[15] Deed - Attribution 4.0 International - Creative Commons, (n.d.). https://creativecommons.org/licenses/by/4.0/ (accessed April 23, 2025).

[16] A. Bogaerts, E.C. Neyts, O. Guaitella, A.B. Murphy, Foundations of plasma catalysis for environmental applications, Plasma Sources Sci. Technol. 31 (2022) 053002. https://doi.org/10.1088/1361-6595/ac5f8e.

[17] J.A. Dumesic, G.W. Huber, M. Boudart, Principles of Heterogeneous Catalysis, in: Handbook of Heterogeneous Catalysis, 2008. https://doi.org/10.1002/9783527610044.hetcat0001.

[18] K. Ollegott, P. Wirth, C. Oberste-Beulmann, P. Awakowicz, M. Muhler, Fundamental Properties and Applications of Dielectric Barrier Discharges in Plasma-Catalytic Processes at Atmospheric Pressure, Chem. Ing. Tech. 92 (2020) 1542–1558. https://doi.org/10.1002/cite.202000075.

[19] R. Brandenburg, Dielectric barrier discharges: progress on plasma sources and on the understanding of regimes and single filaments, Plasma Sources Sci. Technol. 26 (2017) 053001. https://doi.org/10.1088/1361-6595/aa6426.

[20] W. Siemens, Ueber die elektrostatische Induction und die Verzögerung des Stroms in Flaschendrähten, Annalen Der Physik 178 (1857) 66–122. https://doi.org/10.1002/andp.18571780905.

[21] R. Brandenburg, K.H. Becker, K.-D. Weltmann, Barrier Discharges in Science and Technology Since 2003: A Tribute and Update, Plasma Chem. Plasma Process. 43 (2023) 1303–1334. https://doi.org/10.1007/s11090-023-10364-5.

[22] F. Massines, N. Gherardi, N. Naudé, P. Ségur, Recent advances in the understanding of homogeneous dielectric barrier discharges, Eur. Phys. J. Appl. Phys. 47 (2009) 22805. https://doi.org/10.1051/epjap/2009064.

[23] S. Nijdam, J. Teunissen, U. Ebert, The physics of streamer discharge phenomena, Plasma Sources Sci. Technol. 29 (2020) 103001. https://doi.org/10.1088/1361-6595/abaa05.

[24] R. Brandenburg, V.A. Maiorov, Y.B. Golubovskii, H.-E. Wagner, J. Behnke, J.F. Behnke, Diffuse barrier discharges in nitrogen with small admixtures of oxygen: discharge mechanism and transition to the filamentary regime, J. Phys. D: Appl. Phys. 38 (2005) 2187–2197. https://doi.org/10.1088/0022-3727/38/13/017.

[25] N. Naudé, J.-P. Cambronne, N. Gherardi, F. Massines, Electrical model and analysis of the transition from an atmospheric pressure Townsend discharge to a filamentary discharge, J. Phys. D: Appl. Phys. 38 (2005) 530–538. https://doi.org/10.1088/0022-3727/38/4/004.

[26] C. Bajon, S. Dap, A. Belinger, O. Guaitella, T. Hoder, N. Naudé, Homogeneous dielectric barrier discharge in CO_2, Plasma Sources Sci. Technol. 32 (2023) 045012. https://doi.org/10.1088/1361-6595/acc9d9.

[27] N. Osawa, A. Takashi, Y. Yoshioka, R. Hanaoka, Generation of high pressure homogeneous dielectric barrier discharge in air, Eur. Phys. J. Appl. Phys. 61 (2013) 24317. https://doi.org/10.1051/epjap/2012120398.

[28] A. Bogaerts, X. Tu, J.C. Whitehead, G. Centi, L. Lefferts, O. Guaitella, F. Azzolina-Jury, H.-H. Kim, A.B. Murphy, W.F. Schneider, T. Nozaki, J.C. Hicks, A. Rousseau, F. Thevenet, A. Khacef, M. Carreon, The 2020 plasma catalysis roadmap, J. Phys. D: Appl. Phys. 53 (2020) 443001. https://doi.org/10.1088/1361-6463/ab9048.

[29] J. Van Turnhout, K. Rouwenhorst, L. Lefferts, A. Bogaerts, Plasma catalysis: What is needed to create synergy?, EES Catal. (2025) 10.1039.D5EY00027K. https://doi.org/10.1039/D5EY00027K.

[30] J.C. Whitehead, Plasma–catalysis: the known knowns, the known unknowns and the unknown unknowns, J. Phys. D: Appl. Phys. 49 (2016) 243001. https://doi.org/10.1088/0022-3727/49/24/243001.

[31] Y. Gorbanev, Y. Engelmann, K. van't Veer, E. Vlasov, C. Ndayirinde, Y. Yi, S. Bals, A. Bogaerts, Al2O3-Supported Transition Metals for Plasma-Catalytic NH3 Synthesis in a DBD Plasma: Metal Activity and Insights into Mechanisms, Catalysts 11 (2021). https://doi.org/10.3390/catal11101230.

[32] P. Barboun, P. Mehta, F.A. Herrera, D.B. Go, W.F. Schneider, J.C. Hicks, Distinguishing Plasma Contributions to Catalyst Performance in Plasma-Assisted Ammonia Synthesis, ACS Sustain. Chem. Eng. 7 (2019) 8621–8630. https://doi.org/10.1021/acssuschemeng.9b00406.

[33] X. Tu, H.J. Gallon, M.V. Twigg, P.A. Gorry, J.C. Whitehead, Dry reforming of methane over a Ni/Al2O3 catalyst in a coaxial dielectric barrier discharge reactor, J. Phys. D: Appl. Phys. 44 (2011) 274007. https://doi.org/10.1088/0022-3727/44/27/274007.

[34] L. Brune, A. Ozkan, E. Genty, T. Visart de Bocarmé, F. Reniers, Dry reforming of methane via plasma-catalysis: influence of the catalyst nature supported on alumina in a packed-bed DBD configuration, J. Phys. D: Appl. Phys. 51 (2018) 234002. https://doi.org/10.1088/1361-6463/aac047.

[35] Z. Farshidrokh, M.R. Khani, A. Khodadadi, M. Gharibi, B. Shokri, Dry Reforming of Methane over Ni/γ-MgO Catalysts in a Coaxial Dielectric Barrier Discharge Reactor, Chem. Eng. Technol. 44 (2021) 589–599. https://doi.org/10.1002/ceat.202000455.

[36] T. Suttikul, S. Nuchdang, D. Rattanaphra, C. Phalakornkule, Influence of Operating Parameters, Al2O3 and Ni/Al2O3 Catalysts on Plasma-Assisted CO2 Reforming of CH4 in a Parallel Plate Dielectric Barrier Discharge for High H2/CO Ratio Syngas Production, Plasma Chem. Plasma Process. 40 (2020) 1445–1463. https://doi.org/10.1007/s11090-020-10118-7.

[37] C. Ndayirinde, Y. Gorbanev, R.-G. Ciocarlan, R. De Meyer, A. Smets, E. Vlasov, S. Bals, P. Cool, A. Bogaerts, Plasma-catalytic ammonia synthesis: Packed catalysts act as plasma modifiers, Catal. Today (2023) 114156. https://doi.org/10.1016/j.cattod.2023.114156.

[38] Y. Uytdenhouwen, S. Van Alphen, I. Michielsen, V. Meynen, P. Cool, A. Bogaerts, A packed-bed DBD micro plasma reactor for CO2 dissociation: Does size matter?, Chem. Eng. J. 348 (2018) 557–568. https://doi.org/10.1016/j.cej.2018.04.210.

[39] T. Butterworth, R. Elder, R. Allen, Effects of particle size on CO2 reduction and discharge characteristics in a packed bed plasma reactor, Chem. Eng. J. 293 (2016) 55–67. https://doi.org/10.1016/j.cej.2016.02.047.

[40] L.L. Alves, M.M. Becker, J. van Dijk, T. Gans, D.B. Go, K. Stapelmann, J. Tennyson, M.M. Turner, M.J. Kushner, Foundations of plasma standards, Plasma Sources Sci. Technol. 32 (2023) 023001. https://doi.org/10.1088/1361-6595/acb810.

[41] H. Luo, J. Jiao, K. Liu, Y. Yue, X. Wang, Characteristics of Shallow Traps in the Dielectric Surface and Their Effects on Diffuse Dielectric Barrier Discharge in Air, IEEE Trans. Plasma Sci. 45 (2017) 749–753. https://doi.org/10.1109/TPS.2017.2679210.

[42] A. Belinger, J. Haton, B. Lina, E. Sammier, S. Dap, L. Stafford, N. Naudé, Impact of the memory effect on the homogeneity of a Townsend Dielectric Barrier Discharge in air, in: ISPC25 Conference proceedings, 2023.

[43] E.C. Neyts, K. (Ken) Ostrikov, M.K. Sunkara, A. Bogaerts, Plasma Catalysis: Synergistic Effects at the Nanoscale, Chem. Rev. 115 (2015) 13408–13446. https://doi.org/10.1021/acs.chemrev.5b00362.

[44] E.C. Neyts, Plasma-Surface Interactions in Plasma Catalysis, Plasma Chem. Plasma Process. 36 (2016) 185–212. https://doi.org/10.1007/s11090-015-9662-5.

[45] M. Wilson, J. DeRose, C. Greb, Microscope Resolution: Concepts, Factors and Calculation, (2023). https://www.leica-microsystems.com/science-lab/life-science/microscope-resolution-concepts-factors-and-calculation/ (accessed April 21, 2025).

[46] wavelength of electron | Glossary | JEOL Ltd., Wavelength of Electron | Glossary | JEOL Ltd. (n.d.). https://www.jeol.com/ (accessed April 21, 2025).

[47] D.B. Williams, C.B. Carter, Transmission Electron Microscopy, Springer US, Boston, MA, 2009. https://doi.org/10.1007/978-0-387-76501-3.

[48] W. Van Den Broek, A. Rosenauer, B. Goris, G.T. Martinez, S. Bals, S. Van Aert, D. Van Dyck, Correction of non-linear thickness effects in HAADF STEM electron tomography, Ultramicroscopy 116 (2012) 8–12. https://doi.org/10.1016/j.ultramic.2012.03.005.

[49] K.J. Batenburg, S. Bals, J. Sijbers, C. Kübel, P.A. Midgley, J.C. Hernandez, U. Kaiser, E.R. Encina, E.A. Coronado, G. Van Tendeloo, 3D imaging of nanomaterials by discrete

tomography, Ultramicroscopy 109 (2009) 730–740. https://doi.org/10.1016/j.ultramic.2009.01.009.

[50] J.I. Goldstein, D.E. Newbury, J.R. Michael, N.W.M. Ritchie, J.H.J. Scott, D.C. Joy, Scanning Electron Microscopy and X-Ray Microanalysis, Springer New York, New York, NY, 2018. https://doi.org/10.1007/978-1-4939-6676-9.

[51] What is WDS? | Wavelength Dispersive Spectroscopy, (n.d.). https://www.bruker.com/en/landingpages/bna/technology/what-is-wds.html (accessed April 22, 2025).

[52] T.C. Manley, The Electric Characteristics of the Ozonator Discharge, Trans. Electrochem. Soc. 84 (1943) 83. https://doi.org/10.1149/1.3071556.

[53] Floran Peeters, Tom Butterworth, Electrical Diagnostics of Dielectric Barrier Discharges, in: Anton Nikiforov, Zhiqiang Chen (Eds.), Atmospheric Pressure Plasma, IntechOpen, Rijeka, 2018: p. Ch. 2. https://doi.org/10.5772/intechopen.80433.

[54] Y. Zeng, X. Zhu, D. Mei, B. Ashford, X. Tu, Plasma-catalytic dry reforming of methane over γ-Al2O3 supported metal catalysts, Catal. Today 256 (2015) 80–87. https://doi.org/10.1016/j.cattod.2015.02.007.

[55] M.L. Carreon, Plasma catalytic ammonia synthesis: state of the art and future directions, J. Phys. D: Appl. Phys. 52 (2019) 483001. https://doi.org/10.1088/1361-6463/ab3b2c.

[56] R. Snoeckx, A. Bogaerts, Plasma technology – a novel solution for CO_2 conversion?, Chem. Soc. Rev. 46 (2017) 5805–5863. https://doi.org/10.1039/C6CS00066E.

[57] K.H.R. Rouwenhorst, Y. Engelmann, K. van 't Veer, R.S. Postma, A. Bogaerts, L. Lefferts, Plasma-driven catalysis: green ammonia synthesis with intermittent electricity, Green Chem. 22 (2020) 6258–6287. https://doi.org/10.1039/D0GC02058C.

[58] X. Tu, H.J. Gallon, J.C. Whitehead, Electrical and spectroscopic diagnostics of a single-stage plasma-catalysis system: effect of packing with TiO2, J. Phys. D: Appl. Phys. 44 (2011) 482003. https://doi.org/10.1088/0022-3727/44/48/482003.

[59] B. Loenders, R. Michiels, A. Bogaerts, Is a catalyst always beneficial in plasma catalysis? Insights from the many physical and chemical interactions, J. Energy Chem. (2023). https://doi.org/10.1016/j.jechem.2023.06.016.

[60] R. Snoeckx, Y.X. Zeng, X. Tu, A. Bogaerts, Plasma-based dry reforming: improving the conversion and energy efficiency in a dielectric barrier discharge, RSC Adv. 5 (2015) 29799–29808. https://doi.org/10.1039/C5RA01100K.

[61] K. van 't Veer, Y. Engelmann, F. Reniers, A. Bogaerts, Plasma-Catalytic Ammonia Synthesis in a DBD Plasma: Role of Microdischarges and Their Afterglows, J. Phys. Chem. C 124 (2020) 22871–22883. https://doi.org/10.1021/acs.jpcc.0c05110.

[62] J.A. Andersen, M.C. Holm, K. van 't Veer, J.M. Christensen, M. Østberg, A. Bogaerts, A.D. Jensen, Plasma-catalytic ammonia synthesis in a dielectric barrier discharge reactor: A combined experimental study and kinetic modeling, Chem. Eng. J. 457 (2023) 141294. https://doi.org/10.1016/j.cej.2023.141294.

[63] G. Chen, J. Qu, P. Cheah, D. Cao, Y. Zhao, Y. Xiang, Size-Dependent Activity of Iron Nanoparticles in Both Thermal and Plasma Driven Catalytic Ammonia Decomposition, Ind. Eng. Chem. Res. 61 (2022) 11436–11443. https://doi.org/10.1021/acs.iecr.2c02092.

[64] Y. Zhang, S. Li, Z. Yuan, H. Chen, X. Fan, Mechanochemical Synthesis of RuCo/MgTiO3 Catalysts for Nonthermal Plasma-Assisted Ammonia Synthesis, Ind. Eng. Chem. Res. 61 (2022) 14199–14210. https://doi.org/10.1021/acs.iecr.2c02216.

[65] X. Zhu, X. Hu, X. Wu, Y. Cai, H. Zhang, X. Tu, Ammonia synthesis over γ-Al2O3 pellets in a packed-bed dielectric barrier discharge reactor, J. Phys. D: Appl. Phys. 53 (2020) 164002. https://doi.org/10.1088/1361-6463/ab6cd1.

[66] K.H.R. Rouwenhorst, H.G.B. Burbach, D.W. Vogel, J. Núñez Paulí, B. Geerdink, L. Lefferts, Plasma-catalytic ammonia synthesis beyond thermal equilibrium on Ru-based catalysts in non-thermal plasma, Catal. Sci. Technol. 11 (2021) 2834–2843. https://doi.org/10.1039/D0CY02189J.

[67] J.A. Andersen, J.M. Christensen, M. Østberg, A. Bogaerts, A.D. Jensen, Plasma-catalytic dry reforming of methane: Screening of catalytic materials in a coaxial packed-bed DBD reactor, Chem. Eng. J. 397 (2020) 125519. https://doi.org/10.1016/j.cej.2020.125519.

[68] A.H. Khoja, M. Tahir, N.A.S. Amin, A. Javed, M.T. Mehran, Kinetic study of dry reforming of methane using hybrid DBD plasma reactor over La2O3 co-supported Ni/MgAl2O4 catalyst, Int. J. Hydrog. Energy 45 (2020) 12256–12271. https://doi.org/10.1016/j.ijhydene.2020.02.200.

[69] Y. Uytdenhouwen, K.M. Bal, E.C. Neyts, V. Meynen, P. Cool, A. Bogaerts, On the kinetics and equilibria of plasma-based dry reforming of methane, Chem. Eng. J. 405 (2021) 126630. https://doi.org/10.1016/j.cej.2020.126630.

[70] L. Wang, Y. Wang, L. Fan, H. Xu, B. Liu, J. Zhang, Y. Zhu, X. Tu, Direct conversion of CH4 and CO2 to alcohols using plasma catalysis over Cu/Al(OH)3 catalysts, Chem. Eng. J. 466 (2023) 143347. https://doi.org/10.1016/j.cej.2023.143347.

[71] W.-C. Chung, K.-L. Pan, H.-M. Lee, M.-B. Chang, Dry Reforming of Methane with Dielectric Barrier Discharge and Ferroelectric Packed-Bed Reactors, Energy Fuels 28 (2014) 7621–7631. https://doi.org/10.1021/ef5020555.

[72] D. Mei, M. Sun, S. Liu, P. Zhang, Z. Fang, X. Tu, Plasma-enabled catalytic dry reforming of CH4 into syngas, hydrocarbons and oxygenates: Insight into the active metals of γ-Al2O3 supported catalysts, J. CO2 Util. 67 (2023) 102307. https://doi.org/10.1016/j.jcou.2022.102307.

[73] D. Mei, G. Duan, J. Fu, S. Liu, R. Zhou, R. Zhou, Z. Fang, P.J. Cullen, K. (Ken) Ostrikov, CO2 reforming of CH4 in single and double dielectric barrier discharge reactors: Comparison of discharge characteristics and product distribution, J. CO2 Util. 53 (2021) 101703. https://doi.org/10.1016/j.jcou.2021.101703.

[74] F. Gorky, J.M. Lucero, J.M. Crawford, B.A. Blake, S.R. Guthrie, M.A. Carreon, M.L. Carreon, Insights on cold plasma ammonia synthesis and decomposition using alkaline earth metal-based perovskites, Catal. Sci. Technol. 11 (2021) 5109–5118. https://doi.org/10.1039/D1CY00729G.

[75] J. Hong, M. Aramesh, O. Shimoni, D.H. Seo, S. Yick, A. Greig, C. Charles, S. Prawer, A.B. Murphy, Plasma Catalytic Synthesis of Ammonia Using Functionalized-Carbon Coatings in an Atmospheric-Pressure Non-equilibrium Discharge, Plasma Chem. Plasma Process. 36 (2016) 917–940. https://doi.org/10.1007/s11090-016-9711-8.

[76] B.S. Patil, A.S.R. van Kaathoven, F.J.J. Peeters, N. Cherkasov, J. Lang, Q. Wang, V. Hessel, Deciphering the synergy between plasma and catalyst support for ammonia synthesis in a packed dielectric barrier discharge reactor, J. Phys. D: Appl. Phys. 53 (2020) 144003. https://doi.org/10.1088/1361-6463/ab6a36.

[77] S. Li, T. van Raak, F. Gallucci, Investigating the operation parameters for ammonia synthesis in dielectric barrier discharge reactors, J. Phys. D: Appl. Phys. 53 (2019) 014008. https://doi.org/10.1088/1361-6463/ab4b37.

[78] J. Liu, X. Zhu, X. Hu, F. Zhang, X. Tu, Plasma-assisted ammonia synthesis in a packed-bed dielectric barrier discharge reactor: effect of argon addition, Vacuum 197 (2022) 110786. https://doi.org/10.1016/j.vacuum.2021.110786.

[79] F.A. Herrera, G.H. Brown, P. Barboun, N. Turan, P. Mehta, W.F. Schneider, J.C. Hicks, D.B. Go, The impact of transition metal catalysts on macroscopic dielectric barrier discharge (DBD) characteristics in an ammonia synthesis plasma catalysis reactor, J. Phys. D: Appl. Phys. 52 (2019) 224002. https://doi.org/10.1088/1361-6463/ab0c58.

[80] Y. Wang, M. Craven, X. Yu, J. Ding, P. Bryant, J. Huang, X. Tu, Plasma-Enhanced Catalytic Synthesis of Ammonia over a Ni/Al2O3 Catalyst at Near-Room Temperature: Insights into the Importance of the Catalyst Surface on the Reaction Mechanism, ACS Catal. 9 (2019) 10780–10793. https://doi.org/10.1021/acscatal.9b02538.

[81] B.S. Patil, N. Cherkasov, N.V. Srinath, J. Lang, A.O. Ibhadon, Q. Wang, V. Hessel, The role of heterogeneous catalysts in the plasma-catalytic ammonia synthesis, Catal. Today 362 (2021) 2–10. https://doi.org/10.1016/j.cattod.2020.06.074.

[82] J.A. Andersen, J.M. Christensen, M. Østberg, A. Bogaerts, A.D. Jensen, Plasma-catalytic ammonia decomposition using a packed-bed dielectric barrier discharge reactor, Int. J. Hydrog. Energy 47 (2022) 32081–32091. https://doi.org/10.1016/j.ijhydene.2022.07.102.

[83] B.S. Patil, N. Cherkasov, J. Lang, A.O. Ibhadon, V. Hessel, Q. Wang, Low temperature plasma-catalytic NOx synthesis in a packed DBD reactor: Effect of support materials and supported active metal oxides, Appl. Catal. B: Environ. 194 (2016) 123–133. https://doi.org/10.1016/j.apcatb.2016.04.055.

[84] T. Butterworth, R. Elder, R. Allen, Effects of particle size on CO2 reduction and discharge characteristics in a packed bed plasma reactor, Chem. Eng. J. 293 (2016) 55–67. https://doi.org/10.1016/j.cej.2016.02.047.

[85] D. Mei, X. Zhu, Y.-L. He, J.D. Yan, X. Tu, Plasma-assisted conversion of CO2 in a dielectric barrier discharge reactor: understanding the effect of packing materials, Plasma Sources Sci. Technol. 24 (2014) 015011. https://doi.org/10.1088/0963-0252/24/1/015011.

[86] F.J.J. Peeters, M.C.M. van de Sanden, The influence of partial surface discharging on the electrical characterization of DBDs, Plasma Sources Sci. Technol. 24 (2014) 015016. https://doi.org/10.1088/0963-0252/24/1/015016.

[87] B. Seynnaeve, J. Lauwaert, P. Van Der Voort, A. Verberckmoes, Comprehensive Model for the Synthesis of γ-Al_2O_3 Microsphere-Supported Bimetallic Iron- and Copper Oxide Materials, ACS Omega 7 (2022) 41796–41803. https://doi.org/10.1021/acsomega.2c06273.

[88] X. Gao, Z. Lin, T. Li, L. Huang, J. Zhang, S. Askari, N. Dewangan, A. Jangam, S. Kawi, Recent Developments in Dielectric Barrier Discharge Plasma-Assisted Catalytic Dry Reforming of Methane over Ni-Based Catalysts, Catalysts 11 (2021) 455. https://doi.org/10.3390/catal11040455.

[89] K. Stanley, S. Kelly, J.A. Sullivan, Effect of Ni NP morphology on catalyst performance in non-thermal plasma-assisted dry reforming of methane, Appl. Catal. B: Environ. 328 (2023) 122533. https://doi.org/10.1016/j.apcatb.2023.122533.

[90] X. Li, Y. Jiao, Y. Cui, C. Dai, P. Ren, C. Song, X. Ma, Synergistic Catalysis of the Synthesis of Ammonia with Co-Based Catalysts and Plasma: From Nanoparticles to a Single Atom, ACS Appl. Mater. Interfaces 13 (2021) 52498–52507. https://doi.org/10.1021/acsami.1c12695.

[91] Y. Uytdenhouwen, V. Meynen, P. Cool, A. Bogaerts, The Potential Use of Core-Shell Structured Spheres in a Packed-Bed DBD Plasma Reactor for CO2 Conversion, Catalysts 10 (2020). https://doi.org/10.3390/catal10050530.

[92] A. Nanakoudis, SEM: Types of Electrons and the Information They Provide, Advancing Materials (2019). https://www.thermofisher.com/blog/materials/sem-signal-types-electrons-and-the-information-they-provide/ (accessed September 22, 2023).

[93] What does Bronkhorst mean by ln/min or ls/min?, Bronkhorst (n.d.). https://www.bronkhorst.com/int/service-support-1/faq/flow-theory/what-does-bronkhorst-mean-by-ln-min-or-ls-min/ (accessed February 28, 2023).

[94] N. Pinhão, A. Moura, J.B. Branco, J. Neves, Influence of gas expansion on process parameters in non-thermal plasma plug-flow reactors: A study applied to dry reforming of methane, Int. J. Hydrog. Energy 41 (2016) 9245–9255. https://doi.org/10.1016/j.ijhydene.2016.04.148.

[95] B. Wanten, R. Vertongen, R. De Meyer, A. Bogaerts, Plasma-based CO2 conversion: How to correctly analyze the performance?, J. Energy Chem. (2023). https://doi.org/10.1016/j.jechem.2023.07.005.

[96] Y. Uytdenhouwen, K.M. Bal, I. Michielsen, E.C. Neyts, V. Meynen, P. Cool, A. Bogaerts, How process parameters and packing materials tune chemical equilibrium and kinetics in plasma-based CO2 conversion, Chem. Eng. J. 372 (2019) 1253–1264. https://doi.org/10.1016/j.cej.2019.05.008.

[97] N. Jidenko, M. Petit, J.P. Borra, Electrical characterization of microdischarges produced by dielectric barrier discharge in dry air at atmospheric pressure, J. Phys. D: Appl. Phys. 39 (2006) 281–293. https://doi.org/10.1088/0022-3727/39/2/008.

[98] 4100.pdf, (n.d.). https://www.pearsonelectronics.com/pdf/4100.pdf (accessed March 28, 2023).

[99] Bueno, Mayer, Weber, Bechelany, Klotz, Farrusseng, Impregnation Protocols on Alumina Beads for Controlling the Preparation of Supported Metal Catalysts, Catalysts 9 (2019) 577. https://doi.org/10.3390/catal9070577.

[100] B. Seynnaeve, J. Lauwaert, P. Vermeir, P. Van Der Voort, A. Verberckmoes, Model-based control of iron- and copper oxide particle distributions in porous γ-Al2O3 microspheres through careful tuning of the interactions during impregnation, Mater. Chem. Phys. 276 (2022) 125428. https://doi.org/10.1016/j.matchemphys.2021.125428.

[101] V.A. Hackley, A.B. Stefaniak, “Real-world” precision, bias, and between-laboratory variation for surface area measurement of a titanium dioxide nanomaterial in powder form, J. Nanoparticle Res. 15 (2013) 1742. https://doi.org/10.1007/s11051-013-1742-y.

[102] Nicolas Gherardi, Gamal Gouda, Eric Gat, André Ricard, François Massines, Transition from glow silent discharge to micro-discharges in nitrogen gas, Plasma Sources Sci. Technol. 9 (2000) 340. https://doi.org/10.1088/0963-0252/9/3/312.

[103] H.-H. Kim, Y. Teramoto, A. Ogata, Time-resolved imaging of positive pulsed corona-induced surface streamers on TiO_2 and γ-Al_2O_3-supported Ag catalysts, J. Phys. D: Appl. Phys. 49 (2016) 415204. https://doi.org/10.1088/0022-3727/49/41/415204.

[104] S. Suzuki, H. Itoh, Gradual increase in secondary ionization coefficient γ and charge accumulation on a dielectric electrode during DBD with repeated breakdown, Plasma Sources Sci. Technol. 24 (2015) 055016. https://doi.org/10.1088/0963-0252/24/5/055016.

[105] M.A. Cazalilla, N. Lorente, R.D. Muiño, J.-P. Gauyacq, D. Teillet-Billy, P.M. Echenique, Theory of Auger neutralization and deexcitation of slow ions at metal surfaces, Phys. Rev. B 58 (1998) 13991–14006. https://doi.org/10.1103/PhysRevB.58.13991.

[106] B. Bhushan, ed., Cold Field Electron Emission from Nanostructured Materials, in: Encyclopedia of Nanotechnology, Springer Netherlands, Dordrecht, 2016: pp. 604–604. https://doi.org/10.1007/978-94-017-9780-1_100190.

[107] J. Kruszelnicki, K.W. Engeling, J.E. Foster, Z. Xiong, M.J. Kushner, Propagation of negative electrical discharges through 2-dimensional packed bed reactors, J. Phys. D: Appl. Phys. 50 (2016) 025203. https://doi.org/10.1088/1361-6463/50/2/025203.

[108] W. Wang, H.-H. Kim, K. Van Laer, A. Bogaerts, Streamer propagation in a packed bed plasma reactor for plasma catalysis applications, Chem. Eng. J. 334 (2018) 2467–2479. https://doi.org/10.1016/j.cej.2017.11.139.

[109] R. Snoeckx, R. Aerts, X. Tu, A. Bogaerts, Plasma-Based Dry Reforming: A Computational Study Ranging from the Nanoseconds to Seconds Time Scale, J. Phys. Chem. C 117 (2013) 4957–4970. https://doi.org/10.1021/jp311912b.

[110] J. Van Turnhout, D. Aceto, A. Travert, P. Bazin, F. Thibault-Starzyk, A. Bogaerts, F. Azzolina-Jury, Observation of surface species in plasma-catalytic dry reforming of methane in a novel atmospheric pressure dielectric barrier discharge *in situ* IR cell, Catal. Sci. Technol. 12 (2022) 6676–6686. https://doi.org/10.1039/D2CY00311B.

[111] A. Parastaev, N. Kosinov, E.J.M. Hensen, Mechanistic study of catalytic CO_2 hydrogenation in a plasma by operando DRIFT spectroscopy, J. Phys. D: Appl. Phys. 54 (2021) 264004. https://doi.org/10.1088/1361-6463/abeb96.

[112] E.K. Gibson, C.E. Stere, B. Curran-McAteer, W. Jones, G. Cibin, D. Gianolio, A. Goguet, P.P. Wells, C.R.A. Catlow, P. Collier, P. Hinde, C. Hardacre, Probing the Role of a Non-Thermal Plasma (NTP) in the Hybrid NTP Catalytic Oxidation of Methane, Angew. Chem. Int. Ed. 56 (2017) 9351–9355. https://doi.org/10.1002/anie.201703550.

[113] Y. Engelmann, P. Mehta, E.C. Neyts, W.F. Schneider, A. Bogaerts, Predicted Influence of Plasma Activation on Nonoxidative Coupling of Methane on Transition Metal Catalysts, ACS Sustain. Chem. Eng. 8 (2020) 6043–6054. https://doi.org/10.1021/acssuschemeng.0c00906.

[114] L. Hollevoet, E. Vervloessem, Y. Gorbanev, A. Nikiforov, N. De Geyter, A. Bogaerts, J.A. Martens, Energy-Efficient Small-Scale Ammonia Synthesis Process with Plasma-Enabled Nitrogen Oxidation and Catalytic Reduction of Adsorbed NOx, ChemSusChem 15 (2022) e202102526. https://doi.org/10.1002/cssc.202102526.

[115] Y. Engelmann, K. Van 'T Veer, Y. Gorbanev, E.C. Neyts, W.F. Schneider, A. Bogaerts, Plasma Catalysis for Ammonia Synthesis: A Microkinetic Modeling Study on the Contributions of Eley–Rideal Reactions, ACS Sustain. Chem. Eng. 9 (2021) 13151–13163. https://doi.org/10.1021/acssuschemeng.1c02713.

[116] G. Borcia, C.A. Anderson, N.M.D. Brown, Dielectric barrier discharge for surface treatment: application to selected polymers in film and fibre form, Plasma Sources Sci. Technol. 12 (2003) 335–344. https://doi.org/10.1088/0963-0252/12/3/306.

[117] H.-E. Wagner, R. Brandenburg, K.V. Kozlov, A. Sonnenfeld, P. Michel, J.F. Behnke, The barrier discharge: basic properties and applications to surface treatment, Vacuum 71 (2003) 417–436. https://doi.org/10.1016/S0042-207X(02)00765-0.

[118] M.H. Lapena, C.M.A. Lopes, Improvement of aerospace thermoplastic composite adhesion to coating with dielectric barrier discharge atmospheric pressure plasma surface treatment, Plasma Process. Polym. 20 (2023) 2200081. https://doi.org/10.1002/ppap.202200081.

[119] P. Mierczynski, A. Mierczynska-Vasilev, M. Szynkowska-Jozwik, K. Vasilev, Atmospheric plasma in the preparation and pre-treatment of catalytic materials – A mini review, Catal. Commun. 187 (2024) 106839. https://doi.org/10.1016/j.catcom.2023.106839.

[120] Z. Wang, Y. Zhang, E.C. Neyts, X. Cao, X. Zhang, B.W.-L. Jang, C. Liu, Catalyst Preparation with Plasmas: How Does It Work?, ACS Catal. 8 (2018) 2093–2110. https://doi.org/10.1021/acscatal.7b03723.

[121] A.H. Khoja, M. Tahir, N.A.S. Amin, Cold plasma dielectric barrier discharge reactor for dry reforming of methane over Ni/ɤ-Al2O3-MgO nanocomposite, Fuel Process. Technol. 178 (2018) 166–179. https://doi.org/10.1016/j.fuproc.2018.05.030.

[122] J. He, X. Wen, L. Wu, H. Chen, J. Hu, X. Hou, Dielectric barrier discharge plasma for nanomaterials: Fabrication, modification and analytical applications, Trends Anal. Chem. 156 (2022) 116715. https://doi.org/10.1016/j.trac.2022.116715.

[123] N. HafezKhiabani, S. Fathi, B. Shokri, S.I. Hosseini, A novel method for decoking of Pt–Sn/Al2O3 in the naphtha reforming process using RF and pin-to-plate DBD plasma systems, Appl. Catal. A: Gen. 493 (2015) 8–16. https://doi.org/10.1016/j.apcata.2014.12.041.

[124] M. Kim, J. Jeoung, J. Kim, K.-S. Ha, Regeneration of deactivated H-ZSM-5 for aromatization by dielectric barrier discharge plasma, Appl. Catal. A: Gen. 575 (2019) 214–222. https://doi.org/10.1016/j.apcata.2019.02.027.

[125] T.M.C. Nishime, N. Wannicke, S. Horn, K.-D. Weltmann, H. Brust, A Coaxial Dielectric Barrier Discharge Reactor for Treatment of Winter Wheat Seeds, Appl. Sci. 10 (2020) 7133. https://doi.org/10.3390/app10207133.

[126] S. Roy, B. Choudhury, J. Johnson, A. Schindler-Tyka, Application of dielectric barrier discharge for improving food shelf life and reducing spoilage, Sci. Rep. 11 (2021) 19200. https://doi.org/10.1038/s41598-021-96887-3.

[127] D.A. Laroque, S.T. Seó, G.A. Valencia, J.B. Laurindo, B.A.M. Carciofi, Cold plasma in food processing: Design, mechanisms, and application, J. Food Eng. 312 (2022) 110748. https://doi.org/10.1016/j.jfoodeng.2021.110748.

[128] G. Daeschlein, S. Scholz, R. Ahmed, T. Von Woedtke, H. Haase, M. Niggemeier, E. Kindel, R. Brandenburg, K.-D. Weltmann, M. Juenger, Skin decontamination by low-temperature atmospheric pressure plasma jet and dielectric barrier discharge plasma, J. Hosp. Infect. 81 (2012) 177–183. https://doi.org/10.1016/j.jhin.2012.02.012.

[129] R.E. Hanson, N.M. Houser, P. Lavoie, Dielectric material degradation monitoring of dielectric barrier discharge plasma actuators, J. Appl. Phys. 115 (2014) 043301. https://doi.org/10.1063/1.4862309.

[130] D. Bian, Y. Wu, C. Long, B. Lin, Effects of material degradation on electrical and optical characteristics of surface dielectric barrier discharge, J. Appl. Phys. 124 (2018) 183301. https://doi.org/10.1063/1.5049463.

[131] A. Wang, Z. Tian, Y. Peng, H. Wang, M. Zhang, S. Sun, Z. Hou, The time evolution of electrical and thermodynamic characteristics of surface dielectric barrier discharge caused by dielectric degradation, J. Phys. D: Appl. Phys. 57 (2024) 445203. https://doi.org/10.1088/1361-6463/ad632e.

[132] R.T. Nguyen-Smith, A. Böddecker, L. Schücke, N. Bibinov, I. Korolov, Q.-Z. Zhang, T. Mussenbrock, P. Awakowicz, J. Schulze, µs and ns twin surface dielectric barrier discharges operated in air: from electrode erosion to plasma characteristics, Plasma Sources Sci. Technol. 31 (2022) 035008. https://doi.org/10.1088/1361-6595/ac5452.

[133] I. Selivonin, A. Lazukin, I. Moralev, S. Krivov, I. Roslyakov, Erosion of the sputtered electrodes in the surface barrier discharge, J. Phys. Conf. Ser. 1394 (2019) 012027. https://doi.org/10.1088/1742-6596/1394/1/012027.

[134] I. Selivonin, I. Moralev, Microdischarges properties in sDBD: the role of the exposed electrode oxidation, Plasma Sources Sci. Technol. 30 (2020) 035005. https://doi.org/10.1088/1361-6595/abe0a1.

[135] H.W. Lilliefors, On the Kolmogorov-Smirnov Test for Normality with Mean and Variance Unknown, J. Am. Stat. Assoc. 62 (1967) 399–402. https://doi.org/10.1080/01621459.1967.10482916.

[136] J. Ráhel, Z. Szalay, J. Čech, T. Morávek, On spatial stabilization of dielectric barrier discharge microfilaments by residual heat build-up in air, Eur. Phys. J. D 70 (2016) 92. https://doi.org/10.1140/epjd/e2016-70061-5.

[137] N.Y. Babaeva, M.J. Kushner, Ion energy and angular distributions onto polymer surfaces delivered by dielectric barrier discharge filaments in air: I. Flat surfaces, Plasma Sources Sci. Technol. 20 (2011) 035017. https://doi.org/10.1088/0963-0252/20/3/035017.

[138] N.Y. Babaeva, N. Ning, D.B. Graves, M.J. Kushner, Ion activation energy delivered to wounds by atmospheric pressure dielectric-barrier discharges: sputtering of lipid-like surfaces, J. Phys. D: Appl. Phys. 45 (2012) 115203. https://doi.org/10.1088/0022-3727/45/11/115203.

[139] Y. Yamamura, H. Tawara, Energy dependence of ion-induced sputtering yields from monatomic solids at normal incidence, At. Data Nucl. Data Tables 62 (1996) 149–253. https://doi.org/10.1006/adnd.1996.0005.

[140] N.A. Mauchamp, S. Hamaguchi, Why are physical sputtering yields similar for incident ions with different masses?—physical sputtering yields of the Lennard–Jones system, J. Phys. D: Appl. Phys. 55 (2022) 225209. https://doi.org/10.1088/1361-6463/ac57dc.

[141] G.A. Mesyats, Ecton mechanism of the vacuum arc cathode spot, IEEE Trans. Plasma Sci. 23 (1995) 879–883. https://doi.org/10.1109/27.476469.

[142] G.A. Mesyats, Ecton Mechanism of the Cathode Spot Phenomena in a Vacuum Arc, IEEE Trans. Plasma Sci. 41 (2013) 676–694. https://doi.org/10.1109/TPS.2013.2247064.

[143] R. Vertongen, G. De Felice, H. Van Den Bogaard, F. Gallucci, A. Bogaerts, S. Li, Sorption-Enhanced Dry Reforming of Methane in a DBD Plasma Reactor for Single-Stage Carbon Capture and Utilization, ACS Sustain. Chem. Eng. 12 (2024) 10841–10853. https://doi.org/10.1021/acssuschemeng.4c02502.

[144] C. Egbuna, V.K. Parmar, J. Jeevanandam, S.M. Ezzat, K.C. Patrick-Iwuanyanwu, C.O. Adetunji, J. Khan, E.N. Onyeike, C.Z. Uche, M. Akram, M.S. Ibrahim, N.M. El Mahdy, C.G. Awuchi, K. Saravanan, H. Tijjani, U.E. Odoh, M. Messaoudi, J.C. Ifemeje, M.C. Olisah, N.J. Ezeofor, C.J. Chikwendu, C.G. Ibeabuchi, Toxicity of Nanoparticles in Biomedical Application: Nanotoxicology, J. Toxicol. 2021 (2021) 1–21. https://doi.org/10.1155/2021/9954443.

[145] L. Bröcker, T. Winzer, N. Steppan, J. Benedikt, C. Klages, Plasma polymerization of allyltrimethylsilane with single-filament dielectric-barrier discharges—Evidence of cationic surface processes, Plasma Process. Polym. 21 (2024) 2300177. https://doi.org/10.1002/ppap.202300177.

[146] A. Lin, M. Gromov, A. Nikiforov, E. Smits, A. Bogaerts, Characterization of Non-Thermal Dielectric Barrier Discharges for Plasma Medicine: From Plastic Well Plates to Skin Surfaces, Plasma Chem. Plasma Process. 43 (2023) 1587–1612. https://doi.org/10.1007/s11090-023-10389-w.

[147] P. Bílek, L. Kuthanová, T. Hoder, M. Šimek, Atmospheric pressure Townsend discharge in pure nitrogen—a test case for N_2 (A3Σu+,v) kinetics under low E/N conditions, Plasma Sources Sci. Technol. 31 (2022) 084004. https://doi.org/10.1088/1361-6595/ac7ad1.

[148] A. Belinger, S. Dap, N. Naudé, Influence of the dielectric thickness on the homogeneity of a diffuse dielectric barrier discharge in air, J. Phys. D: Appl. Phys. 55 (2022) 465201. https://doi.org/10.1088/1361-6463/ac9067.

[149] N. Gherardi, G. Gouda, E. Gat, A. Ricard, F. Massines, Transition from glow silent discharge to micro-discharges in nitrogen gas, Plasma Sources Sci. Technol. 9 (2000) 340–346. https://doi.org/10.1088/0963-0252/9/3/312.

[150] N. Naudé, J.-P. Cambronne, N. Gherardi, F. Massines, Electrical model of an atmospheric pressure Townsend-like discharge (APTD), Eur. Phys. J. Appl. Phys. 29 (2005) 173–180. https://doi.org/10.1051/epjap:2004197.

[151] N. Osawa, Y. Yoshioka, R. Hanaoka, Y. Mochizuki, Y. Kobayashi, Y. Yamada, Generation of uniform discharge by dielectric barrier discharge device in atmospheric-pressure air, Elect. Eng. Jpn. 180 (2012) 1–9. https://doi.org/10.1002/eej.21253.

[152] L. Cacot, G. Carnide, M.L. Kahn, R. Clergereaux, N. Naudé, L. Stafford, Kinetics driving thin-film deposition in dielectric barrier discharges using a direct liquid injector operated in a pulsed regime, J. Phys. D: Appl. Phys. 55 (2022) 475202. https://doi.org/10.1088/1361-6463/ac94de.

[153] G. Carnide, L. Cacot, Y. Champouret, V. Pozsgay, T. Verdier, A. Girardeau, M. Cavarroc, A. Sarkissian, A.-F. Mingotaud, C. Vahlas, M.L. Kahn, N. Naudé, L. Stafford, R. Clergereaux, Direct Liquid Reactor-Injector of Nanoparticles: A Safer-by-Design Aerosol Injection for Nanocomposite Thin-Film Deposition Adapted to Various Plasma-Assisted Processes, Coatings 13 (2023) 630. https://doi.org/10.3390/coatings13030630.

[154] S. Zhang, G.S. Oehrlein, From thermal catalysis to plasma catalysis: a review of surface processes and their characterizations, J. Phys. D: Appl. Phys. 54 (2021) 213001. https://doi.org/10.1088/1361-6463/abe572.

[155] G. Chen, J. Qu, P. Cheah, D. Cao, Y. Zhao, Y. Xiang, Size-Dependent Activity of Iron Nanoparticles in Both Thermal and Plasma Driven Catalytic Ammonia Decomposition, Ind. Eng. Chem. Res. 61 (2022) 11436–11443. https://doi.org/10.1021/acs.iecr.2c02092.

[156] S. Wang, V. Rohani, T. Ye, P. Dupont, S. Pagnon, M. Sennour, L. Fulcheri, Effect of K-promoter use in iron-based plasma-catalytic conversion of CO2 and CH4 into higher value products, Appl. Catal. A: Gen. 663 (2023) 119315. https://doi.org/10.1016/j.apcata.2023.119315.

[157] L. Hein, S. Coulombe, Synthesis and Characterization of Magnetic Nanoparticle-Decorated Multiwalled Carbon Nanotubes, ACS Omega (2024) acsomega.4c05027. https://doi.org/10.1021/acsomega.4c05027.

[158] M. Stafe, A. Marcu, N.N. Puscas, Pulsed Laser Ablation of Solids: Basics, Theory and Applications, Springer, Berlin, Heidelberg, 2014. https://doi.org/10.1007/978-3-642-40978-3.

[159] L. J. van der Pauw, A method of measuring specific resistivity and Hall effect of discs of arbitrary shape, Philips Res. Rep. 13 (1958) 1–9.

[160] M.A. McArthur, L. Jorge, S. Coulombe, S. Omanovic, Synthesis and characterization of 3D Ni nanoparticle/carbon nanotube cathodes for hydrogen evolution in alkaline electrolyte, J. Power Sources 266 (2014) 365–373. https://doi.org/10.1016/j.jpowsour.2014.05.036.

[161] E. Pajootan, S. Omanovic, S. Coulombe, Controllable dry synthesis of binder-free nanostructured platinum electrocatalysts supported on multi-walled carbon nanotubes and their performance in the oxygen reduction reaction, Chem. Eng. J. 426 (2021) 131706. https://doi.org/10.1016/j.cej.2021.131706.

[162] A. Pipa, R. Brandenburg, The Equivalent Circuit Approach for the Electrical Diagnostics of Dielectric Barrier Discharges: The Classical Theory and Recent Developments, Atoms 7 (2019) 14. https://doi.org/10.3390/atoms7010014.

[163] F. Peeters, T. Butterworth, Electrical Diagnostics of Dielectric Barrier Discharges, in: A. Nikiforov, Z. Chen (Eds.), Atmospheric Pressure Plasma - from Diagnostics to Applications, IntechOpen, 2019. https://doi.org/10.5772/intechopen.80433.

[164] Z. Falkenstein, J.J. Coogan, Microdischarge behaviour in the silent discharge of nitrogen - oxygen and water - air mixtures, J. Phys. D: Appl. Phys. 30 (1997) 817–825. https://doi.org/10.1088/0022-3727/30/5/015.

[165] R. Brandenburg, M. Schiorlin, M. Schmidt, H. Höft, A.V. Pipa, V. Brüser, Plane Parallel Barrier Discharges for Carbon Dioxide Splitting: Influence of Discharge Arrangement on Carbon Monoxide Formation, Plasma 6 (2023) 162–180. https://doi.org/10.3390/plasma6010013.

[166] R.H. Rad, V. Brüser, R. Brandenburg, Electrical characterization and imaging of discharge morphology in a small-scale packed bed dielectric barrier discharge, Plasma Sources Sci. Technol. 33 (2024) 025027. https://doi.org/10.1088/1361-6595/ad27ed.

[167] A. Fridman, Plasma Chemistry, Cambridge University Press, Cambridge, 2008. https://doi.org/10.1017/CBO9780511546075.

[168] S. Ding, J. Jia, B. Xu, Z. Dai, Y. Wang, S. Shen, Y. Yin, X. Li, Overrated energy storage performances of dielectrics seriously affected by fringing effect and parasitic capacitance, Nat. Commun. 16 (2025) 608. https://doi.org/10.1038/s41467-025-55855-5.

[169] H. Mahdikia, V. Brüser, M. Schiorlin, R. Brandenburg, CO2 Dissociation in Barrier Corona Discharges: Effect of Elevated Pressures in CO2/Ar Mixtures, Plasma Chem. Plasma Process. 43 (2023) 2035–2063. https://doi.org/10.1007/s11090-023-10411-1.

[170] M. Laroussi, Low-Temperature Plasma Jet for Biomedical Applications: A Review, IEEE Trans. Plasma Sci. 43 (2015) 703–712. https://doi.org/10.1109/TPS.2015.2403307.

[171] L. Lin, Q. Wang, Microplasma: A New Generation of Technology for Functional Nanomaterial Synthesis, Plasma Chem. Plasma Process. 35 (2015) 925–962. https://doi.org/10.1007/s11090-015-9640-y.

[172] A. Bogaerts, E. Neyts, R. Gijbels, J. van der Mullen, Gas Discharge Plasmas and Their Applications, Spectrochim. Acta B 57 (2002) 609–658. https://doi.org/10.1016/S0584-8547(01)00406-2.

[173] J.T. Gudmundsson, A. Hecimovic, Foundations of DC Plasma Sources, Plasma Sources Sci. Technol. 26 (2017) 123001. https://doi.org/10.1088/1361-6595/aa940d.

[174] W.-H. Chiang, D. Mariotti, R.M. Sankaran, J.G. Eden, K. (Ken) Ostrikov, Microplasmas for Advanced Materials and Devices, Adv. Mater. 32 (2020) 1905508. https://doi.org/10.1002/adma.201905508.

[175] K.H. Schoenbach, K. Becker, 20 Years of Microplasma Research: A Status Report, Eur. Phys. J. D 70 (2016) 29. https://doi.org/10.1140/epjd/e2015-60618-1.

[176] F. Iza, G.J. Kim, S.M. Lee, J.K. Lee, J.L. Walsh, Y.T. Zhang, M.G. Kong, Microplasmas: Sources, Particle Kinetics, and Biomedical Applications, Plasma Process. Polym. 5 (2008) 322–344. https://doi.org/10.1002/ppap.200700162.

[177] R. Foest, M. Schmidt, K. Becker, Microplasmas, an Emerging Field of Low-Temperature Plasma Science and Technology, Int. J. Mass Spectrom. 248 (2006) 87–102. https://doi.org/10.1016/j.ijms.2005.11.010.

[178] V. Karanassios, Microplasmas for Chemical Analysis: Analytical Tools or Research Toys?, Spectrochim. Acta B 59 (2004) 909–928. https://doi.org/10.1016/j.sab.2004.04.005.

[179] K. Matra, Y. Mizobuchi, H. Furuta, A. Hatta, Local Sputter Etching by Micro Plasma Jet in SEM, Vacuum 87 (2013) 132–135. https://doi.org/10.1016/j.vacuum.2012.03.011.

[180] J. Mulders, P. Trompenaars, An In-Situ Low Energy Argon Ion Source for Local Surface Modification, in: European Microscopy Congress 2016: Proceedings, John Wiley & Sons, Ltd, 2016: pp. 453–454. https://doi.org/10.1002/9783527808465.EMC2016.6024.

[181] K. Pardinas, Design and Implementation of an In-Situ Microplasma Cell in an Environmental Scanning Electron Microscope for the Study of Plasma-Surface Interaction, Undergraduate Thesis, Princeton University, 2016.

[182] K. Tomatsu, T. Aoki, K. Kobayashi, T. Omura, A. Hatta, *In situ* scanning electron microscopy of hydrogen embrittlement by near atmospheric-pressure hydrogen microplasma jet, Rev. Sci. Instrum. 94 (2023) 023707. https://doi.org/10.1063/5.0129618.

[183] A. Massone, A. Manhard, W. Jacob, A. Drexler, W. Ecker, A. Hohenwarter, S. Wurster, D. Kiener, An SEM compatible plasma cell for *in situ* studies of hydrogen-material interaction, Rev. Sci. Instrum. 91 (2020) 043705. https://doi.org/10.1063/1.5142043.

[184] D. Phifer, L. Tuma, T. Vystavel, P. Wandrol, R.J. Young, Improving SEM Imaging Performance Using Beam Deceleration, Microscopy Today 17 (2009) 40–49. https://doi.org/10.1017/S1551929509000170.

[185] J. Jiruše, M. Havelka, F. Lopour, Novel Field Emission SEM Column with Beam Deceleration Technology, Ultramicroscopy 146 (2014) 27–32. https://doi.org/10.1016/j.ultramic.2014.05.006.

[186] R. Isaacs, A. Prokhodtseva, T. Vystavel, In-Situ Low Energy Argon Ion Source for the Improvement of EBSD Pattern Acquisition, Microsc. Microanal. 24 (2018) 1060–1061. https://doi.org/10.1017/S1431927618005780.

[187] M. Dutka, R. Isaacs, A. Prokhodtseva, T. Vystavěl, In-Situ Low Energy Argon Ion Source for Artifact Free High Resolution STEM Imaging, Microsc. Microanal. 25 (2019) 548–549. https://doi.org/10.1017/S1431927619003477.

[188] G.D. Danilatos, Foundations of Environmental Scanning Electron Microscopy, in: P.W. Hawkes (Ed.), Advances in Electronics and Electron Physics, Academic Press, 1988: pp. 109–250. https://doi.org/10.1016/S0065-2539(08)60902-6.

[189] K. Matra, H. Furuta, A. Hatta, Current-Voltage Characteristics of DC Discharge in Micro Gas Jet Injected into Vacuum Environment, J. Phys. Conf. Ser. 441 (2013) 012021. https://doi.org/10.1088/1742-6596/441/1/012021.

[190] K. Matra, Characteristics of Micro Plasma Jet in SEM and Its Applications, PhD Thesis, Kochi University of Technology, 2013.

[191] K. Matra, H. Furuta, A. Hatta, DC Microplasma Jet for Local a:C-H Deposition Operated in SEM Chamber, Micromachines 8 (2017) 211. https://doi.org/10.3390/mi8070211.

[192] X. Lu, M. Laroussi, V. Puech, On Atmospheric-Pressure Non-Equilibrium Plasma Jets and Plasma Bullets, Plasma Sources Sci. Technol. 21 (2012) 034005. https://doi.org/10.1088/0963-0252/21/3/034005.

[193] E.P. Muntz, S.J. Abel, B.L. Maguire, The Electron Beam Fluorescence Probe in Experimental Gas Dynamics, IEEE Trans. Aerosp. AS-3 (1965) 210–222. https://doi.org/10.1109/TA.1965.4319804.

[194] F. Sharipov, Numerical Simulation of Rarefied Gas Flow through a Thin Orifice, J. Fluid Mech. 518 (2004) 35–60. https://doi.org/10.1017/S0022112004000710.

[195] S. Misdanitis, S. Pantazis, D. Valougeorgis, Pressure Driven Rarefied Gas Flow through a Slit and an Orifice, Vacuum 86 (2012) 1701–1708. https://doi.org/10.1016/j.vacuum.2012.02.014.

[196] N.Y. Bykov, V.V. Zakharov, Binary Gas Mixture Outflow into Vacuum through an Orifice, Phys. Fluids 32 (2020) 067109. https://doi.org/10.1063/5.0009548.

[197] F. Salehi, A.J. Goers, L. Feder, B. Miao, D. Woodbury, H.M. Milchberg, Characterization of a 100 Micrometer-Scale Cryogenically Cooled Gas Jet for near-Critical Density Laser-Plasma Experiments, Rev. Sci. Instrum. 90 (2019) 103001. https://doi.org/10.1063/1.5109033.

[198] M. Patel, J. Thomas, H.C. Joshi, Flow Characterization of Supersonic Gas Jets: Experiments and Simulations, Vacuum 192 (2021) 110440. https://doi.org/10.1016/j.vacuum.2021.110440.

[199] V.A. Lisovskiy, S.D. Yakovin, V.D. Yegorenkov, Low-Pressure Gas Breakdown in Uniform Dc Electric Field, J. Phys. D: Appl. Phys. 33 (2000) 2722. https://doi.org/10.1088/0022-3727/33/21/310.

[200] V.A. Lisovskiy, R.O. Osmayev, A.V. Gapon, S.V. Dudin, I.S. Lesnik, V.D. Yegorenkov, Electric Field Non-Uniformity Effect on Dc Low Pressure Gas Breakdown between Flat Electrodes, Vacuum 145 (2017) 19–29. https://doi.org/10.1016/j.vacuum.2017.08.022.

[201] P. Mathew, J. George, S. Mathews T, P.J. Kurian, Experimental Verification of Modified Paschen's Law in DC Glow Discharge Argon Plasma, AIP Adv. 9 (2019) 025215. https://doi.org/10.1063/1.5086246.

[202] Y. Fu, P. Zhang, J.P. Verboncoeur, X. Wang, Electrical Breakdown from Macro to Micro/Nano Scales: A Tutorial and a Review of the State of the Art, Plasma Res. Express 2 (2020) 013001. https://doi.org/10.1088/2516-1067/ab6c84.

[203] L. Grünewald, D. Chezganov, R. De Meyer, A. Orekhov, S. Van Aert, A. Bogaerts, S. Bals, J. Verbeeck, In Situ Plasma Studies Using a Direct Current Microplasma in a Scanning Electron Microscope, Adv. Mater. Technol. 9 (2024) 2301632. https://doi.org/10.1002/admt.202301632.

[204] D.J. Stokes, Environmental Scanning Electron Microscopy for Biology and Polymer Science, Wiley Analytical Science (2012).

[205] V. Neděla, E. Tihlaříková, J. Runštuk, J. Hudec, High-Efficiency Detector of Secondary and Backscattered Electrons for Low-Dose Imaging in the ESEM, Ultramicroscopy 184 (2018) 1–11. https://doi.org/10.1016/j.ultramic.2017.08.003.

[206] A. Güntherschulze, W. Tollmien, Neue Untersuchungen über die Kathodenzerstäubung der Glimmentladung, Z. Phys. 119 (1942) 685–695. https://doi.org/10.1007/BF01340472.

[207] O. Auciello, Ion Interaction with Solids: Surface Texturing, Some Bulk Effects, and Their Possible Applications, J. Vac. Sci. Technol. 19 (1981) 841–867. https://doi.org/10.1116/1.571224.

[208] G.K. Wehner, Cone Formation as a Result of Whisker Growth on Ion Bombarded Metal Surfaces, J. Vac. Sci. Technol. A 3 (1985) 1821–1835. https://doi.org/10.1116/1.573386.

[209] A. van Teijlingen, S. A. Davis, S. R. Hall, Size-Dependent Melting Point Depression of Nickel Nanoparticles, Nanoscale Adv. 2 (2020) 2347–2351. https://doi.org/10.1039/D0NA00153H.

[210] C. Pabari, Size Dependent Properties of Metallic Nanoparticles, Mater. Today: Proc. 55 (2022) 98–101. https://doi.org/10.1016/j.matpr.2021.12.375.

[211] Z. Ye, L. Zhao, A. Nikiforov, J.-M. Giraudon, Y. Chen, J. Wang, X. Tu, A Review of the Advances in Catalyst Modification Using Nonthermal Plasma: Process, Mechanism and Applications, Adv. Colloid Interface Sci. 308 (2022) 102755. https://doi.org/10.1016/j.cis.2022.102755.

[212] D. Serafin, W.J. Nowak, B. Wierzba, The Effect of Surface Preparation on High Temperature Oxidation of Ni, Cu and Ni-Cu Alloy, Appl. Surf. Sci. 476 (2019) 442–451. https://doi.org/10.1016/j.apsusc.2019.01.122.

[213] P. Song, D. Wen, Z.X. Guo, T. Korakianitis, Oxidation Investigation of Nickel Nanoparticles, Phys. Chem. Chem. Phys. 10 (2008) 5057–5065. https://doi.org/10.1039/B800672E.

[214] R. Sainju, D. Rathnayake, H. Tan, G. Bollas, A.M. Dongare, S.L. Suib, Y. Zhu, In Situ Studies of Single-Nanoparticle-Level Nickel Thermal Oxidation: From Early Oxide Nucleation to Diffusion-Balanced Oxide Thickening, ACS Nano 16 (2022) 6468–6479. https://doi.org/10.1021/acsnano.2c00742.

[215] S. Kunze, L.C. Tănase, M.J. Prieto, P. Grosse, F. Scholten, L. de S. Caldas, D. van Vörden, T. Schmidt, B.R. Cuenya, Plasma-Assisted Oxidation of Cu(100) and Cu(111), Chem. Sci. 12 (2021) 14241–14253. https://doi.org/10.1039/D1SC04861A.

[216] Y. Xia, P. Sautet, Plasma Oxidation of Copper: Molecular Dynamics Study with Neural Network Potentials, ACS Nano 16 (2022) 20680–20692. https://doi.org/10.1021/acsnano.2c07712.

[217] T. von Woedtke, S. Reuter, K. Masur, K.-D. Weltmann, Plasmas for Medicine, Phys. Rep. 530 (2013) 291–320. https://doi.org/10.1016/j.physrep.2013.05.005.

[218] W. Grimm, Eine neue Glimmentladungslampe für die optische Emissionsspektralanalyse, Spectrochim. Acta B 23 (1968) 443–454. https://doi.org/10.1016/0584-8547(68)80023-0.

[219] G. Gamez, M. Voronov, S.J. Ray, V. Hoffmann, G.M. Hieftje, J. Michler, Surface Elemental Mapping via Glow Discharge Optical Emission Spectroscopy, Spectrochim. Acta B 70 (2012) 1–9. https://doi.org/10.1016/j.sab.2012.04.007.

[220] L. Pillatsch, F. Östlund, J. Michler, FIBSIMS: A Review of Secondary Ion Mass Spectrometry for Analytical Dual Beam Focussed Ion Beam Instruments, Prog. Cryst. Growth Charact. Mater. 65 (2019) 1–19. https://doi.org/10.1016/j.pcrysgrow.2018.10.001.

[221] X. Llovet, A. Moy, P.T. Pinard, J.H. Fournelle, Electron Probe Microanalysis: A Review of Recent Developments and Applications in Materials Science and Engineering, Prog. Mater. Sci. 116 (2021) 100673. https://doi.org/10.1016/j.pmatsci.2020.100673.

[222] N. Brodusch, H. Demers, A. Gellé, A. Moores, R. Gauvin, Electron Energy-Loss Spectroscopy (EELS) with a Cold-Field Emission Scanning Electron Microscope at Low Accelerating Voltage in Transmission Mode, Ultramicroscopy 203 (2019) 21–36. https://doi.org/10.1016/j.ultramic.2018.12.015.

[223] K. Tai, T.J. Houlahan, J.G. Eden, S.J. Dillon, Integration of Microplasma with Transmission Electron Microscopy: Real-time Observation of Gold Sputtering and Island Formation, Sci. Rep. 3 (2013) 1325. https://doi.org/10.1038/srep01325.

[224] W. Becker, The Turbomolecular Pump, Its Design, Operation and Theory; Calculation of the Pumping Speed for Various Gases and Their Dependence on the Forepump, Vacuum 16 (1966) 625–632. https://doi.org/10.1016/0042-207X(66)91425-4.

[225] L. Grünewald, D. Chezganov, R. De Meyer, A. Orekhov, S. Van Aert, A. Bogaerts, S. Bals, J. Verbeeck, Supplementary Information for “In-situ Plasma Studies Using a Direct Current Microplasma in a Scanning Electron Microscope,” (2023). https://doi.org/10.5281/zenodo.8042029.

[226] F. de la Peña, E. Prestat, V.T. Fauske, P. Burdet, J. Lähnemann, P. Jokubauskas, T. Furnival, M. Nord, T. Ostasevicius, K.E. MacArthur, D.N. Johnstone, M. Sarahan, J. Taillon, T. Aarholt, pquinn-dls, V. Migunov, A. Eljarrat, J. Caron, C. Francis, T. Nemoto, T. Poon, S. Mazzucco, actions-user, N. Tappy, N. Cautaerts, S. Somnath, T. Slater, M. Walls, F. Winkler, H.W. Ånes, Hyperspy/Hyperspy: Release v1.7.3, (2022). https://doi.org/10.5281/zenodo.7263263.